

AD-A139 603

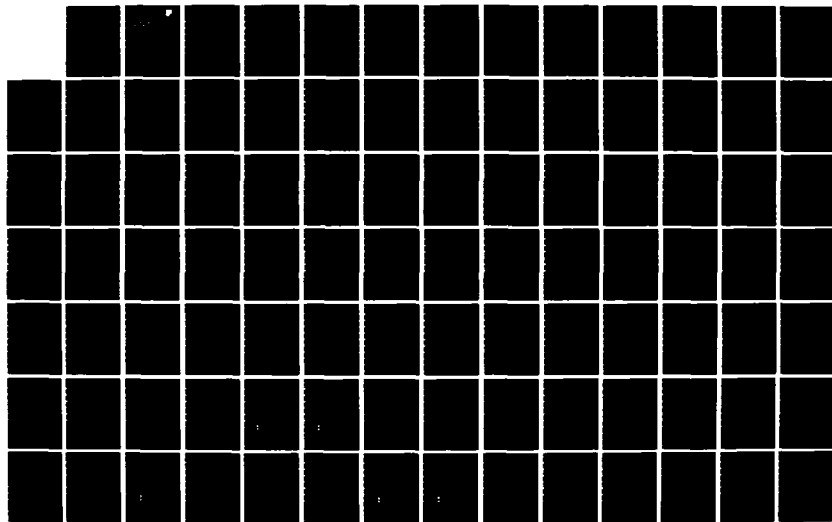
MATHEMATICAL MODELLING OF WAVEGUIDING TECHNIQUES AND
ELECTRON TRANSPORT VOLUME 1(U) ARCON CORP WALTHAM MA
S MOOLF ET AL. JAN 84 RADC-TR-83-313-VOL-1
F19628-78-C-0188

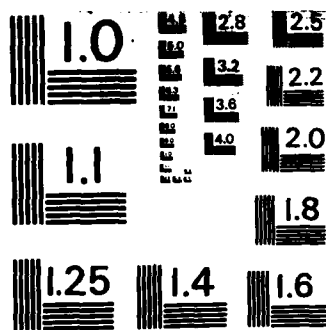
1/3

UNCLASSIFIED

F/G 12/1

NL





MICROCOPY RESOLUTION TEST CHART
NATIONAL BUREAU OF STANDARDS-1963-A

72
RADC-TR-83-313, Vol I (of two)
Final Technical Report
January 1984



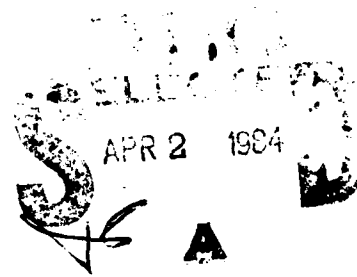
MATHEMATICAL MODELLING OF WAVEGUIDING TECHNIQUES AND ELECTRON TRANSPORT

Arcon Corporation

Peter P. Wintersteiner
Stanley Woolf

APPROVED FOR PUBLIC RELEASE; DISTRIBUTION UNLIMITED

ROME AIR DEVELOPMENT CENTER
Air Force Systems Command
Griffiss Air Force Base, NY 13441



DTIC FILE COPY


84 03 30 005

AD A139603

This report has been reviewed by the RADC Public Affairs Office (PA) and is releasable to the National Technical Information Service (NTIS). At NTIS it will be releasable to the general public, including foreign nations.

RADC-83-313, Vol I (of two) has been reviewed and is approved for publication.

APPROVED:



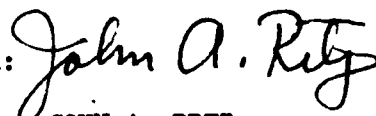
PETER D. GIANINO
Project Engineer

APPROVED:



HAROLD ROTH, Director
Solid State Sciences Division

FOR THE COMMANDER:



JOHN A. RITZ
Acting Chief, Plans Office

If your address has changed or if you wish to be removed from the RADC mailing list, or if the addressee is no longer employed by your organization, please notify RADC (ESO), Hanscom AFB MA 01731. This will assist us in maintaining a current mailing list.

Do not return copies of this report unless contractual obligations or notices on a specific document requires that it be returned.

UNCLASSIFIED

SECURITY CLASSIFICATION OF THIS PAGE (When Data Entered)

REPORT DOCUMENTATION PAGE		READ INSTRUCTIONS BEFORE COMPLETING FORM
1. REPORT NUMBER RADC-TR-83-313, Vol I (of two)	2. GOVT ACCESSION NO. AD 1139103	3. RECIPIENT'S CATALOG NUMBER
4. TITLE (and Subtitle) MATHEMATICAL MODELLING OF WAVEGUIDING TECHNIQUES AND ELECTRON TRANSPORT		5. TYPE OF REPORT & PERIOD COVERED Final Technical Report 1 Feb 78 - 30 Sep 82
7. AUTHOR(s) Stanley Woolf Peter P. Wintersteiner		6. PERFORMING ORG. REPORT NUMBER N/A
9. PERFORMING ORGANIZATION NAME AND ADDRESS Arcon Corporation 260 Bear Hill Road Waltham MA 02154		8. CONTRACT OR GRANT NUMBER(s) F19628-78-C-0188
11. CONTROLLING OFFICE NAME AND ADDRESS Rome Air Development Center (ESO) Hanscom AFB MA 01731		10. PROGRAM ELEMENT, PROJECT, TASK AREA & WORK UNIT NUMBERS 61102F 2306J230
14. MONITORING AGENCY NAME & ADDRESS (if different from Controlling Office) Same		12. REPORT DATE January 1984
		13. NUMBER OF PAGES 274
		15. SECURITY CLASS. (of this report) UNCLASSIFIED
		16. DECLASSIFICATION/DOWNGRADING SCHEDULE N/A
16. DISTRIBUTION STATEMENT (of this Report) Approved for public release; distribution unlimited		
17. DISTRIBUTION STATEMENT (of the abstract entered in Block 20, if different from Report) Same		
18. SUPPLEMENTARY NOTES RADC Project Engineer: Peter D. Gianino (ESO)		
19. KEY WORDS (Continue on reverse side if necessary and identify by block number)		
Dielectric Waveguides	Multilayered Waveguides	Electron Transport
Coupled Waveguides	Integral Equation Technique	Energy Deposition
Propagation	Variational Principle	Charge Deposition
Modal Properties	Photorefractive Effect	Dose-Depth Distri-
Crosstalk	Phase Conjugate Optics	bution (Over)
20. ABSTRACT (Continue on reverse side if necessary and identify by block number) In this report we will describe the techniques and computer programs developed to analyze various problems. The scope of ^{this} work extended into three technical areas: 1) the study of dielectric waveguide modes and arrays of dielectric waveguides; 2) the study of a mechanism for producing diffraction gratings in crystals exhibiting photorefractivity; ⁱⁿ 3) the problem of electron scattering and transport in solids.		

DD FORM 1473

1 JAN 73

EDITION OF 1 NOV 68 IS OBSOLETE

UNCLASSIFIED

SECURITY CLASSIFICATION OF THIS PAGE (When Data Entered)

UNCLASSIFIED

SECURITY CLASSIFICATION OF THIS PAGE (When Data Entered)

Block 18. Key Words (Cont'd)

Method of Discrete Ordinates
Multigroup Transport
Monte Carlo Method
Multiple Scattering
Polymer Irradiation by Electrons



Accession For	
NTIS GRA&I	<input checked="" type="checkbox"/>
DTIC TAB	<input type="checkbox"/>
Unannounced	<input type="checkbox"/>
Justification	
By	
Distribution/	
Availability Codes	
Dist	Avail and/or Special
A-1	

UNCLASSIFIED

SECURITY CLASSIFICATION OF THIS PAGE (When Data Entered)

TABLE OF CONTENTS

<u>Section</u>	<u>Page</u>
PREFACE	viii
I. INTRODUCTION	1
II. MODES OF DIELECTRIC WAVEGUIDES AND ARRAYS OF DIELECTRIC WAVEGUIDES	2
1. Introduction	2
2. Isolated Step-Index Guides	4
2.1 The Basic Integral Equation	4
2.2 Equivalent Linear Equations	7
2.3 Symmetry Considerations	12
2.4 Computational Considerations	14
2.5 Results	19
2.5.1 Rectangular Cross-Sections	19
2.5.2 Elliptical Cross Sections	31
2.5.3 Other Results	40
3. Arrays of Step-Index Guides	41
3.1 Introduction	41
3.2 Equations for a General Array	42
3.3 The Two-Guide Problem	48
3.3.1 Linear Equation for Two Guides	48
3.3.2 Normalized Parameters for the Two-Guide Problem	52
3.3.3 Special Cases for Two Guides	57
3.3.4 Results of Two Guides	60
3.3.4.1 General Discussion	60
3.3.4.2 Results for Two Identical Guides	61
3.3.4.3 Results for Two Dissimilar Guides	78
3.4 Final Equations for a General Array	83
3.5 Linear Arrays of More than Two Guides	86
3.5.1 General Considerations	86
3.5.2 Results for a Linear Array	88
3.6 Summary	94

TABLE OF CONTENTS (Continued)

<u>Section</u>	<u>Page</u>
4. Multilayered Step-Index Guides	94
4.1 Introduction	94
4.2 Outline of the Formulation for Multilayered Guides	96
4.3 Equations for the Cladded Guides	99
4.3.1 Parameterization	99
4.3.2 Cosine Solutions	100
4.3.3 Sine Solutions	102
4.3.4 Special Considerations	103
4.4 Equations for the Ring Guide	104
4.4.1 Parameterization	104
4.4.2 Cosine Solutions	105
4.4.3 Sine Solutions	106
4.4.4 Special Cases	107
5. A Variational Approach to Composite Systems	107
5.1 Introduction	107
5.2 Basic Equations	109
5.3 Equations for the Core-Ring Guide	113
5.4 Results for the Core-Ring Guide	117
5.4.1 Illustrative Results	117
5.4.2 Power Transfer by Composite Mode Pairs; Comparison with Coupled Mode Theory	121
5.4.3 Power Transfer with Several Modes	128
5.5 Adjacent Coupled Guides	134
6. Use of the Programs	137
6.1 General Comments	137
6.2 Function	137
6.3 Input Parameters for the Integral-Equation Technique Programs	138
6.3.1 Organization	138
6.3.2 Program Parameters	139
6.3.3 Physical Parameters	140

TABLE OF CONTENTS (Continued)

<u>Section</u>	<u>Page</u>
6.4 Job Control Language	142
6.5 Program VAR	143
7. References	149
III. QUANTITATIVE STUDY OF A MECHANISM FOR PRODUCING DIFFRACTION GRATINGS IN CRYSTALS EXHIBITING PHOTOREFRACTIVITY	152
1. Introduction	152
2. Formulation	153
2.1 Definitions of Fields	153
2.2 Initial Conditions	153
2.3 Basic Equations	154
2.4 Differential Equations	154
3. Software and Numerical Procedures	157
3.1 GRATING	157
3.2 PDECOL	157
3.3 Boundary Conditions	159
3.4 Initial Conditions	161
3.5 Evaluation of the Space-Charge Field	162
3.6 Erase Mode	163
3.7 Working-time Increments	163
4. Results	165
4.1 Introduction	165
4.2 Time Scales	166
4.3 Time Development of the Space-Charge Field	167
4.4 Spatial Distributions	168
4.5 Effect of Varying R	170
4.6 Miscellaneous Results; Limiting Case	171
5. References	192
IV. ELECTRON TRANSPORT	193
A. SOLUTION OF THE ELECTRON TRANSPORT EQUATION BY THE METHOD OF DISCRETE ORDINATES	193
1. Introduction	193
2. The Method of Discrete Ordinates-General Discussion	193

TABLE OF CONTENTS (Continued)

<u>Section</u>	<u>Page</u>
2.1 The Diamond Differences Approximation	197
2.2 Coarse Mesh Rebalance	199
2.3 The Finite Element or Linear Discontinuous Flux Extrapolation Scheme	202
2.4 The ARCON Discrete Ordinates Code Collection-SNARC	203
2.4.1 Program ONEDSN	204
2.4.2 Application of Program BEAMSRC to Henyey-Greenstein Scattering	206
2.4.3 Application of Program BEAMSRC to Electron Transport Problems	209
2.4.3.1 One-Group Calculations	209
2.4.3.2 Multigroup Calculations	214
2.5 Electron Transport Calculations with ONETRAN ⁽¹⁾	219
B. SOLUTION OF ELECTRON TRANSPORT PROBLEMS BY THE MONTE CARLO METHOD	229
1. Introduction	229
2. Program MCEL - A Single Scattering Monte Carlo Code for KeV Electron Transport	230
2.1 Objective	230
2.2 Quantities Calculated	230
2.3 Principles of Operation	231
2.4 Description of Routines	232
2.4.1 MCEL (= Main Program)	232
2.4.2 SETRUN	233
2.4.3 ESET	233
2.4.4 SETHIS	233
2.4.5 PENET	234
2.4.6 ENERGY	234
2.4.7 ANGLES	235
2.4.8 SCORE	237
2.4.9 PROC	237
2.4.10 STATS	238
2.5 Comparison of MCEL Results with other Calculations and Experimental Data	239
3. Program MULTSCT - Multiple Scattering Monte Carlo Code for KeV Electron Transport	240

TABLE OF CONTENTS (Continued)

<u>Section</u>	<u>Page</u>
3.1 Objective	240
3.2 Quantities Calculated	240
3.3 Principles of Operation	242
3.3.1 Incorporation of Electric Field Equations	243
3.4 Description of Routines	246
3.4.1 MULTSCT (= Main Program)	246
3.4.2 SETRUN	246
3.4.3 ESET	247
3.4.4 SETHIS	247
3.4.5 PENET	247
3.4.6 ENERGY	247
3.4.7 ANGLES	248
3.4.8 SCORE, PROC, STATS	248
3.5 Comparison of MULTSCT Results with other Calculations and Experimental Data	248
3.6 MULTSCT Simulation of Polymer Irradiation by Electrons	250
4. Program MCINIF, a set of Three Monte Carlo Programs to Treat the Interface Dose Problem for Electrons in the 1 MeV Energy Range	252
4.1 Objective	252
4.2 Principles of Operation	252
4.3 Program BIGSLAB, Quantities Calculated	253
4.4 Program INTFC, Quantities Calculated	257
4.5 Program MCSPLIT, Quantities Calculated	259
5. Application of the TIGER ⁽¹⁰⁾ Monte Carlo Code to the Determination of Charge Deposition in Electron Irradiated Polymers	261
6. References	264

PREFACE

The analysis, computer programs and results discussed herein are the result of analytical research performed for

Rome Air Development Center
Deputy for Electronic Technology
L.G. Hanscom Air Force Base, Massachusetts 01731.

Sections II and III of this report were prepared by Peter P. Wintersteiner, and Section IV was prepared by Stanley Woolf.

I. INTRODUCTION

During the past fifty-six months our work consisted of technical efforts in the areas of dielectric waveguide mode and array studies, a quantitative study of mechanism for producing diffraction gratings in crystals exhibiting photorefractivity, and electron scattering, transport and energy deposition in solids. These efforts resulted in the construction of mathematical models and accompanying computer programs which will be described in the following sections (Volume I). The computer program listings are provided in Volume II.

II. MODES OF DIELECTRIC WAVEGUIDES AND ARRAYS OF DIELECTRIC WAVEGUIDES

1. Introduction

A substantial effort was devoted to the study of the properties of the modes of various constant-index dielectric waveguides and systems of such guides. This portion of the work can be broken down in the following manner:

- 1) Use of an integral-equation technique to find the modes of two-medium step-index waveguides of arbitrary cross-section, using the scalar approximation.
- 2) Use of the integral-equation technique to find the modes of arrays of parallel guides of arbitrary shape and arbitrary orientation in the cross-sectional plane. The scalar approximation was used here as well.
- 3) Use of the integral-equation technique to find the modes of single guides with three concentric regions of differing refractive index.
- 4) Use of a variational calculation to approximate the modes of simple composite systems. In particular, the problem of a circular concentric configuration (the "multiple-layered" or "core-ring" guide) was treated with emphasis on multimode operation. The problem of two adjacent circular guides was also considered.

The usefulness of establishing the propagation properties of the various waveguiding systems mentioned above has been understood for many years. Simple two-region guides are used for optical communications and remote sensing systems in hundreds of ways, and also have microwave applications. Arrays of guides, particularly in single-mode operation, are the key elements of switches, modulators, and other devices having a multitude of applications. Multilayered guides are also finding their way into new systems. In particular, tube guides and W-profile guides have superior dispersion characteristics; and concentric core-ring guides are being explored for duplex transmission and secure-communication purposes.

The integral-equation technique offers the opportunity to solve for the modes of all these configurations within a uniform framework. Also, since it is indifferent to the shape of the guide cross-sections encountered, it applies to a variety of situations which normally would require separate formulations. (The need to study non-circular cross-sections derives from problems involving imperfectly-formed near-round cores, purposely-designed

elliptical cores, and rectangular or near-rectangular shapes used in integrated optics---among others.) For these reasons we have carried through the analysis and developed several FORTRAN programs to deal with the most important configurations. The programs have not been combined into a single software package, but this could be accomplished with a modest effort.

The effort reported here was restricted to the scalar, or weakly-guiding, approximation which is appropriate for most optical wave-guides. However, as indicated in Reference 1, the integral-equation technique can be extended to obtain the full vector solutions for the waveguide modes, and as such is also applicable to microwave problems and problems involving the polarization of optical signals.

The formulation we have developed is basically a two-dimensional one, and as such does not apply to guides or arrays which have geometrical variations in the longitudinal direction.

The direct results of the computations described below are the normalized propagation curves and the spatial mode patterns. Once the physical parameters of a system---the wavelength, the guide dimensions, the geometrical configuration (in the case of an array), and the indices of refraction---are specified, these quantities and others which can be derived from them can be obtained. The latter include dispersion, beat-lengths, and power transfer among elements of arrays.

The principle scientific accomplishments of this work have been published in References 1-5. They include, apart from the numerical data themselves:

- 1) the demonstration of the efficacy and usefulness of the integral-equation technique and the variational calculation;
- 2) the development of an ability to study modal properties of complicated systems which could not otherwise be treated;
- 3) the simplification of the computations for relatively modest systems, like the two-region elliptical core waveguide, which can be treated by other means (e.g., separation of variables) at a gruesome cost in complexity;
- 4) the evaluation of evanescent-field crosstalk in circular concentric core-ring guides, leading to the recognition that:
 - a) the crosstalk is due almost entirely to the modes nearest cutoff, and
 - b) the crosstalk is extremely sensitive to changes in the physical parameters of the system;

- 5) the direct comparison of modal properties of guides as their shapes are varied continuously; and
- 6) the confirmation of many results from previous work of other authors, production of the only reliable estimates of errors resulting from approximations which are required by their techniques, and identification of general circumstances in which these errors may or may not be significant.

Most of the results that we present involve elliptical and rectangular cross-sections, but calculations for other shapes were also done.

Section II is organized according to the four divisions indicated at the beginning of this introduction. The formulation of the various problems in terms of integral equations is similar and relies upon the same basic ideas. As a consequence, much of the discussion of Section II.2, although not repeated, applies to Sections II.3 and II.4.

2. Isolated Step-Index Guides

2.1 The Basic Integral Equation

The general procedure of the integral-equation technique is to derive an integral representation for the various field components that is equivalent to the appropriate differential equations inside and outside the guiding regions and that guarantees as well that the boundary conditions are satisfied. These differential equations for the field components inside the guides have a known set of solutions which can be considered a set of basis functions. The field components can be expanded in series of these basis functions, with unknown coefficients. On introducing the expansions into the integral representations, they become sets of linear (matrix) equations whose matrix elements involve the basis functions in line integrals that are taken over the boundary of the cross-sectional shape. This is the only way the boundary enters; there is no need to match interior and exterior solutions across it. Since the set of matrix equations is a homogeneous one, it has solutions only for certain allowed values of the parameters involved. One of these parameters is the propagation constant which we seek.

The description above applies to guides of index n_1 embedded in a medium of smaller index n_2 , with no other restrictions on the magnitudes of n_1 , or n_2 . In practice, however, it is very common for n_1

to be very close to n_2 . In this "weakly-guiding" case certain vectorial aspects of the general procedure outlined above become simpler, and in fact the problem can be reduced in a good approximation to a scalar one. We have therefore concentrated on this scalar formulation and based our numerical calculations upon it.

The geometrical arrangement which we assume for isolated step-index waveguides is shown in Fig. 1. The cladding (n_2) is assumed to be infinite in extent. In all that follows, we assume that the t - and z -dependence of the solutions corresponding to wave propagation along the guide is entirely contained in the factor $\exp(ik_g z - i\omega t)$, k_g being the propagation constant to be found. With the definitions

$$k_0 = \omega c \quad (1a)$$

$$k_1 = k_0 n_1 \quad (1b)$$

$$k_2 = k_0 n_2 \quad (1c)$$

and

$$\gamma_1^2 = k_1^2 - k_g^2 \quad (2a)$$

$$\gamma_2^2 = k_2^2 - k_g^2 \quad (2b)$$

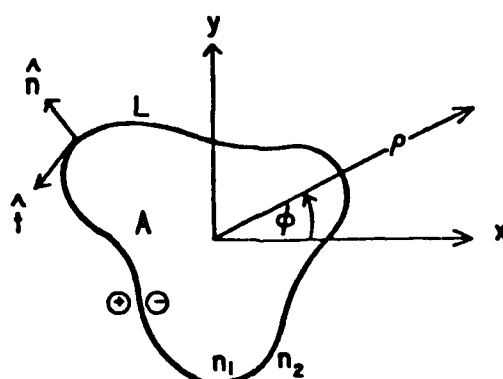


Fig. 1 The cross-section of a cylindrical dielectric waveguide parallel to the z -axis. The interior is denoted by A , and the boundary curve by L . The outward normal to the cylinder is \hat{n} and the unit vector tangent to L is \hat{t} . The positive z -axis is out of the plane of the paper.

one can immediately show from the wave equation that the electric field (and, separately, each component of it) satisfies

$$(\vec{\nabla}^2 + \gamma_1^2) \vec{E}(\vec{r}) = 0 \quad \vec{r} \text{ inside } A \quad (3a)$$

$$(\vec{\nabla}^2 + \gamma_2^2) \vec{E}(\vec{r}) = 0 \quad \vec{r} \text{ outside } A \quad (3b)$$

where $\vec{\nabla}^2$ is the two-dimensional Laplacian. The magnetic field $\vec{B}(\vec{r})$ satisfies the same equations. Of course, as is well known, the propagation constant satisfies the inequality $k_1 > k_g > k_2$ for guided modes, so γ_1 is real and γ_2 is purely imaginary.

The basic idea of the scalar approximation is that the longitudinal field components (E_z, B_z) are small compared to the transverse components, and can in fact be neglected. This is a consequence of the nearly-vanishing difference between n_1 and n_2 , because under those conditions the only waves which can be guided by means of total internal reflections are those whose propagation directions are very nearly parallel to the longitudinal direction (z). It follows, as is explained in some detail in References 1 and 2, that a single field function can be used to represent any transverse field component and that this (scalar) function satisfies the boundary conditions imposed by the nature of the problem. The integral equation for this function, Φ , is

$$\Phi(\vec{r}) = -(\gamma_1^2 - \gamma_2^2) \int \Phi(\vec{r}') g_2(\vec{r}, \vec{r}') dA' \quad (4)$$

where the integration is over the interior area and $g_2(\vec{r}, \vec{r}')$ is the Green function satisfying

$$(\vec{\nabla}^2 + \gamma_2^2) g_2(\vec{r}, \vec{r}') = \delta(\vec{r} - \vec{r}') \quad (5)$$

Its equivalence with the Helmholtz equations, Eqns. (3a) and (3b), can be demonstrated by acting on both sides of Eqn. (4) with $\vec{\nabla}^2 + \gamma_2^2$ and using Eqn. (5). Because of the delta function, one gets two separate equations depending on whether \vec{r} is inside or outside the guiding region. That the boundary conditions are satisfied follows from the properties of the Green function $\langle 1 \rangle$.

An alternative form of Eqn. (4), which leads to simpler computational procedures, results from converting the integral over the interior area

to a line integral over the boundary, using Green's second identity. For any point \vec{p} in the interior,

$$\int \left[g_2(\vec{p}, \vec{p}') \frac{\partial \Phi(\vec{p}')}{\partial n'} - \Phi(\vec{p}') \frac{\partial g_2(\vec{p}, \vec{p}')}{\partial n'} \right] dL' = 0 \quad (6)$$

where $\frac{\partial}{\partial n'}$ represents the outward normal derivative at points \vec{p}' , on the boundary.

Eqn. (6) represents the general formulation of the waveguide problem for single guides. It is still necessary to introduce explicit expressions for g_2 , Φ , and $\frac{\partial}{\partial n'}$, in order to reduce the equation to a useful form; and then one must perform the required integration and solve for the actual propagation constants and fields. However, those explicit expressions are completely general in form---that is, they are not dependent on the geometry or the values of the physical parameters involved. As a result, the method is applicable to any configuration for which the weakly-guiding condition obtains. It is true that the more bizarre shapes may require a lot of computational work---due to poor convergence of series---but the generality of the method is not diminished by this fact. In truth, a great many very different configurations may be treated quite economically within this framework.

Eqn. (6) is of further importance because the procedures leading to it are easily generalized to apply to N separate guiding regions embedded in a single cladding. Such arrays of guides could be viewed as a single guide with very peculiar boundaries (with infinitesimally thin "fins" connecting them, for example) and Eqn. (6) would therefore be written as a sum of line integrals (over the different boundaries) instead of a single integral. Insofar as such configurations fall into the "bizarre" category, at least within the class of "single guides", convergence would generally be poor. In fact, it is advantageous to introduce N separate coordinate systems, each with its origin within a different core. This results in N separate homogeneous equations like Eqn. (6), each one a sum of N line integrals. Nevertheless the ideas behind this procedure, which is laid out in Sec. II.3, are exactly the same as those given above.

2.2 Equivalent Linear Equations

To proceed from Eqn. (6), the starting point, two of the things we need are an assumed general form for the solution, $\Phi(\vec{p})$, and an approx-

priate representation of the Green function for Helmholtz' equation. The Green function is

$$g_2(\vec{r}, \vec{r}') = -\frac{i}{4} H_0(\gamma_2 |\vec{r} - \vec{r}'|) \quad (7)$$

where H_0 is the Hankel function of the first kind of order zero. The representation we choose is one which converges for $\rho < \rho'$, and which can be derived by application of Graf's addition theorem <6> to H_0 :

$$g_2(\vec{r}, \vec{r}') = -\frac{i}{4} \sum_{l=0}^{\infty} \epsilon_l H_l(\gamma_2 \rho') J_l(\gamma_2 \rho) [\cos l\phi \cos l\phi' + \sin l\phi \sin l\phi'] \quad (8)$$

$\rho < \rho'$

In this equation, J_l and H_l are Bessel and Hankel functions of order l . ϵ_l is the Neumann factor, equal to 1 for $l = 0$ and 2 otherwise. This choice is dictated by the fact that Eqn. (6) applies to observation points $\vec{\rho}$ which lie in the interior region, while the "source" points, $\vec{\rho}'$, lie on the boundary. Thus, in terms of any coordinate system whose origin is in the interior, there is at least one point, $\vec{\rho}$, (e.g., that at the origin) satisfying the inequality for all possible values of $\vec{\rho}'$, no matter how peculiar the boundary. The representation, Eqn. (8), will therefore converge for all the integration points we will choose as we perform the line integral indicated in Eqn. (6).

The complementary representation, valid for $\rho > \rho'$, is needed together with Eqn. (8) to treat the problem of multiple guides (arrays). We set it down for future reference.

$$g_2(\vec{r}, \vec{r}') = -\frac{i}{4} \sum_{l=0}^{\infty} \epsilon_l J_l(\gamma_2 \rho') H_l(\gamma_2 \rho) [\cos l\phi \cos l\phi' + \sin l\phi \sin l\phi'] \quad (9)$$

$\rho > \rho'$

For ϕ we assume the most general solution of Helmholtz' Equation for the interior region:

$$\Xi(\rho') = \sum_{s=0}^{\infty} J_s(\gamma_1 \rho') [C_s \cos s\phi' + D_s \sin s\phi'] \quad (10)$$

where the C_s and D_s are expansion coefficients. Of course, for many cases of importance, symmetry considerations allow one to eliminate some or most of the expansion coefficients by inspection. This is discussed in Sec. II.2.3, but for now we continue with our outline of the general formulation.

In the two dimensions presently under consideration, an arbitrary point \vec{p} is specified by components (ρ, ϕ) . The boundary L is some curve, $\rho(\phi)$, parameterized by the angular coordinate. As a result of this parameterization, the unit vector perpendicular to the boundary is given by

$$\hat{n} = \left| \frac{dL}{d\phi} \right|^{-1} \left\{ \frac{\partial \rho}{\partial \phi} \hat{\phi} - \rho \hat{\rho} \right\} \quad (11)$$

Using this and the expression for the gradient in cylindrical coordinates, we find the normal derivative at the boundary to be

$$\frac{\partial}{\partial n} = \hat{n} \cdot \vec{\nabla} = \left| \frac{dL}{d\phi} \right|^{-1} \left\{ \rho \frac{\partial}{\partial \rho} - \frac{1}{\rho} \left(\frac{\partial \rho}{\partial \phi} \right) \frac{\partial}{\partial \phi} \right\} \quad (12)$$

When this operator is put into the integral equation (using primed coordinates, of course) the differential path length dL drops out in favor of $d\phi$. As a result, therefore, of being able to express the boundary as some differentiable function $\rho(\phi)$, the line integral becomes a simple one-dimensional integral over the angular coordinate which is quite suitable for calculations.

We have not considered boundaries for which $\rho(\phi)$ is multivalued or nondifferentiable.

(Eqn. (11) can be derived by writing the tangential unit vector on the boundary, \hat{t} , as

$$\hat{t} = \frac{d\vec{L}}{|d\vec{L}|} = \frac{\hat{\rho} d\rho + \hat{\phi} \rho d\phi}{|d\vec{L}|} = \left| \frac{dL}{d\phi} \right|^{-1} \left\{ \hat{\rho} \frac{\partial \rho}{\partial \phi} + \rho \hat{\phi} \right\} \quad (13)$$

and requiring $\hat{t} \cdot \hat{n} = 0$ and $\hat{n} \cdot \hat{n} = 1$.)

The application of the normal derivative to the infinite series for $\Phi(\vec{p})$ and $g_2(\vec{p}, \vec{p}')$ is straightforward, and the manipulation following the introduction of these derivatives and functions into Eqn. (6) is merely tedious. However, the fact that each term in the Green function expansion, Eqn. (8), is separable into a factor containing the primed coordinates and a factor containing the unprimed coordinates is of great importance because it allows all the functions containing the unprimed coordinates to be drawn outside the integral. The left-hand side of the equation then reduces to a sum of terms each of which consists of one of these functions multiplied by a constant coefficient (a line integral). These functions

are all of the form $J_l(\gamma_2 \rho) \cos(l\phi)$ and $J_l(\gamma_2 \rho) \sin(l\phi)$ and as such constitute a linearly-independent set whose coefficients, because the integral equation is homogeneous, must separately be equal to zero. Thus, the single integral becomes a set of simultaneous equations. The unknowns in these linear equations are the coefficients, C_s and D_s , of the field expansion, Eqn. (10). It is our job to write these equations, simplify them wherever possible, and then specify a means of solution.

To see how this develops, we record the results of some of the intermediate steps without much further comment on the mathematics. The normal derivatives are

$$\frac{\partial \Xi(\hat{r}')}{\partial n'} = \left| \frac{dL}{d\phi} \right|^{-1} \sum_{s=0}^{\infty} \left\{ \gamma_1 \rho' J_s'(\gamma_1 \rho') [C_s \cos s\phi' + D_s \sin s\phi'] \right. \\ \left. + \frac{\partial \rho'}{\partial \phi} \frac{s}{\rho'} J_s(\gamma_1 \rho') [C_s \sin s\phi' - D_s \cos s\phi'] \right\} \quad (14)$$

$$\frac{\partial q_2(\hat{r}, \hat{r}')}{\partial n'} = -\frac{i}{4} \left| \frac{dL}{d\phi} \right|^{-1} \sum_{s=0}^{\infty} J_s(\gamma_2 \rho) \epsilon_s \left\langle \left\{ \gamma_2 \rho' H_s'(\gamma_2 \rho') \cos s\phi' + \frac{\partial \rho'}{\partial \phi} \frac{s}{\rho'} H_s(\gamma_2 \rho') \sin s\phi' \right\} \cos s\phi \right. \\ \left. + \left\{ \gamma_2 \rho' H_s'(\gamma_2 \rho') \sin s\phi' - \frac{\partial \rho'}{\partial \phi} \frac{s}{\rho'} H_s(\gamma_2 \rho') \cos s\phi' \right\} \sin s\phi \right\rangle \quad (15)$$

where the primes on the Bessel and Hankel functions indicate differentiation with respect to their arguments and are not to be confused with the primes on the coordinates, which have a completely different significance. The integral equation attains the form,

$$\sum_{s=0}^{\infty} S_{1s} J_s(\gamma_2 \rho) \cos s\phi + \sum_{s=0}^{\infty} S_{2s} J_s(\gamma_2 \rho) \sin s\phi = 0 \quad (16)$$

As we indicated previously, equations of this form can hold in general---that is, for arbitrary points \hat{r} ---only if the coefficients are separately equal to zero:

$$S_{1l} = 0 \quad l = 0, 1, 2, \dots \quad (17a)$$

$$S_{2l} = 0 \quad l = 1, 2, \dots \quad (17b)$$

(S_{2l} is identically zero for $l = 0$.) They are

$$S_{2l} = \int_l d\phi' \epsilon_2 \left\{ \left[H_l(\gamma_2 \rho') \cos l\phi' \right] \left[\sum_{s=0}^{\infty} \gamma_1 \rho' J_s'(\gamma_1 \rho') \{ C_s \cos s\phi' + D_s \sin s\phi' \} \right. \right. \\ \left. \left. + \frac{\partial \rho'}{\partial \phi'} \frac{s}{\rho'} J_s(\gamma_1 \rho') \{ C_s \sin s\phi' - D_s \cos s\phi' \} \right] \right\} \quad (18a)$$

$$- \left[\gamma_2 \rho' H_l'(\gamma_2 \rho') \cos l\phi' + \frac{\partial \rho'}{\partial \phi'} \frac{l}{\rho'} H_l(\gamma_2 \rho') \sin l\phi' \right] \left[\sum_{s=0}^{\infty} J_s(\gamma_1 \rho') \{ C_s \cos s\phi' + D_s \sin s\phi' \} \right] \Bigg\}$$

$$S_{2l} = \int_l d\phi' \epsilon_2 \left\{ \left[H_l(\gamma_2 \rho') \sin l\phi' \right] \left[\textcircled{2} \right] \right. \quad (18b)$$

$$\left. - \left[\gamma_2 \rho' H_l'(\gamma_2 \rho') \sin l\phi' - \frac{\partial \rho'}{\partial \phi'} \frac{l}{\rho'} H_l(\gamma_2 \rho') \cos l\phi' \right] \left[\textcircled{4} \right] \right\}$$

where the terms in brackets labelled by "2" and "4" in Eqn. (18b) are identical to those in the brackets in the corresponding positions in Eqn. (18a). They can be rearranged by grouping the field-expansion coefficients C_s and D_s . In fact, if we make the definitions

$$E_{ls}(\rho') = \epsilon_2 \left\{ \gamma_1 \rho' H_l(\gamma_2 \rho') J_s'(\gamma_1 \rho') - \gamma_2 \rho' H_l'(\gamma_2 \rho') J_s(\gamma_1 \rho') \right\} \quad (19a)$$

$$E_{ls}(\rho', \frac{\partial \rho'}{\partial \phi'}) = \epsilon_2 H_l(\gamma_2 \rho') J_s(\gamma_1 \rho') \frac{\partial \rho'}{\partial \phi'} / \rho' \quad (19b)$$

and

$$R_{\ell s} = \int d\psi \left[F_{\ell s}(\psi) \cos \ell\psi \cos s\psi' + E_{\ell s}(\psi, \frac{\partial \psi'}{\partial \psi}) \left\{ s \cos \ell\psi' \sin s\psi' - \ell \sin \ell\psi' \sin s\psi' \right\} \right] \quad (20a)$$

$$U_{\ell s} = \int d\psi \left[F_{\ell s}(\psi) \cos \ell\psi' \sin s\psi' - E_{\ell s}(\psi, \frac{\partial \psi'}{\partial \psi}) \left\{ s \cos \ell\psi' \cos s\psi' + \ell \sin \ell\psi' \sin s\psi' \right\} \right] \quad (20b)$$

$$V_{\ell s} = \int d\psi \left[F_{\ell s}(\psi) \sin \ell\psi \cos s\psi' + E_{\ell s}(\psi, \frac{\partial \psi'}{\partial \psi}) \left\{ s \sin \ell\psi' \sin s\psi' + \ell \cos \ell\psi' \cos s\psi' \right\} \right] \quad (20c)$$

$$T_{\ell s} = \int d\psi \left[F_{\ell s}(\psi) \sin \ell\psi' \sin s\psi' - E_{\ell s}(\psi, \frac{\partial \psi'}{\partial \psi}) \left\{ s \sin \ell\psi' \cos s\psi' - \ell \cos \ell\psi' \sin s\psi' \right\} \right] \quad (20d)$$

Eqs. (17) become

$$S_{1\ell} = \sum_{s=0}^{\infty} [C_s R_{\ell s} + D_s U_{\ell s}] = 0 \quad \ell = 0, 1, 2, \dots \quad (21a)$$

$$S_{2\ell} = \sum_{s=0}^{\infty} [C_s V_{\ell s} + D_s T_{\ell s}] = 0 \quad \ell = 1, 2, \dots \quad (21b)$$

In matrix form this is

$$\begin{pmatrix} R & U \\ V & T \end{pmatrix} \begin{pmatrix} C \\ D \end{pmatrix} = 0 \quad (22)$$

The condition that a set of homogeneous linear equations, such as this is, have a solution is that the determinant of the matrix be zero. The final equation in the general analysis is therefore

$$\det \begin{pmatrix} R & U \\ V & T \end{pmatrix} = 0 \quad (23)$$

2.3 Symmetry Considerations

At this point, we pause to assess the simplifications which can be made if the contour representing the boundary between the core and the cladding demonstrates certain symmetries, as happens in most practical

guides. The preceding discussion is general, and as a result the equations are a little more cumbersome than is usually necessary. The only reason for writing this section in this manner is that all our previous publications, particularly those on arrays, have taken the simplified approach from the start, thereby avoiding setting down the general formulation.

The most important simplification occurs in guides which have a single reflection axis, which we may define as the x-axis or the $\phi = 0$ direction. In this case, all the matrix elements U_{ls} and V_{ls} are identically zero.

This can be seen, with some travail, from the fact that the integrands change sign as ϕ goes to $-\phi$, causing the 0 to π portion of the integral to cancel the π to 2π part. Because of the resulting block diagonal form of the matrix, Eqn. (22) splits into two separate systems of equations which can be solved for the C_s or the D_s coefficients. Equivalently, we could have started at Eqn. (10) with either the cosine or sine expansion instead of the more general combination, using the rationale that the field function can only be a symmetric (cosine) or antisymmetric (sine) function of position.

If there is a second orthogonal reflection axis (the y-axis), a further simplification derives from the fact that unless the indices l and s are both even or both odd, the matrix elements R_{ls} and T_{ls} are also zero. In this case, the 0 to $\pi/2$ integration cancels the $\pi/2$ to π part. Then, to solve the matrix equation

$$(R)(C) = 0, \quad (24)$$

for example, one could reorder the rows and columns so as to group all the even coefficients together and all the odd coefficients together. Again what results is a block-diagonal form which breaks apart into two separate systems of equations, one solving for C_0, C_2, C_4, \dots and the other for C_1, C_3, C_5, \dots . Equivalently, for such guides, we could simply have started at Eqn. (10) with any of four field functions---"even cosine", "odd cosine", "even sine", or "odd sine" expansions---and obtained the requisite matrix equations as separate cases.

Needless to say, most waveguide cross-sections which are of interest to experimenters---e.g., ellipses, rectangles, and special cases thereof---have this two-fold symmetry, and the field functions corresponding to all the modes of such guides fall into one of these four categories. All of the programs we developed to obtain the final results demand, as input, the specification of one of these categories, and then proceed to find all the solutions (modes) corresponding to the requested expansion.

If in addition there is a third reflection axis (e.g., $\phi = \pi/4$), even-index matrix elements for which ℓ and s do not differ by an integer multiple of four are zero. That is, $R_{02} = R_{06} = R_{24} = \dots = 0$, but R_{04}, R_{26}, \dots are not (necessarily) zero. The consequence of this is that, for example for guides with square cross sections, the "even cosine" and "even sine" series each split into two separate series, with indices $0, 4, 8, \dots$ and $2, 6, 10, \dots$. The odd series are not affected, so there are six possible sorts of expansions for these cases.

The last case is that of the circular cross-section for which (R) and (T) are diagonal matrices (and in fact are equal to each other so that sine and cosine series yield the same modes exactly). Each field "expansion" therefore has only one term, which may be indexed by any integer. The integral equation formulation reduces, analytically, to the well-known set of transcendental equations whose solutions have been available for many years <7>.

2.4 Computational Considerations

We have yet to address some of the practical requirements which allow one to take Eqn. (23)---or some reduced form of it, whatever is allowed by symmetry conditions---and solve it numerically.

One requirement, obviously, is to truncate the set of equations and the series within them at a finite number, M . It turns out that, except for circular guides, three terms are generally needed for three-place accuracy in the propagation constant. For highly elongated (e.g., 10:1) cross-sections, or for much greater accuracy (six figures) it is necessary to go to at least six terms.

Another requirement is to write $F_{\ell s}$ and $E_{\ell s}$ in terms of real rather than complex functions, and to eliminate the derivatives of the Bessel and Hankel functions. It is also useful to define normalized parameters for the propagation constants and the index-of-refraction differences, since then we can specify the system in terms of fewer parameters and compare different cases more readily. It is sensible to discuss these together, since the normalized parameterization involves terms containing $i = \sqrt{-1}$.

To fully specify the problem one needs to know the vacuum wavenumber, k_0 ; the size and the shape of the guide; and the indices of refraction, n_1 and n_2 .

It is convenient to specify the size of the guide in terms of a single linear parameter, such as the radius of a circular guide or the length of one side of a rectangular one. We choose to label this "characteristic dimension" by the symbol b , and to take it to be the semi-minor axis of the guide, for all cross-sections demonstrating two-fold symmetry. Definition of the shape, for most regular perimeters, can then be given by one or two more parameters. We define the aspect ratio, \tilde{R} , to be one of these. It is the ratio of the semi-major axis to the semi-minor axis. Any ellipse or rectangle, for example, is defined by its semiminor axis, b , and its aspect ratio; a square is a rectangle with $\tilde{R} = 1$. Later in this section we describe a particular function which we have used for the perimeter.

We define a normalized frequency, B , by

$$B = \frac{bk_0}{\pi}(n_1^2 - n_2^2)^{1/2} = \frac{bk_0 n_1}{\pi} \sqrt{\delta} \quad (25)$$

If we give a value for this quantity at the beginning of any calculation, we eliminate the need to independently specify k_0 , n_1 , n_2 , and b . (B is positive and is related to the commonly-used parameter, V , by $V = \pi B$; δ , which is defined by Eqn. (25), is also common notation.) We also define the normalized propagation constant,

$$P^2 = \frac{k_2^2 - k_1^2}{k_1^2 - k_2^2} = \frac{-\gamma_2^2}{\gamma_1^2 - \gamma_2^2} \quad (26)$$

which satisfies the relation $0 < P^2 < 1$. With these definitions and Eqns.(1) and (2), one can show that the arguments of the Bessel and Hankel functions appearing in F_{ls} and E_{ls} are given by

$$\gamma_1 \rho' = \pi B (1 - P^2)^{1/2} (f') \quad (27a)$$

$$\gamma_2 \rho' = i\pi B P (f') \quad (27b)$$

Thus the matrix elements are complicated functions of the unknown propagation constant, P^2 . The problem is then specified when B and whatever parameters (besides b , which drops out) define the shape of the guide are given. It can be considered solved when suitable values of P^2 are found that the determinantal equation is satisfied.

There is still some algebra to endure before the matrix elements are cast in real form. The derivatives of the Bessel functions in F_{ls} and E_{ls} are eliminated by the use of recursion relations:

$$J_n'(x) = J_{n-1}(x) - \frac{x}{2} J_{n+1}(x) \quad (28a)$$

$$H_n'(x) = H_{n-1}(x) - \frac{x}{2} H_{n+1}(x) \quad (28b)$$

We also use the Modified Bessel functions of the second kind instead of the Hankel functions:

$$H_n(ix) = \frac{2}{\pi} i^{-(n+1)} K_n(x) \quad (29)$$

With these substitutions and modifications, F_{ls} and E_{ls} can be written as

$$\begin{aligned} F_{ls}(p') &= i^{-(l+1)} \epsilon_2 \left[2B \frac{p'}{b} (1-p^2)^{\frac{1}{2}} K_2\left(\frac{\pi B p'}{b}\right) J_{s-1}\left(\frac{\pi B p'}{b} (1-p^2)^{\frac{1}{2}}\right) \right. \\ &\quad \left. + p K_{l-1}\left(\frac{\pi B p'}{b}\right) J_s\left(\frac{\pi B p'}{b} (1-p^2)^{\frac{1}{2}}\right) \right. \\ &\quad \left. + \frac{2}{\pi} (l-s) K_l\left(\frac{\pi B p'}{b}\right) J_s\left(\frac{\pi B p'}{b} (1-p^2)^{\frac{1}{2}}\right) \right] \quad (30a) \end{aligned}$$

$$E_{ls}(p', \frac{dp'}{p'}) = i^{-(l+1)} \epsilon_2 \frac{2}{\pi} K_2\left(\frac{\pi B p'}{b}\right) J_s\left(\frac{\pi B p'}{b} (1-p^2)^{\frac{1}{2}}\right) \frac{dp'}{p'} / p' \quad (30b)$$

The matrix elements, Eqns. (20), are computed directly from these expressions. The powers of i are dependent on l alone. Consequently they are a constant factor in each row of the determinant, and can be ignored.

A few further comments will serve to describe the specific choices we have made for the evaluation of the elements of the determinant and the solution of the determinantal equation.

First of all, we have concentrated on guides with two-fold reflection symmetry. In fact, throughout our work we have used for the perimeter the function <8,9>

$$\rho(\phi) = b \left[(\cos \phi / \tilde{R})^{2\tilde{N}} + (\sin \phi)^{2\tilde{N}} \right]^{-1/2\tilde{N}} \quad (31)$$

where \tilde{R} is the aspect ratio and \tilde{N} is a parameter defining the actual shape. This gives a figure with a short axis (along $\phi = \pi/2$) of $2b$ and a long axis (along $\phi = 0, \pi$) of $2\tilde{R}b$. In general, for arbitrary \tilde{R} ,

Eqn. (31) describes a rectangle if the parameter \tilde{N} is chosen to be infinity and an ellipse if $\tilde{N} = 1$. Shapes with $1 < \tilde{N} < \infty$ are called "superellipses" and can be regarded as a continuous deformation of an ellipse into a rectangle as \tilde{N} increases. Those with $\tilde{N} < 1$ give a variety of other shapes <2>. From Eqn. (31), $\frac{\partial \rho}{\partial \phi}$ can be obtained analytically. A quick inspection of Eqns. (30a) and (30b) also reveals that b drops out of F_{ls} and E_{ls} everywhere, making the numerical specification of this parameter unnecessary.

Rectangles are well represented by Eqn. (31) when \tilde{N} is chosen to be 20 or greater. The rounding of the corners is barely noticable for $\tilde{N} = 20$ and the numerical results for the modal parameters differ negligibly from those found using larger values of \tilde{N} .

Since we concentrate on guides with two-fold reflection symmetry, we are solving, at any time, either of the equations

$$\det(R) = 0 \quad (32a)$$

$$\det(T) = 0 \quad (32b)$$

where (R) and (T) are M by M matrices and, in each case, the matrix elements are evaluated numerically and are indexed either by even values of l and s or by odd values. Because of this symmetry, the integrals need be done only over the interval $(0, \pi/2)$. With the transformation, $z = \cos(2\phi)$ they become susceptible to Chebyshev integration <10>, which takes equally-spaced points over the range $(-1, 1)$ with equal weights. That is, to evaluate any integral like those of Eqns. (20), we take

$$\int_0^{\pi/2} g(\phi) d\phi = \frac{1}{2} \int_{-1}^1 \frac{dz}{\sqrt{1-z^2}} g(\phi(z)) = \frac{\pi}{2n} \sum_{i=1}^n g(\phi(z_i)) \quad (33)$$

where

$$z_i = \cos\left(\frac{(2i-1)\pi}{2n}\right) \quad (34)$$

Thus the n values of $\phi(z_i)$ which we need to evaluate the integrands in Eqns. (20) are

$$\phi(z_i) = \frac{\pi}{4n} (2(n-i) + 1) \quad (35)$$

and the integration is especially simple to perform. Generally, 50 integration points are sufficient for accurate results, unless the truncation order is high. The correctness of the roots depends most strongly on the order of truncation, and secondly on the number of integration points taken.

Since all the possible roots, P^2 , corresponding to guided modes are limited to the range 0 to 1, one chooses a small number of points spaced throughout this range and tabulates the determinant at these points. In our programs, the determinant is found with a standard matrix-inversion subroutine using Gaussian reduction with complete pivoting <11>. The roots fall between pairs of consecutive points at which the determinant has opposite signs, and can be found accurately by using various root-finding algorithms.

It is important that the table entries be spaced closely enough together that two roots not fall within one interval.

The root-finding algorithm we have developed works well when consecutive tabulated values of the determinant are of approximately the same magnitude, as is the case with $M < 3$, and also when they change extremely rapidly with P^2 , as is typical with $M > 3$ (and for the array problems). If (and only if) consecutive table entries differ by more than two orders of magnitude, a half-interval search <12> narrows the range within which the root may fall. Then we use a bracketing version of Muller's method <13,14> to locate the root to any desired accuracy. Muller's method, which is an inverse parabolic interpolation scheme, converges very rapidly in the neighborhood of the root. The method of Regula Falsi <15>, using inverse linear interpolation, is almost as fast for most examples we tried.

Once each root (P^2) is determined, the matrix elements are recomputed and the coefficients (C_s or D_s) are determined. Since the equations are homogeneous, one coefficient is arbitrary (and is set equal to unity) and $M - 1$ equations are solved by matrix inversion. The arbitrary coefficient is chosen to be the one corresponding to the largest diagonal matrix element, since this coefficient (as it turns out) almost always appears in the most important term in the field expansion. Usually, but not always, the first term in the series is the most important one.

A FORTRAN program to perform these calculations (program TRUNCN, the use of which is described elsewhere in this report) required about 20000 CM words and was run on a CDC-6600. The minimum execution time for a single root occurs when 1-term truncation (exact for circular guides) is used with only three or four table entries (as when the root location is known approximately beforehand). For four-place accuracy, less than a second

may be required. For higher orders of truncation, the cost in time increases much less rapidly than N^2 because of efficient recurrence computations for the Bessel functions. Twelve modes of a 2:1 elliptical guide (4-term truncation) have been located in 1.7 times the time required for 12 modes of a circle.

2.5 Results

The numerical results which we have obtained mainly consist of plots of P^2 versus B for different cross-sections, and curves giving the field intensity in the interior. We also demonstrate the efficacy and economy of the method by considering the effect of truncation at various numbers of terms, and compare our results with those of other authors.

We concentrate primarily on rectangular and elliptical guides. We have used a special notation to designate the various modes. For rectangles, it has the form R_n^X where X indicates one of the four field expansions discussed in Sec. II.2.3 and n specifies which mode, among all those derived from that field expansion, is being considered. $X = I$ corresponds to the even cosine expansion; $X = II$, to odd cosine; $X = III$, to even sine; and $X = IV$, to odd sine. Within each group, the modes are ordered according to the value of B at which they cut off. R_1^I designates the fundamental mode (even cosine expansion, "cutoff" at $B = 0$). For ellipses, this notation is E_n^X .

2.5.1 Rectangular Cross-Sections

For rectangular waveguides having aspect ratios $1 < \bar{R} \leq 2$ we have located all the modes in the range $0 < B \leq 4$. The first dozen or so are plotted for $B \leq 2.5$ in Figs. 2-5 for different aspect ratios.

Due to the considerations of Sec. II.2.3, we can write the field expansion, Eqn. (10), for the R_1^I mode of a square---the fundamental mode, which does not cut off---as

$$\bar{I}(\bar{\rho}) = C_0 J_0(\gamma_1 \bar{\rho}) + C_4 J_4(\gamma_1 \bar{\rho}) \cos(4\phi) + C_8 J_8(\gamma_1 \bar{\rho}) \cos(8\phi) + \dots \quad (36a)$$

whereas for a rectangle with $\bar{R} > 1$ the expansion is

$$\bar{I}(\bar{\rho}) = C_0 J_0(\gamma_1 \bar{\rho}) + C_2 J_2(\gamma_1 \bar{\rho}) \cos(2\phi) + C_4 J_4(\gamma_1 \bar{\rho}) \cos(4\phi) + \dots \quad (36b)$$

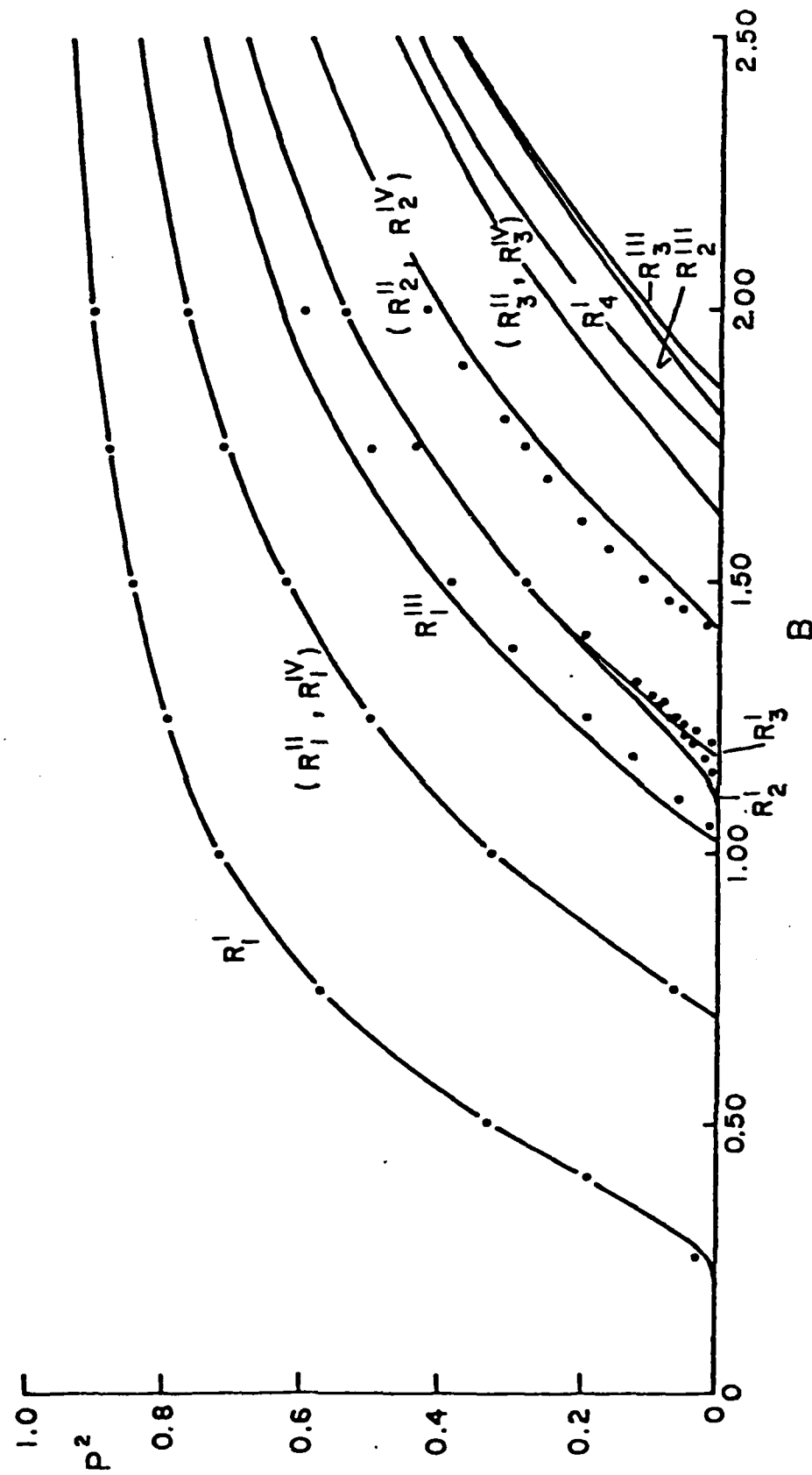


Fig. II.2 Modes of the weakly guiding square guide. Dots were taken from Fig. 16 of Ref. 16.

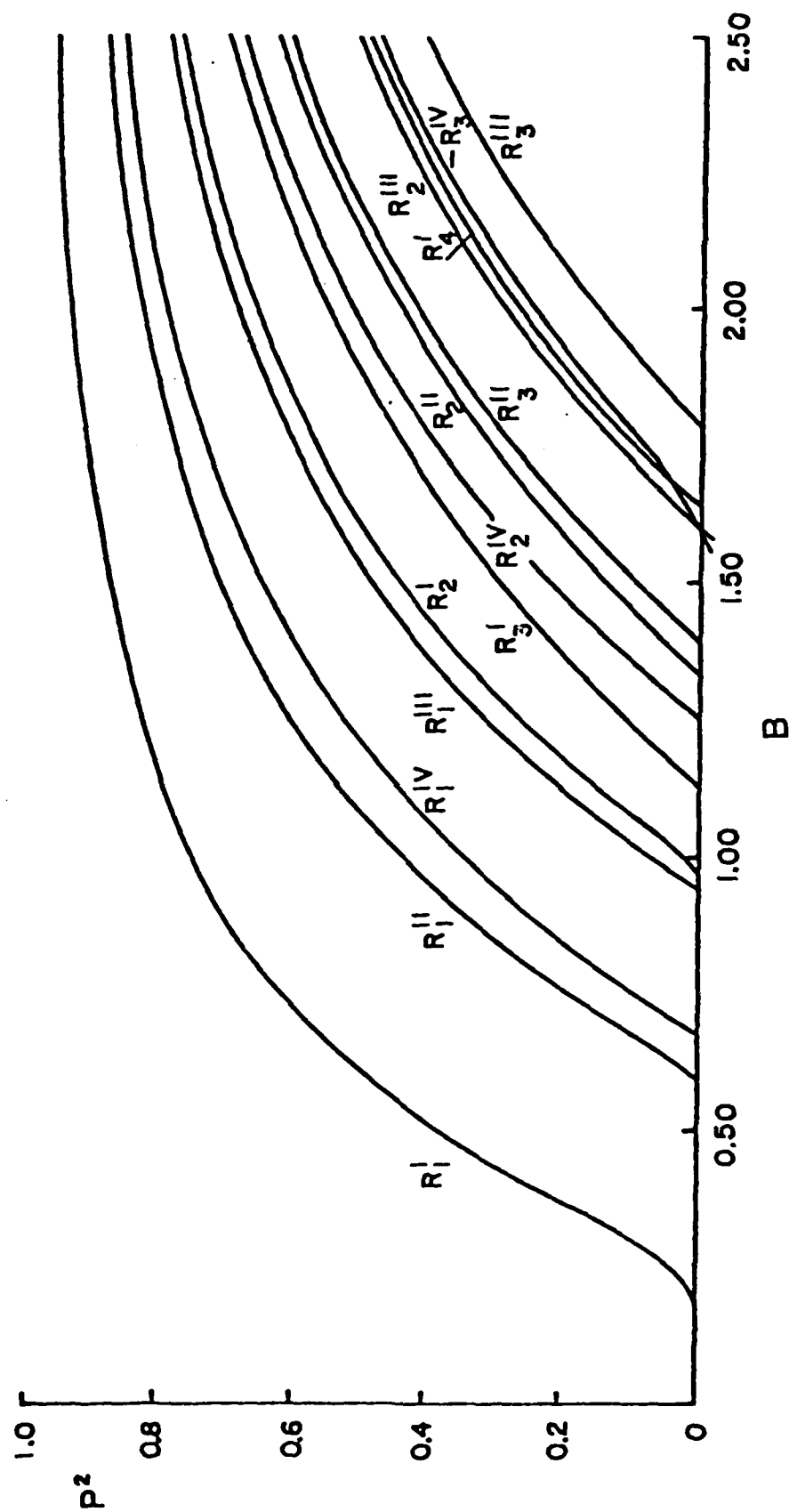


Fig. II.3 Modes of the weakly guiding rectangular guide with $\tilde{R} = 1.2$.

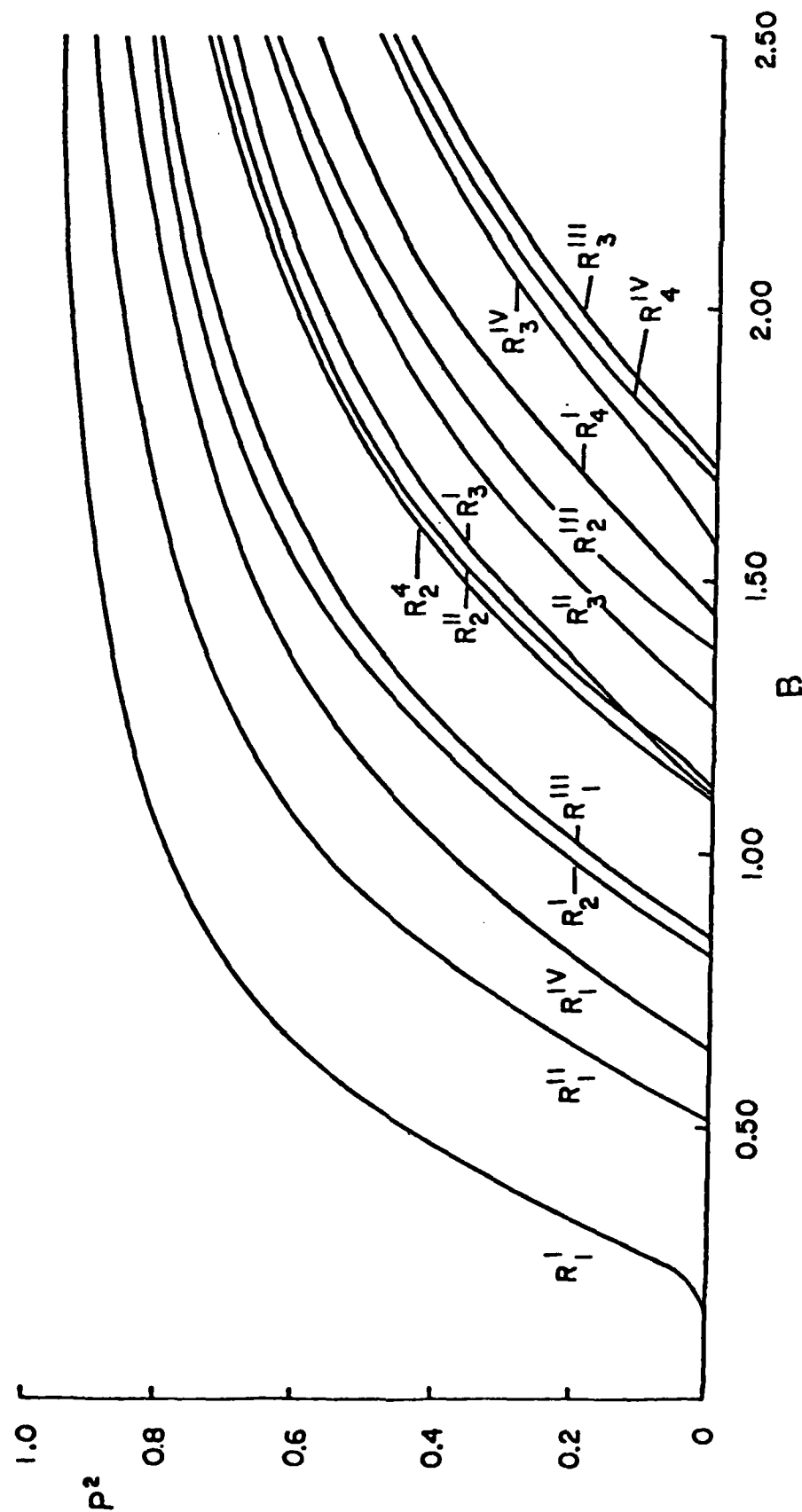


Fig. II.4 Modes of the weakly guiding rectangular guide with $\tilde{R} = 1.5$.

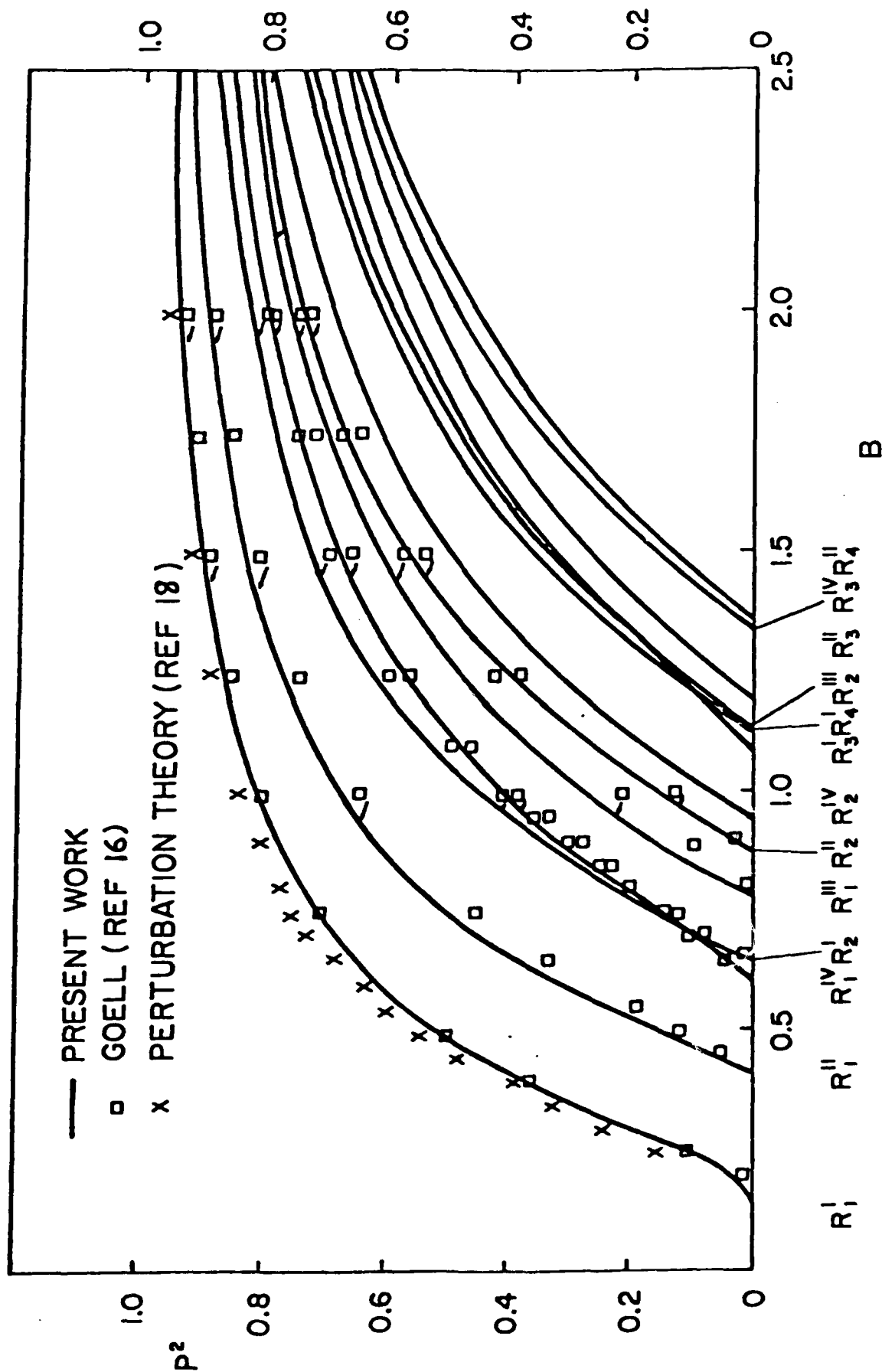


Fig. II.5 Modes of the weakly guiding rectangular guide with $\tilde{R} = 2$. Square points were taken from Fig. 17 of Ref. 16. X's represent results of a perturbation calculation for the R_1^I mode <18>.

The convergence of these expansions is rapid for both the square and rectangular guides. For the square guide, Table 1 gives the values of P^2 obtained for this mode after truncation of Eqn. (32a) at 1, 2, or 3 terms for selected values of B . Clearly, the two term truncation is only a small improvement, in terms of locating the roots, on the single-term result, which is obtained by setting $R_{00} = 0$ in Eqn. (32a). Moreover, the extra work involved in taking three terms leads to no gain whatsoever. In view of this, it is reassuring that the ratios of the second term of the field expansion to the first ($C_4 J_4 / C_0 J_0$), and the third to the first ($C_8 J_8 / C_0 J_0$) show that the J_0 term is dominant for this mode. The term ratios listed in the 5th and 6th columns of Table 1 were evaluated on the perimeter at the middle of one side (that is, $\rho = b$, $\phi = 0$). Since J_4 and J_8 become smaller as ρ decreases, the term ratios are generally greatest at the perimeter and as such constitute the "worst case" for convergence. (For $B = 3$ at $(\rho, \phi) = (0.5b, 0)$ the term ratios are -0.007 and $<10^{-5}$, respectively. The intensity is 0.576 .)

Table 1 also lists the field intensity at $\rho = b$, $\phi = 0$, normalized to a value of 1 at the center of the guide. For the more tightly bound cases, (higher B), the field drops off to a few percent at the edge, whereas for weakly bound cases (smaller B) the intensity is still appreciable there, indicating that a greater fraction of the beam is extending beyond the guiding core. One can also see that for those cases in which the second term ($C_4 J_4 / C_0 J_0$) makes the largest percent contribution to the

B	P^2			Term Ratios at Perimeter ($\phi = 0$)		Intensity at Perimeter ($\phi = 0$)
	1 Term	2 Terms	3 Terms	$C_4 J_4 / C_0 J_0$	$C_8 J_8 / C_0 J_0$	
3.0	0.9511	0.9546	0.9546	-0.314	0.0006	0.023
2.5	0.9329	0.9371	0.9372	-0.266	0.0009	0.032
2.0	0.9023	0.9072	0.9072	-0.213	0.0005	0.046
1.5	0.8442	0.8497	0.8497	-0.153	0.0005	0.076
1.0	0.7122	0.7175	0.7175	-0.089	0.0004	0.143
0.5	0.3263	0.3290	0.3291	-0.029	0.0003	0.371

Table II.1. Results for the dominant (noncutoff) R_1^I mode of the weakly guiding square guide. Listed values of P^2 were obtained after a 1-, 2-, or 3-term truncation of the field expansion. Term ratios derived from the 3-term solution give $C_4 J_4 \cos 4\phi / C_0 J_0$ and $C_8 J_8 \cos 8\phi / C_0 J_0$ at $\rho = b$, $\phi = 0$. The field intensity at $\rho = b$, $\phi = 0$ is also given. The intensity at $\rho = 0$ is 1.

field, the total field is small; whereas for weakly bound cases the second term is a much smaller fraction of a considerably larger field. (Similarly, in the interior, the percent contribution of the second term drops quickly as the field intensity increases.) Viewing the guide as a whole, therefore, all terms beyond the first one make unimportant contributions to the total intensity for the dominant mode of the square guide. The same holds true for rectangular cross sections.

In Fig. 6 the field intensity is plotted as a function of ρ/b for this mode both along a line through the center of perimeter ($\phi = 0^\circ$) and along a diagonal ($\phi = 45^\circ$).

We also obtain good convergence of the field expansions for the remaining (cutoff) modes. Table 2 compares the 1-, 2-, 3-, and 4-term truncation results of Eqn. (32a) or (32b) for the first several modes of the square. Comparing the 2- and 4-term truncations, we see that only two terms are required for an accuracy of 0.01 in P^2 for 7 of the first 13 modes of the square. As for the remaining modes, three terms are sufficient to bring the accuracy to within 0.01, except for the degenerate $R_2^{II}-R_2^{IV}$ mode, which is accurate to within 0.02.

Table 2, which also lists the mode designations, specifies in its last column which term is dominant in the field expansion. This is indicated by the underlined value. Thus, we see that for most of the modes the first term does dominate, and it is this term used alone in Eqn. (32a) or (32b) which produces the 1-term truncation result in Table 2. For example, $R_{22} = 0$ was used for the R_3^I mode, $T_{22} = 0$ for the R_1^{III} , $T_{44} = 0$ for the R_3^{III} and either R_{11} or $T_{11} = 0$ for the degenerate $R_1^{II}-R_1^{IV}$ mode. The observation stated above concerning the R_1^I mode is generally applicable to these other modes. That is, for many modes the higher terms in the expansion are comparable in magnitude to the first term only where the field intensity is small; otherwise, they are negligible.

However, there are some modes for which the second term in the field expansion is the most important one. For example, the field intensity of the R_4^I mode of the square guide is plotted in Fig. 7. It shows peaks at two different radial distances from the center. In the peak near the origin, the C_0J_0 term turns out to be the dominant one, but in the second peak the first term ratio has values ranging up to 20 and is consistently greater than 1, showing the $C_4J_4 \cos 4\phi$ term is the most important one there. For this mode, setting $R_{44} = 0$ produces the 1-term truncation

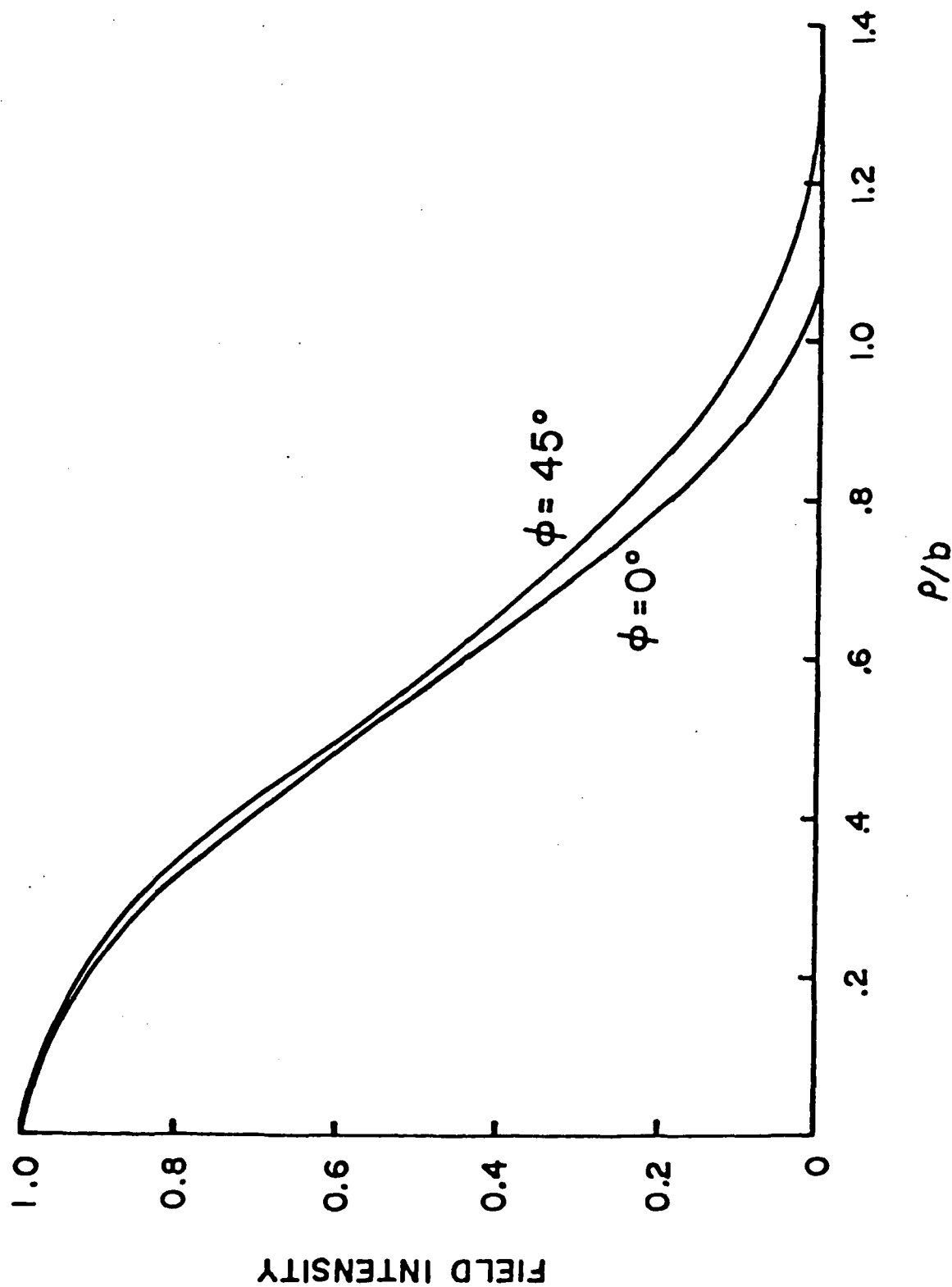


Fig. II.6 Field intensity as a function of ρ/b for the R_1^I mode of a square guide with $B = 3$. The two values of ϕ chosen represent the extremes of the intensity distribution.

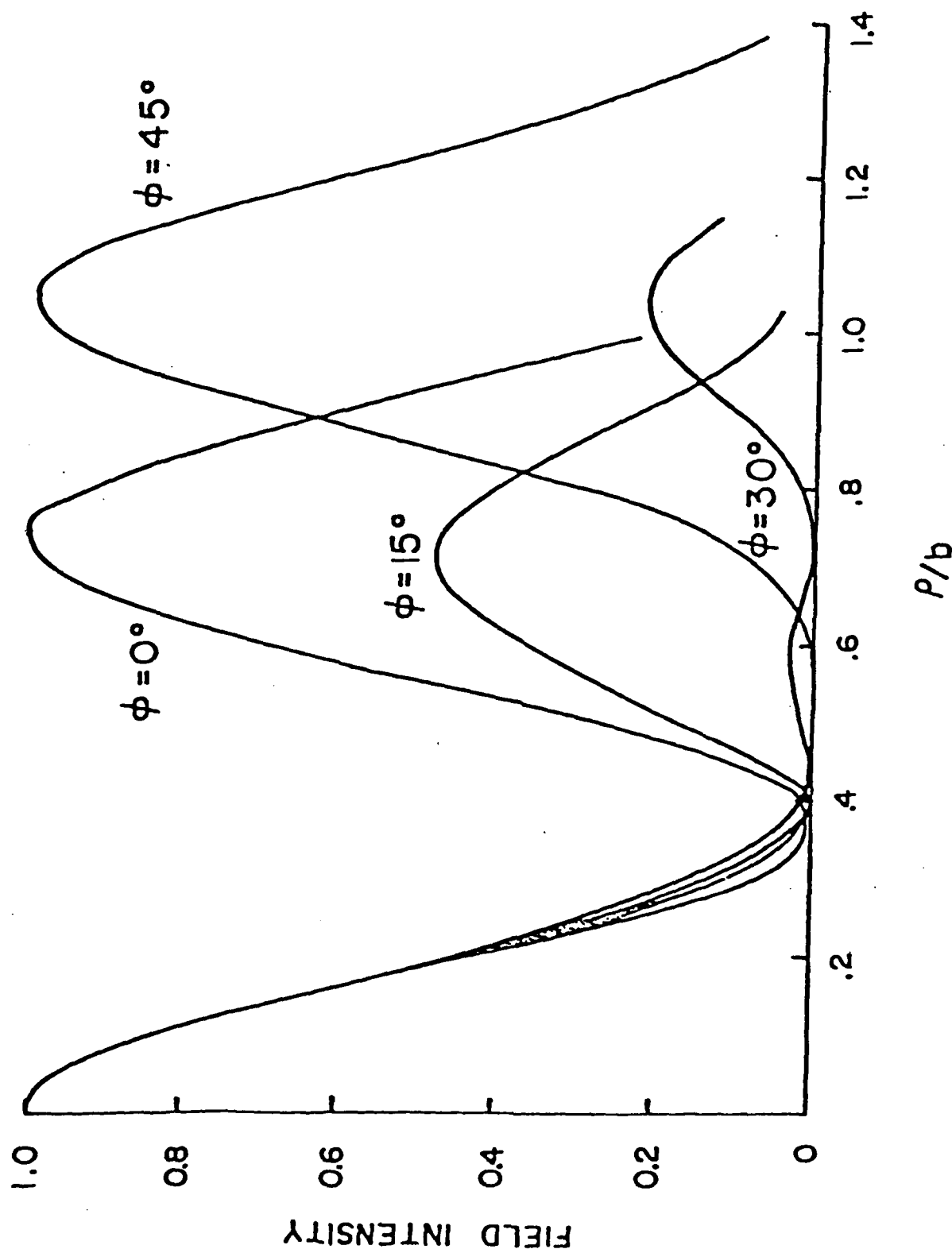


Fig. II.7 Field intensity as a function of ρ/b for the R_4^I mode of the square guide with $B = 3$ and various values of ϕ . When $\rho > .4b$ the second term ($C_4 J_4 \cos 4\phi$) dominates the field expansion.

result shown in Table 2. Another example in which the second term predominates is the degenerate $R_{22}^{IV-R_{11}^{II}}$ mode. Here, the 1-term truncation result was obtained by setting either R_{33} or $T_{33} = 0$. In such cases as these, it is obvious from a perusal of the Table 2 results that a 1-term truncation is inadequate for proper convergence and that a least three terms in the expansion are necessary.

The mode R_2^{III} is an example in which even though the first term is dominant, the other terms are still making a significant contribution. From Table 2 one can see that here, also, three terms are required in the expansion.

Mode Designation		B at Cutoff	P^2 at $B = 2$				Expansion Indices
This Work	Goell ²		1 Term	2 Terms	3 Terms	4 Terms	
R_1^I	$E_{11}^{x,y}$	0	0.9023	0.9072	0.9072	0.9072	<u>0</u> , 4, 8, ...
R_1^{II}	$E_{21}^{x,y}$	0.70	0.7546	0.7614	0.7688	0.7695	<u>1</u> , 3, 5, ...
R_1^{IV}	$E_{12}^{x,y}$						<u>1</u> , 3, 5, ...
R_1^{III}	$E_{22}^{x,y}$	1.04	0.6107	0.6321	0.6323	0.6323	<u>2</u> , 6, 10, ...
R_2^I	$E_{31}^{x,y}$	1.10	0.5037	0.5410	0.5457	0.5458	<u>0</u> , 4, 8, ...
R_3^I	$E_{13}^{x,y}$	1.17	0.5390	0.5446	0.5446	0.5446	<u>2</u> , 6, 10, ...
R_2^{IV}	$E_{23}^{x,y}$	1.41	0.3383	0.3754	0.3850	0.4071	<u>1</u> , <u>3</u> , 5, ...
R_2^{II}	$E_{82}^{x,y}$						<u>1</u> , <u>3</u> , 5, ...
R_3^{II}		1.62	0.2300	0.2230	0.2461	0.2447	<u>1</u> , 3, 5, ...
R_3^{IV}							<u>1</u> , 3, 5, ...
R_4^I		1.74	0.0784	0.1508	0.1892	0.1902	0, <u>4</u> , 8, ...
R_2^{III}		1.81	0.0591	0.1118	0.1240	0.1243	<u>2</u> , 6, 10, ...
R_3^{III}		1.87	0.0914	0.1091	0.1089	0.1089	<u>4</u> , 8, 12, ...

Table II.2. Values of the propagation constant, P^2 , for $B = 2$ for the first 13 modes of a square guide, obtained with determinants up to order 4. Modes are ordered according to the value of B at cutoff. Our mode designation and Goell's are listed, and the dominant term in the field expansion is indicated by an underlined expansion index. With 1-term truncation, the dominant term only is used.

Tables 3 and 4 give the same type of information for the $\tilde{R} = 2$ rectangle as Tables 1 and 2 did for the square. One would expect the convergence at a given order of truncation to become increasingly worse for higher and higher modes. This is borne out in Table 4. Here are shown the effects on P^2 of truncating up to seventh order for the first 13 modes of the $\tilde{R} = 2$ rectangular guide at a fixed value of B . These results demonstrate that either a 2- or 3-term truncation is sufficient for an accuracy of 0.01 or less in P^2 for 7 of 13 modes of this rectangle.

Furthermore, for the first mode of each family (that is, R_1^X), the single-term truncation provides accuracies in P^2 ranging from 0.04 to 0.14. As in the case of the square, the 1-term truncation results shown in Table 4 were obtained by utilizing only the dominant term in the appropriate determinantal equation, Eqns. (32a) or (32b).

For rectangular guides, our results agree quite well with those of other authors <16,17,18>. In Figs. 2 and 5 we show some points taken from Goell's paper <16> which appears to use the most reliable approach other than ours. For the 2:1 rectangle and the dominant mode ($E_{11}^{X,Y}$ in Goell's notation) there is no discernible difference between his curve and ours. For several other modes there are nearly uniform differences of less than 0.07 in P^2 . That is, the curves are adjacent and parallel, and certainly correspond to each other. For the square guide, the same type of results have also been found.

Many qualitative features which can be seen in our Figs. 3 and 6--such as the splitting of R_2^I and R_3^I (square) near cutoff and the crossing of R_1^{IV} and R_2^I (rectangle)--are also present in Goell's curves, although there are numerical discrepancies. Only with the $R_1^{III}(E_{22}^{X,Y})$ mode of the rectangle are there discrepancies greater than 0.1 in P^2 .

B	P^2				Intensity at	
	1 Term	2 Terms	3 Terms	4 Terms	$\phi = 0$	$\phi = \pi/2$
3.0	0.9512	0.9732	0.9726	0.9711	0.007	0.023
2.5	0.9333	0.9628	0.9607	0.9597	0.009	0.031
2.0	0.9035	0.9444	0.9406	0.9402	0.013	0.047
1.5	0.8488	0.9074	0.9022	0.9021	0.023	0.075
1.0	0.7354	0.8170	0.8116	0.8118	0.047	0.142
0.5	0.4456	0.5149	0.5122	0.5124	0.155	0.355

Table 11.3. Results for the dominant (noncutoff) R_1^I mode of the weakly guiding 2:1 rectangular guide. Listed values of P^2 were obtained after a 1-, 2-, 3-, or 4-term truncation of the field expansion. The field intensity at two points on the perimeter is also given. The field intensity at $\phi = 0$ is 1.

Mode Designation		B at Cutoff	P^2 at $B = 2$							Expansion Indices
This Work	Goell ²		1 Term	2 Terms	3 Terms	4 Terms	5 Terms	6 Terms	7 Terms	
R_I^I	E_1^X, Y	0	0.8035	0.9444	0.9406	0.9402	0.9402	0.9402	0.9402	<u>0</u> , <u>2</u> , <u>4</u> , ...
R_I^{II}	E_{2A}^X, Y	0.42	0.7974	0.9141	0.9001	0.9001	0.9001	0.9001	0.9001	<u>1</u> , <u>3</u> , <u>5</u> , ...
R_I^{IV}	E_1^X, Y	0.60	0.7516	0.7959	0.8044	0.8025	0.8022	0.8023	0.8023	<u>1</u> , <u>3</u> , <u>5</u> , ...
R_2^I	E_3^X, Y	0.64	0.5380	---	0.8482	0.8338	0.8335	0.8334	0.8334	<u>0</u> , <u>2</u> , <u>4</u> , ...
R_I^{III}	E_2^X, Y	0.77	0.6206	0.7531	0.7684	0.7620	0.7622	0.7622	0.7622	<u>2</u> , <u>4</u> , <u>6</u> , ...
R_2^{II}	E_4^X, Y	0.87	0.3318	---	0.7470	0.7430	0.7405	0.7405	0.7405	<u>1</u> , <u>3</u> , <u>5</u> , ...
R_2^{IV}		0.95	0.2935	0.4273	0.6934	0.7006	0.6954	0.6957	0.6957	<u>1</u> , <u>3</u> , <u>5</u> , ...
R_3^I		1.08	0.0786	---	0.4935	0.5752	0.5785	0.5777	0.5776	<u>0</u> , <u>2</u> , <u>4</u> , ...
R_4^I		1.12	0.5068	---	0.5723	0.6186	0.6281	0.6216	0.6219	<u>0</u> , <u>2</u> , <u>4</u> , ...
R_2^{III}		1.14	0.0849	---	0.6101	0.6035	0.6036	0.6031	0.6030	<u>2</u> , <u>4</u> , <u>6</u> , ...
R_3^{II}		1.18	0.3823	---	0.5080	0.5353	0.5409	0.5375	0.5377	<u>1</u> , <u>3</u> , <u>5</u> , ...
R_3^{IV}		1.33	0.2174	0.2745	0.2681	0.4942	0.4819	0.4868	0.4848	<u>1</u> , <u>3</u> , <u>5</u> , ...
R_4^{II}		1.35	---	0.2667	0.4115	0.4697	0.4876	0.4783	0.4786	<u>1</u> , <u>3</u> , <u>5</u> , ...

Table II.4. Results for the first 13 modes of the 2:1 rectangular guide, ordered according to the value of B at cutoff. Values of P^2 were obtained for $B = 2$, from the roots of the determinants 1×1 to 7×7 in dimension. Our designation and Goell's are listed. The dominant term in the field expansion is indicated by an underlined expansion index. With 1-term truncation, the dominant term only is used. For certain modes 2-term truncation failed to locate the roots at certain values of B.

With the square guide, all the odd modes are degenerate in pairs (sine and cosine) because of symmetry. (See Fig. 2 and Table 2.) Moreover, except for R_1^I and R_1^{III} , those even modes in which the first term dominates are degenerate in pairs away from cutoff. This can be seen clearly in Fig. 2 for the R_2^I - R_3^I modes. Furthermore, if the B-axis were extended to larger values, then this degeneracy would be more apparent for the R_2^{III} - R_3^{III} modes, as well as for higher modes which are not shown.

As a result of the foregoing, one could take a linear combination of the field expansions for two of these modes and derive an intensity pattern corresponding to neither of the individual modes, but rather to the combination. In fact, with our technique this would automatically occur if one did not recognize the simplifications implied by the symmetry and therefore effect the separation of the field expansions at the beginning. In Goell's Figure 5, intensity patterns for those modes which are degenerate reflect this combination of what appear—especially for the even indices—to be distinct modes. For rectangular cross sections ($\bar{R} > 1$) our field intensity patterns agree with Goell's (see his Fig. 6).

2.5.2 Elliptical Cross Sections

The same calculations which were performed for rectangular guides were repeated using circular ($\bar{R} = 1$) and elliptical ($\bar{R} > 1$) cross sections.

The propagation constants of the circular guide, which are the same (that is, degenerate) for the sine and cosine modes, derive from single-term truncation. They are shown over the range $0 < B < 2.5$ in Fig. 8. As \bar{R} increases from 1 to 2, the sine and cosine modes split and shift. The results of ellipses with $\bar{R} = 1.2, 1.5$ and 2 are depicted in Figs. 9, 10, and 11, respectively. These modes are qualitatively very similar to those of their rectangular counterparts shown in Figs. 3, 4, and 5. In fact, if one makes correspondence $E_n^X \sim R_n^X$, then the order in which the first dozen modes of the elliptical guides reach cutoff is nearly the same as the order for the rectangular guides. Moreover, the actual values of B at cutoff are similar for the two shapes for all \bar{R} . Table 5 gives the actual values of B at cutoff for ellipses with $1 < \bar{R} < 2$ and also, for comparison, for the rectangular guide with $\bar{R} = 2$. Furthermore, the correspondence between the E_m^X and R_m^X modes extends to the field configurations, which comprise very similar patterns.

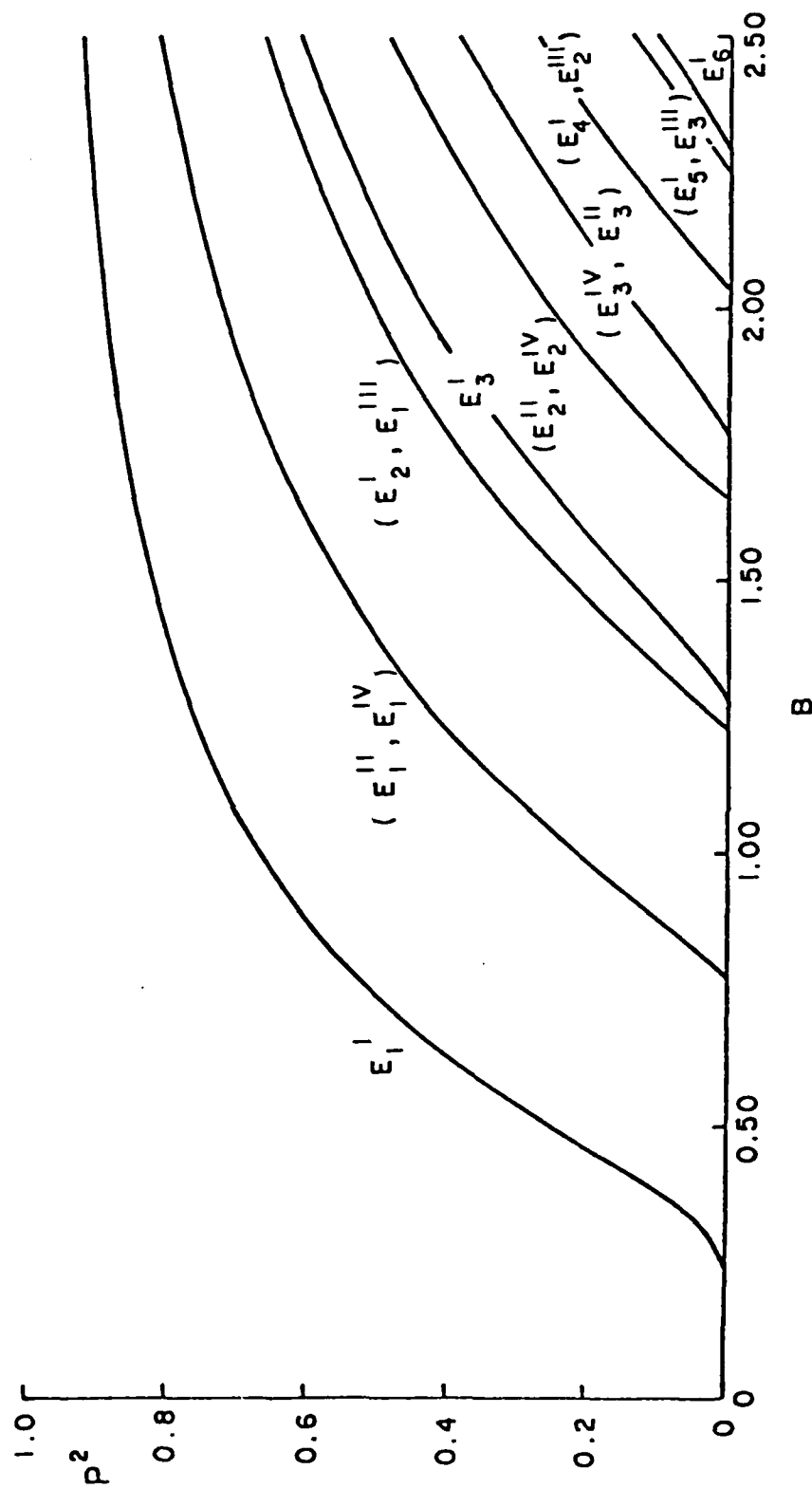


Fig. II.8 Modes of the weakly guiding circular guide.

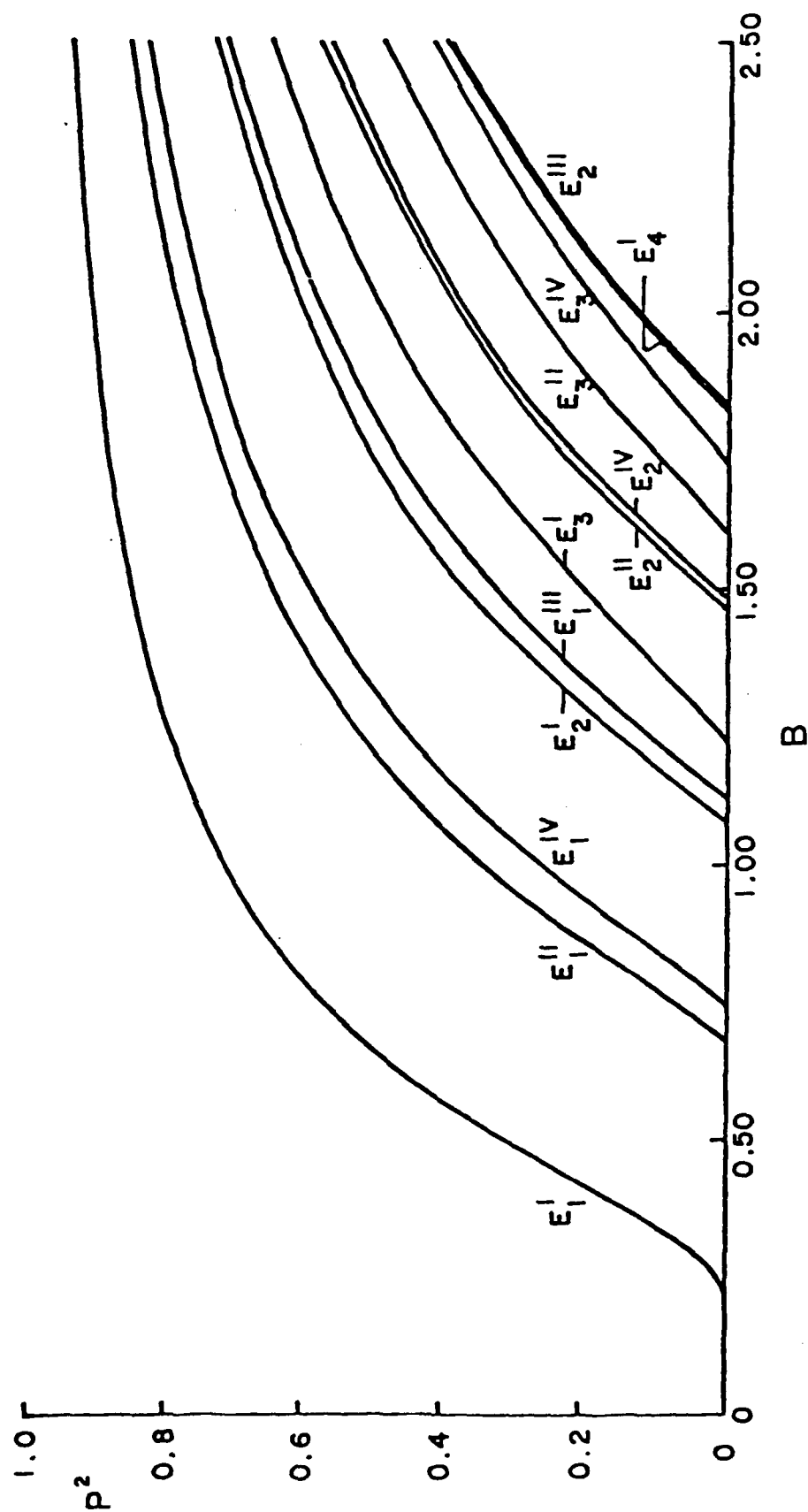


Fig. II.9 Modes of the weakly guiding elliptical guide with $\tilde{R} = 1.2$.

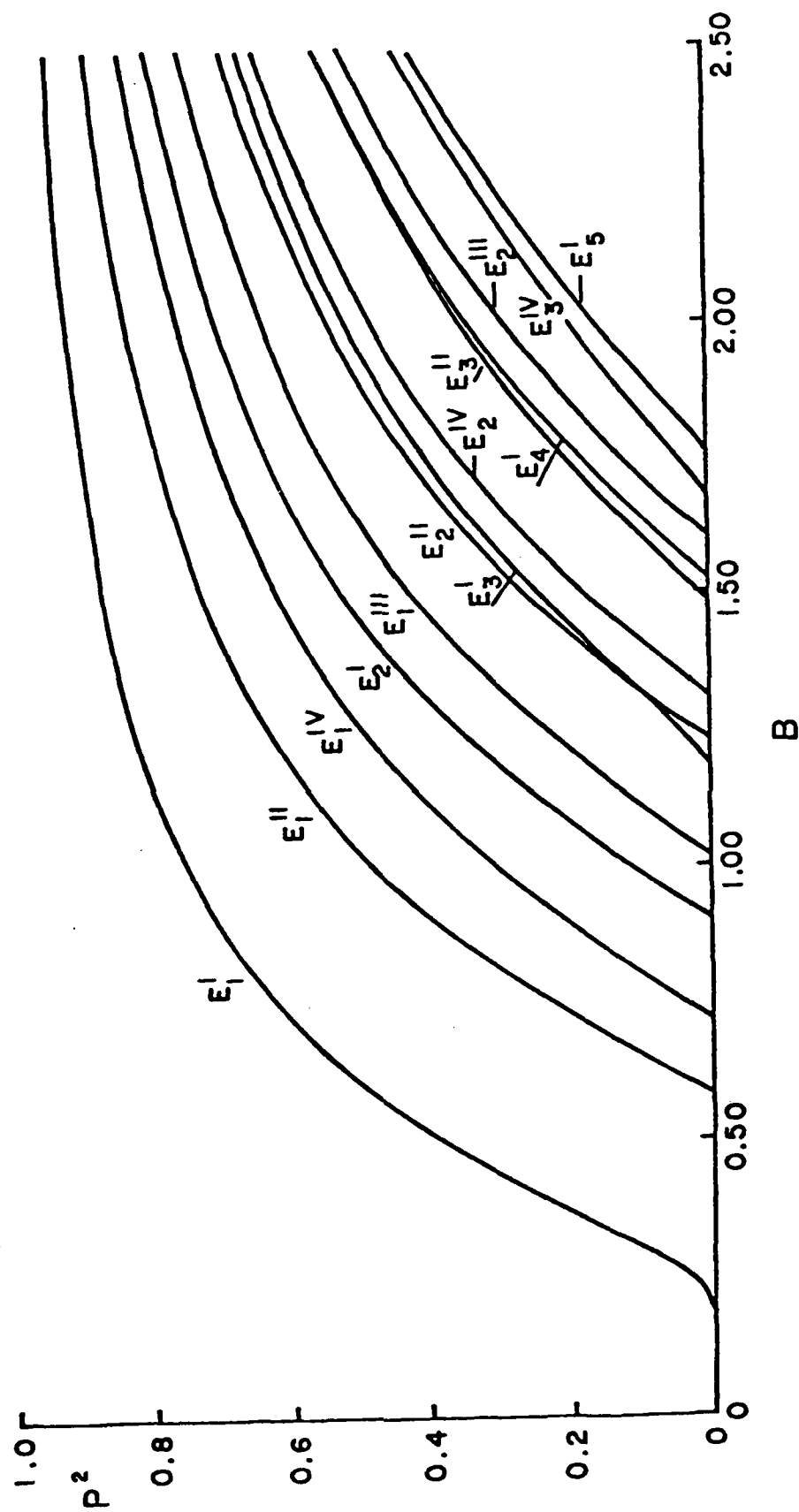


Fig. II.10 Modes of the weakly guiding elliptical guide with $\tilde{R} = 1.5$.

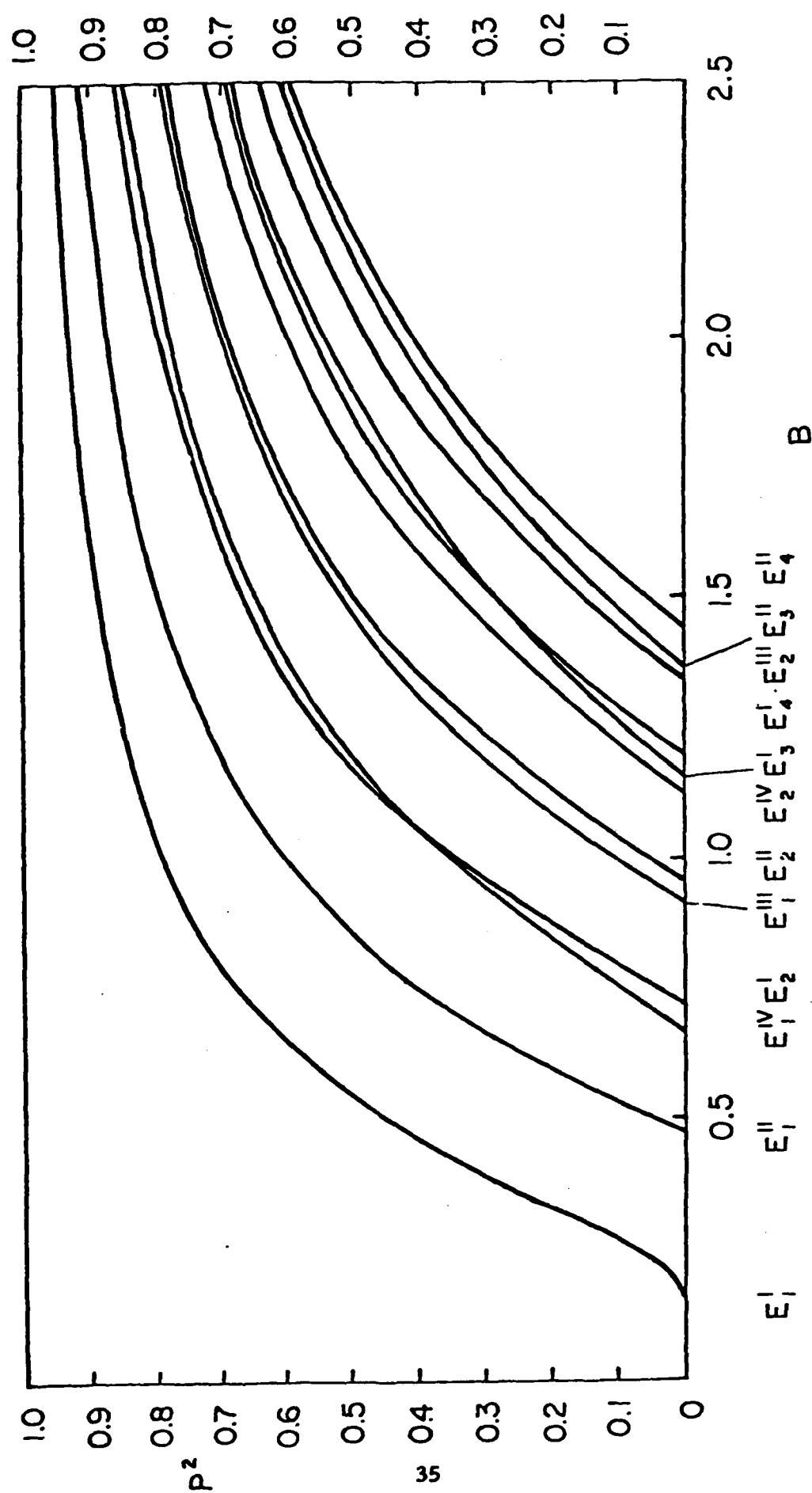


Fig. II.11 Modes of the weakly guiding elliptical guide with $\tilde{R} = 2$.

Mode Designation	Values of Bat Cutoff					Mode Designation
	For Ellipse				For Rectangle	
	$\bar{R} = 1$	$\bar{R} = 1.2$	$\bar{R} = 1.5$	$\bar{R} = 2.0$	$\bar{R} = 2.0$	
E_1^I	0	0	0	0	0	R_1^I
E_1^{II}	0.78	0.68	0.58	0.48	0.42	R_1^{II}
E_1^{IV}	0.78	0.74	0.72	0.67	0.60	R_1^{IV}
E_1^{III}	1.23	1.12	1.01	0.92	0.77	R_1^{III}
E_2^I	1.23	1.07	0.89	0.72	0.64	R_2^I
E_3^I	1.28	1.22	1.18	1.15	1.08	R_3^I
E_2^{IV}	1.65	1.48	1.30	1.13	0.95	R_2^{IV}
E_2^{II}	1.65	1.59*	1.48*	1.37*	1.18	R_3^{II}
E_3^{II}	1.77	1.46*	1.22*	0.96*	0.87	R_2^{II}
E_3^{IV}	1.77	1.72	1.68			
E_4^I	2.03	1.82	1.52	1.20	1.12	R_4^I
E_2^{III}	2.03	1.83	1.60	1.35	1.14	R_2^{III}

Table II.5. Values of B at cutoff for elliptical guides with different aspect ratios and for a rectangular guide with $\bar{R} = 2$. Asterisks indicate where the designations E_2^{II} and E_3^{II} should be interchanged.

The qualitative similarities between modes of the rectangular and elliptical guides approach numerical agreement as the aspect ratio becomes large. In fact, for $R = 10$ the first few modes of either shape guide are virtually indistinguishable for $B > 1.5$. In general, the propagation constants for either differ by more than 0.03 only very close to cutoff.

In Figures (12a) through (12u) we present contour plots of the field intensity, $|\phi(\vec{r})|^2$, for a variety of modes of circular guides and 2:1 ellipses. The field maxima are in the center of the oval or circular shaped contours.

In Figures (12a-c) the fundamental E_1^I mode of the circular guide is drawn for different values of B . The most tightly bound mode (12c, corresponding to the largest B) shows the greatest concentration of the field within the core. For smaller B (12a) the field does not diminish greatly between the center and the core-cladding interface, indicating that a substantial field intensity is found in the cladding. Figures (12d-f) indicate the same thing for elliptical guides.

Figures (12g) and (12h) demonstrate, using the E_1^{II} mode of a circle, that even a substantial increase in B (from .79 to 1.27, for a mode that cuts off at $B = .78$) does not change the field intensity pattern greatly. This is generally true (e.g., Figs. (12i-j) and (12k-l)) for modes other than the fundamental mode, and it is even true of the fundamental mode for values of B which yield propagation constants, P^2 , greater than about .2.

For circles the E_1^{IV} mode is the same as the E_1^{II} mode, except that the pattern is rotated 90° and the maxima appear on the y-axis. Obviously there is no physical significance to this difference. However in Figures (12j) and (12l), which of course do represent distinct modes for the elliptical cross-section, a qualitative similarity can be seen when comparison is made with the corresponding E_1^{II} and E_1^{IV} modes of the circle.

In Figures (12m-u) some higher-order modes are depicted for various values of B .

Our results for circular cross-sections are the same as those previously reported <7, 19>. This is the result of the fact, noted earlier, that the one-term truncation of our equation set is analytically equivalent to the simple transcendental equation derived for circular guides. For elliptical cross-sections, however, there are discrepancies between our work and that of Yeh <19>. The problem is that Yeh lists what appear to be two different, but degenerate, modes for the circular guide; HE_{11} and HE_{01} in his notation.

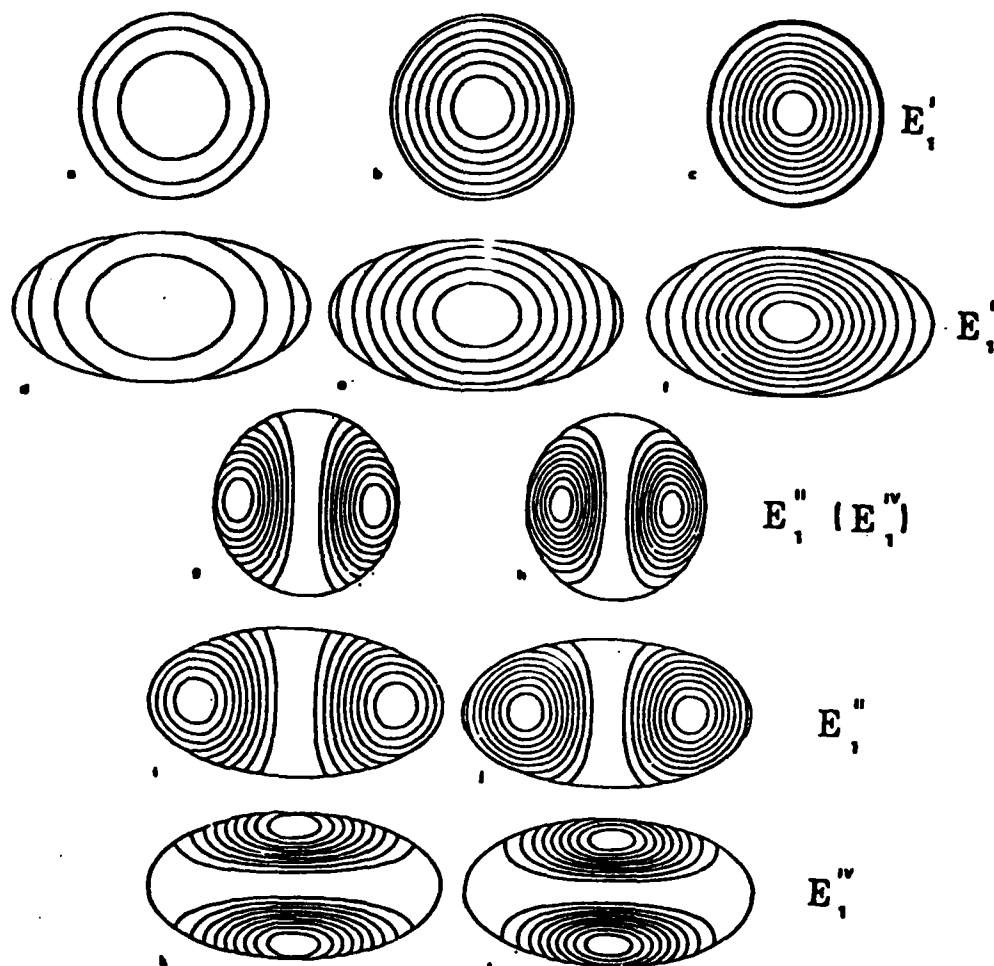


Fig. II.12 Contours of constant intensity inside the core region for various modes of the circular and 2:1 elliptical guides. The regions near the centers of the oval or circular shaped contours possess the maximum intensity, with each successive receding contour denoting a 10% decrease in intensity. The B values corresponding to each figure are (a) 0.25, (b) 0.5, (c) 1.27, (d) 0.18, (e) 0.33, (f) 0.85, (g) 0.78, (h) 1.27, (i) 0.49, (j) 0.73, (k) 0.68, and (l) 0.85. The modes of the circular guide which are degenerate are designated within parentheses.

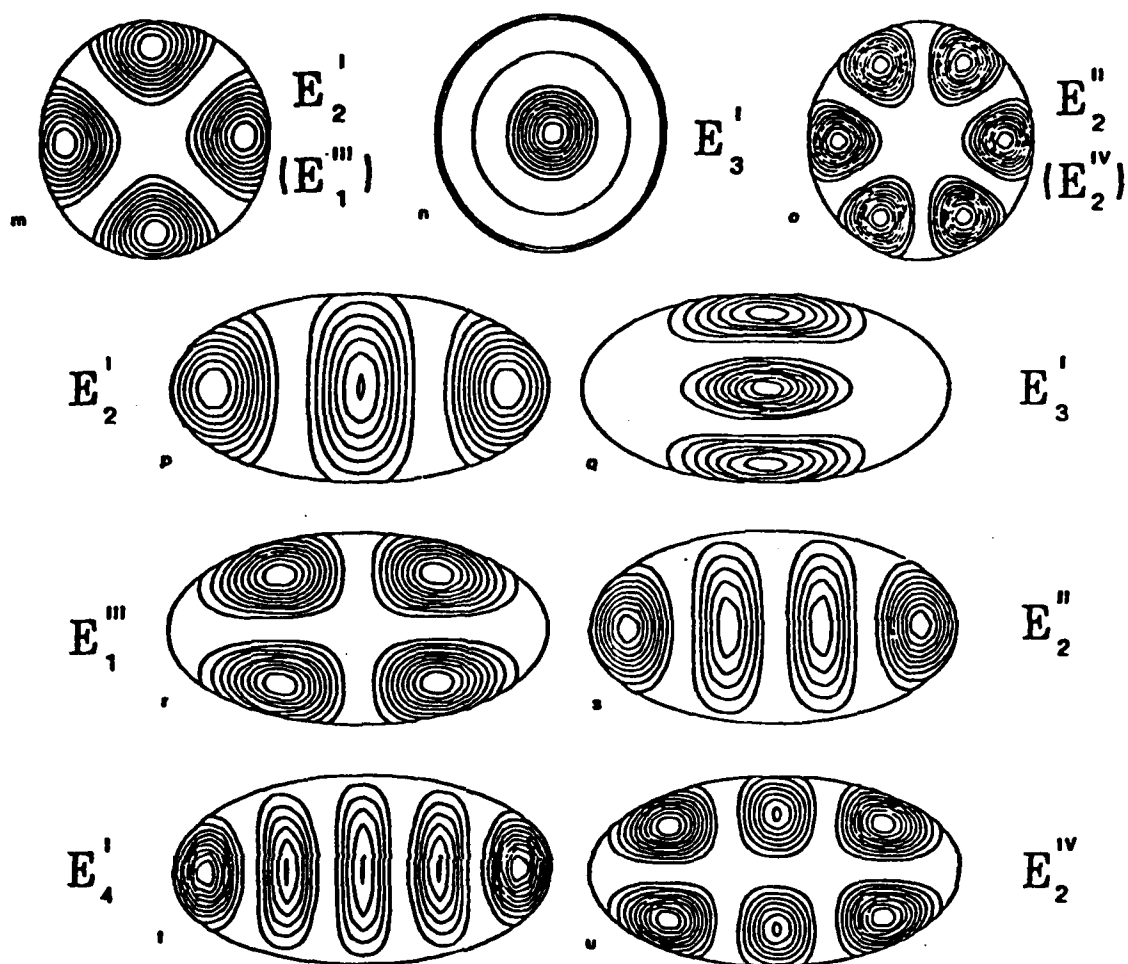


Fig. II.12 The B values are (m) 1.27, (n) 2.0, (o) 2.75,
 (cont.) (p) 0.85, (q) 1.85, (r) 1.5, (s) 1.5, (t) 1.85,
 and (c) 1.8.

Then, as the circle deforms into an ellipse, he shows each of these modes becoming a nondegenerate mode, with the propagation constants of one mode being greater in magnitude than those of the circular guide and those of the other mode being less. However, we find just one dominant mode (E_1^I) for the circle which does not split into two modes as \tilde{R} increases. In addition, our results for this single noncutoff mode agree very well with a perturbation calculation of Eyges <18>. Furthermore, Yeh's data for an elliptical guide having an aspect ratio of 2.164 do not correspond at all to our results for either an $\tilde{R} = 2$ ellipse (plotted in Fig. 11) or an $\tilde{R} = 2.164$ ellipse. Hence, we are unable to correlate our results with his.

2.5.3 Other Results

We have used our technique to study the propagation modes of guides of certain other shapes obtainable from Eqn. (31), mostly with $\tilde{R} = 1$. Among these are superellipses with $\tilde{N} = 2$ and $\tilde{N} = 5$, and a cusped shape deriving from $\tilde{N} = 0.3$. These are described in Reference 2. They show few qualitative differences from the results described in Sections 2.5.1 and 2.5.2.

There are many similarities between the elliptical and rectangular guides, so it is no surprise that all the measurable characteristics of the intermediate superelliptical shape (the propagation constants, field configurations, cutoff values, order of the modes, dependence on \tilde{R} , convergence of the series) fall between those of the former shapes. In fact, for $\tilde{N} = 2$ and $\tilde{R} = 1$, the superellipse is closer to the square than the circle in all respects, and for $\tilde{N} = 5$ it is practically indistinguishable from the square. For $\tilde{R} = 1$ the modes all shift in a smooth and orderly manner as \tilde{N} changes from 1 to 30.

The convergence of the series is marginally better for the elliptical shape than for the superellipses and rectangles.

The cusped shape ($\tilde{N} < .5$) is quite different in appearance, and the characteristics of the modes reflect this. The order in which the modes cut off is quite different, as are the propagation constants themselves.

In view of the fact that our results for the rectangle and square agree quite closely with those of Goell and the fact that his point-matching method requires the evaluation of a determinant of order $4M$, with $3 < M < 9$, the economy of our method becomes obvious. Furthermore, unlike the differential equation approach utilized by Goell, our integral representation

technique avoids the necessity of having to use a coordinate system dictated by the guide's cross-sectional shape as well as the special functions characteristic of that system. This means that in the case of the elliptic guides, for example, one need not be forced to use elliptic cylinder coordinates nor the complicated Mathieu functions associated with such coordinates.

3. Arrays of Step-Index Guides

3.1 Introduction

We wish to consider a general array of N parallel guides embedded in a uniform cladding of infinite extent. The guiding regions, distinguished by the superscript or subscript i , have indices of refraction $n_1^{(i)}$ and cross-sections A_i . The cladding region has an index n_2 . Any or all of these regions may guide electromagnetic energy. The problem is to calculate the properties of all the waves which can propagate in the entire system.

The traditional way of approaching this problem is to first calculate the properties of the regions, A_i , individually by some means and then to account for the influence of the evanescent fields of each individual region on the waves in any other regions which they may overlap. This two-step process, best exemplified by coupled-mode theory <20,21>, is successful in predicting the properties of some arrays with two guiding elements, e.g. two adjacent circular cylinders. However the difficulty of doing this for arbitrary geometries is twofold: it requires the fields of the individual regions, which may be difficult or impossible to obtain in analytical form---or even numerical form; and it then requires the integration of these fields over the areas of all the other regions. Moreover the boundary conditions may be satisfied for each region separately in the first step, but there is no such requirement for the array as a whole at the end. The resulting solutions are therefore approximate field amplitudes rather than the normal modes of the system. This means that the poorest approximation occurs when two or more regions are quite close together, which is generally the configuration which is most important and interesting.

The integral-equation technique does not have these disadvantages. One does obtain the normal modes, and they are found in a single step without separate procedures for separate regions. In fact, a solitary

waveguide is a special case of the general array, or any array can be viewed as a single guide with a very complicated cross-section. Because this technique is indifferent to the cross-sections, these really constitute a single kind of problem, at least in principle.

This is not to say that the technique solves every possible problem. There are probably very extreme and peculiar geometrical configurations for which the field expansions will not converge. And the analytical and computational cost of calculating the modes of large arrays lacking any convenient symmetry simplifications might be prohibitive. Nevertheless it does yield the normal modes of a great many configurations which cannot be otherwise solved at all, and it generally does so quickly and efficiently.

The general procedure of the integral equation technique is, as for single guides, to derive an integral representation for the field components which is equivalent to the differential equations inside the guiding regions and in the cladding and which guarantees that the boundary conditions are satisfied. The principal difference comes about in the assignment of separate coordinate systems to each core region. This allows the line integrals about the locus of source points, $\vec{\rho}'$, on each perimeter to be performed without heroic efforts. However, in order to reduce the integral equation to terms containing the basis functions in the observation points, $\vec{\rho}$, (e.g., Eqn. (16)) it is necessary to express these basis functions in some commonly recognized coordinates. It is therefore crucial to have transformations which relate the basis functions in the various coordinate systems to each other. It is obvious that the more complicated these coordinate transformations are, the more difficult it is to write down and solve the linear equations for the system. Symmetry considerations are therefore very important.

The most common problem is that of two guides with reflection symmetry. This problem is simplified considerably if the line joining the origins of the two coordinate systems is coincident with a reflection axis of each guide. A further simplification of great importance occurs when the two guides are identical---that is, they have the same shape and the same index of refraction. Therefore, at the point where the basis function transformations must be introduced, we will specialize the analysis to the two-guide problem and then indicate how the two above-mentioned simplifications make life easier. Later on, we will write down the formulation for the general array.

3.2 Equations for a General Array

Since, at this stage, we wish to consider a general array of guides, the problem can initially be written as $N+1$ Helmholtz equations,

almost exactly as in Eqn. (3):

$$(\nabla^2 + \epsilon_i^{(1)})\Phi(\vec{\rho}) = 0 \quad \vec{\rho} \text{ in } A_i, \quad i = 1, \dots, N \quad (37a)$$

$$(\nabla^2 + \epsilon_2^2)\Phi(\vec{\rho}) = 0 \quad \vec{\rho} \text{ in cladding} \quad (37b)$$

The notation will be to place a superscript or subscript (i) on each quantity which is uniquely associated with the ith guide, and to denote the coordinates of the ith system by subscripts---e.g., (ρ_i, ϕ_i) ---so as not to conflict with the primes. (Both the notation and the analysis follow Section II-2 quite closely.) The scalar function

$$\Phi(\vec{\rho}) = - \sum_{i=1}^N (\epsilon_i^{(1)} - \epsilon_2^2) \int_{A_i} \Phi(\vec{\rho}') g_2(\vec{\rho}, \vec{\rho}') dA' \quad (38)$$

satisfies all these equations. For $\vec{\rho}$ inside some core region, A_j , this is equivalent to

$$\sum_{i=1}^N \int_{L_i} \left\{ g_2(\vec{\rho}, \vec{\rho}') \frac{\partial \Phi(\vec{\rho}')}{\partial n_i'} - \Phi(\vec{\rho}') \frac{\partial g_2(\vec{\rho}, \vec{\rho}')}{\partial n_i'} \right\} dL' = 0 \quad \vec{\rho} \text{ in } A_i \quad (39)$$

Eqn. (39) is quite similar to what we had before except that now there is a separate line integral equation for each of the N possibilities denoted by j, and the left-hand side of each equation consists of a sum of N terms. We have already put the subscript i on the normal derivative, indicating the implicit dependence on the particular contour over which each integral in the sum is to be performed. The general solution, $\Phi(\vec{\rho})$, will also be written as a different expansion in each coordinate system:

$$\Phi^{(i)}(\vec{\rho}) = \sum_{s=0}^{\infty} J_s(\epsilon_i \rho_i') [C_s^{(i)} \cos(s\phi_i') + D_s^{(i)} \sin(s\phi_i')] \quad (40)$$

It is the representations of the Green functions, Eqns. (8) and (9), that must be considered carefully since it is here that the coordinate $\vec{\rho}$ appears.

Consider, among the N equations, the jth one, in which the observation point is (near) the origin of the jth coordinate system. This same point, $\vec{\rho}$, appears in each of the line integrals which, of course, are each performed in the coordinate systems centered in their respective guides. The geometry of this situation, which is illustrated in Fig. 13, makes clear the need for representations of the Green function which converge regardless of whether $\rho > \rho'$ or $\rho < \rho'$. That is, in the jth term of the sum appearing in the jth equation, we have the situation which characterizes the single-guide problem: the observation point, $\vec{\rho}$, is

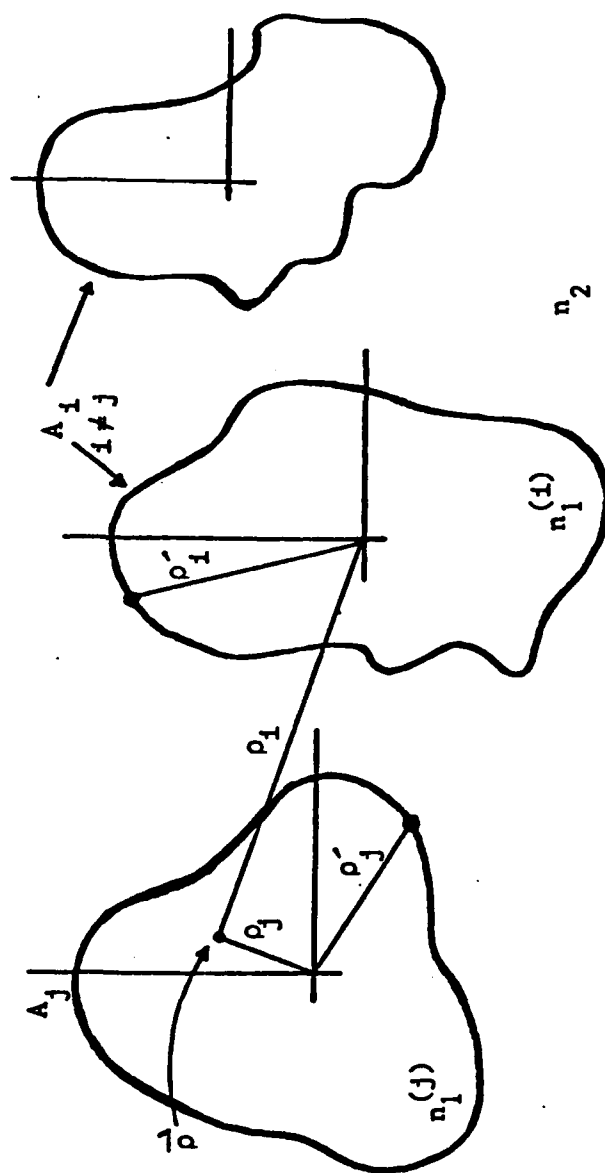


Fig. II.13 An array of guides with separate (x, y) or (ρ, ϕ) coordinate systems. The observation point, ρ , lies inside the core indexed by j .

closer to the origin than all the source points $\vec{\rho}'$, and Eqn. (8) is used for $g_2(\vec{\rho}, \vec{\rho}')$. But in the $N-1$ terms in this sum for which $i \neq j$, the opposite situation occurs: the source points $\vec{\rho}'$, which lie on the other perimeters, are closer to the origins of the coordinate systems in which these integrals are being performed than the observation point, which is still within the j th guide. In these cases, Eqn. (9) must be taken for $g_2(\vec{\rho}, \vec{\rho}')$.

(It is possible to imagine closely-spaced elongated guides in which $\rho > \rho'$ for only some of the points on the i th perimeter, and $\rho < \rho'$ for others. For most geometries, this does not occur.)

From the foregoing, it is clear that for each equation there is one line integral in which Eqn. (8) is used for the Green function, and $N-1$ in which Eqn. (9) is used. The formulation involves all N equations simultaneously, and each of the N guides becomes the special (j th) one in one equation.

Before proceeding, it is worth noting that the two representations of $g_2(\vec{\rho}, \vec{\rho}')$ are the same algebraically except that the Bessel and Hankel functions are exchanged. In Eqn. (8) the unprimed coordinates are in the argument of the Bessel functions; in Eqn. (9) they are in the Hankel functions. One can thus write the analog of Eqn. (15) by inspection.

Consider, once again, a single one of the N equations, Eqns. (39), denoted by the index j . To proceed, one inserts the expressions for $\Phi(\vec{\rho})$ and its derivative into this equation using a separate expansion for each line integral in it. One substitutes the expressions for g_2 and its derivative into each term, using the appropriate representations. The obvious analogs of Eqns. (14) and (15) are used for the derivatives. After much manipulation, the result for this single equation takes the form

$$\sum_{l=0}^{\infty} S_{1l}^{(j)} J_l(x_l \rho_j) \cos(2l\phi_j) + \sum_{l=0}^{\infty} S_{2l}^{(j)} J_l(x_l \rho_j) \sin(2l\phi_j) \quad (41)$$

$$+ \sum_{i \neq j}^N \left[\sum_{l=0}^{\infty} S_{3l}^{(i)} H_l(x_l \rho_i) \cos(2l\phi_i) + \sum_{l=0}^{\infty} S_{4l}^{(i)} H_l(x_l \rho_i) \sin(2l\phi_i) \right] = 0$$

The first two terms, of course, result from the j th term in the sum and are exactly the same as the corresponding expressions in Eqn. (16), except for the superscripts and subscripts which distinguish the j th coordinate system. The last terms, on the other hand, come from those integrals performed in coordinate systems other than the j th one, and

as such constitute the departure from the single-guide analysis previously considered. Also, the basis functions in the unprimed coordinate appearing in these terms are Hankel functions instead of Bessel functions, as a consequence of the exchange of H_ℓ and J_ℓ in the second representation of the Green function.

The coefficients $S_{1\ell}^{(j)}$ and $S_{2\ell}^{(j)}$ are exactly the same as before, having been derived by an identical analysis. They are given, respectively, by the right-hand sides of Eqns. (18a) and (18b) with the understanding that superscripts (j) should appear on the coefficients C_s and D_s and on γ_1 , and furthermore that all references to the coordinates (ρ', ϕ') imply the jth coordinate system. (E.g., the integration is over $d\phi_j'$.) The other coefficients are

$$S_{3\ell}^{(i)} = \int_{L_i} d\phi_i' \epsilon_2 \left\{ \left[J_\ell(r_2 \rho_i') \cos(\ell \phi_i') \right] \left[\sum_{s=0}^{\infty} \gamma_s^{(i)} \rho_i' J_s'(r_1^{(i)} \rho_i') \right] \left\{ C_s^{(i)} \cos(s \phi_i') + D_s^{(i)} \sin(s \phi_i') \right\} \right. \\ \left. + \frac{\partial \rho_i'}{\partial \phi_i'} \frac{s}{\rho_i'} J_s(r_1^{(i)} \rho_i') \left\{ C_s^{(i)} \sin(s \phi_i') - D_s^{(i)} \cos(s \phi_i') \right\} \right] \quad (42a)$$

$$- \left[r_2 \rho_i' J_\ell'(r_2 \rho_i') \cos \ell \phi_i' + \frac{\partial \rho_i'}{\partial \phi_i'} \frac{\ell}{\rho_i'} J_\ell(r_2 \rho_i') \sin(\ell \phi_i') \right] \left[\sum_{s=0}^{\infty} J_s(r_1^{(i)} \rho_i') \left\{ C_s^{(i)} \cos(s \phi_i') + D_s^{(i)} \sin(s \phi_i') \right\} \right] \Bigg\}$$

$$S_{4\ell}^{(i)} = \int_{L_i} d\phi_i' \epsilon_2 \left\{ \left[J_\ell(r_2 \rho_i') \sin(\ell \phi_i') \right] \left[\textcircled{2} \right] \right. \\ \left. - \left[r_2 \rho_i' J_\ell'(r_2 \rho_i') \sin(\ell \phi_i') - \frac{\partial \rho_i'}{\partial \phi_i'} \frac{\ell}{\rho_i'} J_\ell(r_2 \rho_i') \cos(\ell \phi_i') \right] \left[\textcircled{4} \right] \right\} \quad (42b)$$

where "2" and "4" in Eqn. (42b) are the same as the corresponding terms in Eqn. (42a).

Before introducing the basis function transformations, we make some definitions which allow us to write the coefficients $S_{1\ell}$ through $S_{4\ell}$ more compactly. First of all, quantities $F_{\ell s}(\rho')$ and $E_{\ell s}(\rho', \frac{\partial \rho'}{\partial \phi})$ are defined exactly as in Eqns. (19) with the exception that γ_1 now carries

the superscript (j) and the coordinates have that as a subscript. In addition,

$$H_{22}^{(i)}(\rho_i) = \epsilon_2 \left\{ r_1 \rho_i J_2(r_2 \rho_i) J_2'(r_1^{(i)} \rho_i) - r_2 \rho_i J_2'(r_2 \rho_i) J_2(r_1^{(i)} \rho_i) \right\} \quad (43a)$$

$$G_{22}^{(i)}(\rho_i, \frac{\partial \rho_i}{\partial \phi_i}) = \epsilon_2 J_2(r_2 \rho_i) J_2'(r_1^{(i)} \rho_i) \frac{\partial \rho_i}{\partial \phi_i} / \rho_i \quad (43b)$$

Furthermore the matrix elements $R_{ls}^{(j)}$, $U_{ls}^{(j)}$, $V_{ls}^{(j)}$, and $T_{ls}^{(j)}$ are defined as in Eqns. (20), except that superscripts or subscripts (j) apply to F_{ls} , E_{ls} , and the coordinates whenever they appear. To deal with the nonprivileged terms designated by (i) rather than (j), we write

$$\bar{R}_{22}^{(i)} = \int_{L_i} d\phi_i \left[H_{22}^{(i)}(\rho_i) \cos 2\phi_i \cos s\phi_i + G_{22}^{(i)}(\rho_i, \frac{\partial \rho_i}{\partial \phi_i}) \{ s \cos 2\phi_i \sin s\phi_i - l \sin 2\phi_i \cos s\phi_i \} \right] \quad (44a)$$

$$\bar{U}_{22}^{(i)} = \int_{L_i} d\phi_i \left[H_{22}^{(i)}(\rho_i) \cos 2\phi_i \sin s\phi_i - G_{22}^{(i)}(\rho_i, \frac{\partial \rho_i}{\partial \phi_i}) \{ s \cos 2\phi_i \cos s\phi_i + l \sin 2\phi_i \sin s\phi_i \} \right] \quad (44b)$$

$$\bar{V}_{22}^{(i)} = \int_{L_i} d\phi_i \left[H_{22}^{(i)}(\rho_i) \sin 2\phi_i \cos s\phi_i + G_{22}^{(i)}(\rho_i, \frac{\partial \rho_i}{\partial \phi_i}) \{ s \sin 2\phi_i \sin s\phi_i + l \cos 2\phi_i \cos s\phi_i \} \right] \quad (44c)$$

$$\bar{T}_{22}^{(i)} = \int_{L_i} d\phi_i \left[H_{22}^{(i)}(\rho_i) \sin 2\phi_i \sin s\phi_i - G_{22}^{(i)}(\rho_i, \frac{\partial \rho_i}{\partial \phi_i}) \{ s \sin 2\phi_i \cos s\phi_i - l \cos 2\phi_i \sin s\phi_i \} \right] \quad (44d)$$

Then the coefficients can be written in compact form:

$$S_{12}^{(i)} = \sum_{s=0}^{\infty} \left[C_s^{(i)} R_{2s}^{(i)} + D_s^{(i)} U_{2s}^{(i)} \right] \quad (45a)$$

$$S_{22}^{(i)} = \sum_{s=0}^{\infty} \left[C_s^{(i)} V_{2s}^{(i)} + D_s^{(i)} T_{2s}^{(i)} \right] \quad (45b)$$

$$S_{32}^{(i)} = \sum_{s=0}^{\infty} \left[C_s^{(i)} \bar{R}_{2s}^{(i)} + D_s^{(i)} \bar{U}_{2s}^{(i)} \right] \quad (45c)$$

$$S_{42}^{(i)} = \sum_{s=0}^{\infty} \left[C_s^{(i)} \bar{V}_{2s}^{(i)} + D_s^{(i)} \bar{T}_{2s}^{(i)} \right] \quad (45d)$$

3.3 The Two-Guide Problem

3.3.1 Linear Equations for Two Guides

In order to make use of Eqn. (41), or rather the N equations which all have that form, it becomes necessary (finally) to introduce the transformation functions for the unprimed coordinates' basis functions. Since the general transformations make things quite complicated, we begin with the example of just two guides.

Assume that the central points which are chosen for the origins of the two coordinate systems are separated by a fixed distance d . We may then without prejudice choose the x -axes of these systems to be co-linear, as in Fig. 14a. With this choice, one can take advantage of the following expansions <6>:

$$H_2(r_2, \phi_2) \cos[l(\pi - \phi_2)] = \sum_{k=-\infty}^{\infty} H_{2+k}(r_2, d) J_k(r_2, \rho_1) \cos(k\phi_1) \quad (46a)$$

$$H_2(r_2, \phi_2) \sin[l(\pi - \phi_2)] = \sum_{k=-\infty}^{\infty} H_{2+k}(r_2, d) J_k(r_2, \rho_1) \sin(k\phi_1) \quad (46b)$$

to relate the functions containing the Hankel functions and $\hat{\rho}_2$ with those containing the Bessel functions and $\hat{\rho}_1$. This is another form of Graf's addition theorem, which relates cylinder functions of integer order to Bessel functions of the first kind, when the arguments can be given in terms of the sides and interior angles of a triangle such as is drawn in Fig. 14a.

Alternatively, we may wish to not restrict the orientation of the two guides' coordinate systems with respect to the line connecting the origins. In this case, illustrated in Fig. 14b, the same theorem has the more complicated form

$$H_2(r_2, \phi_2) \cos[l(\gamma + \pi - \phi_2)] = \sum_{k=-\infty}^{\infty} H_{2+k}(r_2, d) J_k(r_2, \rho_1) \cos[k(\phi_1 - \gamma)] \quad (47a)$$

$$H_2(r_2, \phi_2) \sin[l(\gamma + \pi - \phi_2)] = \sum_{k=-\infty}^{\infty} H_{2+k}(r_2, d) J_k(r_2, \rho_1) \sin[k(\phi_1 - \gamma)] \quad (47b)$$

For the two-guide problem, there is no advantage to the second choice (unless, possibly, the guides have reflection symmetry about the two

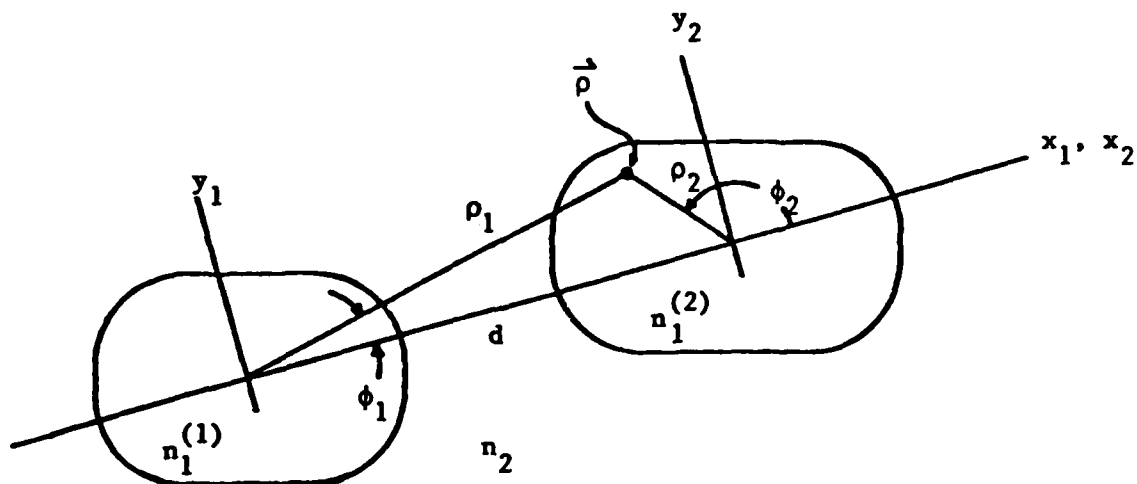


Fig. II.14(a) The coordinates of a point $\vec{\rho}$ in a two-guide array with the x-axes of the coordinate systems chosen to be co-linear so as to simplify the transformation functions.

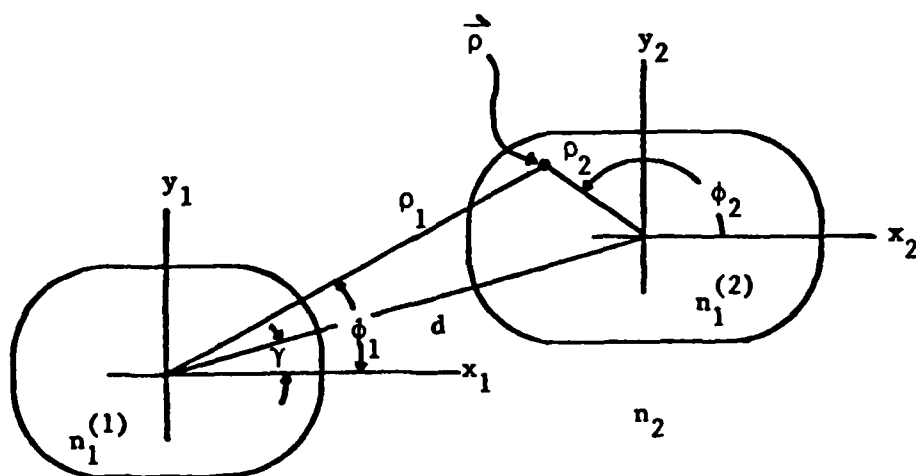


Fig. II.14(b) The coordinates of a point $\vec{\rho}$ in a two-guide array with the x-axes chosen to take advantage of the symmetry of the individual cross-sections.

x-axes; even then it is marginal). For cases in which there are more than two guides which are not in a line, however, the more complicated expression must be applied.

Eqns. (46) allow us to express the requisite function of $\vec{\rho}$, given in coordinate system #2, in terms of coordinates (ρ_1, ϕ_1) . By making use of trigonometric identities and properties of the Bessel and Hankel functions of negative order, we convert these equations to

$$H_2(r_2 \rho_2) \cos l \phi_2 = \sum_{k=0}^{\infty} \alpha_{ke} J_k(r_2 \rho_1) \cos k \phi_1 \quad (48a)$$

$$H_2(r_2 \rho_2) \sin l \phi_2 = \sum_{k=0}^{\infty} \beta_{ke} J_k(r_2 \rho_1) \sin k \phi_1 \quad (48b)$$

where the constant coefficients depend on the distance, d :

$$\alpha_{ke} = \frac{1}{2} (-1)^k \epsilon_k \left\{ H_{k-2}(r_2 d) (-1)^k + H_{k+2}(r_2 d) \right\} \quad (49a)$$

$$\beta_{ke} = (-1)^k \left\{ H_{k-2}(r_2 d) (-1)^k - H_{k+2}(r_2 d) \right\} \quad (49b)$$

These expressions can be used in Eqn. (41). For the two-guide case, however, there are two such equations to be considered. For the first one ($\vec{\rho}$ in A_1 , $j=1$, $i=2$) we need $S_{1l}^{(1)}$, $S_{2l}^{(1)}$, $S_{3l}^{(2)}$ and $S_{4l}^{(2)}$ and functions of $\vec{\rho}$ given in the first coordinate system (as in Eqns. (48)). For the second equation ($\vec{\rho}$ in A_2 , $j=2$, $i=1$) we not only need $S_{1l}^{(2)} \dots S_{4l}^{(1)}$ ---that is, the same integrands integrated over different perimeters---but also the functions of $\vec{\rho}$ must be written in the second coordinate system. This requirement forces us to obtain a parallel set of transformations by exchanging the coordinate systems, or by letting ϕ_1 go into $\pi - \phi_2$ and vice versa in Eqns. (46). The result is

$$H_2(r_2 \rho_1) \cos l \phi_1 = \sum_{k=0}^{\infty} \eta_{ke} J_k(r_2 \rho_2) \cos k \phi_2 \quad (50a)$$

$$H_2(r_2 \rho_1) \sin l \phi_1 = \sum_{k=0}^{\infty} \mu_{ke} J_k(r_2 \rho_2) \sin k \phi_2 \quad (50b)$$

where

$$\eta_{kl} = \frac{1}{2} \epsilon_k (-1)^k \{ H_{k-2}(\gamma_2 d) (-1)^l + H_{k+2}(\gamma_2 d) \} = \alpha_{kl} (-1)^{k-2} \quad (51a)$$

$$\mu_{kl} = (-1)^k \{ H_{k-2}(\gamma_2 d) (-1)^l - H_{k+2}(\gamma_2 d) \} = \beta_{kl} (-1)^{k-2} \quad (51b)$$

Now, with the introduction of the Kronecker delta δ_{kl} , the two versions of Eqn. (41) can be written down as

$$\sum_{l=0}^{\infty} S_{1l}^{(1)} \sum_{k=0}^{\infty} \delta_{kl} J_k(\gamma_2 \rho_1) \cos k\phi_1 + \sum_{l=0}^{\infty} S_{2l}^{(1)} \sum_{k=0}^{\infty} \delta_{kl} J_k(\gamma_2 \rho_1) \sin k\phi_1 \quad (52a)$$

$$+ \sum_{l=0}^{\infty} S_{3l}^{(2)} \sum_{k=0}^{\infty} \alpha_{kl} J_k(\gamma_2 \rho_1) \cos k\phi_1 + \sum_{l=0}^{\infty} S_{4l}^{(2)} \sum_{k=0}^{\infty} \beta_{kl} J_k(\gamma_2 \rho_1) \sin k\phi_1 = 0$$

$$\sum_{l=0}^{\infty} S_{3l}^{(1)} \sum_{k=0}^{\infty} \eta_{kl} J_k(\gamma_2 \rho_2) \cos k\phi_2 + \sum_{l=0}^{\infty} S_{4l}^{(1)} \sum_{k=0}^{\infty} \mu_{kl} J_k(\gamma_2 \rho_2) \sin k\phi_2 \quad (52b)$$

$$+ \sum_{l=0}^{\infty} S_{1l}^{(2)} \sum_{k=0}^{\infty} \delta_{kl} J_k(\gamma_2 \rho_2) \cos k\phi_2 + \sum_{l=0}^{\infty} S_{2l}^{(2)} \sum_{k=0}^{\infty} \delta_{kl} J_k(\gamma_2 \rho_2) \sin k\phi_2 = 0$$

These equations can be satisfied in general only if the coefficients of each of the basis functions, $J_k(\gamma_2 \rho_1) \cos(k\phi_1)$, $J_k(\gamma_2 \rho_1) \sin(k\phi_1)$,

$J_k(\gamma_2 \rho_2) \cos(k\phi_2)$, and $J_k(\gamma_2 \rho_2) \sin(k\phi_2)$ is zero. For each value of k ,

therefore, there are four separate equations. (In principle, k runs from 0 to ∞ .) Inverting the summation order in k and l , this leads to

$$\sum_{l=0}^{\infty} (S_{1l}^{(1)} \delta_{kl} + S_{3l}^{(2)} \alpha_{kl}) = 0 \quad k = 0, 1, \dots \quad (53a)$$

$$\sum_{l=0}^{\infty} (S_{2l}^{(1)} \delta_{kl} + S_{4l}^{(2)} \beta_{kl}) = 0 \quad k = 0, 1, \dots \quad (53b)$$

$$\sum_{l=0}^{\infty} (S_{3l}^{(1)} \eta_{kl} + S_{1l}^{(2)} \delta_{kl}) = 0 \quad k = 0, 1, \dots \quad (53c)$$

$$\sum_{l=0}^{\infty} (S_{4l}^{(1)} \mu_{kl} + S_{2l}^{(2)} \delta_{kl}) = 0 \quad k = 0, 1, \dots \quad (53d)$$

Now, in a manner not much more complicated than that leading to Eqn. (16), we have converted the two integral equations into a 4-fold infinity of linear equations in the coefficients $C_s^{(1)}$, $D_s^{(1)}$, $C_s^{(2)}$, and $D_s^{(2)}$. With truncation at some suitable number of terms, M , the use of Eqns. (45), and some algebraic manipulation (e.g., exchanging the l and s summations, reordering the coefficients) the linear equations work out to be, in matrix form,

$$\begin{pmatrix} R_{ks}^{(1)} & U_{ks}^{(1)} & \sum_{l=0}^{\infty} \alpha_{kl} \bar{R}_{ls}^{(2)} & \sum_{l=0}^{\infty} \alpha_{kl} \bar{U}_{ls}^{(2)} \\ V_{ks}^{(1)} & T_{ks}^{(1)} & \sum_{l=0}^{\infty} \beta_{kl} \bar{V}_{ls}^{(2)} & \sum_{l=0}^{\infty} \beta_{kl} \bar{T}_{ls}^{(2)} \\ \sum_{l=0}^{\infty} \gamma_{kl} \bar{R}_{ls}^{(1)} & \sum_{l=0}^{\infty} \gamma_{kl} \bar{U}_{ls}^{(1)} & R_{ks}^{(2)} & U_{ks}^{(2)} \\ \sum_{l=0}^{\infty} \mu_{kl} \bar{V}_{ls}^{(1)} & \sum_{l=0}^{\infty} \mu_{kl} \bar{T}_{ls}^{(1)} & V_{ks}^{(2)} & T_{ks}^{(2)} \end{pmatrix} \begin{pmatrix} C_s^{(1)} \\ D_s^{(1)} \\ C_s^{(2)} \\ D_s^{(2)} \end{pmatrix} = 0 \quad (54)$$

where we have symbolized each submatrix by its (ks) matrix element and each vector by its (s) element. In Eqn. (54) each of the submatrices is M by M , and each of the four vectors of coefficients is of length M . This equation has a solution when the determinant of the matrix is zero. Thus, as before, we will vary the propagation constant appearing in the matrix elements until the determinant vanishes, and then evaluate the coefficients for those conditions.

The summation over l which appears in each matrix element in the upper right and lower left quadrants must also be truncated at some value, M' . We find that a value between M and $2M$ is usually sufficient. For circular guides, $M' = M$ because of the diagonal property of (\bar{R}) , (\bar{U}) , (\bar{V}) and (\bar{T}) .

3.3.2 Normalized Parameters for the Two-Guide Problem

When we considered the single guide, we were able to specify the physical parameters of the problem by giving the normalized frequency, B , and the parameters (\tilde{N}, \tilde{R}) describing the guide's perimeter. The "characteristic dimension", b , conveniently dropped out.

In the array problem the two guides will in general differ in their indices of refraction, sizes, and shapes. It thus becomes necessary to specify several additional parameters: a second normalized frequency, a second set (\tilde{N}, \tilde{R}) for the shape, a second "characteristic dimension" to determine the size, and also a distance d separating the (origins centered within the) two guides. Moreover, the question of how to define the normalized propagation constant is reopened, unless $n_1^{(1)} = n_1^{(2)}$.

With these considerations in mind, it becomes convenient to define a "special" guide, which is identified by the super- or subscript (1) and is the one with the greatest value of n_1 . Thus with the definition

$$p^2 = \frac{k_1^2 - k_2^2}{k_1'^2 - k_2^2} = \frac{-\gamma_2^2}{\gamma_1'^2 - \gamma_2^2} \quad (55)$$

p^2 retains its range of 0 to 1, since the limits on the propagation constant, k_g , of the normal modes of the array are k_2 and $k_1^{(1)}$, the latter being greater than $k_1^{(2)}$. Moreover, the characteristic dimension of this special guide, b_1 , will appear in the different normalized frequencies which are defined to account for the index-of-refraction differences:

$$B_i = \frac{b_i k_0}{\pi} (\eta_i'^2 - n_2^2)^{\frac{1}{2}} = \frac{b_i k_0}{\pi} \sqrt{\delta_i} \quad i = 1, 2 \quad (56)$$

With these definitions one can show that the quantities $\gamma_1^{(i)}$ and γ_2 are

$$\gamma_i^{(i)} = \frac{\pi B_i}{b_i} \left[\frac{B_i^2}{B_1^2} - p^2 \right]^{\frac{1}{2}} \quad i = 1, 2 \quad (57a)$$

$$\gamma_2 = \frac{i\pi B_1 p}{b_1} \quad (57b)$$

where $i = \sqrt{-1}$ in Eqn. (57b) should not be confused with the index i designating one guide or the other. Thus, if $n_1^{(1)} = n_1^{(2)}$, the two values of γ_1 are the same. The differences between the guides enter when $\gamma_1 \rho$ is calculated. Let us write, for the i th perimeter,

$$\rho(\phi_i) = b_i g_i(\phi_i) \quad i = 1, 2 \quad (58)$$

where $g_i(\phi_i)$ might be the "superellipse" formula indicated in Eqn. (31) with parameters \tilde{N}_i and \tilde{R}_i , or some other function. We define the ratio of the semiminor axes by

$$r_i = b_i/b_1, \quad i=1,2 \quad (59)$$

Then we have, for ρ on the i th boundary,

$$\gamma_i^{(1)} \rho = \pi r_i g_i(\phi_i) B_1 \left[\frac{B_1^2}{B_i^2} - \rho^2 \right]^{\frac{1}{2}} \quad i=1,2 \quad (60a)$$

$$\gamma_i \rho = i\pi r_i g_i(\phi_i) B_1 \rho \quad (60b)$$

Moreover, the argument of the Hankel functions appearing in the transformation coefficients α_{kl} and β_{kl} is

$$\gamma_i d = i\pi B_1 \rho d/b_1 \quad (61)$$

From the above, one can see that b_1 serves as a "unit distance", with b_2 and d appearing only in their ratios to b_1 . From now on, we will assume that d is in units of b_1 and drop the latter from Eqn. (61).

Reduction of the quantities in the matrix elements to real form is only slightly more complicated than in Section II-2.4. As before, the recurrence relations, Eqns. (28), eliminate the derivatives of the Bessel and Hankel functions. The Hankel functions of complex argument are converted to Modified Bessel functions of the second kind using Eqn. (29). The Bessel functions of complex argument are converted to Modified Bessel functions of the first kind by using

$$J_\ell(ix) = i^\ell I_\ell(x) \quad (62)$$

Then Eqns. (19) and (43) become

$$\begin{aligned}
\Gamma_{ks}^{(i)}(\rho_i) = & i^{-(k+1)} \epsilon_k \left[2B_i \frac{\rho_i(\phi_i)}{b_i} \left\{ \left(\frac{B_i^2}{B_i^2} - P^2 \right)^{\frac{1}{2}} K_k \left(\frac{\pi B_i P \rho_i}{b_i} \right) J_{s+1} \left(\frac{\pi B_i P \rho_i}{b_i} \left[\frac{B_i^2}{B_i^2} - P^2 \right]^{\frac{1}{2}} \right) \right. \right. \\
& + P K_{k-1} \left(\frac{\pi B_i P \rho_i}{b_i} \right) J_s \left(\frac{\pi B_i P \rho_i}{b_i} \left[\frac{B_i^2}{B_i^2} - P^2 \right]^{\frac{1}{2}} \right) \left. \right\} \quad (63a) \\
& + \frac{2}{\pi} (k-s) K_k \left(\frac{\pi B_i P \rho_i}{b_i} \right) J_s \left(\frac{\pi B_i P \rho_i}{b_i} \left[\frac{B_i^2}{B_i^2} - P^2 \right]^{\frac{1}{2}} \right) \left. \right]
\end{aligned}$$

$$E_{ks}^{(i)}(\rho_i, \frac{\partial \rho_i}{\partial \phi_i}) = i^{-(k+1)} \epsilon_k \frac{2}{\pi} K_k \left(\frac{\pi B_i P \rho_i}{b_i} \right) J_s \left(\frac{\pi B_i P \rho_i}{b_i} \left[\frac{B_i^2}{B_i^2} - P^2 \right]^{\frac{1}{2}} \right) \frac{\partial \rho_i}{\partial \phi_i} / \rho_i \quad (63b)$$

$$\begin{aligned}
H_{ks}^{(i)}(\rho_i) = & ik \epsilon_k \left[\pi B_i \frac{\rho_i(\phi_i)}{b_i} \left\{ \left(\frac{B_i^2}{B_i^2} - P^2 \right)^{\frac{1}{2}} I_k \left(\frac{\pi B_i P \rho_i}{b_i} \right) J_{s+1} \left(\frac{\pi B_i P \rho_i}{b_i} \left[\frac{B_i^2}{B_i^2} - P^2 \right]^{\frac{1}{2}} \right) \right. \right. \\
& - P I_{k-1} \left(\frac{\pi B_i P \rho_i}{b_i} \right) J_s \left(\frac{\pi B_i P \rho_i}{b_i} \left[\frac{B_i^2}{B_i^2} - P^2 \right]^{\frac{1}{2}} \right) \left. \right\} \quad (64a) \\
& + (k-s) I_k \left(\frac{\pi B_i P \rho_i}{b_i} \right) J_s \left(\frac{\pi B_i P \rho_i}{b_i} \left[\frac{B_i^2}{B_i^2} - P^2 \right]^{\frac{1}{2}} \right) \left. \right]
\end{aligned}$$

$$G_{ks}^{(i)}(\rho_i, \frac{\partial \rho_i}{\partial \phi_i}) = ik \epsilon_k I_k \left(\frac{\pi B_i P \rho_i}{b_i} \right) J_s \left(\frac{\pi B_i P \rho_i}{b_i} \left[\frac{B_i^2}{B_i^2} - P^2 \right]^{\frac{1}{2}} \right) \frac{\partial \rho_i}{\partial \phi_i} / \rho_i \quad (64b)$$

The transformation coefficients become

$$\alpha_{k\ell} = i^{-(k-\ell+1)} \frac{1}{\pi} \epsilon_k \left\{ K_{k-\ell}(\pi B_i P d) + K_{k+\ell}(\pi B_i P d) \right\} \quad (65a)$$

$$\beta_{k\ell} = i^{-(k-\ell+1)} \frac{2}{\pi} \left\{ K_{k-\ell}(\pi B_i P d) - K_{k+\ell}(\pi B_i P d) \right\} \quad (65b)$$

with $\eta_{k\ell}$ and $\mu_{k\ell}$ related to them as in Eqn. (51).

Now the only remaining task is to combine the powers of i properly. Consider, for simplicity, a reduced form of Eqn. (54):

$$\left(\begin{array}{c|c} R^{(1)} & \left(\sum_{l=0}^{N'} \alpha_{kl} \bar{R}_{ls}^{(1)} \right) \\ \hline \left(\sum_{l=0}^{N'} \eta_{kl} \bar{R}_{ls}^{(1)} \right) & R^{(2)} \end{array} \right) \begin{pmatrix} C_s^{(1)} \\ C_s^{(2)} \end{pmatrix} = 0 \quad (66)$$

We note from the definition of (R) , Eqn. (20a), and from Eqns. (63) that the (ks) matrix elements of the submatrices on the upper left and lower right are all real quantities multiplied by $i^{-(k+1)}$. Similarly, from Eqns. (44a) and (64) the (ls) matrix elements of $\bar{R}^{(1)}$ and $\bar{R}^{(2)}$ are real quantities times i^l , and from Eqns. (65a) and (51) the transformation coefficients α_{kl} and η_{kl} contain the $(-k+l-1)$ and $(k-l-1)$ powers of i multiplied by the real part of α_{kl} . Powers of i can now be removed completely by multiplying each row of the matrix by $i^{(k+1)}$, since (it turns out) only even powers are left after this operation. If we change our notation slightly so that (R) , (\bar{R}) , (α) , and (η) refer explicitly to the real factors which are built into these quantities (e.g., Eqn. (65a) without the $i^{-(k-l+1)}$ for α_{kl}) and if we symbolize each submatrix by its (ks) matrix element, Eqn. (66) can be written entirely in terms of real quantities:

$$\left(\begin{array}{c|c} R_{ks}^{(1)} & \sum_{l=0}^{N'} (-1)^l \alpha_{kl} \bar{R}_{ls}^{(2)} \\ \hline (-1)^k \sum_{l=0}^{N'} \alpha_{kl} \bar{R}_{ls}^{(1)} & R_{ks}^{(2)} \end{array} \right) \begin{pmatrix} C_s^{(1)} \\ C_s^{(2)} \end{pmatrix} = 0 \quad (67)$$

One can readily show that (U) , (V) , and (T) behave like (R) , and the corresponding quantities with bars like (\bar{R}) , and the (β) like (α) . It is therefore easy to generalize from Eqn. (67) to a final real matrix equation for the general two-guide problem, with all coefficients $C_s^{(1)} \dots D_s^{(2)}$ as unknowns. In other words, if in Eqn. (54) we take $R_{ks}, \dots, \bar{T}_{ks}$ and $\alpha_{kl}, \dots, \eta_{kl}$ to mean the real factors contained in the most recent equation specifying each of these, and if we multiply by $(-1)^l$ inside each sum in the upper right quadrant, and if we multiply each matrix element on the lower left by $(-1)^k$, we get the final real matrix equation for the two-guide problem.

3.3.3 Special Cases for Two Guides

Consider the general case once again. When the distance, d , between the guides is much greater than the guide dimensions the transformation coefficients α , β , η , and μ become small because of the Hankel functions defining them. In such cases the top right and lower left submatrices go to zero and Eqn. (54) splits into separate matrix equations for $C_s^{(1)}$, $D_s^{(1)}$, and $C_s^{(2)}$, $D_s^{(2)}$. By physical reasoning, this amounts to separately solving for the modes of two distinct isolated waveguides. Mathematically, each part of Eqn. (54) is equivalent to Eqn. (22) applied to one guide or the other.

When one or the other of the guides has reflection symmetry about its x -axis (or y -axis) the corresponding submatrices (U) , (V) , (\bar{U}) , and (\bar{V}) are all zero. If both guides have this property the equations split completely and the solutions for $C_s^{(1)}$ and $C_s^{(2)}$ (cosine expansions, as Eqn. (66)) and $D_s^{(1)}$ and $D_s^{(2)}$ (sine expansions) are obtained independently. If, in addition, both guides have a second axis with reflection symmetry, half of the matrix elements of (R) , (T) , (\bar{R}) , and (\bar{T}) are also zero and the cosine and sine solutions split into even and odd series.

As with single guides, these separations could all have been effected from the beginning.

For circular cross-sections the (R) and (T) submatrices are diagonal and the sums in the matrix elements at the upper right and lower left have only one term each.

In the special case for which the two guides are identical, and have a plane of symmetry between them, as in Fig. 15, we can simplify in a different way. We can assert, a priori, that the solutions, Eqn. (40), be symmetric or antisymmetric about the plane. That is, the solutions $\phi^{(1)}(\rho_1, \phi_1)$ must be equal to plus or minus $\phi^{(2)}(\rho_2, \pi - \phi_2)$. This can happen if and only if

$$C_s^{(1)} = (-1)^s C_s^{(2)} \quad \text{symmetric solutions} \quad (68a)$$

$$D_s^{(1)} = (-1)^{s+1} D_s^{(2)} \quad (68b)$$

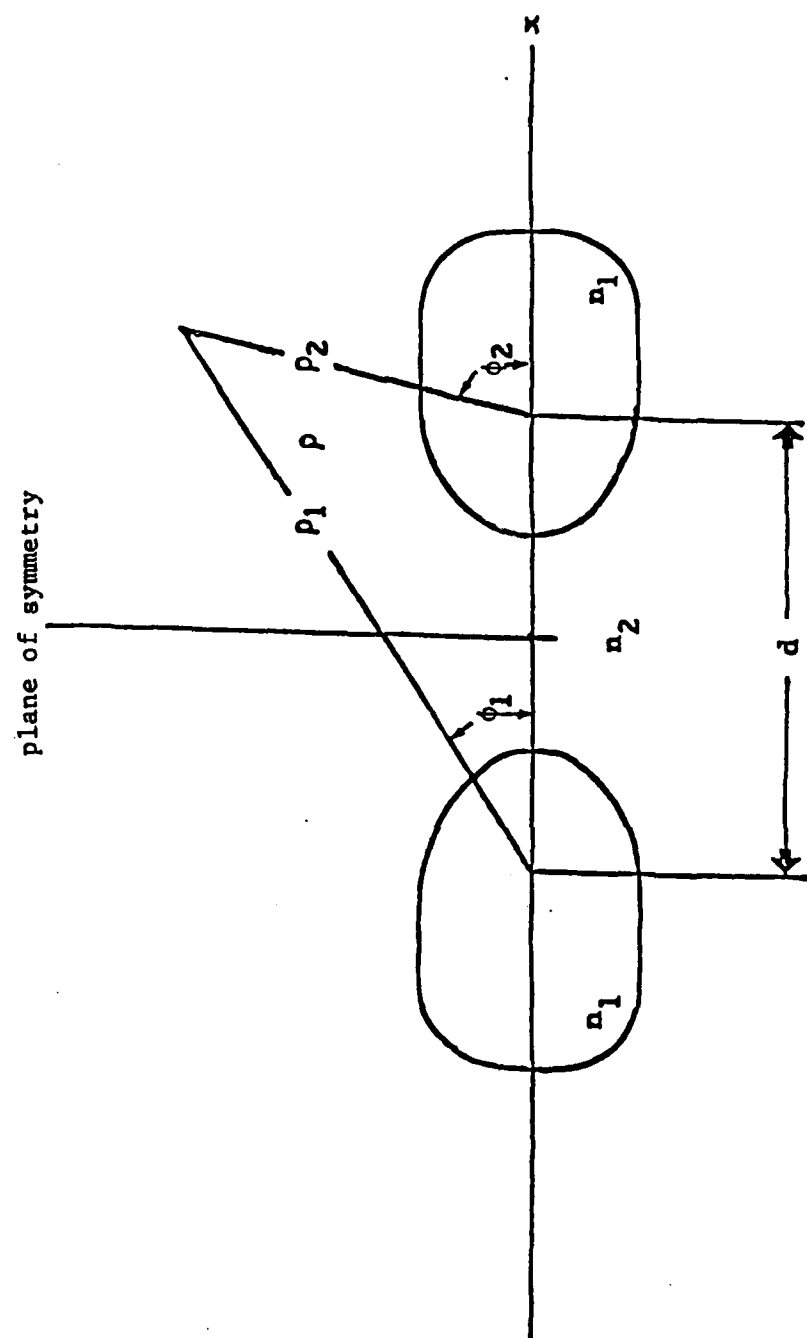


Fig. II.15 Two identical guides a distance d apart.

or

$$C_s^{(1)} = (-1)^{s+1} C_s^{(2)} \quad (69a)$$

$$D_s^{(1)} = (-1)^s D_s^{(2)} \quad \text{antisymmetric solutions} \quad (69b)$$

Then, if we specify which class of solutions we wish, these relations can be used to eliminate half of the equations in the general set.

Alternatively, we can start from the general set and derive Eqs. (68) and (69). The fact that the identity of the two guides simplifies the mathematical relations expressed in Eqn. (54) and leads to Eqs. (68) and (69) shows that the symmetric and antisymmetric solutions are implied by our formulation. To demonstrate this, consider the real equation for the cosine solutions, Eqn. (67). If the guides are identical, as in Fig. 15, the matrices $(R^{(1)})$ and $(R^{(2)})$ are identical except for a factor of $(-1)^{k+s}$ which enters the (ks) matrix element because of the transformation $\phi_1 \rightarrow \pi - \phi_2$ and has to do with the direction of integration about the cross-sections. (This can be derived quickly from Eqn. (20a) using trigonometric identities.) That is,

$$R_{ks}^{(2)} = (-1)^{k+s} R_{ks}^{(1)} \quad (70)$$

with a similar relation for the (\bar{R}) . Then Eqn. (67) can be rewritten as

$$\begin{pmatrix} R_{ks}^{(1)} & | & (-1)^s \sum_{k'=0}^{N'} \alpha_{kk'} \bar{R}_{ks}^{(1)} \\ \hline (-1)^k \sum_{k'=0}^{N'} \alpha_{k'k} \bar{R}_{ks}^{(1)} & | & (-1)^{k+s} R_{ks}^{(1)} \end{pmatrix} \begin{pmatrix} C_s^{(1)} \\ C_s^{(2)} \end{pmatrix} = \begin{pmatrix} R_{ks}^{(1)} & | & \pm \sum_{k'=0}^{N'} \alpha_{kk'} \bar{R}_{ks}^{(1)} \\ \hline (-1)^k \sum_{k'=0}^{N'} \alpha_{k'k} \bar{R}_{ks}^{(1)} & | & \pm (-1)^k \bar{R}_{ks}^{(1)} \end{pmatrix} \begin{pmatrix} C_s^{(1)} \\ \pm (-1)^s C_s^{(2)} \end{pmatrix} = 0 \quad (71)$$

The operations leading to Eqn. (71) are purely formal. They can be carried further by multiplying the rows of the lower submatrices by $\pm(-1)^k$. Then, with S_{ks} defined as $\sum_{k'} \alpha_{k'k} \bar{R}_{ks}^{(1)}$ and $C_s' = \pm(-1)^s C_s^{(2)}$, the equation takes the form

$$\begin{pmatrix} R & \pm S \\ \pm S & R \end{pmatrix} \begin{pmatrix} C \\ C' \end{pmatrix} = 0 \quad (72)$$

An equation like this has a nontrivial solution if and only if (C) and (C') are identical vectors. To show this, assume that they differ by an arbitrary

vector, (ϵ) : $(C) = (C') + (\epsilon)$. Writing the matrix equations separately, it immediately follows that

$$(S - R)(\epsilon) = (0) \quad (73)$$

This has a nontrivial solution if the rank of $(S-R)$ is less than the matrix dimension, M . (S) and (R) being different, this cannot be. Therefore $(\epsilon) \equiv (0)$, (C) and (C') are the same, and Eqns. (68a) and (69a) follow with the appropriate choice of sign. The relations between the sine coefficients, $D_s^{(1)}$ and $D_s^{(2)}$, can be proved in an analogous manner.

The final form of Eqn. (72) with $(C) = (C')$ shows how to collapse the $2M$ by $2M$ set into the M by M set (which we would have derived if we had started by assuming Eqns. (68) and (69)) because it is equal to two copies of

$$(R \pm S)(C) = \left(R_{ks}^{(n)} \pm \sum_{l=0}^{N'} \alpha_{kl} \bar{R}_{ls}^{(n)} \right) (C_s^{(n)}) = 0 \quad (74)$$

This is the very important equation that is to be solved for the cosine solutions of the two identical guides with reflection symmetry about the common x -axes. The corresponding equation for the sine solutions is

$$\left(T_{ks}^{(n)} \pm \sum_{l=0}^{N'} \beta_{kl} \bar{T}_{ls}^{(n)} \right) (D_s^{(n)}) = 0 \quad (75)$$

It must be remembered that we have explicitly written (and thereby cancelled out) all powers of i and thus dropped them from expressions for all the matrices. Also, without reflection symmetry about the common x -axis, the U and V submatrices reappear, and the general $4M$ by $4M$ system only collapses into a $2M$ by $2M$ one. In any case, however, the identity of the two guides reduces the size of the system of equations by a factor of two, the only cost being the necessity of separately solving for the symmetric and antisymmetric modes by choosing one sign or the other.

3.3.4 Results for Two Guides

3.3.4.1 General Discussion

The principal goals in carrying out this work were to (1) calculate the modal properties of some of the more important configurations in which

coupled guides are used; (2) demonstrate the efficacy of the integral equation technique for arrays; and (3) identify situations in which this technique is capable of providing significantly better results than other approaches and, conversely, those situations in which other approaches are quite accurate. In view of these goals, we have concentrated primarily on the two-guide problem, both because of its importance and because other techniques have not (with one exception) been applied to anything else.

We have calculated the modes of arrays consisting of circles, ellipses, and rectangles in various combinations, all with their axes of symmetry coincident with the line between the origins ($\gamma = 0$ in Fig. (14b)). The series converge quickly for all cases we tried, including some combinations of elongated cores. The integral equation technique is clearly an efficient and versatile way to correctly calculate these modes. We believe that extending the effort to more complicated situations ($\gamma \neq 0$, cores without symmetry) would allow us to demonstrate similar virtues, the cost merely being the computation of more matrix elements and Bessel functions. The same applies to N-guide systems, with $N > 2$. In that context, we have restricted ourselves to consideration of a line of up to six identical guides, which is discussed in Section II-3.4. We do set down the general formulation for N guides, however.

Regarding the comparison with other authors, discussed below, we find that we agree completely with that formulation <22> which calculates, as we do, the normal modes of an array. We also find, not surprisingly, that coupled-mode theory provides quite accurate results except when the guide separations are quite small.

To obtain results for the two-guide case, two FORTRAN programs were written. The first, IDGS, solves for the symmetric and antisymmetric modes of identical guides. The second, NIDGS, is used for the non-identical two-guide problem. The means of using them are described in another section of this report. The numerical techniques employed are virtually the same as for TRUNCN, and have been described in Section II-2.4.

Since other authors use V for the normalized frequency, we have expressed our results in terms of this parameter also ($V = \pi B$). δ , given in Eqn. (25), is also used for the index-of-refraction differences.

3.3.4.2 Results for Two Identical Guides

In discussing the normal modes of the array consisting of two identical cores with a plane of symmetry between them, it is illuminating to relate them to the modes of the isolated individual guides. Thus, if the guides, numbered 1 and 2, are far apart they do not affect each other, and there is a modal solution in which the wave amplitude and propagation constant are characteristic of a single-guide mode centered on guide number 1.

We label this solution $\phi_{\infty}(1)$. There is of course another solution with the same kind of single-guide mode centered on guide number 2, i.e., $\phi_{\infty}(2)$. As in quantum mechanics, two solutions with the same propagation constant (energy) but different wave amplitudes are called degenerate. A linear combination of degenerate solutions is still a solution with the same propagation constant, and we can form two special linear combinations: a combination ϕ_S that is symmetric under reflection about the plane of symmetry (interchange of guide numbers 1 and 2) and a combination ϕ_A that is antisymmetric, given by

$$\phi_S = \phi_{\infty}(1) + \phi_{\infty}(2) \quad (76a)$$

$$\phi_A = \phi_{\infty}(1) - \phi_{\infty}(2) \quad (76b)$$

Thus, for every mode of the individual isolated guide, these two combinations will approximate two modes of the widely spaced composite guide. As d decreases, however, and the tails of the isolated-guide modes begin to overlap, ϕ_S and ϕ_A will cease to be solutions in the overlap region, and it will be found that the exact symmetric and antisymmetric solutions will differ from the single-guide solutions, as will the propagation constants. It is said that the single-guide modes split. In fact, the approximate wave functions, Eqn. (76), can be used in, say, a variational calculation to calculate this splitting.

In this light consider Fig. 16, in which P^2 is plotted versus V for two identical circular guides of radius unity separated by varying distances d . In the families of curves shown there, the central solid lines represent modes for $d \rightarrow \infty$ and, more specifically, those modes of an isolated single circular guide for which $\phi = J_s(\gamma_1 \rho) \cos s\phi$. The single-guide modes correspond respectively to $s = 0, 1$, and 2 for the uppermost, middle, and lower family of curves.

The dashed lines above and below these single-guide modes are the corresponding symmetric or antisymmetric cosine modes for the values of d that are indicated. The symmetric mode curves all lie above the single-guide curve, and the antisymmetric ones all lie below. Note that the splitting of the symmetric and antisymmetric modes is not uniform; for a given d , the symmetric curve is not necessarily the same distance above the single-guide mode as the antisymmetric curve is below it. Furthermore, the dominant mode is the lowest-order symmetric mode; all the other modes cut off.

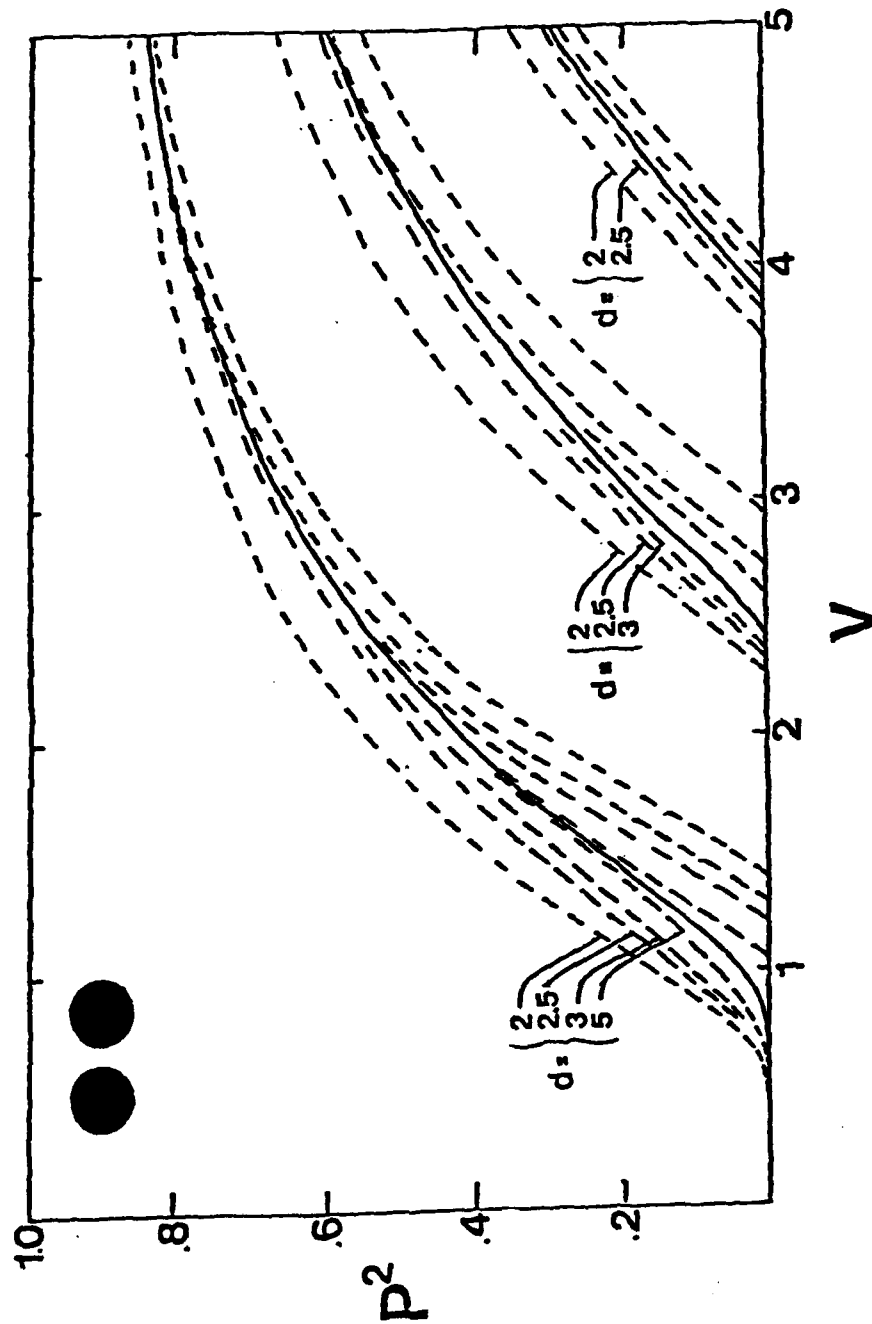


Fig. II.16 Cosine modes of a composite system consisting of two identical circular guides. The three solid lines correspond to isolated guide modes with single-term field expansions $[\Phi = J_s(\gamma_1 \rho) \cos s\phi]$, with $s = 0, 1$, and 2 . The dashed lines correspond to modes that are symmetric (antisymmetric) with respect to the y axis when they fall above (below) the isolated guide curves. The separation distances d are the same for the antisymmetric modes as for the symmetric ones.

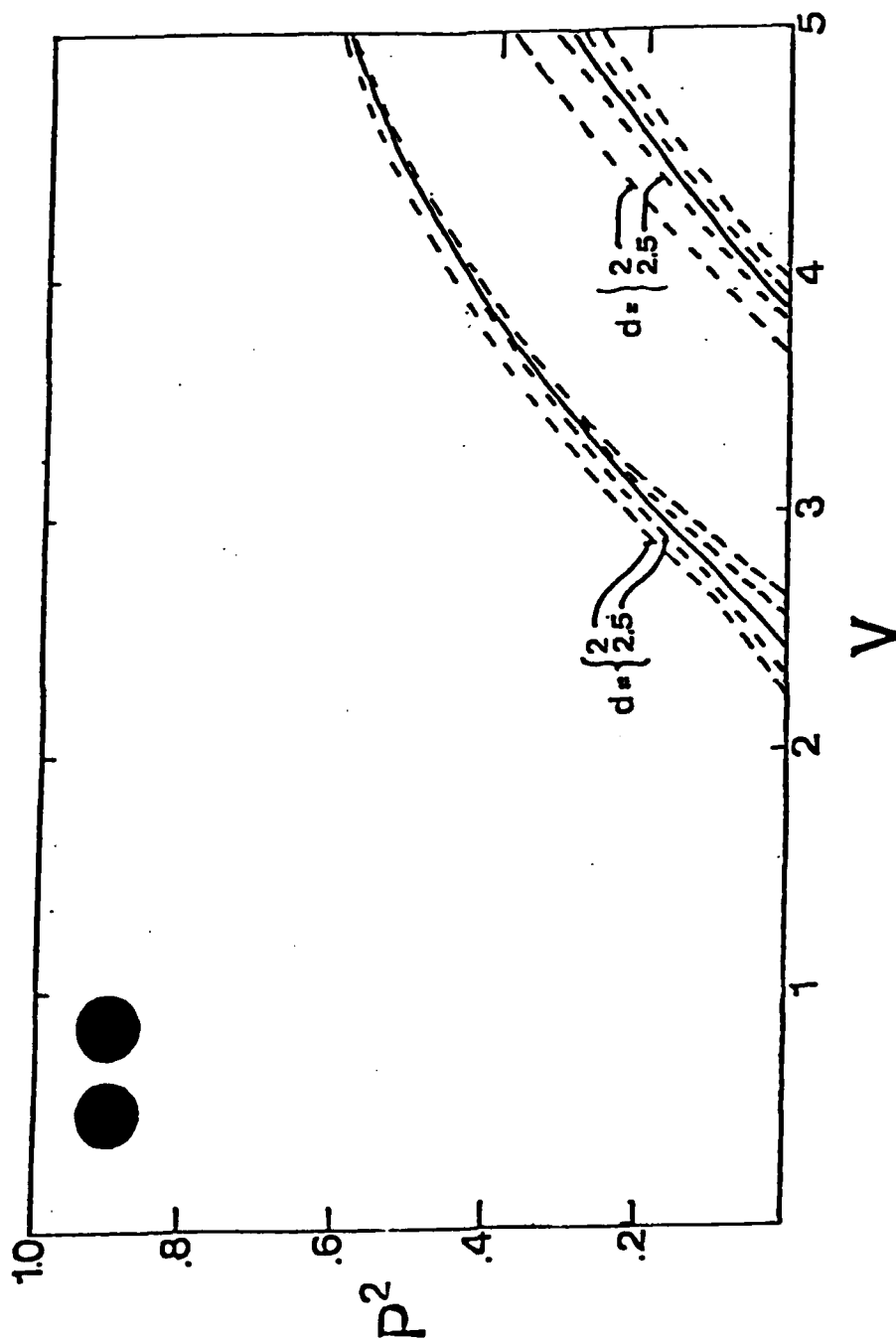


Fig. II.17 Sine modes of a composite system of two identical circular guides. As in Fig. 16, the symmetric modes are above the isolated-guide curves, the antisymmetric ones below. The two solid lines correspond to single-term field expansions with $s = 1$ and 2.

In Fig. 17 we plot the propagation constants of the first two modes derived from the sine expansions for identical circular guides. Each of these modes is degenerate, in the limit $d \rightarrow \infty$, with a cosine mode in Fig. 16. For smaller separations, the proximity of the two guides clearly affects the modal properties of the sine and cosine modes differently. This is not surprising, in view of the field configurations of the large-separation modes, which are like those given in Figs. 12g and 12m. In the case of the modes cutting off between $V = 2$ and $V = 3$, the cosine modes (Fig. 12g) have their maximum intensity along the x-axis, which is the region where the guides are closest together. The sine modes' intensity maxima are along the y-axes, away from the region of proximity. There is less distortion of the $d \rightarrow \infty$ fields in the latter case, and apparently this results in smaller changes in the propagation constant. In the case of the modes cutting off near $V = 4$, however, the sine and cosine modes have identical field patterns in the limit (Fig. 12m). This undoubtedly accounts for the similar behavior as the guides are brought closer to each other.

It should be pointed out that, if we had chosen the y-axes to be co-linear instead of the x-axes, the behavior differences between the sine and cosine modes we have discussed would be exactly reversed.

For comparison of our results with the work of others we begin with that of Wijngaard <22>, who considers two circular guides, not necessarily identical, and solves the problem by an extension of the standard matching techniques for a single guide. Although Wijngaard's equations are formulated for the general vector case, some of his numerical results are given for weakly guiding cases, where δ goes to zero, and are therefore comparable with ours. For example, for identical touching circular guides at $V = 3.5$, his result for the quantity $V(1 - P^2)^{1/2}$ for the first antisymmetric cosine mode is 1.9341; ours is 1.93412.

A second comparison with Wijngaard is possible in terms of a parameter other than the propagation constant, the beat wavelength λ_B . We briefly introduce it here since much of the discussion of two identical guides in the literature is phrased in terms of it. Suppose that two identical guides are a large but not infinite distance apart so that they are weakly coupled. And suppose that at $z = 0$ one of the guides is excited with an amplitude characteristic of a mode of a single isolated guide. A question of interest is how the amplitude changes as a function of distance down the guide, i.e., how the power in one guide becomes coupled into the other. This question can be answered approximately in terms of the symmetric and antisymmetric

modes of Eqn. (76) and their corresponding propagation constants $k_g^{(S)}$ and $k_g^{(A)}$. Thus consider the following expression for the field amplitude ψ as a function of z :

$$\begin{aligned} \psi(z) &= \frac{1}{2} \left[\Phi_S \exp(ik_g^{(S)} z) + \Phi_A \exp(ik_g^{(A)} z) \right] \\ &= \frac{1}{2} \exp(ik_g^{(S)} z) \left[\Phi_S + \Phi_A \exp\{i(k_g^{(A)} - k_g^{(S)})z\} \right] \end{aligned} \quad (77)$$

At $z = 0$ this is $\psi(0) = \Phi_\infty(1)$ so that it corresponds to an excitation in which guide number 1 is excited in its single-guide mode and guide number 2 is not excited at all. But, at a certain distance $z = L$ down the guide, such that

$$[k_g^{(S)} - k_g^{(A)}]L = \pi, \quad (78)$$

we have

$$\psi(L) = \Phi_\infty(2) \exp[ik_g^{(S)} L], \quad (79)$$

which corresponds to an excitation of the single-guide mode of guide number 2. That is, all the power is now associated with this second mode. This distance L over which this power transfer takes place is the coupling length. The beat wavelength λ_B is that distance that is required for the original amplitude to be restored (except for a phase factor) and is equal to $2L$.

Following the method of Wijngaard <22> it is convenient to define a normalized beat length γ by

$$\gamma = \frac{1}{2} \delta n_1 \frac{\lambda_B}{\lambda}, \quad (80)$$

where λ is the vacuum wavelength. This can be expressed in terms of our normalized propagation constants, for small δ , by writing $k_g^{(S)}$ and $k_g^{(A)}$ in terms of them, using Eqn. (55), expanding the square roots, forming $[k_g^{(S)} - k_g^{(A)}]$, and neglecting terms in δ^2 . The result is

$$\gamma = (P_S^2 - P_A^2)^{-1} \left\{ 1 - \frac{1}{2} \delta \left[1 - \frac{1}{2} (P_S^2 + P_A^2) \right] \right\}. \quad (81)$$

Wijngaard's calculation of γ as a function of V for $\delta \rightarrow 0$ (presented in his Table 2) agrees with our results [using Eqn. (81) with $\delta = 0$] to the three significant figures given.

Although we have motivated the introduction of the beat wavelength by an approximate treatment, the operational definition, Eqn. (78), should be considered as involving the exact propagation constants $k_g^{(S)}$ and $k_g^{(A)}$ rather than those obtained by using Eqns. (76). Also, there is an obvious approximation in specifying the total field as the sum of only two modes (even the correct S and A modes) and consequently obtaining a simple periodic function of z for the power distribution. Nevertheless, this approximation allows us to connect our results with those of coupled-mode theory because those results are expressed in terms of constants coupling pairs of modes individually.

In the coupled-mode theory, the field amplitude in each guide is expressed as a sum of isolated-guide modes, with expansion coefficients a function of z . As an approximation to this sometimes intractable series, the expansion in each guide may be limited to a single term. Then, if at $z = 0$ guide number 1 is excited with a single isolated-guide mode and guide number 2 is not excited at all, the solutions of the equations—the expansion coefficients—are sinusoidal in z . The resulting beat wavelength is expressed in terms of a normalized coupling constant K that for two identical circular guides with $\delta \rightarrow 0$ has a simple analytical form [20,21]. The relationship between K and λ_B is

$$K = \frac{\pi b}{\lambda_B} (\delta)^{-1/2} \quad (82)$$

We can, of course, derive an expression for the right-hand side of Eqn. (82) in terms of P_S^2 and P_A^2 by using our beat wavelength and the relationships expressed in Eqns. (80) and (81). If we call this equivalent coupling constant \bar{K} , we find that

$$\bar{K} = \frac{1}{4} V (P_S^2 - P_A^2) \left\{ 1 - \frac{1}{2} \delta \left[1 - \frac{1}{2} (P_S^2 + P_A^2) \right] \right\}^{-1} \quad (83)$$

We can now compare this with the results of coupled-mode theory. There is only one superficial difficulty: the quantity K depends only on V and the guide separation d , whereas our comparable result \bar{K} depends on δ as well. Happily, the dependence on δ is small when δ is small. Therefore our comparisons with coupled-mode theory are made by setting $\delta = 0$. We note that small corrections must be made for finite δ .

In Figs. 18-20 we compare our results with those of coupled-mode theory for identical circular guides. The coupling constant K (solid lines, computed directly from the formula in Reference 21) and our equivalent results from Eqn. (83) are plotted versus d for fixed values of V for the dominant modes (Fig. 18) and the second pair of modes (Fig. 19). The complementary results are given in Fig. 20 for the dominant modes by plotting γ from the coupled-mode theory (solid lines) and our values of $(P_S^2 - P_A^2)^{-1}$ versus V for fixed d .

Over most of the range of parameters that we have investigated, our results are in excellent agreement with those of coupled-mode theory. To identify what differences there are, we emphasize small values of d in Figs. 18 and 19 because it is there that the weak-coupling approximation is most tenuous. We observe that, except for the smallest values of V on each graph, the only notable discrepancies occur when $d \leq 2.15$; that for some values of V the agreement is practically perfect even for small d , whereas for others the discrepancies are as much as 20%; and in Fig. 19, that our points may fall above or below the coupled-mode results, depending on V . In Fig. 20, we find substantial discrepancies only near those values of V for which the first antisymmetric mode cuts off, a value that of course depends on d , and for touching guides ($d = 2$). In the latter case, the barely noticeable difference of less than 4% at the right-hand edge of the plot, where $V = \pi$, grows considerably larger (to 20% at $V = 2\pi$) as the normalized frequency increases.

The discrepancies associated with the smallest values of V encountered in Figs. 18-20 are not surprising, even for guides that are relatively far apart, in view of the tendency of the fields of all modes to spread substantially outside the core regions in these cases. This makes it risky to ignore single-guide modes other than the two primary ones, as is generally done in the coupled-mode approach.

The discrepancies in γ associated with large values of V and $d \sim 2$ arise from the fact that, although coupled-mode theory in principle expands the field inside each guide in a linear combination of modes of the isolated guides, in practice this combination is restricted to a single mode of the isolated guides. For fixed V and increasing d this approximation obviously becomes better and better. By contrast, for d fixed (especially at small values) there is no reason to suppose that for increasing V the single-mode approximation becomes increasingly accurate. In fact, the true field in the interaction region is rather poorly represented by the linear combination for all values of V . This is more obviously true for identical square or identical rectangular guides, but it holds for identical circular guides as well.

For values of V below the value at which the antisymmetric mode of any chosen pair cuts off, there can be no interference. Because coupled-mode theory does not yield the propagation constants directly, however, this point,

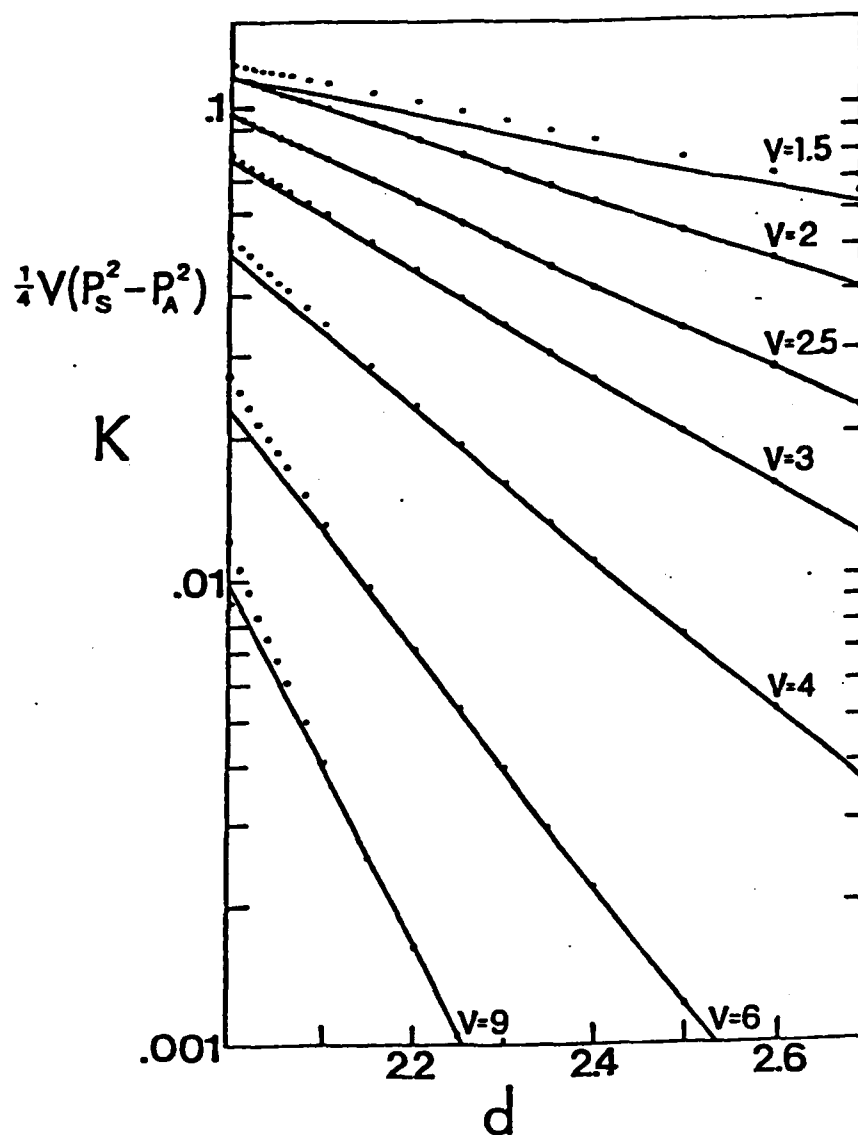


Fig. II.18 Normalized coupling constant from coupled-mode theory (solid lines) and the quantity $\frac{1}{4} V(P_S^2 - P_A^2)$ (points) plotted versus d for the first symmetric and antisymmetric modes of a composite system consisting of two identical circular guides.

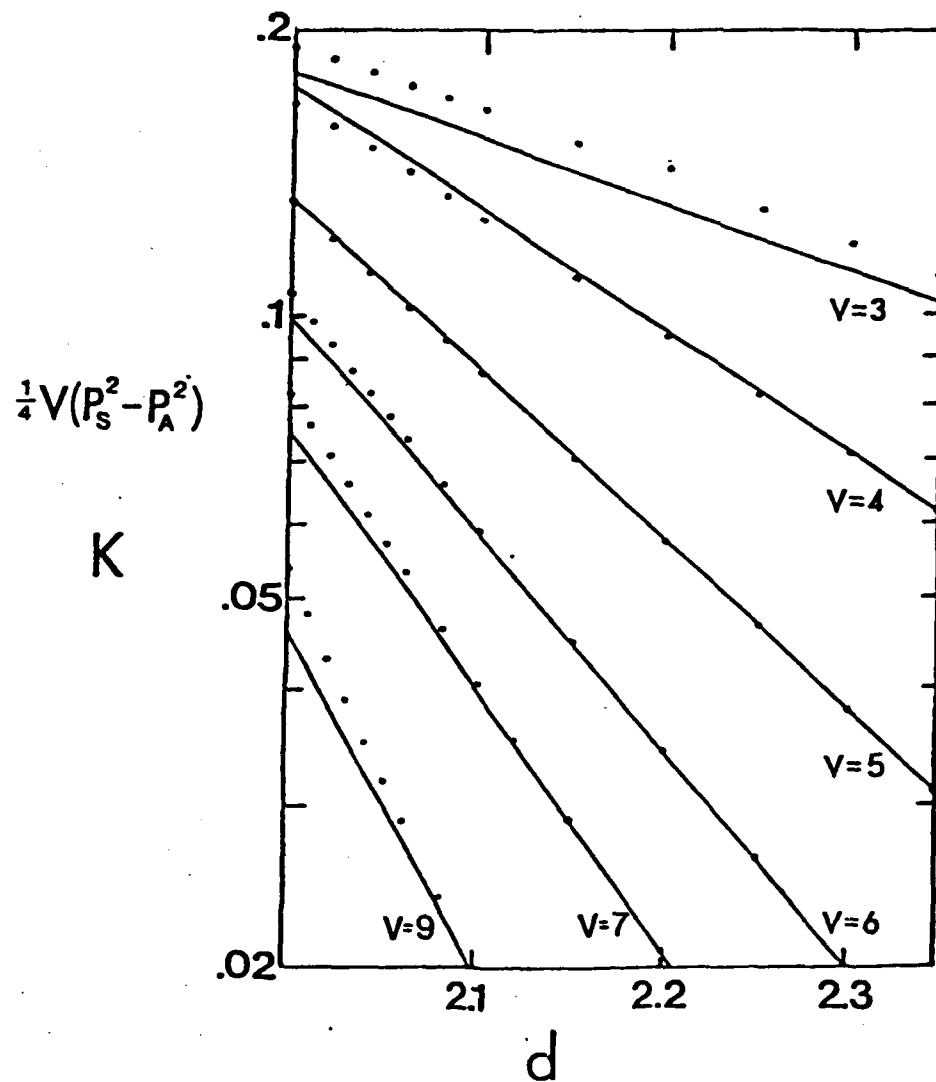


Fig. II.19 Same as Fig. 18 except the second symmetric and antisymmetric modes are used. These correspond to dashed lines of the second family of Fig. 16.

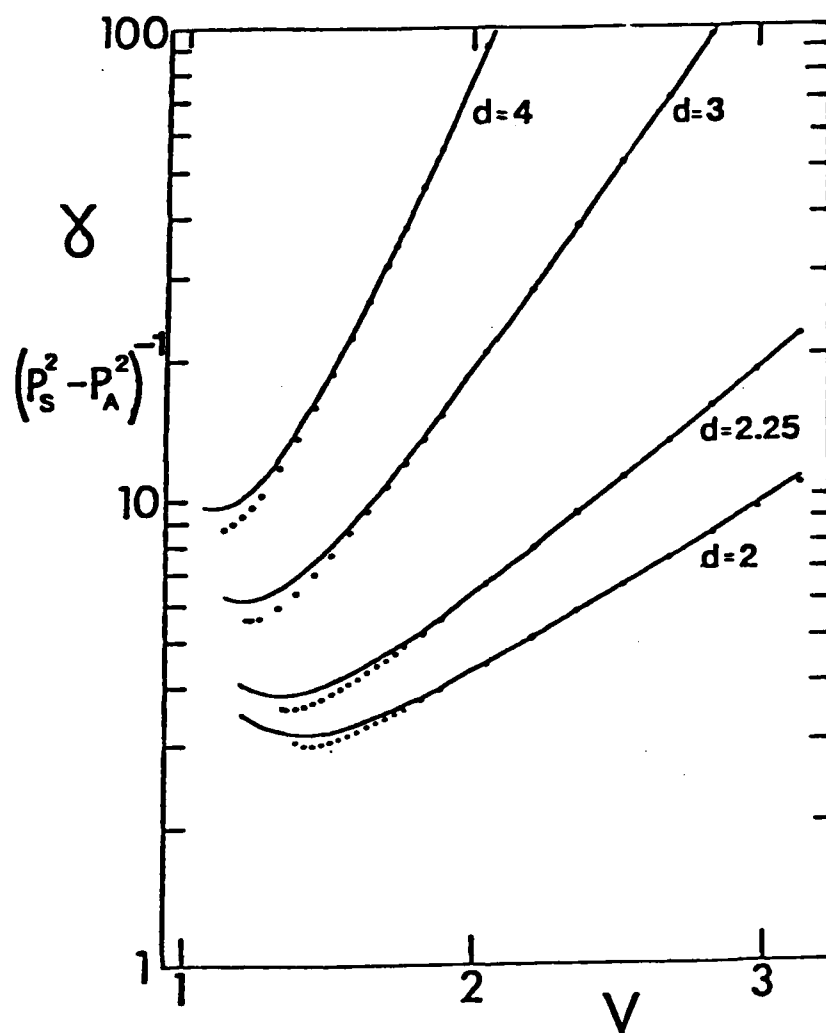


Fig. II.20 Normalized beat length from coupled-mode theory (solid lines) and the quantity $(P_S^2 - P_A^2)^{-1}$ (points) plotted versus V for the first symmetric and antisymmetric modes of a composite system consisting of two identical circular guides. Cutoff of the antisymmetric mode occurs near the left-most dot in each case.

at which computed values of the beat wavelength become meaningless, is obscure. In Fig. 20, we emphasize this possible error by deliberately extending the coupled-mode calculations (solid lines) to values of V below this cutoff point, which is close to the left-most of our computed points for each of the four pairs considered.

We have done similar calculations for pairs of square and pairs of rectangular guides and compared them with published results where possible. The best agreement is with the coupled-mode calculations of Marcatili <17> for tightly bound modes of square guides. What discrepancies we find in these cases closely parallel those indicated for $V > 3$ in Fig. 18; that is our equivalent coupling constant is larger than his for $d < 2.15$. His approximations are not good near cutoff, so extensive comparison is not possible.

In Figs. 21 and 22 we show the first two cosine and sine modes, respectively, of identical square guides. These modes are qualitatively very similar to those of the circular guides shown in Figs. 16 and 17. Since for small separations ($d \rightarrow 2$) somewhat more of the guiding regions are in close proximity to each other than for comparable separations of circular guides, the splitting of the corresponding modes is slightly greater. One should note that for $d = 2$ the modes plotted are identical to those of a single rectangular guide with $R = 2$, given in Fig. 5. That is, the first symmetric mode corresponds to the R_1^I mode, the first antisymmetric mode to the R_1^{II} mode, and so on.

As a final example we show in Fig. 23 the propagation constants for some modes of a pair of rectangular guides.

Also of interest are the field configurations. In the present scalar theory we can exhibit these configurations by plotting contour curves of the squared amplitude in the cross-sectional plane. Such plots are shown in Figs. 24 and 25 for two square guides for the symmetric and antisymmetric modes that derive from the dominant mode of the isolated guide. What is striking about these modal amplitudes of the guiding pair is how quickly, as the guides are separated from touching, they begin to resemble in each guide the modes of isolated single guides. For the symmetric case, for example, the field configuration for the touching guides is markedly different from what would exist in each isolated guide. But separating the guides by only 2.5% of one side ($d = 2.05$) produces a definite resemblance to single-guide modes that becomes pronounced at $d = 2.25$ and is practically perfect at $d = 3.0$. Similar, but even stronger, remarks apply to the antisymmetric mode.

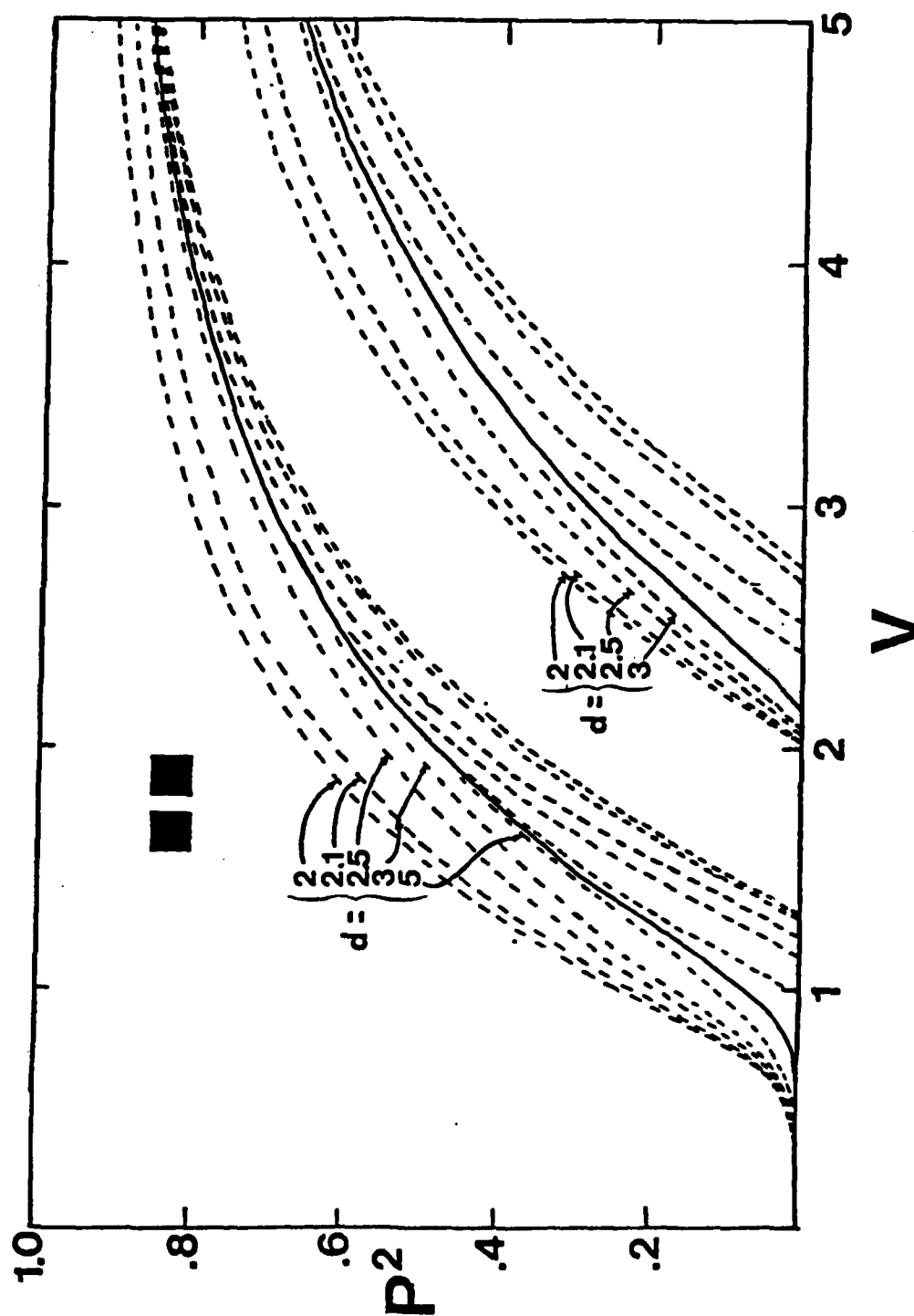


Fig. II-21 Cosine modes of a composite system consisting of two identical square guides. The solid lines correspond to isolated-guide modes. The dashed lines correspond to modes that are symmetric (antisymmetric) with respect to the plane of symmetry when they fall above (below) the isolated-guide curves. The separation distances are indicated for each dashed curve.

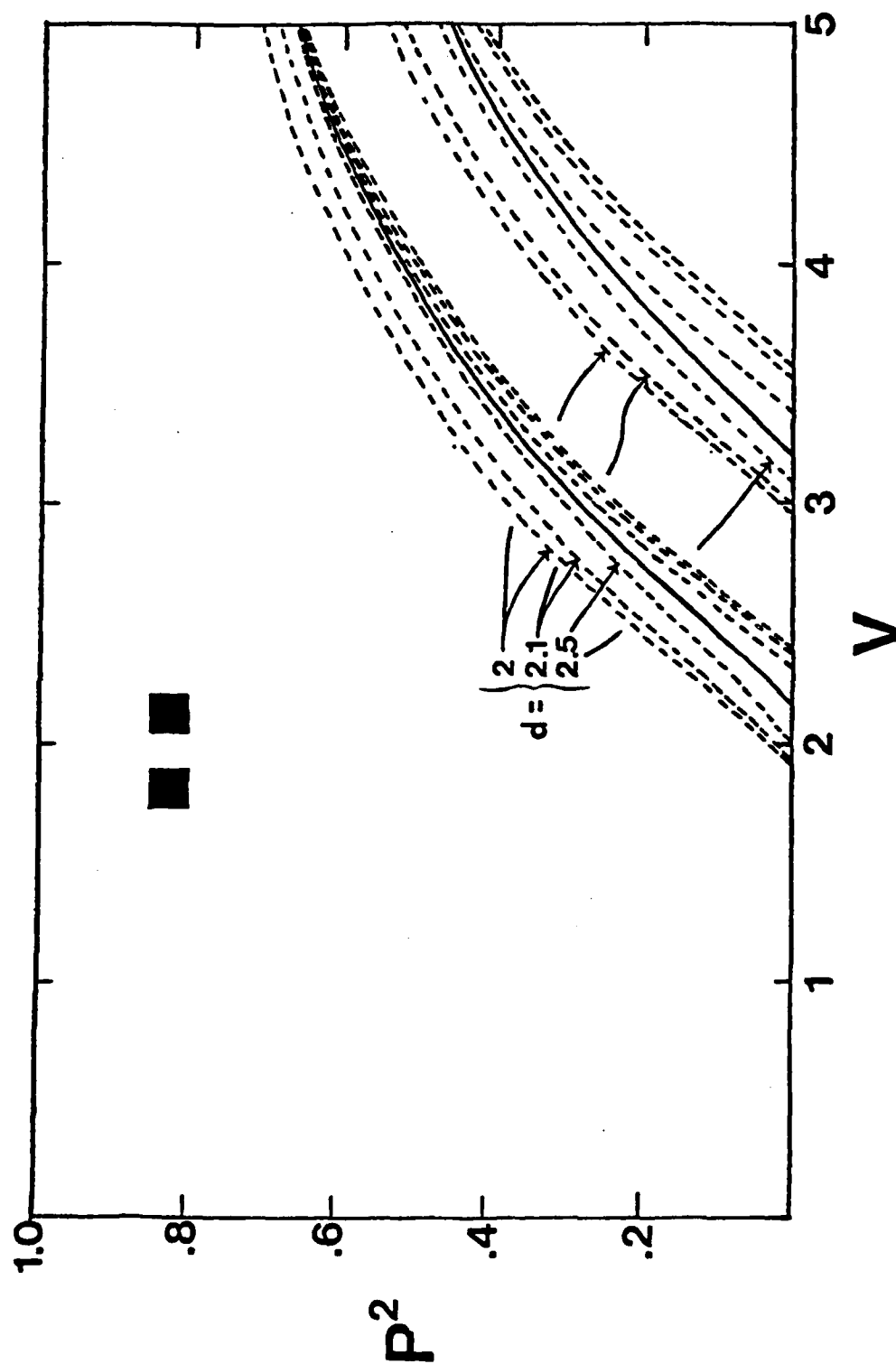


Fig. II.22 Same as Fig. 21, but for the sine modes.

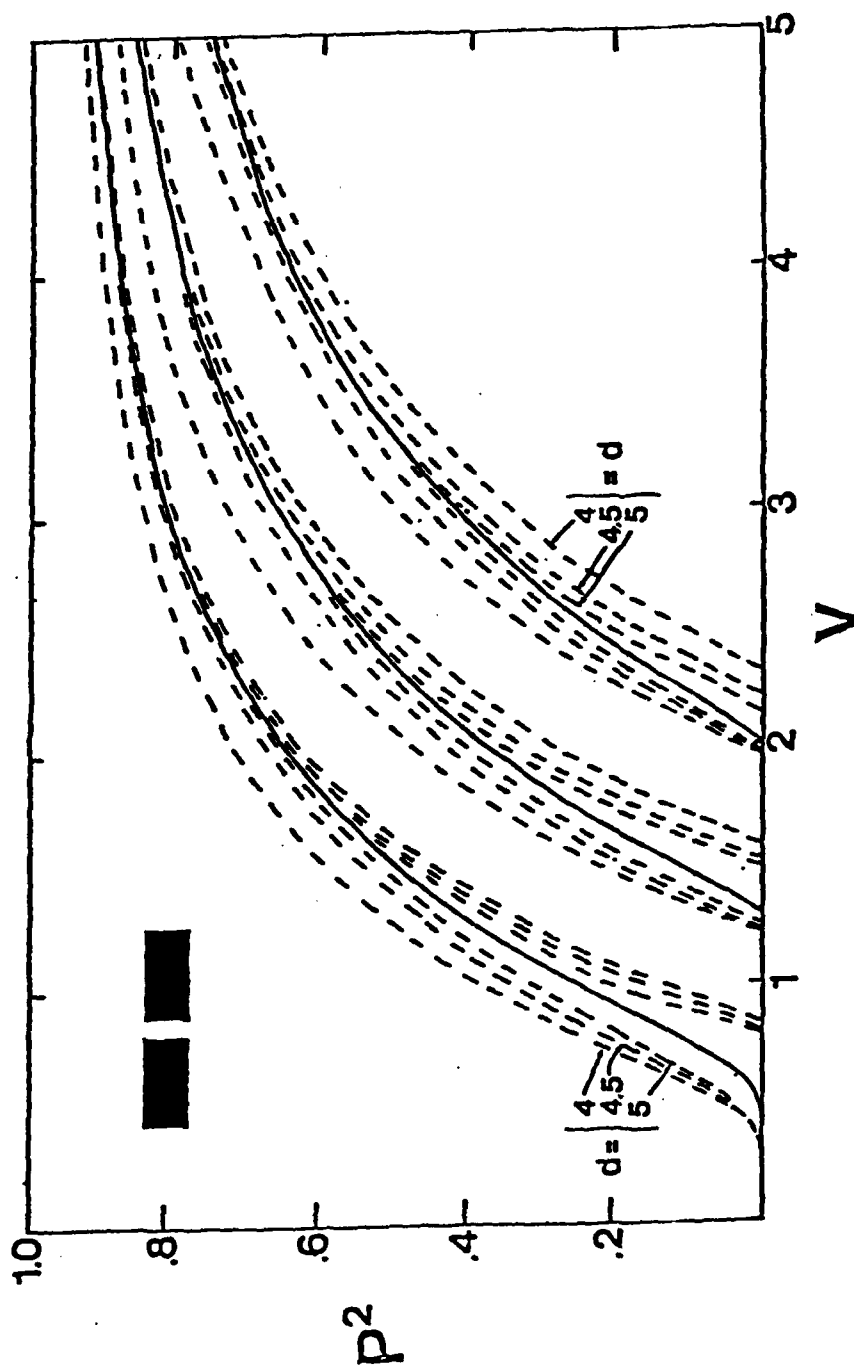


Fig. II.23 Cosine modes of a composite system consisting of two identical rectangular guides with an aspect ratio of 2. The three solid lines correspond to isolated-guide modes. The dashed lines correspond to modes that are symmetric (antisymmetric) with respect to the y axis when they fall above (below) the isolated-guide curves. The separation distances are 4, 4.5, and 5 for each family.

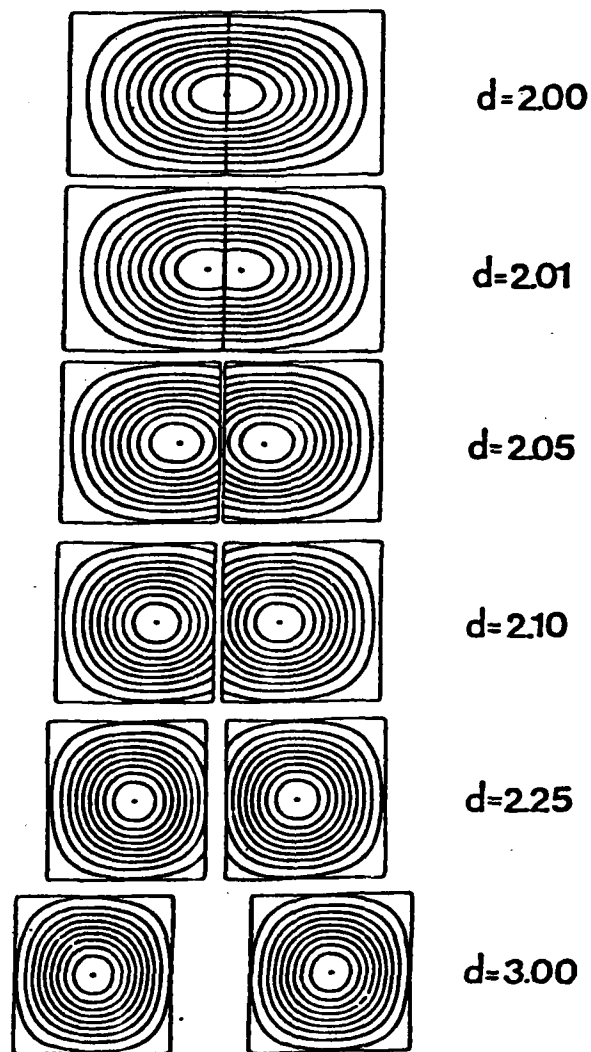


Fig. II.24 Contours of constant squared amplitude ϕ^2 for that symmetric mode of a composite system, consisting of two square guides, that derives from the dominant mode of an isolated guide. The amplitude at the center of the pattern has magnitude unity, and on successively larger contours ϕ^2 changes by 0.1.

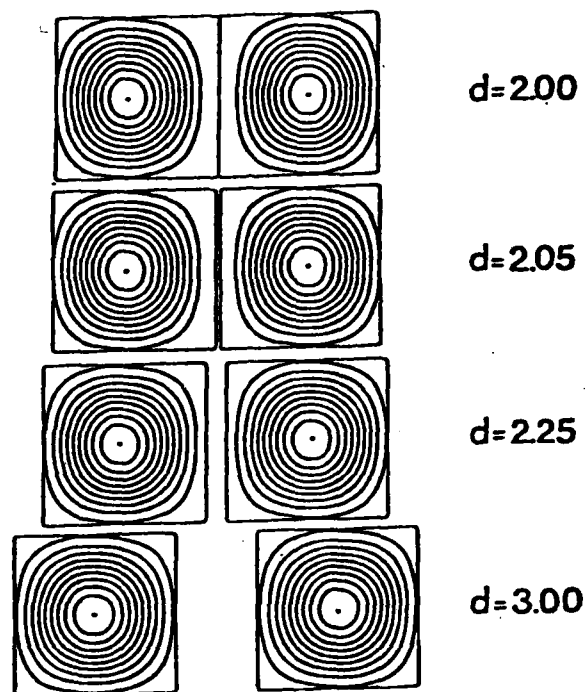


Fig. II.25 Same as Fig. 24, but for the anti-symmetric mode.

3.3.4.3 Results for Two Dissimilar Guides

We have found the solution of Eqn. (54) for a variety of configurations involving two dissimilar guides. The most interesting case is that of circular guides of different size and the same index of refraction. Most of our results were obtained for such examples. In fact, as for identical guides, the general features of composite systems, consisting of pairs of guides of various shapes, are similar to those consisting of two circular guides. We have demonstrated, however, that the technique works quite well for dissimilar ellipses, squares, rectangles, and combinations thereof.

As with identical guides it is convenient to correlate the modes of the guiding pair at finite separation distances with the modes of the pair at infinite separation. These latter are of course the modes of the isolated individual guides. Thus, for d infinite, there are two sets of solutions of Eqn. (54) or, say, Eqn. (66). In one of them, the coefficients $C_s^{(2)}$ are all zero, and the propagation constants and the nonvanishing values of $C_s^{(1)}$ are those that correspond to modes of the isolated guide number 1. For the second set of solutions, the $C_s^{(1)}$ are all zero, and the modes are those of the isolated guide number 2.

For finite separations, the modes have properties which are exemplified in Figs. 26 and 27. In Fig. 26 we show computed results for cosine expansions in which P^2 is plotted against V for various interguide distances for a variety of modes of a composite system consisting of guides with radii of 1.00 and 1.05. V is defined in terms of the radius of the smaller guide. Since the guides are only slightly different in size, the general similarity between Fig. 26 and Fig. 16 (for identical guides) is not surprising. The main difference is that in the present case the modes at infinite distance do not appear as degenerate pairs. In each pair of solid lines in Fig. 26, the upper line represents a certain mode of the larger guide in isolation, whereas the lower line corresponds to a mode of the smaller one.

To give some idea of the convergence of the interior expansions, Eqn. (40), as the distance d decreases from infinity, Tables 6 and 7 give $C_s^{(1)}$ and $C_s^{(2)}$ for modes that become the dominant modes of these two guides in isolation.

In Fig. 27 we present propagation constant curves for a pair of circles with radii of 1.00 and 1.25 (V defined in terms of the former) in order to make some general observations. First of all, as a contrast to Fig. 16 and (to a lesser extent) Fig. 26, some of the composite system modes are barely

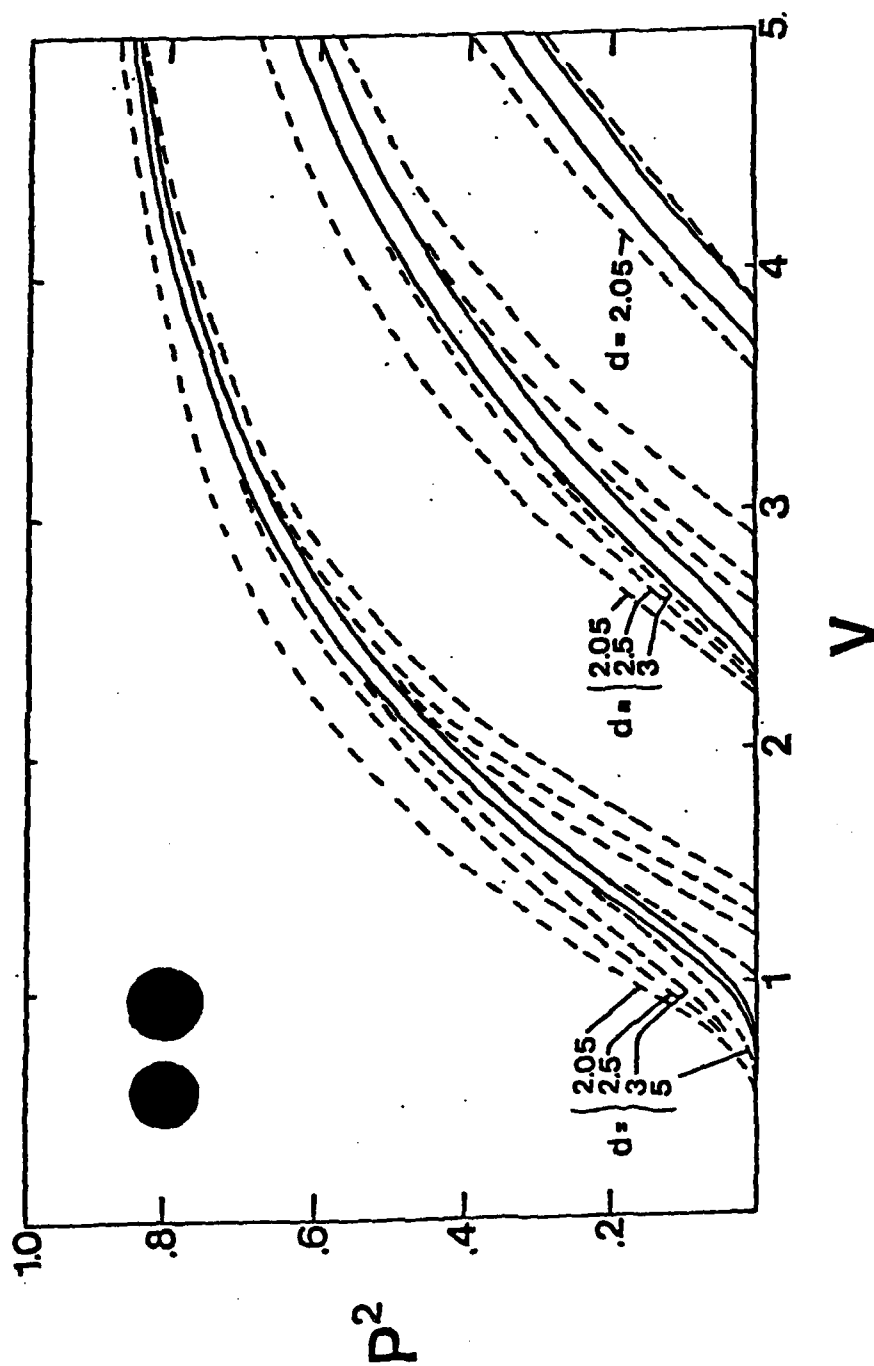


Fig. II.26 Cosine modes of a composite system consisting of two circular guides of radii 1.00 and 1.05. The solid lines are the modes of the larger and smaller guides in isolation with the modes of the larger guide lying above those of the smaller in each case. The dashed lines correspond to finite separations. $d = 2.05$ corresponds to touching guides.

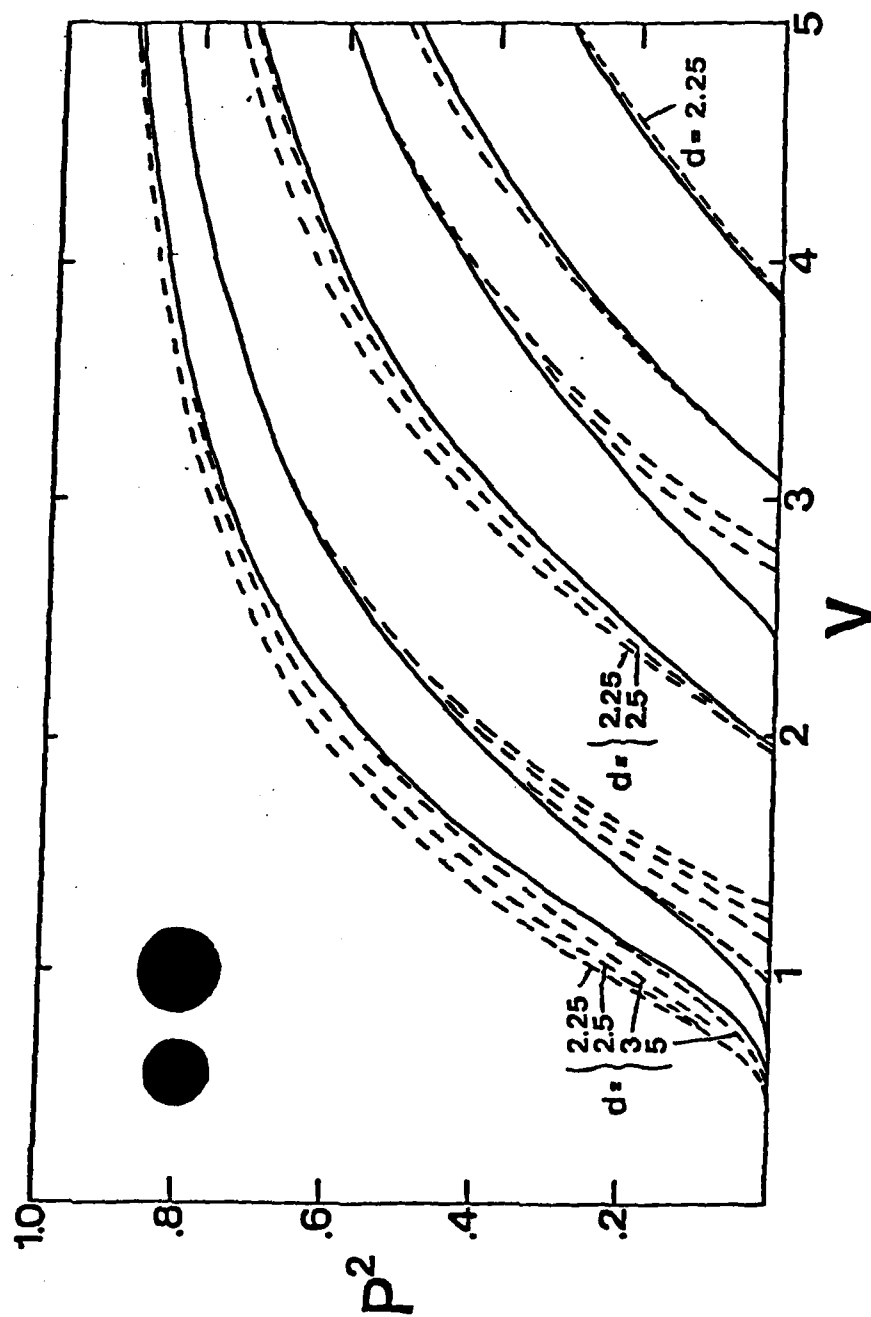


Fig. II.27 As in Fig. 26, except the radii are 1.00 and 1.25.

d	∞	3.00	2.25	2.05
P^2	.7894	.7894	.7965	.8157
$C_0^{(1)}$	0	.035	.438	.630
$C_1^{(1)}$	0	.006	.106	.281
$C_2^{(1)}$	0	.006	.118	.352
$C_3^{(1)}$	0	.010	.212	.702
$C_4^{(1)}$	0	.020	.495	1.846
$C_0^{(2)}$	1	1.000	1.000	1.000
$C_1^{(2)}$	0	-0.000	-.078	-.294
$C_2^{(2)}$	0	0.000	.083	.352
$C_3^{(2)}$	0	-0.000	-.146	-.693
$C_4^{(2)}$	0	0.001	.342	1.824

Table II.6. Coefficients $C_s^{(1)}$ and $C_s^{(2)}$ for the first mode of the composite system of Fig. 26 for different values of d and $V = 4$. This mode evolves into the dominant mode of the larger guide in isolation.

d	∞	3.00	2.25	2.05
P^2	.7727	.7726	.7688	.7626
$C_0^{(1)}$	1	1.000	1.000	1.000
$C_1^{(1)}$	0	-.000	-.039	-.101
$C_2^{(1)}$	0	-.000	-.038	-.096
$C_3^{(1)}$	0	-.000	-.059	-.148
$C_4^{(1)}$	0	-.001	-.121	-.293
$C_0^{(2)}$	0	-.045	-.553	-.797
$C_1^{(2)}$	0	-.008	-.125	-.236
$C_2^{(2)}$	0	.007	.115	.214
$C_3^{(2)}$	0	-.011	-.181	-.333
$C_4^{(2)}$	0	.021	.376	.691

Table II.7. Coefficients $C_s^{(1)}$ and $C_s^{(2)}$ for the second modes of the composite system of Fig. 26 for different values of d and $V = 4$. This mode evolves into the dominant mode of the smaller guide in isolation.

distinguishable from the isolated-guide modes away from cutoff, even for the touching distance. This illustrates the often observed fact that the characteristics of the composite modes are weakly dependent on d when the isolated-guide propagation constants are not the same or close in value. Also, there is a gap between each pair of isolated-guide modes, and unless the two guides have very different physical characteristics, there is no composite mode in this region. The gaps diminish as the guides become more similar. These general characteristics are typical of various two-piece composite systems that we have investigated, consisting of combinations of squares, rectangles, circles, and ellipses in certain orientations.

There is not much to be learned from plots of the sine modes of the systems described in Figs. 26 and 27. Except for the separation between the two $d = \infty$ modes, the curves for these cases are much like those in Fig. 17. For the modes that cut off near $V = 4$, the $d = 2.05$ and $d = 2.25$ (touching) cases are almost indistinguishable, on the scale of these drawings, from the respective $d = \infty$ curves. It is generally true that the greater the difference in size (and hence in unperturbed-mode propagation constants) between the two guides, the smaller is the deviation of the composite modes from the isolated-guide modes. This pattern is more pronounced for some modes, however, than for others.

A few comparisons with Wijngaard's work <22> for different-size circular guides is possible. For touching guides with a radius ratio of 1:1.3, $\delta = 0.1$, and $V = 3.5$, his Table I gives $\mu = 3.3609$ for his II_{π} mode. Our comparable result is 3.3641, which suggests that the weakly guiding approximation is useful even when δ is not close to zero. For this same configuration with $V = 2$, the ratios of the y components of the field at the center of the two guides are, for his I_0 and I_{π} modes, 0.616 and -1.690, respectively. Our ratios turn out to be 0.36 and -1.28, which are of the same order of magnitude and sign.

3.4 Final Equations for a General Array

In this section we set down the formulation which is required to compute the modes of a general array of guides using the integral-equation technique. One could use such a formulation, for example, to solve a system of three guides arranged in some triangular pattern, or four guides at the corners of a square or rectangle. Except for calculating the modes of a linear array of identical guides (a configuration which is greatly simplified by symmetry) we have not made use of this derivation.

The analysis proceeds from Eqn. (41) almost exactly as in the two-guide example, with the same definitions of matrix elements and the same

manipulation required to convert them to real quantities. The only important difference comes in the transformation functions. Since we cannot automatically take γ to be zero (see Fig. 14b), Eqn. (47) is needed to derive the transformation functions for the various coordinate systems. The main effect of this is to connect the $H_\ell \cos(\ell\phi)$ functions in one system with the $J_k \cos(k\phi)$ and $J_k \sin(k\phi)$ functions in the others, rather than just with the former as was previously the case. (The same is of course true of the $H_\ell \sin(\ell\phi)$ functions.) This forces us to write the transformations connecting the i th and j th coordinate systems as

$$H_\ell(r_2, \phi_i) \cos \ell\phi_i = \sum_{k=0}^{\infty} \alpha_{k\ell}^{ij} J_k(r_2, \rho_i) \cos k\phi_i + \sum_{k=0}^{\infty} \bar{\alpha}_{k\ell}^{ij} J_k(r_2, \rho_i) \sin k\phi_i \quad (84a)$$

$$H_\ell(r_2, \phi_i) \sin \ell\phi_i = \sum_{k=0}^{\infty} \bar{\beta}_{k\ell}^{ij} J_k(r_2, \rho_i) \cos k\phi_i + \sum_{k=0}^{\infty} \beta_{k\ell}^{ij} J_k(r_2, \rho_i) \sin k\phi_i \quad (84b)$$

where the coefficients $\bar{\alpha}$ and $\bar{\beta}$ of course did not appear previously. There is an analogous set of equations expressing the basis functions in the i th system in terms of those in the j th system, with coefficients $\eta_{k\ell}^{ij}$, $\bar{\eta}_{k\ell}^{ij}$, $\mu_{k\ell}^{ij}$, and $\bar{\mu}_{k\ell}^{ij}$. After conversion to real form (times powers of i) the coefficients are

$$\alpha_{k\ell} = i^{-(k-\ell+1)} \frac{1}{\pi} E_k \left\{ K_{k-\ell}(\pi B_d P) \cos[(k-\ell)\gamma] + K_{k+\ell}(\pi B_d P) \cos[(k+\ell)\gamma] \right\} \quad (85a)$$

$$\bar{\alpha}_{k\ell} = i^{-(k-\ell+1)} \frac{2}{\pi} \left\{ K_{k-\ell}(\pi B_d P) \sin[(k-\ell)\gamma] + K_{k+\ell}(\pi B_d P) \sin[(k+\ell)\gamma] \right\} \quad (85b)$$

$$\bar{\beta}_{k\ell} = i^{-(k-\ell+1)} \frac{1}{\pi} E_k \left\{ -K_{k-\ell}(\pi B_d P) \sin[(k-\ell)\gamma] + K_{k+\ell}(\pi B_d P) \sin[(k+\ell)\gamma] \right\} \quad (85c)$$

$$\beta_{k\ell} = i^{-(k-\ell+1)} \frac{2}{\pi} \left\{ K_{k-\ell}(\pi B_d P) \cos[(k-\ell)\gamma] - K_{k+\ell}(\pi B_d P) \cos[(k+\ell)\gamma] \right\} \quad (85d)$$

$$\eta_{k\ell} = (-1)^{k-\ell} \alpha_{k\ell} \quad (85e)$$

$$\bar{\eta}_{k\ell} = (-1)^{k-\ell} \bar{\alpha}_{k\ell} \quad (85f)$$

$$\bar{\mu}_{k\ell} = (-1)^{k-\ell} \bar{\beta}_{k\ell} \quad (85g)$$

$$\mu_{k\ell} = (-1)^{k-\ell} \beta_{k\ell} \quad (85h)$$

where, for easy viewing, we have left off the (ij) superscript on all the coefficients and the (ij) subscript which is obviously implied for the distance d between the centers of the two coordinate systems. For $\gamma = 0$, these expressions simplify to the point where the transformations are the same as in the previous section.

The implications of all this are that the $i \neq j$ terms in Eqn. (41) are, for each value of i , twice as numerous as before. Thus when the homogeneous equations are written as constants times the basis functions, the constants contain an extra sum, involving the coefficients $\bar{\alpha}$, $\bar{\beta}$, $\bar{\mu}$, or $\bar{\eta}$. The logic, however, is exactly as before: the coefficients of each of the basis functions $J_k(\gamma_2 \rho_1) \cos(k\phi_1), \dots, J_k(\gamma_2 \rho_N) \sin(k\phi_N)$ must be separately equal to zero.

It is sufficient to simply write down the final matrix equation. It appears on page 85 as Eqn. (86). With the truncation at M terms, the matrix is $2NM$ by $2NM$ in size.

Returning briefly to our discussion of the transformation functions, we should point out that the formulation given in Eqns. (84) and (85), and implied by Fig. 14b, may not necessarily be the simplest for all cases involving a non-linear array. Consider, for example, a configuration consisting of three arbitrarily-shaped guides arranged with their "centers" at the apexes of an equilateral triangle. The transformation functions turn out to be simpler if we choose the x -axes to be oriented at 120° with respect to each other, than if the axes are parallel as in Fig. 14b. Similar considerations may apply to other special cases, but the details will be different in each case.

3.5 Linear Arrays of More Than Two Guides

3.5.1 General Considerations

The simplest configuration involving more than two guides is that in which the origins of the N coordinate systems are all in a line. The formulation of the previous section is then excessive, as $(\bar{\alpha}) = (\bar{\beta}) = 0$. Nevertheless the equations can be quickly written from the general expression. If we consider guides which have reflection symmetry about the common x -axis, and only the cosine solutions, they are

AD-A139 603

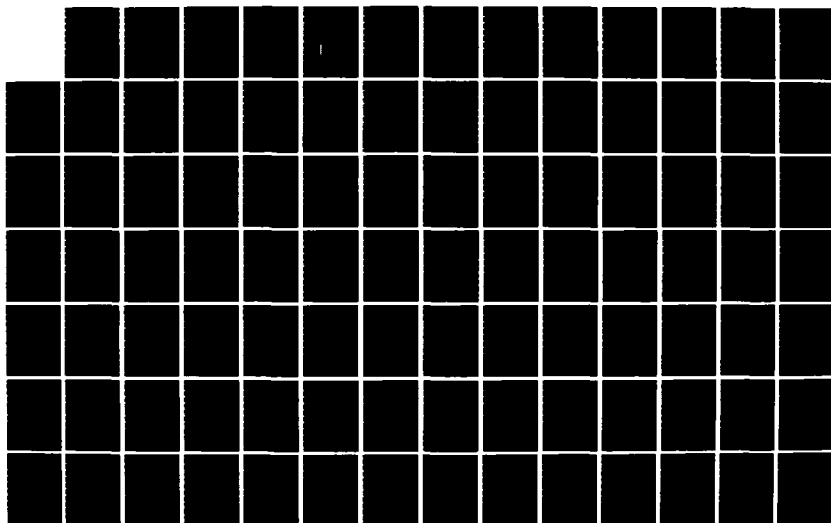
MATHEMATICAL MODELLING OF WAVEGUIDING TECHNIQUES AND
ELECTRON TRANSPORT VOLUME 1(U) ARCON CORP WALTHAM MA
S WOOLF ET AL. JAN 84 RADC-TR-83-313-VOL-1
F19628-78-C-0188

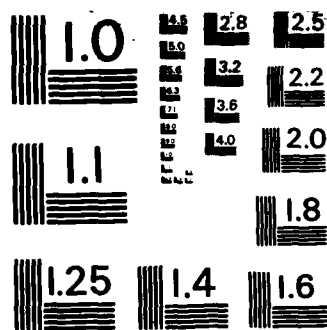
2/3

UNCLASSIFIED

F/G 12/1

NL





MICROCOPY RESOLUTION TEST CHART
NATIONAL BUREAU OF STANDARDS-1963-A

$$\begin{pmatrix}
 R_{hs}^{(1)} & \left(\sum_{k=0}^{N'} (-1)^k \alpha_{ke}^{(2)} \bar{R}_{ks}^{(2)} \right)_{hs} & \dots & \left(\sum_{k=0}^{N'} (-1)^k \alpha_{ke}^{(N)} \bar{R}_{ks}^{(N)} \right)_{hs} & C_s^{(1)} \\
 \left((-1)^k \sum_{k=0}^{N'} \alpha_{ke}^{(2)} \bar{R}_{ks}^{(1)} \right)_{hs} & R_{hs}^{(2)} & \dots & \left(\sum_{k=0}^{N'} (-1)^k \alpha_{ke}^{(N)} \bar{R}_{ks}^{(2)} \right)_{hs} & C_s^{(2)} \\
 \vdots & \vdots & & \vdots & \vdots \\
 \left((-1)^k \sum_{k=0}^{N'} \alpha_{ke}^{(N)} \bar{R}_{ks}^{(1)} \right)_{hs} & \left((-1)^k \sum_{k=0}^{N'} \alpha_{ke}^{(2)} \bar{R}_{ks}^{(2)} \right)_{hs} & \dots & R_{hs}^{(N)} & C_s^{(N)}
 \end{pmatrix} = 0 \quad (87)$$

This equation can be solved directly. On the other hand, if there is a plane of symmetry perpendicular to the common x-axis, simplifications which are completely analogous to the two-identical-guide case are possible. Suppose, for example, $N = 6$. If the guides are numbered from left to right, and if guides 1 and 6, 2 and 5, and 3 and 4 are identical in pairs (shape, orientation, distance from the center, refractive index) then the solutions can only be symmetric or antisymmetric about that plane. As with the two-guide case, one can a priori relate the sets of coefficients in pairs. Alternatively, one can simply relate the matrix elements of the corresponding guides. Viewed either way, the 6M by 6M set contains redundancies, the coefficients are connected by relations like Eqns. (68) and (69) and the set reduces to 3M by 3M:

$$\begin{pmatrix}
 R_{hs} \pm \sum_{k=0}^{N'} \alpha_{ke}^{(6)} \bar{R}_{ks} & \sum_{k=0}^{N'} [(-1)^k \alpha_{ke}^{(2)} \pm \alpha_{ke}^{(5)}] \bar{R}_{ks} & \sum_{k=0}^{N'} [(-1)^k \alpha_{ke}^{(3)} \pm \alpha_{ke}^{(4)}] \bar{R}_{ks} \\
 \sum_{k=0}^{N'} [(-1)^k \alpha_{ke}^{(2)} \pm \alpha_{ke}^{(5)}] \bar{R}_{ks} & R_{hs} \pm \sum_{k=0}^{N'} \alpha_{ke}^{(4)} \bar{R}_{ks} & \sum_{k=0}^{N'} [(-1)^k \alpha_{ke}^{(1)} \pm \alpha_{ke}^{(6)}] \bar{R}_{ks} \\
 \sum_{k=0}^{N'} [(-1)^k \alpha_{ke}^{(3)} \pm \alpha_{ke}^{(4)}] \bar{R}_{ks} & \sum_{k=0}^{N'} [(-1)^k \alpha_{ke}^{(1)} \pm \alpha_{ke}^{(6)}] \bar{R}_{ks} & R_{hs} \pm \sum_{k=0}^{N'} \alpha_{ke}^{(2)} \bar{R}_{ks}
 \end{pmatrix}
 \begin{pmatrix}
 C_s^{(1)} \\
 C_s^{(2)} \\
 C_s^{(3)}
 \end{pmatrix} = 0 \quad (88)$$

where, as before, the symmetric (+) and antisymmetric (-) cases must be solved separately. For any even number of guides the procedures, if not completely obvious, are at least straightforward.

For an odd number of guides with a plane of symmetry bisecting the middle guide, the equations contain redundancies as before, but not exactly in pairs. This is because the coefficients of the field expansion in the middle guide are not related to those in any other guide. Thus, for example, for $N=5$ the $5M$ by $5M$ system collapses to $3M$ by $3M$, with vectors of coefficients $(C^{(1)})$, $(C^{(2)})$, and $(C^{(3)})$ to be determined. For symmetric solutions, however, one can see that $C_s^{(3)} = 0$ for s odd, and for antisymmetric solutions $C_s^{(3)} = 0$ for s even. Therefore, the number of unknown coefficients is exactly halved by the symmetry considerations, as when N is even.

From a programming standpoint, it turns out to be easier not to reduce the dimension of the array to $2\frac{1}{2}M$ from $3M$ (for $N=5$). The mathematical effect of this is to retain one or more equations (depending on M and whether the symmetric or antisymmetric modes are sought) which, written out, are the same as $0 = 0$. It comes about because, in certain rows of the matrix, all terms are zero except the ones which multiply the zero coefficient. The result is the inclusion of one spurious root with each set of N proper roots. This extra root is equal to that which one would obtain for the middle guide in isolation, using the same truncation order.

If one did reduce the dimension to $2\frac{1}{2}M$, it would be by reordering the matrix into a block-diagonal form and dropping the portion responsible for the spurious root. Similar considerations apply to any odd- N array with such a plane of symmetry.

3.5.2 Results for a Linear Array

We have calculated the modes of an array consisting of identical equally-spaced guides of various shapes. Insofar as the results are qualitatively very similar for different shapes, we confine our discussion to those derived for circular guides, a configuration which has been discussed by Meltz and Snitzer <23> using coupled-mode theory as a starting point.

As for the two-guide case, it is illuminating to introduce the qualitative nature of the results by following the changes in the system of N guides as it is assembled, so to speak, by bringing the guides together from infinity. Suppose that each of the identical guides supports a certain mode, say the dominant one, with propagation constant k_g^∞ or P_∞^2 . As the distance between the guides decreases and the composite guide is formed, this propagation constant splits in general into N different propagation constants characteristic of the N -fold guide as a whole:

$$\begin{aligned} P_\infty^2 &\rightarrow P_1^2, P_2^2, \dots, P_N^2, \\ k_g^\infty &\rightarrow k_g^{(1)}, k_g^{(2)}, \dots, k_g^{(N)} \end{aligned} \quad (89)$$

Each propagation constant is associated with a mode that is symmetric or antisymmetric with respect to reflections about the central plane of symmetry.

Figure 28 shows the propagation constants, as a function of V , for an array of six touching circular guides as well as the six-fold degenerate modes corresponding to infinite separation. The "splitting" of each unperturbed mode into six composite modes is evident, as is the noncutoff property of just one (the lowest-order) composite mode. For this first set the symmetric and antisymmetric modes alternate, with the dominant mode being symmetric. For the second set shown, the symmetries also alternate but an antisymmetric mode is the "top" mode. Similar results are obtained for configurations with odd numbers of guides, with the "extra" mode being symmetric for the lowest-order group.

By steps that are similar to those used to derive Eqn. (81), we obtain the following approximate relationship for the propagation constants of a set of N modes:

$$k_g^{(r)} - k_g^\infty \simeq \frac{1}{2} k_1 \delta(P_r^2 - P_\infty^2) \left\{ 1 + \frac{1}{2} \delta \left[1 - \frac{1}{2} (P_r^2 + P_\infty^2) \right] \right\}. \quad (90)$$

Equation (90) will be used to help make a comparison between our numerical results and the results predicted by Eqn. (7) of Ref. 23. The latter approach associates a single-guide mode with each element of the array, with a strength or amplitude that is to be determined. The propagation properties of the array depend on the overlapping of the tails of these individual fields. When a nearest-neighbor approximation and the results of coupled-mode theory for two guides are used, the result for a linear array is

$$\frac{k_g^{(r)} - k_g^\infty}{2\Delta\beta} = \cos\left(\frac{r\pi}{N+1}\right), \quad r=1,2,\dots,N, \quad (91)$$

where $2\Delta\beta$ is the coupled-mode result for the difference between the propagation constants, $k_g^{(S)}$ and $k_g^{(A)}$, of the symmetric and antisymmetric modes of a pair of identical guides. That is,

$$2\Delta\beta = k_g^{(S)} - k_g^{(A)} \quad (92)$$

The amplitude associated with the m th individual guide and the r th mode (Eqn. (8), Ref. 23) is

$$\Lambda_m^{(r)} = [2/(N+1)]^{1/2} \sin\left(\frac{mr\pi}{N+1}\right). \quad (93)$$

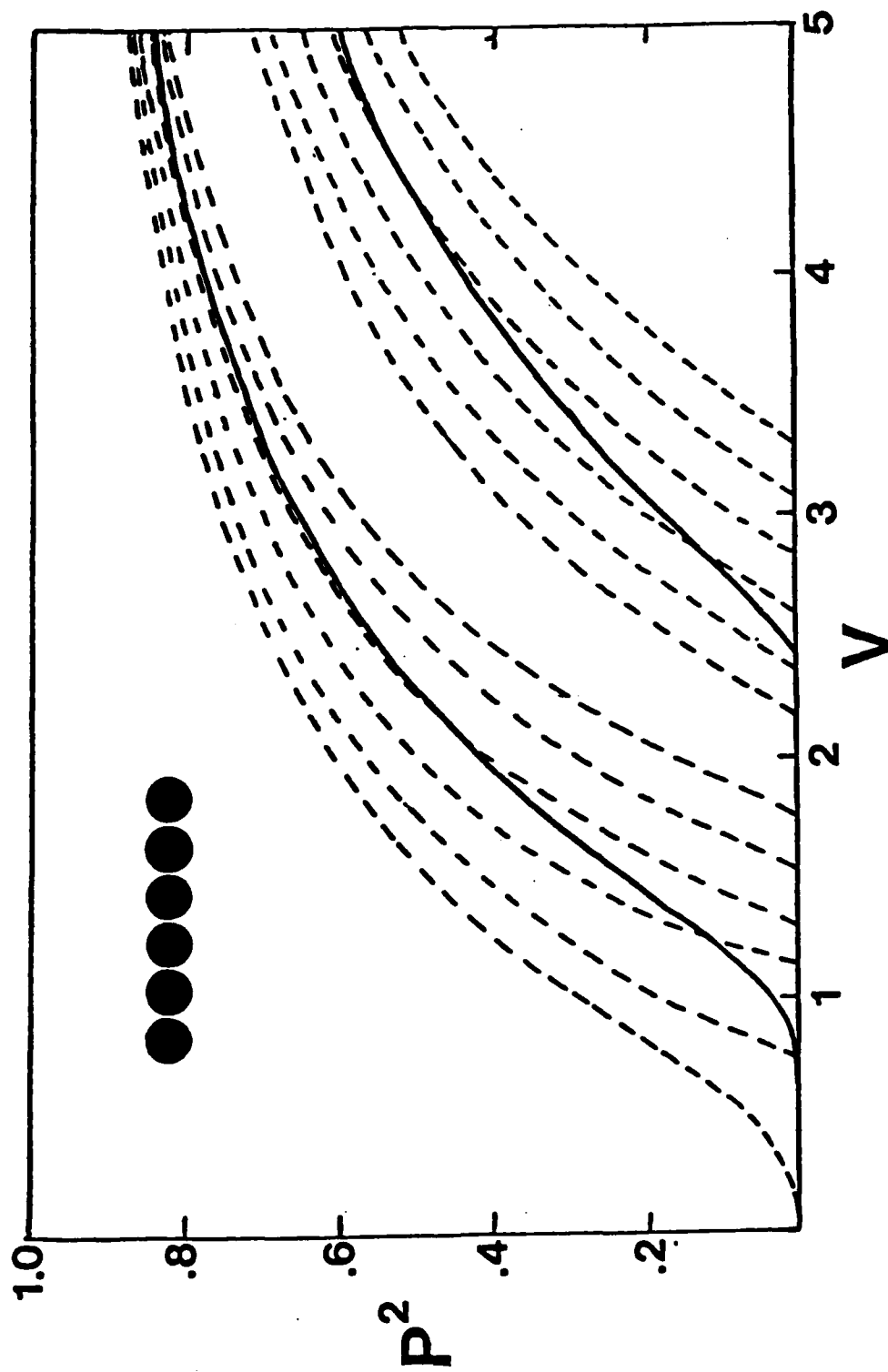


Fig. II.28 First two sets of cosine modes of a composite system consisting of six identical circular guides uniformly spaced along a line. Dashed lines represent modes when the guides are touching; solid lines represent modes when the separation is large.

From Eqn. (90) we can directly write an expression for $k_g^{(S)} - k_g^{(A)}$.

$$k_g^{(S)} - k_g^{(A)} \approx \frac{1}{2} k_1 \delta (P_S^2 - P_A^2) \left\{ 1 + \frac{1}{2} \delta \left[1 - \frac{1}{2} (P_S^2 + P_A^2) \right] \right\}. \quad (94)$$

If we then divide Eqn. (90) by Eqn. (94), we have a result that is directly comparable with Eqn. (91). Since our calculations are for weakly guiding systems, we set $\delta = 0$ and obtain, for an N-guide array,

$$\frac{k_g^{(r)} - k_g^\infty}{k_g^{(S)} - k_g^{(A)}} = \frac{P_r^2 - P_\infty^2}{P_S^2 - P_A^2}, \quad r=1,2,\dots,N. \quad (95)$$

In Fig. 29 we plot the dominant-mode splittings obtained from the right-hand side of Eqn. (95) (solid lines) and the right-hand side of Eqn. (91) (dashed lines) for N between 1 and 6, for four different cases. Figs. 29(a) and 29(b) correspond to fairly tightly bound modes ($V = 5$), whereas Figs. 29(c) and 29(d) give results for a smaller normalized frequency ($V = 2.5$). From the uniformity of the discrepancies between the solid and dashed lines in Figs. 29(a) and 29(b), it seems clear that (for tighter-bound modes; at least) the major source of error is the failure of coupled-mode theory to predict the correct eigenvalues for two guides (particularly the *asymmetric splitting*) rather than the extension of those results to three or more guides. The fact that the uniformity is less evident in Figs. 29(c) and 29(d) suggests that the nearest-neighbor approximation may also contribute to the discrepancies for the more weakly bound modes. We should point out that, in terms of the actual eigenvalues, the agreement is quite good, especially for the cases with $d = 2.25$; the fact that we normalize (by dividing by $2\Delta\beta$) in order to obtain a uniform scale does exaggerate the appearance of the discrepancies in some cases. We also note that the values of the maximum splitting, $k_g^{(N)} - k_g^{(1)}$, agree much more uniformly (within 0.6% for all cases considered) than the individual values of the eigenvalues, $k_g^{(r)}$, do.

It is also of interest to compare the prediction of coupled-mode theory with the present results for the field amplitudes. To be complete, this would require a point-by-point comparison at various locations in the guide array. Instead, we have chosen to compare the fields at the center of each guide for $N = 4$, $V = 5$, and various values of d with the amplitudes given in Eqn. (93).

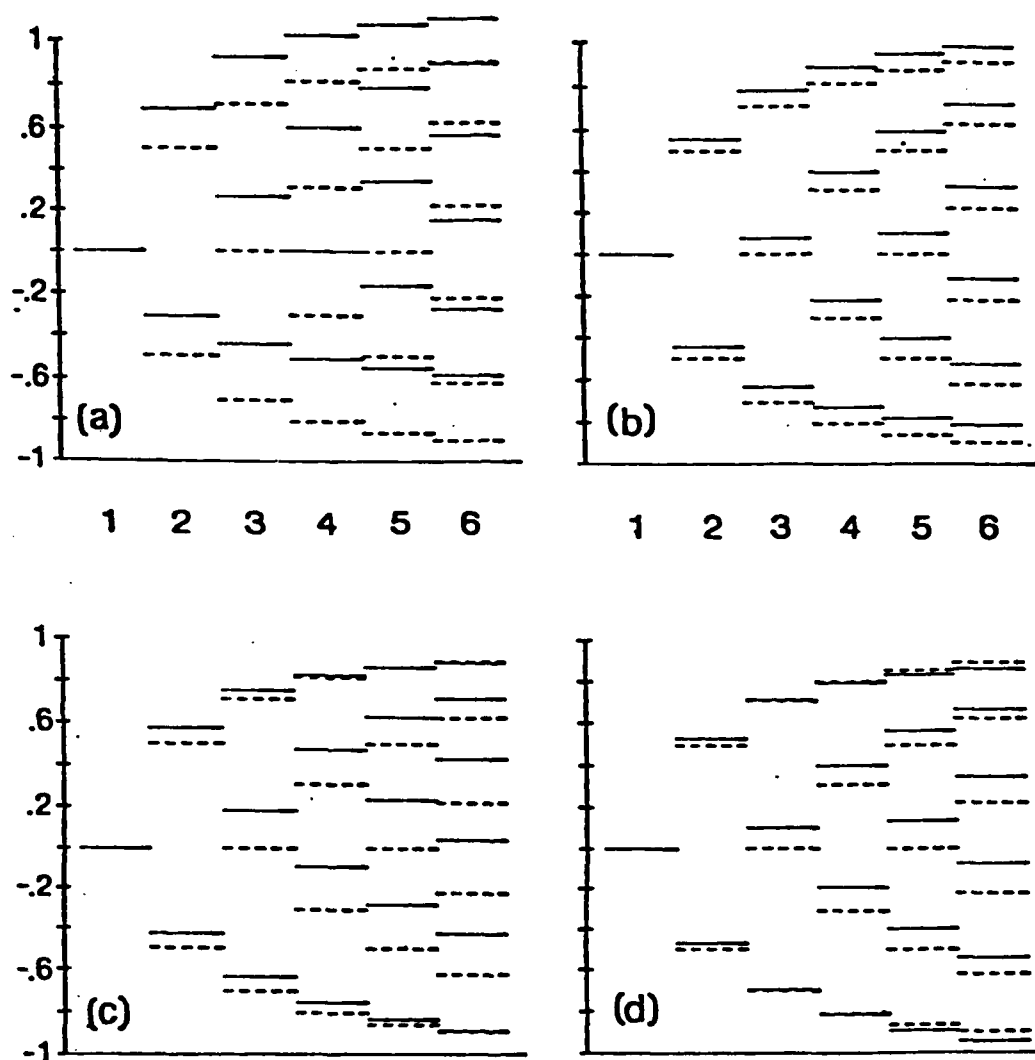


Fig. II.29 Results for modes of composite systems consisting of N identical circular guides uniformly spaced along a line. The solid lines, corresponding to the right-hand side of Eqn. (95), represent our numerical results; the dashed lines, from the right-hand side of Eqn. (91), represent the predictions of the coupled-mode theory <23>. These modes all derive from the dominant mode of an isolated guide. (a) $V=5, d=2$; (b) $V=5, d=2.25$; (c) $V=2.5, d=2$; (d) $V=2.5, d=2.25$.

Mode #	d	Guide #1	Guide #2	Guide #3	Guide #4
1	2.00	.510	1.000	1.000	.510
	2.25	.580	1.000	1.000	.580
	2.50	.606	1.000	1.000	.606
	$\Lambda_m^{(1)}$.618	1.000	1.000	.618
2	2.00	1.000	.770	-.770	-1.000
	2.25	1.000	.660	-.660	-1.000
	2.50	1.000	.630	-.630	-1.000
	$\Lambda_m^{(2)}$	1.000	.618	-.618	-1.000
3	2.00	1.000	-.499	-.499	1.000
	2.25	1.000	-.579	-.579	1.000
	2.50	1.000	-.606	-.606	1.000
	$\Lambda_m^{(3)}$	1.000	-.618	-.618	1.000
4	2.00	.794	-1.000	1.000	-.794
	2.25	.661	-1.000	1.000	-.661
	2.50	.630	-1.000	1.000	-.630
	$\Lambda_m^{(4)}$.618	-1.000	1.000	-.618

Table II.8. Field amplitudes at the centers of each guide (m) in a linear array of four identical equally spaced circular guides, normalized to a maximum of 1.00, for each mode (r), various guide separations, and $V = 5$. Also given, for comparison, are the amplitudes $\Lambda_m^{(r)}$ of Eqn. (93). For $d = 3$ our field amplitudes equal $\Lambda_m^{(r)}$ to three significant figures for all m and r.

In each case we have normalized the maximum field to a value of unity. The results are given in Table 8. One would expect to find the best agreement for large d since then the condition of weak coupling is best satisfied. This expectation is confirmed: for $d = 3.0$ we find exact agreement to three decimal places between our results and Eqn. (93). For smaller d , however, discrepancies begin to appear. Nonetheless, even for $d = 2.0$, which corresponds to touching guides, the difference is not more than about 20%. Similar results are obtained for N other than $N = 4$.

3.6 Summary

We have presented an integral-equation formalism that is useful for obtaining the modes of a completely general array of parallel optical waveguides, provided that the weakly guiding condition holds. The method is applicable to guides of any cross section in any orientation. We have presented numerical results consisting of complete propagation curves for certain cases of interest and have calculated beat lengths for pairs of identical guides, as well as field configurations. Our results have been compared with those of coupled-mode theory, and our calculations indicate that the latter provides good accuracy in most cases. We have shown that for pairs of identical guides, there can be serious errors in coupled-mode calculations near cutoff of the antisymmetric mode and for guides that are touching or close together and have presented curves for K and γ that may be used to estimate the size of these errors.

4. Multilayered Step-Index Guides

4.1 Introduction

The last class of dielectric waveguides to which the integral equation technique has been applied is that of isolated structures containing three concentric regions with different refractive indices. Reasons for finding solutions of this sort of problem vary from such simple ones as assessing the effect of thin cladding on normal fibers to more complex ones like calculating the properties of fundamentally different types of guides (e.g., the ring guide). We refer to such entities indiscriminately as "multilayered" guides.

Among the multitude of problems which fall into this category, we have restricted ourselves to two: that in which $n_1 > n_2 \geq n_3$ (the "cladded guide")

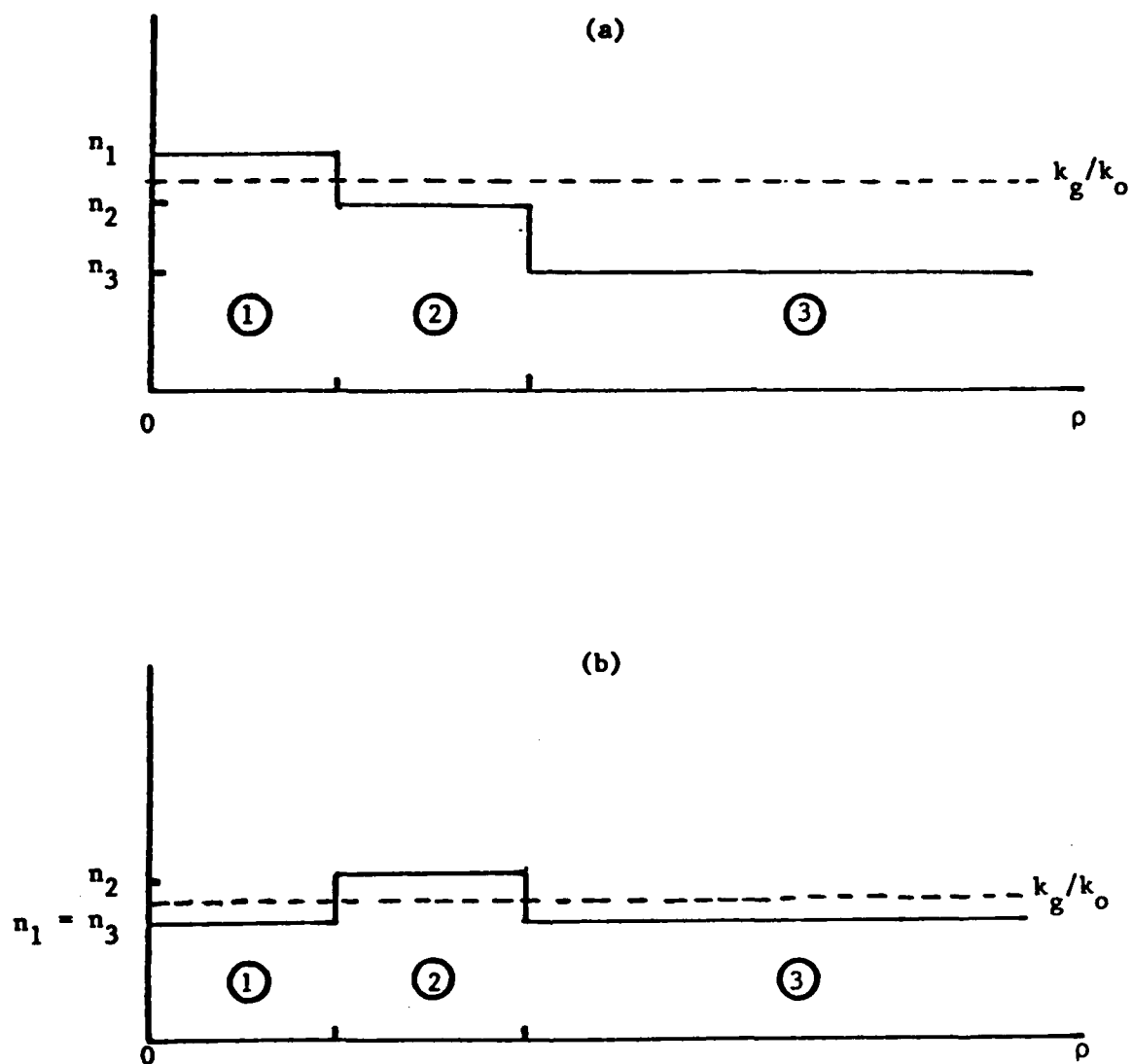


Fig. II.30 Index of refraction profile for multilayered guides, from the origin to the outer layer along some radial path determined by a choice of ϕ . For $\phi = \pi/2$ the boundaries are at $\rho = b_{12}$ and $\rho = b_{23}$. (a) the clad-guided guide; (b) the ring guide.

and that in which $n_2 > n_1 = n_3$ (the "ring guide"). For these two cases, illustrated schematically in Figs. 30(a) and 30(b), we are interested in guided modes confined to regions 1 and 2, respectively. As before, the weakly guiding condition is assumed, the outer medium (n_3) is infinite in extent, and the boundaries L_{12} and L_{23} may be arbitrarily shaped (except that each region must be simply connected and entirely enclosed by the one(s) outside it).

Unlike the work presented in Sections II-2 and II-3, no systematic accumulation of results was obtained as part of this contract effort; rather, we sought only those results which were needed to check programming functions. References 24 and 25 can be consulted for more detail on the formulation and for such results as have been gathered. We hasten to point out, of course, that limiting cases (e.g., $n_2 = n_3$ or $L_{23} \rightarrow \infty$ for the cladded guide; $L_{12} \rightarrow 0$ for the ring guide) have been correlated both analytically and numerically with the single-guide results to which they reduce.

Separate programs were developed to solve for the modes of the cladded guides and the ring guides. These are called COAX and HICOAX, respectively, and the techniques they embody are very similar to those described in Section II-2.4 for program TRUNCN. In a later section we discuss the way to use these programs.

4.2 Outline of the Formulation for Multilayered Guides

The differential equations which must be satisfied by the scalar field function, Φ , in the three regions (denoted by i) are, much as before,

$$(\nabla^2 + \gamma_i^2) \Phi(\vec{\rho}) = 0 \quad i = 1, 2, 3 \quad (96)$$

where γ_i and the quantities entering into it are defined in exact analogy with Eqns. (1) and (2). One integral representation which satisfies these equations is

$$\Phi(\vec{\rho}) = (\gamma_3^2 - \gamma_1^2) \int_{A_1} \Phi(\vec{\rho}') g_3(\vec{\rho}, \vec{\rho}') dA' + (\gamma_3^2 - \gamma_2^2) \int_{A_2} \Phi(\vec{\rho}') g_3(\vec{\rho}, \vec{\rho}') dA' \quad (97)$$

where the Green function satisfies

$$(\nabla^2 + \gamma_3^2) g_3(\vec{\rho}, \vec{\rho}') = \delta(\vec{\rho} - \vec{\rho}') \quad (98)$$

For $\vec{\rho}$ outside of region 3, Eqn. (97) is equivalent to

$$0 = \int_{A_1 + A_2} \left\{ g_3(\vec{\rho}, \vec{\rho}') \vec{\nabla}'^2 \Phi(\vec{\rho}') - \Phi(\vec{\rho}') \vec{\nabla}'^2 g_3(\vec{\rho}, \vec{\rho}') \right\} dA' \quad (99)$$

where the integration is taken over all points $\vec{\rho}'$ in the inner two regions. As before, the equivalent line-integral equation, by Green's second identity, is

$$0 = \int_{L_{23}} \left\{ g_3(\vec{\rho}, \vec{\rho}') \frac{\partial \Phi(\vec{\rho}')}{\partial n'} - \Phi(\vec{\rho}') \frac{\partial g_3(\vec{\rho}, \vec{\rho}')}{\partial n'} \right\} dL' \quad (100)$$

with the integration being taken over the L_{23} boundary just inside the second region.

Another integral representation can be written by analogy to Eqn. (97) using the Green function $g_1(\rho, \rho')$ which satisfies Eqn. (98) if γ_3 is replaced by γ_1 . Ultimately, for points $\vec{\rho}$ not in region 1, this becomes

$$0 = \int_{L_{12}} \left\{ g_1(\vec{\rho}, \vec{\rho}') \frac{\partial \Phi(\vec{\rho}')}{\partial n'} - \Phi(\vec{\rho}') \frac{\partial g_1(\vec{\rho}, \vec{\rho}')}{\partial n'} \right\} dL' \quad (101)$$

The original area integrals having been over A_2 and A_3 in this case, the line integral is taken over L_{12} just inside region 2. (The portion of the line integral at infinity contributes nothing.) Thus in Eqns. (100) and (101) we have a pair of equations both of which require a representation of the solution, Φ , appropriate for the middle region. One of them is valid for points $\vec{\rho}$ in regions 1 and 2, the other for points 2 and 3. This suggests that in Eqn. (100) we should use a representation of the Green function (the exact analog of Eqn. (8), replacing γ_2 with γ_3) which converges for $\rho < \rho'$, and apply it to points near the origin, while Eqn. (101) is useful far from the origin and requires a representation (Eqn. (9) replacing γ_2 with γ_1) converging for $\rho > \rho'$.

One principal difference between the present application of the integral-equation technique and that for simple guides and arrays is the expansion of the field function. In those problems the expansion was appropriate for regions containing the origin, and those terms in the general

solution of Helmholtz' Equation which blow up at the origin were required, explicitly, to have zero coefficients. Here we must take the full expansion:

$$\bar{u}(\hat{r}') = \sum_{s=0}^{\infty} J_s(\chi_2 \rho') [A_s \cos s\phi' + B_s \sin s\phi'] + \sum_{s=0}^{\infty} H_s(\chi_2 \rho') [C_s \cos s\phi' + D_s \sin s\phi'] \quad (102)$$

Then, in general, there are four sets of coefficients to be determined, unlike the simple guide problem where there are only two.

The manipulation of this field function, the Green function representations, and their derivatives after their insertion into Eqns. (100) and (101) is completely analogous to that encountered in Section II-2.2. This time we end up with

$$0 = \sum_{l=0}^{\infty} S_{1l} J_l(\chi_2 \rho) \cos l\phi + \sum_{l=0}^{\infty} S_{2l} J_l(\chi_2 \rho) \sin l\phi \quad (103a)$$

$$0 = \sum_{l=0}^{\infty} S_{3l} H_l(\chi_2 \rho) \cos l\phi + \sum_{l=0}^{\infty} S_{4l} H_l(\chi_2 \rho) \sin l\phi \quad (103b)$$

where S_{1l} , S_{2l} , S_{3l} , and S_{4l} are not the same as before but are just as complicated. For each value of l , each of these coefficients must be zero, as the sets of H_l basis functions are of equal stature with the J_l ones. Thus we obtain a four-fold infinity of linear equations in the coefficients A_s, \dots, D_s . Insofar as the analysis leading to the definitions of the coefficients S_{1l}, \dots, S_{4l} ---and also their reduction and simplification---closely mimics that of the previous sections, we resist the great temptation to set it all down in detail. Rather, we will only define our parameters for the two special cases we have considered, write the final determinantal equations for each, and wind up this section with a few general comments. Moreover, given that most interesting cases involve guides with reflection symmetry (both L_{12} and L_{23}) we will treat the sine and cosine series individually, writing separate equations for the A_s and C_s , or B_s and D_s .

4.3 Equations for the Cladded Guides

4.3.1 Parameterization

For the cladded guides with $n_1 > n_2 \geq n_3$ the guided modes are contained in region 1 for the most part, so the field expansions we obtain (in region 2) are not as interesting as those for other examples. We proceed by direct analogy with Section II-2.4, defining the normalized frequency in terms of the "characteristic distance" b_{12} of the 1-2 boundary:

$$B = \frac{k_0 b_{12}}{\pi} (n_1^2 - n_2^2)^{\frac{1}{2}} = \frac{k_0 b_{12} n_1}{\pi} \sqrt{\delta_{12}} \quad (104)$$

Also,

$$P^2 = \frac{k_g^2 - k_z^2}{k_1^2 - k_z^2} \quad (105)$$

Then the quantities $\gamma_2 \rho'$ and $\gamma_1 \rho'$ which appear in S_{3l} and S_{4l} (take our word for it) are

$$\gamma_1 \rho' = \pi B \frac{\rho'}{b_{12}} (1 - P^2)^{\frac{1}{2}} \quad (106a)$$

$$\gamma_2 \rho' = i \pi B \frac{\rho'}{b_{12}} P \quad (106b)$$

To deal with the third region with its differing index of refraction, an additional parameter must be introduced. We write

$$\delta_{13} = 1 - \frac{n_3^2}{n_1^2} \quad (107)$$

which is analagous to the expression, Eqn. (104), for δ_{12} (n_3 replaces n_2).

The quantity $\gamma_3 \rho'$ is then

$$\gamma_3 \rho' = i \pi B \frac{\rho'}{b_{12}} \left(\frac{\delta_{13}}{\delta_{12}} - 1 + P^2 \right)^{\frac{1}{2}} \equiv i \omega B \pi \frac{\rho'}{b_{12}} \quad (108)$$

The abbreviation w is useful but should not be allowed to obscure the presence of P^2 ($w^2 > P^2$). In the special case $\delta_{12} = \delta_{13}$ ($n_2 = n_3$), γ_2 and γ_3 are obviously the same. This corresponds to the two-medium guide treated in Section II-2.

4.3.2 Cosine Solutions

Under the assumptions stated earlier, the coefficients relevant for cosine solutions are

$$S_{12} = \sum_{s=0}^{\infty} \left\{ A_s M_{1s} + C_s N_{1s} \right\} = 0 \quad (109a)$$

$$S_{32} = \sum_{s=0}^{\infty} \left\{ A_s P_{2s} + C_s Q_{2s} \right\} = 0 \quad (109b)$$

where

$$M_{1s} = \int_{L_{23}} d\phi' \left\{ F_{1s}(\rho') \cos l\phi' \cos s\phi' + \bar{F}_{1s}(\rho', \frac{\partial \rho'}{\partial \phi'}) [s \cos l\phi' \sin s\phi' - l \sin l\phi' \cos s\phi'] \right\} \quad (110a)$$

$$N_{1s} = \int_{L_{23}} d\phi' \left\{ \bar{F}_{1s}(\rho') \cos l\phi' \cos s\phi' + \bar{F}_{1s}(\rho', \frac{\partial \rho'}{\partial \phi'}) [s \cos l\phi' \sin s\phi' - l \sin l\phi' \cos s\phi'] \right\} \quad (110b)$$

$$P_{2s} = \int_{L_{12}} d\phi' \left\{ H_{2s}(\rho') \cos l\phi' \cos s\phi' + \bar{G}_{2s}(\rho', \frac{\partial \rho'}{\partial \phi'}) [s \cos l\phi' \sin s\phi' - l \sin l\phi' \cos s\phi'] \right\} \quad (110c)$$

$$Q_{2s} = \int_{L_{12}} d\phi' \left\{ \bar{H}_{2s}(\rho') \cos l\phi' \cos s\phi' + \bar{G}_{2s}(\rho', \frac{\partial \rho'}{\partial \phi'}) [s \cos l\phi' \sin s\phi' - l \sin l\phi' \cos s\phi'] \right\} \quad (110d)$$

$$\begin{aligned} \bar{F}_{2s}(\rho') = & (i^{-l+s-1}) \left[\epsilon_2 \frac{2B\rho'}{b_{12}} \left\{ PK_l \left(\frac{\pi B w \rho'}{b_{12}} \right) I_{s-1} \left(\frac{\pi B P \rho'}{b_{12}} \right) + w K_{l-1} \left(\frac{\pi B w \rho'}{b_{12}} \right) I_s \left(\frac{\pi B P \rho'}{b_{12}} \right) \right\} \right. \\ & \left. + (l-s) \epsilon_2 \frac{2}{\pi} K_l \left(\frac{\pi B w \rho'}{b_{12}} \right) I_s \left(\frac{\pi B P \rho'}{b_{12}} \right) \right] \quad (111a) \end{aligned}$$

$$E_{2s}(\rho', \frac{\partial \rho'}{\partial \phi'}) = (i^{-l+s-1}) \epsilon_2 \frac{2}{\pi} K_l \left(\frac{\pi B w \rho'}{b_{12}} \right) I_s \left(\frac{\pi B P \rho'}{b_{12}} \right) \frac{\partial \rho'}{\partial \phi'} / \rho' \quad (111b)$$

$$\begin{aligned} \bar{F}_{2s}(\rho') = & (i^{-(l+s)}) \left[\epsilon_2 \frac{4B\rho'}{b_{12}} \left\{ PK_l \left(\frac{\pi B w \rho'}{b_{12}} \right) K_{s-1} \left(\frac{\pi B P \rho'}{b_{12}} \right) - w K_{l-1} \left(\frac{\pi B w \rho'}{b_{12}} \right) K_s \left(\frac{\pi B P \rho'}{b_{12}} \right) \right\} \right. \\ & \left. - \frac{4}{\pi^2} (l-s) \epsilon_2 K_l \left(\frac{\pi B w \rho'}{b_{12}} \right) K_s \left(\frac{\pi B P \rho'}{b_{12}} \right) \right] \quad (111c) \end{aligned}$$

$$\bar{E}_{2s}(\rho', \frac{\partial \rho'}{\partial \phi'}) = -i^{-(l+s)} \epsilon_2 \frac{4}{\pi^2} K_l \left(\frac{\pi B w \rho'}{b_{12}} \right) K_s \left(\frac{\pi B P \rho'}{b_{12}} \right) \frac{\partial \rho'}{\partial \phi'} / \rho' \quad (111d)$$

$$\begin{aligned} H_{2s}(\rho') = & i^s \left[\epsilon_2 \frac{\pi B \rho'}{b_{12}} \left\{ PJ_l \left(\frac{\pi B \rho'}{b_{12}} \sqrt{1-P^2} \right) I_{s-1} \left(\frac{\pi B P \rho'}{b_{12}} \right) - \sqrt{1-P^2} J_{l-1} \left(\frac{\pi B \rho'}{b_{12}} \sqrt{1-P^2} \right) I_s \left(\frac{\pi B P \rho'}{b_{12}} \right) \right\} \right. \\ & \left. + (l-s) \epsilon_2 J_l \left(\frac{\pi B \rho'}{b_{12}} \sqrt{1-P^2} \right) I_s \left(\frac{\pi B P \rho'}{b_{12}} \right) \right] \quad (112a) \end{aligned}$$

$$G_{2s}(\rho', \frac{\partial \rho'}{\partial \phi'}) = i^s \epsilon_2 J_l \left(\frac{\pi B \rho'}{b_{12}} \sqrt{1-P^2} \right) I_s \left(\frac{\pi B P \rho'}{b_{12}} \right) \frac{\partial \rho'}{\partial \phi'} / \rho' \quad (112b)$$

$$\begin{aligned} \bar{H}_{2s}(\rho') = & i^{-s+1} \left[\epsilon_2 \frac{2B\rho'}{b_{12}} \left\{ PJ_l \left(\frac{\pi B \rho'}{b_{12}} \sqrt{1-P^2} \right) K_{s-1} \left(\frac{\pi B P \rho'}{b_{12}} \right) + \sqrt{1-P^2} J_{l-1} \left(\frac{\pi B \rho'}{b_{12}} \sqrt{1-P^2} \right) K_s \left(\frac{\pi B P \rho'}{b_{12}} \right) \right\} \right. \\ & \left. - (l-s) \epsilon_2 \frac{2}{\pi} J_l \left(\frac{\pi B \rho'}{b_{12}} \sqrt{1-P^2} \right) K_s \left(\frac{\pi B P \rho'}{b_{12}} \right) \right] \quad (112c) \end{aligned}$$

$$\bar{G}_{2s}(\rho', \frac{\partial \rho'}{\partial \phi'}) = -i^{-s+1} \left[\epsilon_2 \frac{2}{\pi} J_l \left(\frac{\pi B \rho'}{b_{12}} \sqrt{1-P^2} \right) K_s \left(\frac{\pi B P \rho'}{b_{12}} \right) \frac{\partial \rho'}{\partial \phi'} / \rho' \right] \quad (112d)$$

Of course, the P_{ls} matrix elements are not to be confused with the propagation constant, P^2 .

We define

$$\bar{A}_s = i^s A_s \quad (113a)$$

$$\bar{C}_s = -i^s C_s \quad (113b)$$

This is done in order to incorporate the factors of i^s (which, s being the column index, cannot be cancelled across rows of the matrix) which appear in Eqns. (111) and (112) into the coefficients. The final matrix equation is

$$\begin{pmatrix} M & N \\ P & Q \end{pmatrix} \begin{pmatrix} \bar{A} \\ \bar{C} \end{pmatrix} = 0 \quad (114)$$

where (M), (N), (P), and (Q) now stand for real factors appearing in Eqns. (110). The submatrices in the upper two quadrants consist of line integrals about the 2-3 boundary; those in the lower half depend only on the 1-2 boundary. The solution of the corresponding determinantal equation yields the propagation constant and, ultimately, the coefficient vectors (\bar{A}) and (\bar{C}). These vectors are entirely real, since the matrix is real. The field expansion, of course, contains terms like $(A_s J_s(\gamma_2 \rho) + C_s H_s(\gamma_2 \rho)) \cos(s\phi)$. Since $\gamma_2 \rho$ is pure imaginary, it is convenient to change the Bessel and Hankel functions to Modified Bessel functions of the first and second kind, respectively (as in Eqns. (29) and (62)). In the end the useful form of the field expansion works out to be

$$\Phi(\rho) = \sum_{s=0}^{\infty} (-1)^s \left\{ \bar{A}_s I_s\left(\frac{\pi B P \rho}{b_{12}}\right) + \frac{2}{\pi} \bar{C}_s K_s\left(\frac{\pi B P \rho}{b_{12}}\right) \right\} \cos s\phi \quad (115)$$

4.3.3 Sine Solutions

If the sine solutions are sought, the coefficients are

$$S_{20} = \sum_{s=0}^{\infty} \left\{ B_s M_{es} + D_s N_{es} \right\} = 0 \quad (116a)$$

$$S_{42} = \sum_{s=0}^{\infty} \left\{ B_s P_{es} + D_s Q_{es} \right\} = 0 \quad (116b)$$

The matrix elements are defined differently from Eqns. (110), with

$$M_{ls} = \int_{L_{23}} d\phi' \left\{ F_{ls}(\rho') \sin l\phi' \sin s\phi' - E_{ls}(\rho', \frac{\partial \rho'}{\partial \phi'}) [s \sin l\phi' \cos s\phi' - l \cos l\phi' \sin s\phi'] \right\} \quad (117a)$$

$$N_{ls} = \int_{L_{23}} d\phi' \left\{ \bar{F}_{ls}(\rho') \sin l\phi' \sin s\phi' - \bar{E}_{ls}(\rho', \frac{\partial \rho'}{\partial \phi'}) [s \sin l\phi' \cos s\phi' - l \cos l\phi' \sin s\phi'] \right\} \quad (117b)$$

$$P_{ls} = \int_{L_{12}} d\phi' \left\{ H_{ls}(\rho') \sin l\phi' \sin s\phi' - G_{ls}(\rho', \frac{\partial \rho'}{\partial \phi'}) [s \sin l\phi' \cos s\phi' - l \cos l\phi' \sin s\phi'] \right\} \quad (117c)$$

$$Q_{ls} = \int_{L_{12}} d\phi' \left\{ \bar{H}_{ls}(\rho') \sin l\phi' \sin s\phi' - \bar{G}_{ls}(\rho', \frac{\partial \rho'}{\partial \phi'}) [s \sin l\phi' \cos s\phi' - l \cos l\phi' \sin s\phi'] \right\} \quad (117d)$$

but $F_{ls}, \dots, \bar{G}_{ls}$ are the same as in Eqns. (111) and (112). From this point the discussion leading to Eqns. (114) and (115) has an exact parallel, with (\bar{B}) and (\bar{D}) coefficient vectors replacing (\bar{A}) and (\bar{C}) , and, in Eqns. (115), $\sin(s\phi)$ replacing $\cos(s\phi)$.

4.3.4 Special Considerations

Consider only the cosine solutions for the moment. In the limiting case $n_2 = n_3$, the (M) and (N) submatrices are constant and zero, respectively. (This is easiest to show for a circular 2-3 boundary; clearly in this limit the shape of L_{23} is irrelevant.) Because of these facts submatrix (P) in Eqn. (114) does not have any influence and the coefficient vector (A) is zero. Thus the (Q) submatrix has sole responsibility for determining the modal properties. One can show that its determinant is the same as that of the (R) submatrix in Eqn. (22), which is the only relevant entity when cosine solutions of the simple two-medium waveguide are sought (e.g., Eqn. (32a)). We thus obtain the same propagation constants as we did for the single-guide problem discussed in Section II-2. The only difference is that we then obtained the interior field expansion when we solved for the coefficients; now, as a result of the (A) vector being zero, we obtain the exterior expansion. (Note that the (A) coefficients in this case correspond to the (C) coefficients in the earlier derivation.) In fact, the cladded guide formulation, taken in this limit, complements that for the single guide by providing this exterior expansion.

The limit $b_{23} \rightarrow \infty$ results, again, in a constant (M) and zero (N), with the same consequences: the single-guide eigenvalues are returned.

4.4 Equations for the Ring Guide

4.4.1 Parameterization

For the ring guide, where $n_2 > n_1 = n_3$, the guided modes are found within region 2. Thus the quantity $\gamma_2 \rho'$ which appears in the argument of the Bessel and Hankel functions of the field expansion, Eqn. (102), is real rather than imaginary. It is useful to express the Hankel function in terms of its definition as a linear combination of Bessel functions of the first and second kind, the latter also being known as the Neumann function and denoted by Y_s . The reason for this is the Hankel functions of real arguments are complex while Neumann functions are real. Eqn. (102) can thus be re-expressed (considering only cosine expansions) as

$$\Phi(\rho') = \sum_{s=0}^{\infty} \left\{ A_s J_s(\gamma_2 \rho') + C_s Y_s(\gamma_2 \rho') \right\} \cos s\phi' \quad (118)$$

where the coefficients serve the same purposes as before but are algebraically different.

Using this as a starting point, everything that was said about the cladded guide applies exactly to the ring guide, up to the point where the normalized parameters are introduced. Here we regard the 2-3 boundary as the significant one, as it is the outer edge of the guiding region. Consequently we write

$$B = \frac{k_1 b_{23}}{\pi} (n_2^2 - n_3^2)^{\frac{1}{2}} = \frac{k_1 b_{23} n_2}{\pi} \sqrt{\delta_{23}} \quad (119)$$

$$p^2 = \frac{k_3^2 - k_2^2}{k_1^2 - k_3^2} \quad (120)$$

and we end up with

$$\gamma_2 \rho' = \pi B \frac{\rho'}{b_{23}} (1 - p^2)^{\frac{1}{2}} \quad (121a)$$

$$\gamma_3 \rho' = i\pi B \frac{\rho'}{b_{23}} p \quad (121b)$$

The additional parameter needed to account for n_1 is δ_{21} , from which

$$\gamma_1 \rho' = \frac{\pi B \rho'}{b_{23}} \left(1 - p^2 - \frac{\delta_{21}}{\delta_{23}} \right)^{\frac{1}{2}} \quad (122)$$

but since our example only involves $n_1 = n_3$, this is equivalent to $\gamma_3 \rho'$ and $\gamma_1 \rho'$ is in fact given by Eqn. (121b).

4.4.2 Cosine Solutions

There are no differences whatsoever between the equations for the cladded guide and the ring guide except those due to the definitions of B and P^2 , and those resulting from the use of the Neumann function. The latter removes factors of i^s which appeared in the previous example. We define

$$F_{ls}(\rho') = i^{-(l+1)} \left[\epsilon_l \frac{2B\rho'}{b_{23}} \left\{ \sqrt{1-P^2} K_l\left(\frac{\pi B P \rho'}{b_{23}}\right) J_{s-1}\left(\frac{\pi B \rho'}{b_{23}} \sqrt{1-P^2}\right) + P J_s\left(\frac{\pi B \rho'}{b_{23}} \sqrt{1-P^2}\right) K_{l-1}\left(\frac{\pi B P \rho'}{b_{23}}\right) \right\} \right. \\ \left. + (l-s) \epsilon_l \frac{2}{\pi} K_l\left(\frac{\pi B P \rho'}{b_{23}}\right) J_s\left(\frac{\pi B \rho'}{b_{23}} \sqrt{1-P^2}\right) \right] \quad (123a)$$

$$E_{ls}\left(\rho', \frac{\partial \rho'}{\partial \phi'}\right) = i^{-(l+1)} \epsilon_l \frac{2}{\pi} K_l\left(\frac{\pi B P \rho'}{b_{23}}\right) J_s\left(\frac{\pi B \rho'}{b_{23}} \sqrt{1-P^2}\right) \frac{\partial \rho'}{\partial \phi'} / \rho' \quad (123b)$$

$$\bar{F}_{ls}(\rho') = i^{-(l+1)} \left[\epsilon_l \frac{2B\rho'}{b_{23}} \left\{ \sqrt{1-P^2} K_l\left(\frac{\pi B P \rho'}{b_{23}}\right) Y_{s-1}\left(\frac{\pi B \rho'}{b_{23}} \sqrt{1-P^2}\right) + P K_{l-1}\left(\frac{\pi B P \rho'}{b_{23}}\right) Y_s\left(\frac{\pi B \rho'}{b_{23}} \sqrt{1-P^2}\right) \right\} \right. \\ \left. + (l-s) \epsilon_l \frac{2}{\pi} K_l\left(\frac{\pi B P \rho'}{b_{23}}\right) Y_s\left(\frac{\pi B \rho'}{b_{23}} \sqrt{1-P^2}\right) \right] \quad (123c)$$

$$\bar{E}_{ls}\left(\rho', \frac{\partial \rho'}{\partial \phi'}\right) = i^{-(l+1)} \epsilon_l \frac{2}{\pi} K_l\left(\frac{\pi B P \rho'}{b_{23}}\right) Y_s\left(\frac{\pi B \rho'}{b_{23}} \sqrt{1-P^2}\right) \frac{\partial \rho'}{\partial \phi'} / \rho' \quad (123d)$$

$$H_{2s}(\rho') = i^2 \left[\epsilon_2 \frac{\pi B \rho'}{b_{23}} \left\{ \sqrt{1-\rho'^2} I_2 \left(\frac{\pi B \rho'}{b_{23}} \right) J_{s-1} \left(\frac{\pi B \rho'}{b_{23}} \sqrt{1-\rho'^2} \right) - \rho' I_{2-1} \left(\frac{\pi B \rho'}{b_{23}} \right) J_s \left(\frac{\pi B \rho'}{b_{23}} \sqrt{1-\rho'^2} \right) \right\} \right. \\ \left. + (l-s) \epsilon_2 I_2 \left(\frac{\pi B \rho'}{b_{23}} \right) J_s \left(\frac{\pi B \rho'}{b_{23}} \sqrt{1-\rho'^2} \right) \right] \quad (124a)$$

$$G_{2s}(\rho', \frac{\partial \rho'}{\partial \phi'}) = i^2 \epsilon_2 I_2 \left(\frac{\pi B \rho'}{b_{23}} \right) J_s \left(\frac{\pi B \rho'}{b_{23}} \sqrt{1-\rho'^2} \right) \frac{\partial \rho'}{\partial \phi'} / \rho' \quad (124b)$$

$$\bar{H}_{2s}(\rho') = i^2 \left[\epsilon_2 \frac{\pi B \rho'}{b_{23}} \left\{ \sqrt{1-\rho'^2} I_2 \left(\frac{\pi B \rho'}{b_{23}} \right) Y_{s-1} \left(\frac{\pi B \rho'}{b_{23}} \sqrt{1-\rho'^2} \right) - \rho' I_{2-1} \left(\frac{\pi B \rho'}{b_{23}} \right) Y_s \left(\frac{\pi B \rho'}{b_{23}} \sqrt{1-\rho'^2} \right) \right\} \right. \\ \left. + (l-s) \epsilon_2 I_2 \left(\frac{\pi B \rho'}{b_{23}} \right) Y_s \left(\frac{\pi B \rho'}{b_{23}} \sqrt{1-\rho'^2} \right) \right] \quad (124c)$$

$$\bar{G}_{2s}(\rho', \frac{\partial \rho'}{\partial \phi'}) = i^2 \epsilon_2 I_2 \left(\frac{\pi B \rho'}{b_{23}} \right) Y_s \left(\frac{\pi B \rho'}{b_{23}} \sqrt{1-\rho'^2} \right) \frac{\partial \rho'}{\partial \phi'} / \rho' \quad (124d)$$

Then the matrix elements appearing in the final equation for the cosine solution are those given in Eqns. (110) using these definitions for $F_{ls}, \dots, \bar{G}_{ls}$. There is no need to redefine the coefficients of Eqn. (118) and the result is

$$\begin{pmatrix} M & N \\ P & Q \end{pmatrix} \begin{pmatrix} A \\ C \end{pmatrix} = 0 \quad (125)$$

4.4.3 Sine Solutions

To obtain a final equation for the sine modes (replace A_s, C_s , and $\cos(s\phi)$ with B_s, D_s , and $\sin(s\phi)$ in Eqn. (118)) we simply use Eqns. (123) and (124) in Eqns. (117). The result is

$$\begin{pmatrix} M & N \\ P & Q \end{pmatrix} \begin{pmatrix} B \\ D \end{pmatrix} = 0 \quad (126)$$

4.4.4 Special Cases

The limiting cases for the ring guide do not teach us anything beyond what those of the cladded guide did. Taking $L_{12} \rightarrow 0$ yields the single-guide results much as the limit $L_{23} \rightarrow \infty$ did for the cladded guide. The only difference is that the lower submatrices become zero (P) and constant (Q) rather than the upper ones, as a consequence of the L_{12} boundary being pushed to an extreme. Letting $n_1 \rightarrow n_2$ (using Eqn. (122) rather than (121b) for $\gamma_1 \rho'$) also yields the isolated-guide equations. In both cases the coefficients multiplying the Neumann functions in the field expansion vanish.

5. A Variational Approach to Composite Systems

5.1 Introduction

The problem of two or more coupled waveguides, which can usually be solved completely by use of the integral-equation technique, also yields to certain simpler, but approximate approaches. One of these is a variational calculation very much like that used to solve the helium-atom and hydrogen-molecule-ion problem in the '20s. The idea is that if the wavefunctions (modes) of the pieces of the composite system, viewed as separate entities, are known, then the corresponding function for the composite system can be constructed as a linear combination of these. The coefficients of the linear combination can be determined by minimizing the energy (propagation constant) with respect to the coefficients. The analogy with quantum mechanics works because the time-independent Schroedinger Equation for a particle in a potential field has the same form as the two-dimensional Helmholtz Equation which must be solved for the waveguide problem.

In this section we discuss two simple calculations which use the variational technique. The first is the problem of a concentric core-ring guide with circular symmetry (Fig. (31)) and the second is that of two identical adjacent circular guides. Both of these configurations can be solved by other methods which give results which are exact in principle (e.g., boundary-matching for the core-ring configuration) or at least very accurate <3,22>. The variational technique, however, provides insight which is often lacking in more computationally-intensive approaches. It is also very accurate for many situations. And it can be extended to more complicated systems (e.g., multiple-ring guides). It has proved very convenient for the study of tightly-bound modes in core-ring guides <4> and we have used it to arrive at quantitative estimates for evanescent field crosstalk for this configuration <4>.

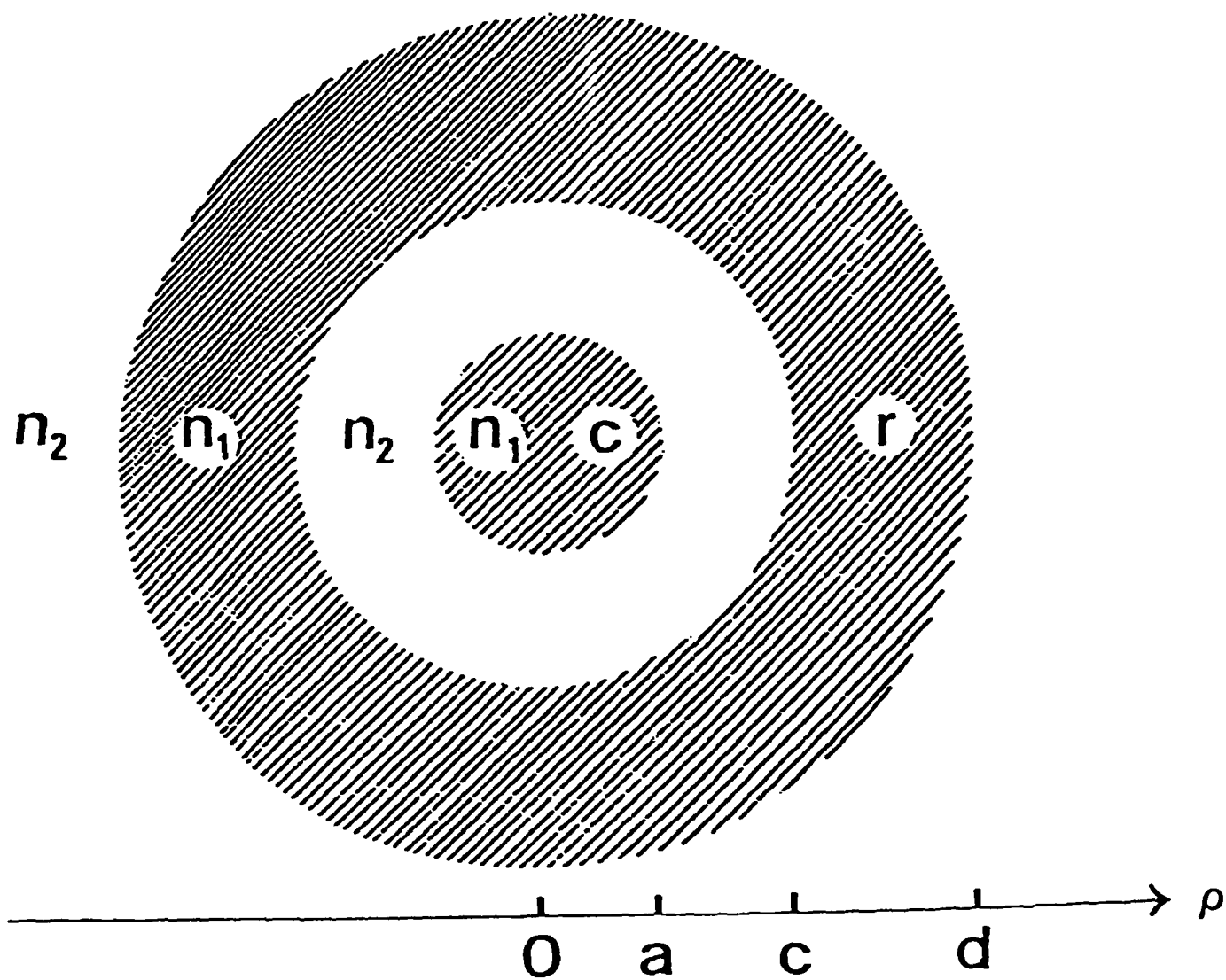


Fig. II.31 A simple multilayered guide with a core (c) of radius a and a ring (r) with radii c and d . The indices of refraction are also given in each region.

5.2 Basic Equations

To illustrate this approach, we suppose that the composite system is comprised of two distinct sections, A and B, whose normalized field functions, ϕ_A and ϕ_B , are known. For the moment we do not specify the geometrical arrangement, but we suppose for simplicity, that the index of refraction n_1 inside each core is the same, and that that of the cladding, n_2 is the same everywhere. In general, also, ϕ_A and ϕ_B may be sums of field functions of all modes of A and B.

The wave amplitude is written as

$$\Psi(\vec{\rho}, z) = \Phi(\vec{\rho}) e^{ik_g z} \quad (127)$$

where k_g is the propagation constant of the composite mode, to be found.

The equations which the composite field must satisfy are

$$(\vec{\nabla}^2 + k_1^2 - k_g^2) \Phi(\vec{\rho}) = (\vec{\nabla}^2 + \gamma_1^2) \Phi(\vec{\rho}) = 0 \quad \text{inside A, B} \quad (128a)$$

$$(\vec{\nabla}^2 + k_2^2 - k_g^2) \Phi(\vec{\rho}) = (\vec{\nabla}^2 + \gamma_2^2) \Phi(\vec{\rho}) = 0 \quad \text{in cladding} \quad (128b)$$

where $k_1 = k_0 n_1$, $k_2 = k_0 n_2$, and $k_0 = 2\pi/\lambda$, λ is the vacuum wavelength, and k_g is the propagation constant of the composite mode. Defining, as is conventional, the normalized frequency V and the normalized propagation constant P^2 by

$$V = k_0 d (n_1^2 - n_2^2)^{1/2} = k_0 d n_1 \sqrt{\delta} \quad (129)$$

$$P^2 = \frac{k_g^2 - k_2^2}{k_1^2 - k_2^2} \quad (130)$$

these equations become after some manipulation

$$[-\nabla^2 - (V/d)^2] \phi(\vec{\rho}) = -(V/d)^2 P^2 \phi(\vec{\rho}) \text{ inside A, B} \quad (131a)$$

$$-\nabla^2 \phi(\vec{\rho}) = -(V/d)^2 P^2 \phi(\vec{\rho}) \text{ in cladding} \quad (131b)$$

Here d is some characteristic dimension of the guide. From this, the analogy of the waveguide problem to that of a particle of energy $-(V/d)^2 P^2$ in a potential well of depth $-(V/d)^2$ is clear. P^2 and ϕ are, of course, to be determined.

We begin with known functions ϕ_A and ϕ_B , defined over all space, which satisfy equations exactly like Eqn. (131) with their own eigenvalues, P_A^2 and P_B^2 . For example, ϕ_A satisfies an equation like Eqn. (131a) in the core region A and one like Eqn. (131b) everywhere else. These we refer to as the "unperturbed" fields since, for example, ϕ_A would completely describe the modes of the system if region B were cladding rather than core—which is to say, if the second core region were absent. The equivalent potentials, $U_A(\vec{\rho})$ and $U_B(\vec{\rho})$ are equal to $-(V/d)^2$ in each core region, respectively, and zero elsewhere.

The composite field is taken to be

$$\phi(\vec{\rho}) = C_A \phi_A(\vec{\rho}) + C_B \phi_B(\vec{\rho}) = C[\phi_A(\vec{\rho}) + \Gamma \phi_B(\vec{\rho})] \quad (132)$$

where the constants are to be determined.

Consider the "energy" of the system under consideration:

$$E = \frac{\int \psi^*(\vec{\rho}) H(\vec{\rho}) \psi(\vec{\rho}) d\tau}{\int |\psi(\vec{\rho})|^2 d\tau} = \frac{\int \psi^*(\vec{\rho}) [-\nabla^2 + U_A(\vec{\rho}) + U_B(\vec{\rho})] \psi(\vec{\rho}) d\tau}{\int |\psi(\vec{\rho})|^2 d\tau} \quad (133)$$

This expression is exact if an exact wavefunction is used for $\phi(\vec{\rho})$, and is a variational or stationary one if an approximate wave function is used. In the latter case, Pauling and Wilson <28> show, for the quantum-mechanical particle, that E is an upper bound on the true energy of the

composite system provided that ϕ is a linear combination of the field functions which satisfy Schroedinger's Equation for the potentials U_A and U_B .

The best estimate to the true energy is then obtained by minimizing E with respect to the coefficients in the linear expansion.

For the waveguide problem, the coordinates τ over which the integration is performed are simply the cross-sectional area; and the composite-mode propagation constants, P^2 , are those values of $-(d/V)^2 E$ corresponding to the minimization condition

$$\frac{\partial E}{\partial C_i} = 0 \quad i = A, B \quad (134)$$

Briefly, to make use of this, one plugs Eqn. (132) into Eqn. (133) and evaluates most of the resulting terms by making use of the fact that ϕ_A and ϕ_B are normalized eigenfunctions of $(-\nabla^2 + U_A)$ and $(-\nabla^2 + U_B)$ respectively. This leaves certain integrals which must be evaluated for the particular geometry at hand, but which are independent of C_A and C_B . Eqn.

(133) then reads

$$E \sum_{ij} C_i C_j \Delta_{ij} = \sum_{ij} C_i C_j H_{ij} \quad (135)$$

where the sums extend over the two terms, A and B , and Δ_{ij} and H_{ij} are the "matrix elements" of 1 and $H(\vec{\rho})$ between ϕ_i and ϕ_j , obtained by integrating over the infinite cross section. Of course, $\Delta_{AA} = \Delta_{BB} = 1$ because the unperturbed wavefunctions are assumed to be normalized. ($H(\vec{\rho})$ is given in Eqn. (133)). Then, applying the minimization conditions, Eqn. (134), to Eqn. (135), one arrives at a 2×2 set of homogeneous linear equations in the coefficients which is, in matrix form,

$$\begin{pmatrix} H_{AA} - E & \frac{1}{2}(H_{AB} + H_{BA}) - E\Delta_{AB} \\ \frac{1}{2}(H_{AB} + H_{BA}) - E\Delta_{BA} & H_{BB} - E \end{pmatrix} \begin{pmatrix} C_A \\ C_B \end{pmatrix} = 0 \quad (136)$$

The matrix elements are given by

$$\left(\frac{d}{V}\right)^2 H_{AA} = J_A - P_A^2 = \int_B \phi_A^2 \rho d\rho d\theta - P_A^2 \quad (137a)$$

$$\left(\frac{d}{V}\right)^2 H_{BB} = J_B - P_B^2 = \int_A \phi_B^2 \rho d\rho d\theta - P_B^2 \quad (137b)$$

$$\left(\frac{d}{V}\right)^2 H_{AB} = K_A - \Delta P_B^2 = \int_A \phi_A \phi_B \rho d\rho d\theta - \Delta P_B^2 \quad (137c)$$

$$\left(\frac{d}{V}\right)^2 H_{BA} = K_B - \Delta P_A^2 = \int_B \phi_A \phi_B \rho d\rho d\theta - \Delta P_A^2 \quad (137d)$$

$$\text{where} \quad \Delta = \Delta_{AB} = \int_{\infty} \phi_A \phi_B \rho d\rho d\theta = \Delta_{BA} \quad (138)$$

$$\text{With} \quad \bar{H} = \frac{1}{2} (H_{AB} + H_{BA}), \quad (139)$$

the composite-system propagation constants can be calculated from

$$-P^2 \left(\frac{V}{d}\right)^2 = E = \frac{H_{AA} + H_{BB} - 2\bar{H}\Delta \pm [(H_{AA} - H_{BB})^2 + 4(\bar{H} - \Delta H_{AA})(\bar{H} - \Delta H_{BB})]^{1/2}}{2(1 - \Delta^2)} \quad (140)$$

As one would expect, there are two separate modes. Corresponding to each of these is a pair of coefficients, C_A and C_B , which can be determined from Eqn. (136) and the normalization condition on ϕ . We choose to use the second form in Eqn. (132), and arrive at

$$\Gamma = -\frac{H_{AA} - E}{\bar{H} - E\Delta} \quad (141a)$$

$$C = (1 + 2\Delta\Gamma + \Gamma^2)^{-1/2} \quad (141b)$$

In this manner, C becomes a normalization coefficient and Γ reflects the ratio of the importance of ϕ_B and ϕ_A in the composite field. This is convenient for examining the behavior of the composite modes as certain parameters are adjusted. Note that different values of C and Γ are derived for each of the two composite modes.

The foregoing is a straightforward application of simple ideas, and it applies to any geometric configuration in which two distinct regions guide energy. The extension to three or more such regions is a little more complicated, algebraically, but is quite easy conceptually. The difficulties obviously arise when evaluation of the integrals is done for specific configurations, and this is as true for two regions as for three or four.

5.3 Equations for the Core-Ring Guide

In this section we record the expressions which are needed to evaluate the solutions for the core-ring guide, which is depicted in Fig. (31). Insofar as regions A and B become the core and ring, respectively, we will denote various quantities by subscripts c and r rather than A and B. Among these are two shorthand expressions which make the equations slightly less cumbersome,

$$\alpha_i = V(1 - P_i^2) \quad i = c, r \quad (142a)$$

$$\beta_i = VP_i \quad i = c, r \quad (142b)$$

where P_c^2 and P_r^2 are the unperturbed-mode propagation constants.

Because of the weakly-guiding condition which we have assumed from the start, the field functions ϕ_c of the isolated circular core can be written, using either cosine or sine functions, as <29>

$$\phi_c(\hat{r}) = \begin{cases} A_\ell J_\ell(\alpha_c \rho/d) \begin{Bmatrix} \cos \\ \sin \end{Bmatrix} \ell \theta & 0 \leq \rho \leq a \\ A_\ell w_1 K_\ell(\beta_c \rho/d) \begin{Bmatrix} \cos \\ \sin \end{Bmatrix} \ell \theta & \rho \geq a \end{cases} \quad (143)$$

where θ is now the angular coordinate and d is the "characteristic distance" appearing in V (Eqn. (129)). The factor w_1 is

$$w_1 = J_\ell(\alpha_c a/d) / K_\ell(\beta_c a/d) \quad (144)$$

The normalizing coefficient is found by integrating ϕ_c over all space, and is given by

$$A_l^{-2} = -\frac{1}{2}\pi(1+\delta_{l0})a^2\frac{1}{p_c^2}J_{l-1}(\alpha_c a/d)J_{l+1}(\alpha_c a/d) \quad (145)$$

To derive this, it is necessary to make use of the eigenvalue equation which results from matching the field and its derivative across the boundary $\rho = a$:

$$\frac{\alpha_c J_{l\pm 1}(\alpha_c a/d)}{J_l(\alpha_c a/d)} = \frac{\pm \beta_c K_{l\pm 1}(\beta_c a/d)}{K_l(\beta_c a/d)} \quad (146)$$

In Eqn. (145), δ_{l0} is the Kronecker delta and p_c^2 is the normalized propagation constant of the core mode under consideration. A_l^2 is positive by virtue of the fact that the two Bessel functions always have opposite signs.

For the ring guide,

$$\phi_r(\vec{r}) = \begin{cases} \bar{A}_l w_3 I_l(\beta_r \rho/d) \left\{ \frac{\cos}{\sin} \right\} l\theta & \rho \leq c \\ \bar{A}_l [J_l(\alpha_r \rho/d) + w_2 Y_l(\alpha_r \rho/d)] \left\{ \frac{\cos}{\sin} \right\} l\theta & c \leq \rho \leq d \\ \bar{A}_l w_4 K_l(\beta_r \rho/d) \left\{ \frac{\cos}{\sin} \right\} l\theta & \rho \geq d \end{cases} \quad (147)$$

The constants w_2 , w_3 , and w_4 can be found in closed form in terms of the geometrical parameters and the ring-mode propagation constant, p_r^2 , by boundary-matching at $\rho = c$ and $\rho = d$. This is an algebraic mess and since it is always easier to compute these quantities numerically when they are

needed we have not gone through the manipulation required to obtain analytical expressions. The normalization constant is given by

$$\left[\bar{A}_e^2 (1 + \delta_{e0}) \pi \right]^{-1} = M_1 + M_2 + M_3 \quad (148)$$

where

$$M_1 = \frac{1}{2} w_3^2 c^2 \left\{ I_e^2(\beta_r c/d) - I_{e-1}(\beta_r c/d) I_{e+1}(\beta_r c/d) \right\} \quad (149a)$$

$$M_2 = \frac{1}{2} d^2 \left\{ J_e^2(d_r) - J_{e-1}(d_r) J_{e+1}(d_r) + w_a \left(2 J_e(d_r) Y_e(d_r) - J_{e-1}(d_r) Y_{e+1}(d_r) - J_{e+1}(d_r) Y_{e-1}(d_r) \right) + w_2^2 \left(Y_e^2(d_r) - Y_{e-1}(d_r) Y_{e+1}(d_r) \right) \right\} \quad (149b)$$

$$- \frac{1}{2} c^2 \left\{ J_e^2(d_r c/d) - J_{e-1}(d_r c/d) J_{e+1}(d_r c/d) + w_2 \left(2 J_e(d_r c/d) Y_e(d_r c/d) - J_{e-1}(d_r c/d) Y_{e+1}(d_r c/d) - J_{e+1}(d_r c/d) Y_{e-1}(d_r c/d) \right) + w_2^2 \left(Y_e^2(d_r c/d) - Y_{e-1}(d_r c/d) Y_{e+1}(d_r c/d) \right) \right\}$$

$$M_3 = - \frac{1}{2} w_4^2 d^2 \left\{ K_e(\beta_r) - K_{e-1}(\beta_r) K_{e+1}(\beta_r) \right\} \quad (149c)$$

Using these results, the evaluation of the integrals appearing in Eqns. (137) is a straightforward, albeit tedious, exercise. The results are

$$J_r = - \frac{\pi}{2} a^2 (1 + \delta_{e0}) w_3^2 \bar{A}_e^2 \left\{ I_e^2(\beta \frac{a}{d}) - I_{e-1}(\beta \frac{a}{d}) I_{e+1}(\beta \frac{a}{d}) \right\} \quad (150a)$$

$$J_e = - \frac{\pi}{2} d^2 (1 + \delta_{e0}) w_2^2 A_e^2 \left\{ K_e^2(\beta_c) - \left(\frac{c}{d} \right)^2 K_e^2(\beta_c \frac{c}{d}) - K_{e-1}(\beta_c) K_{e+1}(\beta_c) + \left(\frac{c}{d} \right)^2 K_{e-1}(\beta_c \frac{c}{d}) K_{e+1}(\beta_c \frac{c}{d}) \right\} \quad (150b)$$

$$K_c = -\pi(1+\delta_{20}) A_2 w_3 \bar{A}_2 \frac{ad}{(\alpha_c^2 + \beta_r^2)} \left\{ \beta_r J_2(\alpha_c \frac{a}{d}) I_{2-1}(\beta_r \frac{a}{d}) - \alpha_c J_{2-1}(\alpha_c \frac{a}{d}) I_2(\beta_r \frac{a}{d}) \right\} \quad (150c)$$

$$K_r = d^2 \pi (1+\delta_{20}) w_1 A_2 \frac{1}{(\alpha_r^2 + \beta_c^2)} \left\{ \bar{A}_2 \left[\beta_c J_2(\alpha_r) K_{2-1}(\beta_c) + \alpha_r J_{2-1}(\alpha_r) K_2(\beta_c) \right. \right. \\ \left. \left. - \frac{c}{d} (\beta_c J_2(\alpha_r \frac{c}{d}) K_{2-1}(\beta_c \frac{c}{d}) + \alpha_r J_{2-1}(\alpha_r \frac{c}{d}) K_2(\beta_c \frac{c}{d})) \right] \right. \\ \left. + w_2 \bar{A}_2 \left[\beta_c Y_2(\alpha_r) K_{2-1}(\beta_c) + \alpha_r Y_{2-1}(\alpha_r) K_2(\beta_c) \right. \right. \\ \left. \left. - \frac{c}{d} (\beta_c Y_2(\alpha_r \frac{c}{d}) K_{2-1}(\beta_c \frac{c}{d}) + \alpha_r Y_{2-1}(\alpha_r \frac{c}{d}) K_2(\beta_c \frac{c}{d})) \right] \right\} \quad (150d)$$

Also, Δ can be evaluated in closed form, as

$$\Delta = M'_1 + M'_2 + M'_3 + M'_4 \quad (151)$$

where

$$M'_1 = \pi(1+\delta_{20}) A_2 w_3 \bar{A}_2 \frac{ad}{(\alpha_c^2 + \beta_r^2)} \left\{ \beta_r J_2(\alpha_c \frac{a}{d}) I_{2-1}(\beta_r \frac{a}{d}) - \alpha_c J_{2-1}(\alpha_c \frac{a}{d}) I_2(\beta_r \frac{a}{d}) \right\} \quad (152a)$$

$$M'_2 = \frac{\pi}{4} (1+\delta_{20}) A_2 w_1 \bar{A}_2 \left\{ c^2 \left[2 I_2(\beta_r \frac{c}{d}) K_2(\beta_c \frac{c}{d}) + I_{2-1}(\beta_r \frac{c}{d}) K_{2-1}(\beta_c \frac{c}{d}) + I_{2-1}(\beta_r \frac{c}{d}) K_{2-1}(\beta_c \frac{c}{d}) \right] \right. \\ \left. - a^2 \left[2 I_2(\beta_r \frac{a}{d}) K_2(\beta_c \frac{a}{d}) + I_{2-1}(\beta_r \frac{a}{d}) K_{2-1}(\beta_c \frac{a}{d}) + I_{2-1}(\beta_r \frac{a}{d}) K_{2-1}(\beta_c \frac{a}{d}) \right] \right\} \quad (152b)$$

$$M'_3 = -\pi(1+\delta_{20}) w_1 A_2 \frac{d^2}{\alpha_r^2 + \beta_c^2} \left\{ \bar{A}_2 \left[\beta_c J_2(\alpha_r) K_{2-1}(\beta_c) + \alpha_r J_{2-1}(\alpha_r) K_2(\beta_c) - \frac{c}{d} (\beta_c J_2(\alpha_r \frac{c}{d}) K_{2-1}(\beta_c \frac{c}{d}) \right. \right. \\ \left. \left. + \alpha_r J_{2-1}(\alpha_r \frac{c}{d}) K_2(\beta_c \frac{c}{d})) \right] + \bar{A}_2 w_2 \left[\beta_c Y_2(\alpha_r) K_{2-1}(\beta_c) + \alpha_r Y_{2-1}(\alpha_r) K_2(\beta_c) \right. \right. \\ \left. \left. - \frac{c}{d} (\beta_c Y_2(\alpha_r \frac{c}{d}) K_{2-1}(\beta_c \frac{c}{d}) + \alpha_r Y_{2-1}(\alpha_r \frac{c}{d}) K_2(\beta_c \frac{c}{d})) \right] \right\} \quad (152c)$$

$$M'_4 = -\pi(1+\delta_{20}) A_2 w_1 \bar{A}_2 w_4 \frac{d^2}{(\beta_c^2 - \beta_r^2)} \left\{ \beta_r K_0(\beta_c) K_{2-1}(\beta_r) - \beta_c K_{2-1}(\beta_c) K_0(\beta_r) \right\} \quad (152d)$$

Using these results, Eqns. (140) and (141) can be evaluated. The modal properties of the composite system derive directly from these quantities. Section II-5.4 is devoted to a discussion of these results for the core-ring guide and their implications for the estimation of evanescent-field crosstalk.

Program VAR was used to obtain these results. The means of using this program is given in Section II-6.

5.4 Results for the Core-Ring Guide

5.4.1 Illustrative Results

We have obtained results for various geometrical configurations of the core-ring guide which consist mainly of plots of P^2 against V , and field-intensity distributions. Much can also be learned from the dependence of the parameter Γ on the physical parameters, so our discussion will focus on this quantity.

To check the validity of the variational results, we have compared them with those obtained from the boundary-matching solution. The most interesting modes of the multilayered guide are those constructed from a core-mode and a ring-mode having nearly the same propagation constant. Since arbitrary choices of all the waveguide parameters will lead to coincidences of this sort only by chance, we have studied the modal spectra as a function of the parameter V . As V is varied, there comes a point where P_C^2 and P_R^2 , the core- and ring-mode propagation constants, are the same. Initially, we confine our attention to results from such regions.

With this in mind, consider Fig. (32) which shows (dashed lines) the propagation constants for a pair of azimuthally-symmetric ($l=0$) composite modes of the guide of Fig. (31) for which a/d and c/d equal .2 and .8, respectively. The solid lines are the separate core- and ring-mode eigenvalues, and boundary-matching results for the guide as a whole are indicated by dotted lines. We see from that figure that the agreement of the approximate eigenvalues and the correct ones is excellent over most of the range considered. We have also found that at higher normalized frequencies where higher order modes are encountered, the agreement improves still further. Moreover, the eigenvalues of the composite system hardly differ from those of the unperturbed system (separate ring and core guides) except in the region near cutoff (where V is smallest). The expanded scale of the insert

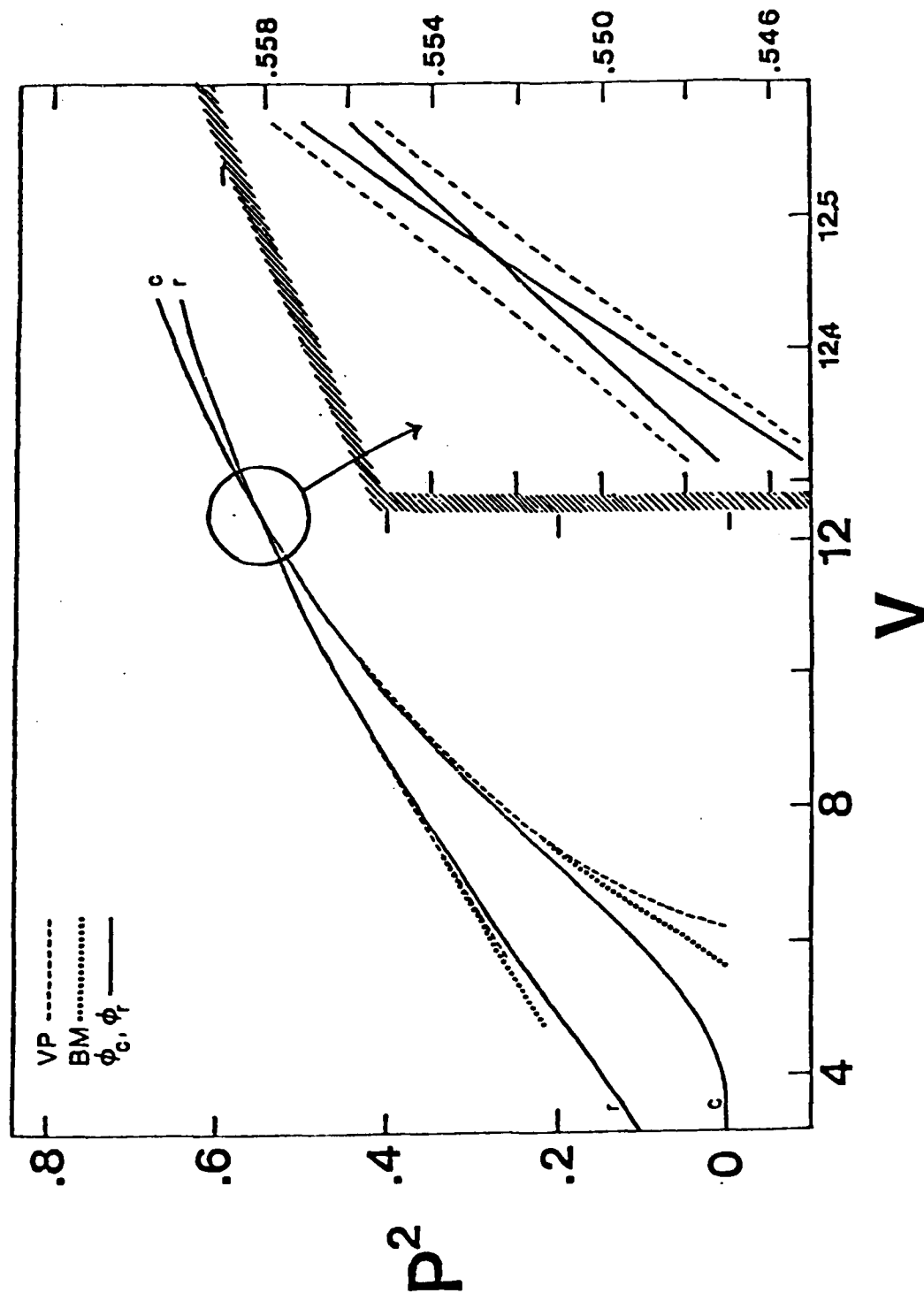


Fig. II.32 Propagation constants of the first pair of composite modes with $l=0$ when $a/d=.2$ and $c/d=.8$, as functions of V . Dashed lines denote the results of the variational calculation (VP); dotted lines are those of the boundary-matching procedure (BM); and the solid lines represent the propagation constants of the separate core and ring modes. In the insert, the scale is expanded for the region where the core- and ring-mode propagation constants are nearly equal.

V	P^2			P^2		
	Eigenvalues of first mode			Eigenvalues of second mode		
	BM	VP	CMT	BM	VP	CMT
9.5	.7738	.7733	.7741	.7015	.7009	.7019
9.0	.7595	.7590	.7604	.6750	.6742	.6760
8.5	.7445	.7439	.7461	.6441	.6431	.6461
8.0	.7286	.7279	.7314	.6076	.6063	.6113
7.5	.7118	.7110	.7163	.5647	.5629	.5711
7.0	.6938	.6929	.7008	.5138	.5110	.5246
6.5	.6744	.6733	.6849	.4530	.4484	.4708
6.0	.6532	.6517	.6685	.3799	.3719	.4090
5.5	.6297	.6274	.6509	.2921	.2764	.3384
5.0	.6030	.5995	.6312	.1874	.1540	.2590
4.75	.5880	.5836	.6200	.1289	.0777	.2161
4.5	.5717	.5663	.6074	.0687	-	.1715

Table II. 9. Eigenvalues, P^2 , of the first two azimuthally symmetric modes of the guide with $a/d=.4$, $c/d=.6$ as a function of V . Results were obtained using boundary-matching (BM), the variational calculation (VP) and coupled-mode theory (CMT).

shows that when the core and ring eigenvalues are the same, the composite modes are quite close to each other as well. In that region, the variational results are indistinguishable from the correct ones, even on the expanded scale. These general characteristics also hold true for other waveguide parameters, in particular for those for which the difference (c-a) is smaller and the overlap of the ring and core modes is therefore greater. It is only in the regions near cutoff, where the approximation represented by Eqn. (132) is most tenuous, that the variational results deviate from the exact ones. Even here, the eigenvalues and field amplitudes are incorrect by only a few percent. These points are illustrated in Table 9, which compares the values of p^2 for two composite modes as calculated by the boundary-matching method and the variational method. Anticipating the results of Section II-5.4.2, we also include in this table the eigenvalues obtained from coupled-mode theory.

The amplitude functions of the composite modes are of as much interest as the propagation constants. These wave functions are characterized by the values of Γ which determine the linear combinations in Eqn. (132). We can write an expression for Γ , which is

$$\Gamma = \frac{\gamma(1-\Delta^2) - \Delta \mp [1 + \gamma^2(1-\Delta^2)]^{\frac{1}{2}}}{1 \pm \Delta [1 + \gamma^2(1-\Delta^2)]^{\frac{1}{2}}} \quad (153a)$$

$$= \gamma \mp (1+\gamma^2)^{\frac{1}{2}} \quad (153b)$$

where γ is defined by

$$\gamma = \frac{P_c^2 - P_r^2}{K_c + K_r} \quad (154)$$

Recalling that the subscripts A and B have become c and r respectively, Eqn. (153a) can be derived from Eqn. (141a) by using Eqns. (137) and (140) and neglecting terms in $(J_c - J_r)$ and $\Delta(J_c + J_r)$ compared to $(K_c + K_r)$. J_c and J_r always have the same sign, as do K_c and K_r , and these approximations are good even in the single-mode region. Eqn. (153b) results when, in addition, Δ is neglected in comparison to unity.

Eqns. (153) are important because they illustrate the fact that the two possible values of Γ are functions of a parameter, γ , which changes dramatically in the regions where $P_c^2 - P_r^2$. When $\gamma=0$, $\Gamma=\pm 1$. When $|\gamma| \gg 1$, the values of $|\Gamma|$ are much larger and much smaller than unity, so the composite modes very nearly resemble the ring and core modes, respectively. In short, the regions which we have been discussing, which have substantial field amplitudes in both the core and the ring by virtue of $|\Gamma|$ being on the order of unity, extend only to those values of V for which $|P_c^2 - P_r^2| \lesssim |K_c + K_r|$; or, equivalently, those for which $|\Gamma| \lesssim 1$.

As an illustration of what has just been said, Table 10 lists values of Γ , as a function of V , for the first two $\ell=0$ modes of the guide with $a/d=.2$, $c/d=.8$. The exact values, computed from Eqn. (141a), differ only beyond the third significant figure from those which result from Eqn. (153a) for these cases. Even Eqn. (153b) is quite a good approximation over most of this range.

One can see from the results in Table 10 that the field amplitudes of the two composite modes parametrized by the two values of Γ are sensitive functions of V . For larger normalized frequencies, however, we encounter behavior which is much more sensitive still. In Fig. (33), we plot the field amplitudes of some composite modes which are constructed from $\ell=0$ modes other than the fundamental modes of the core- and ring-guide. The guide with $a/d=.3$, $c/d=.7$ has a region where $|\gamma| \lesssim 1$ when $V \sim 37.8$. In Fig. (33a), the separate core- and ring-mode amplitudes are drawn as a function of ρ . In Figs. (33b)-(33d), the two composite modes are given for $V=37.8091$, 37.8022 , and 37.8009 , respectively. One can see that in Fig. (33b), the two composite modes are predominantly core and ring modes. In fact, one mode has $\Gamma=-.11$, while the other has $\Gamma=9.3$. In Fig. (33c) there is a more substantial contribution from the ring and core respectively. In Fig. (33d), V was chosen so that the field functions are nearly $\phi_c \pm \phi_r$ (disregarding the normalization constant). It is clear that the modes in Figs. (33b) and (33d) are completely different from each other despite the minute change of only .0082 in V , a fractional difference of about .02%. It is also clear that it is not possible to specify V to such accuracy for any practical fiber, given the inevitable uncertainties in the core or ring radii, to say nothing of the uniform circularity of the cross-sections. This point must be considered in any discussion of realizable multimode multilayered guides.

5.4.2 Power Transfer by Composite Mode Pairs; Comparison with Coupled-Mode Theory

In the previous section we demonstrated that the variational calculation is accurate enough, in the interesting region where the core-mode and

V	$\frac{P^2 - P_T^2}{c}$	$ \gamma $	Γ	Γ
			Eqn. (140)	Eqn. (153b)
11.0	-.0215	3.1	- .171 6.859	- .158 6.325
12.0	-.0061	1.8	- .263 3.975	- .257 3.888
12.2	-.0034	1.2	- .370 2.772	- .365 2.738
12.3	-.0022	.80	- .485 2.094	- .481 2.078
12.4	-.0009	.36	- .703 1.432	- .700 1.428
12.478	.000045	.02	- 1.019 .981	- 1.019 .981
12.5	.0003	.13	- 1.136 .878	- 1.137 .879
12.6	.0015	.69	- 1.896 .522	- 1.906 .525
12.7	.0026	1.3	- 2.944 .333	- 2.972 .337
12.8	.0037	2.0	- 4.180 .233	- 4.236 .236
12.9	.0048	2.8	- 5.654 .171	- 5.751 .174
13.0	.0059	3.7	- 7.305 .131	- 7.459 .134
14.0	.0151	19.6	-37.25 .024	-39.25 .025

Table II.10. Exact (Eqn. (140)) and approximate (Eqn. (153b)) values of Γ for the modes depicted in Fig. 32, for a range of values of V. The isolated-guide propagation constant differences and parameter $|\gamma|$ (Eqn. (154)) are also given.

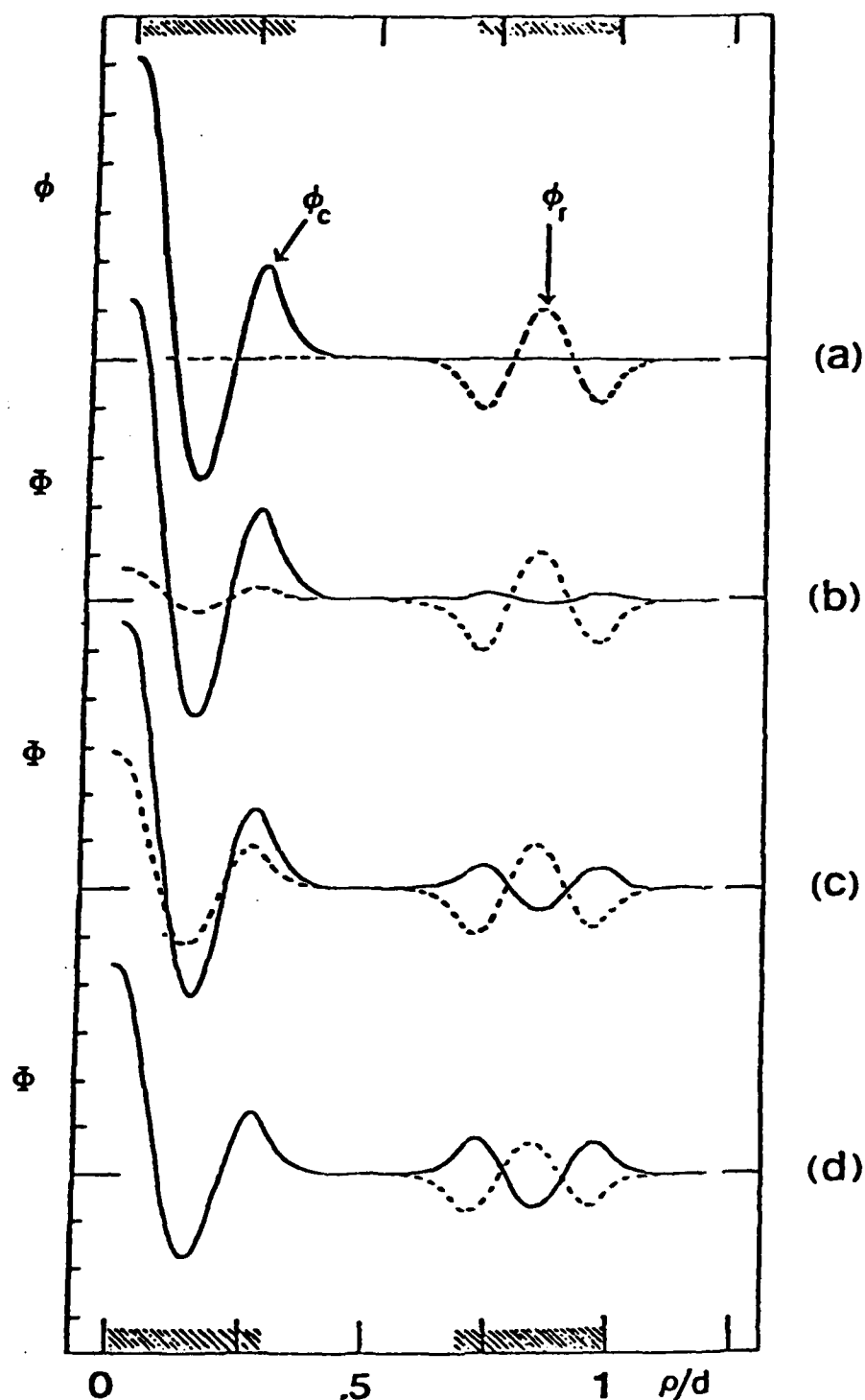


Fig. II.33 Field amplitudes for normalized composite modes with $l=0$ when $a/d=.3$, $c/d=.7$, as a function of radial distance. Hashed areas depict the radial extent of the core and ring.

- a. Separate core (ϕ_c) and ring (ϕ_r) modes when $V=37.8009$
- b. Composite modes from variational calculation with $V=37.8091$
- c. Same as b, for $V=37.8022$
- d. Same as b, for $V=37.8009$. Modes are nearly proportional to $\phi_c \pm \phi_r$.

ring-mode propagation constants cross, to construct the composite modes of the multilayered guide. To obtain the overall power distribution (and the power redistribution) one must invoke some initial condition on the field at $z=0$ and compute the interference of these modes as they propagate along the guide.

Before discussing power transfer for arbitrary core excitations, we introduce a simple model which embodies many of the features which appear in the more general calculation, and also facilitates the comparison with results from coupled-mode theory. It makes possible the calculation of power transfer when the guide is illuminated with an amplitude at $z=0$ which has the general features of interest: a substantial amplitude on the core and little on the ring. The limitation of the model lies in the very specificity of the excitation, which is taken to be some modal amplitude of the isolated core-guide.

Suppose then that a linear combination of the two composite modes propagates along the guide:

$$\psi^{\text{tot}}(\vec{\rho}, z) = D_1 \phi_1(\vec{\rho}) e^{ik_g^{(1)} z} + D_2 \phi_2(\vec{\rho}) e^{ik_g^{(2)} z} \quad (155)$$

The coefficients can be chosen so that at $z=0$ the combination reduces to $\phi_c(\vec{\rho})$:

$$\psi^{\text{tot}}(\vec{\rho}, 0) = \phi_c(\vec{\rho}) \quad (156)$$

It is easy to verify that the appropriate linear combination is:

$$\psi^{\text{tot}}(\vec{\rho}, z) = \frac{1}{\Gamma_2 - \Gamma_1} \left\{ \Gamma_2 (\phi_c + \Gamma_1 \phi_r) e^{ik_g^{(1)} z} - \Gamma_1 (\phi_c + \Gamma_2 \phi_r) e^{ik_g^{(2)} z} \right\} \quad (157)$$

The absolute magnitude squared yields the intensity, or power distribution, as a function of z (and β). One finds that

$$|\psi^{\text{tot}}|^2 = \phi_c^2 - \alpha \sin^2 \left(\frac{\pi z}{\lambda_B} \right) \left[\phi_c^2 + \Gamma_1 \Gamma_2 \phi_r^2 + (\Gamma_1 + \Gamma_2) \phi_c \phi_r \right] \quad (158)$$

where the positive constant, α , is

$$\alpha = - \frac{4\Gamma_1 \Gamma_2}{(\Gamma_2 - \Gamma_1)^2} \quad (159a)$$

$$= [1 + \gamma^2 / (1 - \gamma^2 \Delta^2)]^{-1} \quad (159b)$$

and the beat wavelength is

$$\lambda_B = 2\pi |k_g^{(1)} - k_g^{(2)}|^{-1} \quad (160)$$

Eqn. (159b) results from Eqn. (159a) by the use of Eqn. (153a).

In the special case in which the isolated-guide propagation constants are the same (resulting in $\Gamma_1 = +1$, $\Gamma_2 = -1$ or vice versa) the distribution is:

$$|\psi^{\text{tot}}|^2 = \phi_c^2 \cos^2 \left(\frac{\pi z}{\lambda_B} \right) + \phi_r^2 \sin^2 \left(\frac{\pi z}{\lambda_B} \right) \quad (161)$$

which clearly expresses the oscillation of power within the guide.

Eqns. (158) and (161) give the power distribution in the cross-section as a function of z . For this rather idealized situation, one can therefore calculate the power transfer between regions, or crosstalk, resulting from

the overlap of the evanescent fields of the isolated-guide modes. This term requires some definition. By core-to-ring crosstalk, we mean the amount of power contained in the ring when unit power is initially "put into" or "associated with" the core. (The complementary definition is appropriate for ring-to-core crosstalk, but we are not concerned with this at present.) The crosstalk is therefore determined by integrating the power distribution over the area of the ring.

Defined this way, the crosstalk is obviously a function of z . It is more useful to talk about the average crosstalk, obtained by averaging over z for an integral number of beatlengths $\langle 30 \rangle$, or an upper limit on the crosstalk, obtained by letting $z = \frac{1}{2} \lambda_B$. In either case it is necessary only to integrate Eqn. (158) over the ring, use the previously-established values of K_r and J_c , and evaluate the terms which result. In the case described by Eqn. (161), the upper limit on the crosstalk is ϕ_r^2 integrated over the ring, which is nearly unity. In the general case we can easily compute the crosstalk without approximations. However, in most circumstances the ϕ_r^2 term dominates, so a crude estimate for the upper limit can be obtained by simply calculating $|\Gamma_1 \Gamma_2 \alpha|$. Because $\Delta \gamma$ is almost always much less than unity, $\Gamma_1 \Gamma_2 \sim -1$ (as can be shown from Eqn. (153a)) and the upper limit on the power transfer is, very roughly,

$$X \sim \frac{1}{1+\gamma^2} \quad (162)$$

Thus, we confirm that the crosstalk is greatest in those regions discussed in Section II-5.4.1 where $|\gamma| \lesssim 1$, and much smaller otherwise.

At this point it is appropriate to make a comparison between the variational calculation and the results of coupled-mode theory (CMT). In fact, the former reduces to the latter when the integrals J_r , J_c , and Δ defined in Eqn. (137) are set equal to zero, as a consequence of the fact that $(K_r + K_c)$ is equivalent to the coupling constant of CMT $\langle 30 \rangle$. In Table 9, the eigenvalues of the first two azimuthally symmetric modes of a system with $a/d = .4$ and $c/d = .6$, obtained by these two methods, are compared with those obtained by the boundary-matching technique. One can see that, for lower values of V for which both approximate methods are in error, the variational results are closer to the correct ones. For larger values of V , both methods are excellent approximations, becoming better as V increases. If one changes the geometrical configuration by increasing the gap between core and ring, and hence decreasing the overlap, the CMT eigenvalues improve somewhat.

V	ξ			ξ		
	$a/d = .3$		$c/d = .7$	$a/d = .4$		$c/d = .6$
	VP	BM	CMT	VP	BM	CMT
4.5	-	-	-	-	1.99	2.29
4.75	-	-	-	1.98	2.18	2.48
5	2.56	3.03	3.43	2.24	2.41	2.69
6	4.85	5.02	5.31	3.57	3.66	3.85
7	8.73	8.80	9.00	4.45	5.56	5.68
8	15.95	15.98	16.12	8.22	8.26	8.33
9	27.84	27.83	27.95	11.80	11.83	11.85
10	35.74	35.72	35.77	15.89	15.91	15.90
12	30.331	30.333	30.331	23.10	23.12	23.08
14	27.169	27.168	27.169	27.64	27.66	27.63

Table II.11. Normalized beat length, ξ , obtained from boundary-matching (BM), the variational calculation (VP) and coupled-mode theory (CMT), for azimuthally-symmetric modes of guides with $a/d=.3$, $c/d=.7$ and $a/d=.4$, $c/d=.6$.

In Table 11, we present a comparison of the normalized beatlengths, ξ , obtained by the different methods. ξ is defined by

$$\xi = \frac{1}{2} \delta n_1 \frac{\lambda_B}{\lambda} \quad (163)$$

where δ can be found from Eqn. (129). λ_B is obtained in terms of the composite-mode normalized propagation constants, P_1^2 and P_2^2 , by using Eqn. (130) for the two values of k_g^2 , expanding the square root and neglecting terms in δ^2 (which is small because of the weakly-guiding assumption). One thus obtains

$$\xi = \frac{1}{|P_1^2 - P_2^2|} \quad (164)$$

Use of this normalized parameter obviates the need to specify n_1 , n_2 , and λ individually.

For all of the configurations we have studied, the variational calculation provides an approximation to the boundary-matching results which is better than, or at least as good as, the results from CMT. This holds true whether one measures the agreement by the eigenvalues, the field amplitudes, or the power contained in the different regions. Of course, both methods are quite accurate most of the time. The configuration used in Table 9 was chosen to emphasize the discrepancies between all three methods. For most modes not in the cutoff region, both approximate methods will give results for the eigenvalues which are correct to four significant figures or better, and field amplitudes which are within .5% of the actual values.

5.4.3 Power Transfer with Several Modes

In the previous section we discussed core-to-ring crosstalk in the limited context of just two interfering modes and the rather specific excitation given by Eqn. (156). In this section we relax these conditions. The principal result will turn out to be that for many situations the crosstalk is predominantly due to the interference between the two composite guided modes which are nearest cutoff. This fact greatly simplifies the task of estimating core-to-ring crosstalk due to evanescent-field coupling.

We will write the initial excitation as a sum of all the guided modes, evaluated at $z=0$. Without the radiation modes, these do not comprise a complete set, so the assumed initial excitation is only approximately reproduced. (With eight or more guided modes, however, quite reasonable representations of some trial excitations were obtained.) Also, by assuming an ideal guide, we neglect the effects of mode-conversion as well as all other contributions to the crosstalk resulting from processes (e.g., scattering) other than evanescent-field coupling.

We proceed by analogy to the previous section, Eqns. (155) - (158). The total field is written as a sum over all, rather than just two, guided modes.

$$\psi^{\text{tot}}(\vec{\rho}, z) = \sum_q D_q \phi_q(\vec{\rho}) e^{ik_g^{(q)} z} \quad (165)$$

The right-hand side of Eqn. (156) is replaced by an arbitrary initial condition, $\phi_0(\vec{\rho})$. The q th amplitude is, because of the orthonormality of the guided modes,

$$D_q = \int \phi_q(\vec{\rho}) \phi_0(\vec{\rho}) \rho d\rho d\theta \quad (166)$$

with ϕ_q being a composite mode of the form given by Eqn. (132). The power distribution is obtained by taking the square magnitude of Eqn. (165).

As before, the power transferred between core and ring results from interference between pairs of composite modes. This can be visualized by simply isolating pairs of terms in the series of Eqn. (165). One obtains, in the power distribution, terms like $D_q^2 \phi_q^2$ as well as cross-terms containing $\cos(2\pi z/\lambda_B)$, where λ_B is the beatlength for different modes, q and q' . With the inclusion of many such pairs, the z -dependence of the power distribution, and hence the crosstalk, becomes very complicated. If, however, we are satisfied with an upper limit on the evanescent-field crosstalk, we may calculate the "worst case" by replacing $\cos(2\pi z/\lambda_B)$ with unity everywhere. Then for all values of z , the power in the ring must be less than the resulting integral, X :

$$X = \sum_q \left\{ D_q^2 \int \phi_q^2 \rho d\rho d\theta + \sum_{q' \neq q} |D_q D_{q'}| \left| \int \phi_q \phi_{q'} \rho d\rho d\theta \right| \right\} \quad (167)$$

A useful and interesting example is an initial excitation consisting of a uniform circular spot of radius a' centered on the axis;

$$\phi_0 = \begin{cases} (\sqrt{\pi}a')^{-1} & \rho \leq a' \\ 0 & \rho > a' \end{cases} \quad (168)$$

This choice eliminates from Eqn. (165) all modes with $l \neq 0$. We assume $a' \leq a$, so the coefficients D_q can be evaluated analytically from Eqn. (166):

$$D_q = (2\sqrt{\pi}) C_q \left[A_0 \frac{1}{\alpha_c} J_1(\alpha_c \frac{a'}{d}) + \Gamma_q \bar{A}_0 w_0 \frac{1}{\beta_r} I_1(\beta_r \frac{a'}{d}) \right] \quad (169)$$

where A_0 and \bar{A}_0 are given by Eqns. (146) and (148) for $l=0$, α_c and β_r are given by Eqns. (142) and C_q and Γ_q are related as in Eqn. (141b).

Then X can be computed from Eqn. (167). We present the results as \bar{X} in units of decibels:

$$\bar{X} = 10 \log X \quad (170)$$

Typical results are given in Fig. (34) where \bar{X} is plotted against V for the guide with $a/d=.3$ and $c/d=.7$. The two curves represent two different spot sizes: $a'/d=.05$ and $a'/d=.30$.

In the region $35 < V < 44$, eight guided modes contribute to the sum. In the region $45 < V < 55$, ten such modes are included. The extra two modes which cut off at $V \sim 45$ account for the discontinuities in the solid curves at that frequency. The dashed lines represent the values obtained for \bar{X} when these two additional modes are not counted, and the magnitude of the gaps between the dotted and solid lines (15 dB or more) indicates that the total evanescent field crosstalk (the solid lines) is dominated by the contributions of these two modes. It is also true that in most of the region $35 < V < 44$, \bar{X} is dominated by the two composite modes nearest to cutoff: if the other six were not even considered, the curves would shift by a few dB at most.

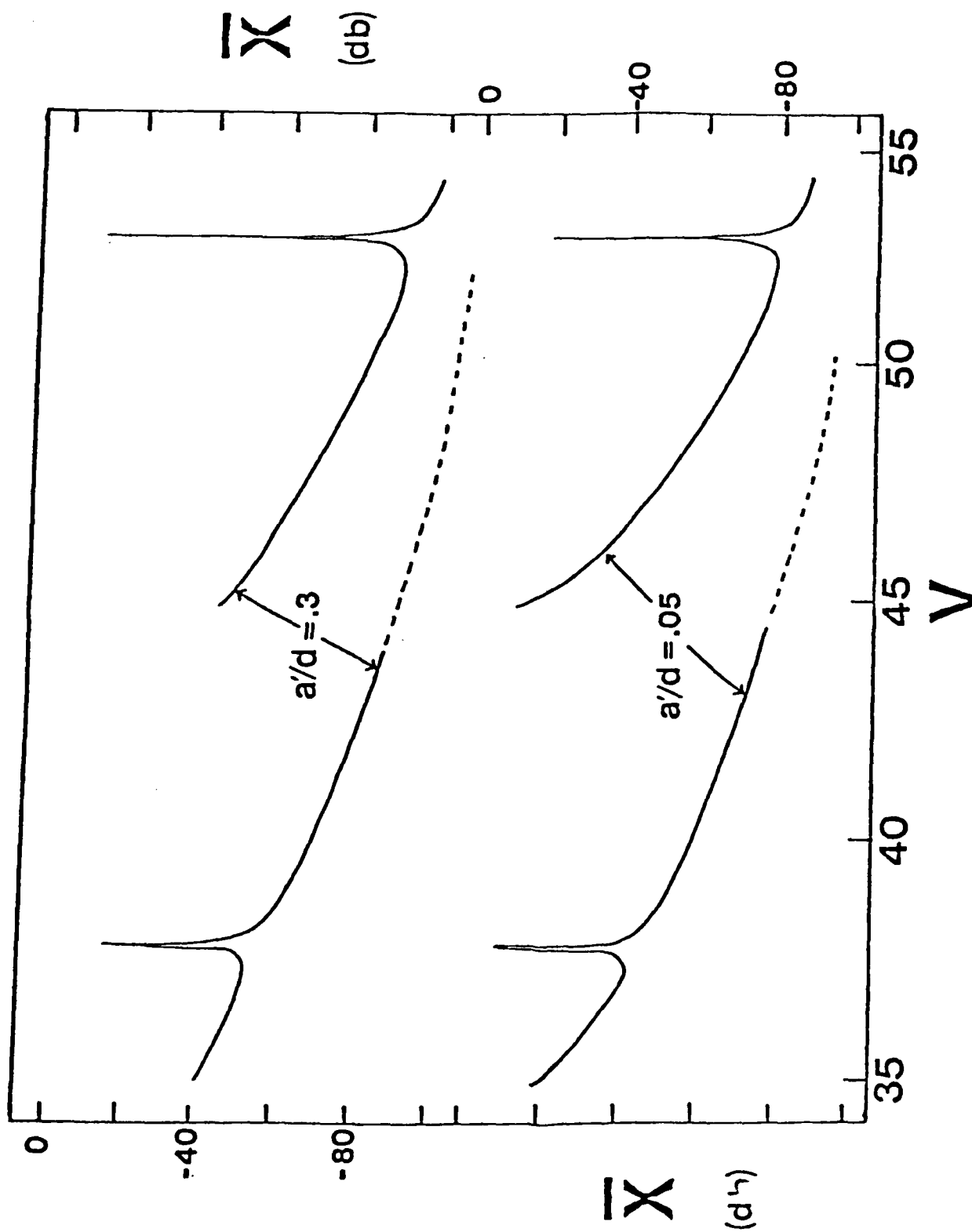


Fig. II.34 Upper bound, \bar{X} , on the crosstalk due to evanescent-field coupling, as a function of V for the guide with $a/d = .3$, $c/d = .7$ and a uniform spot excitation of radius a' at $z = 0$. Except for the sharp peaks, crosstalk is predominantly due to the two modes nearest cutoff.

- a. large spot: $a'/d = .3$
- b. small spot: $a'/d = .05$

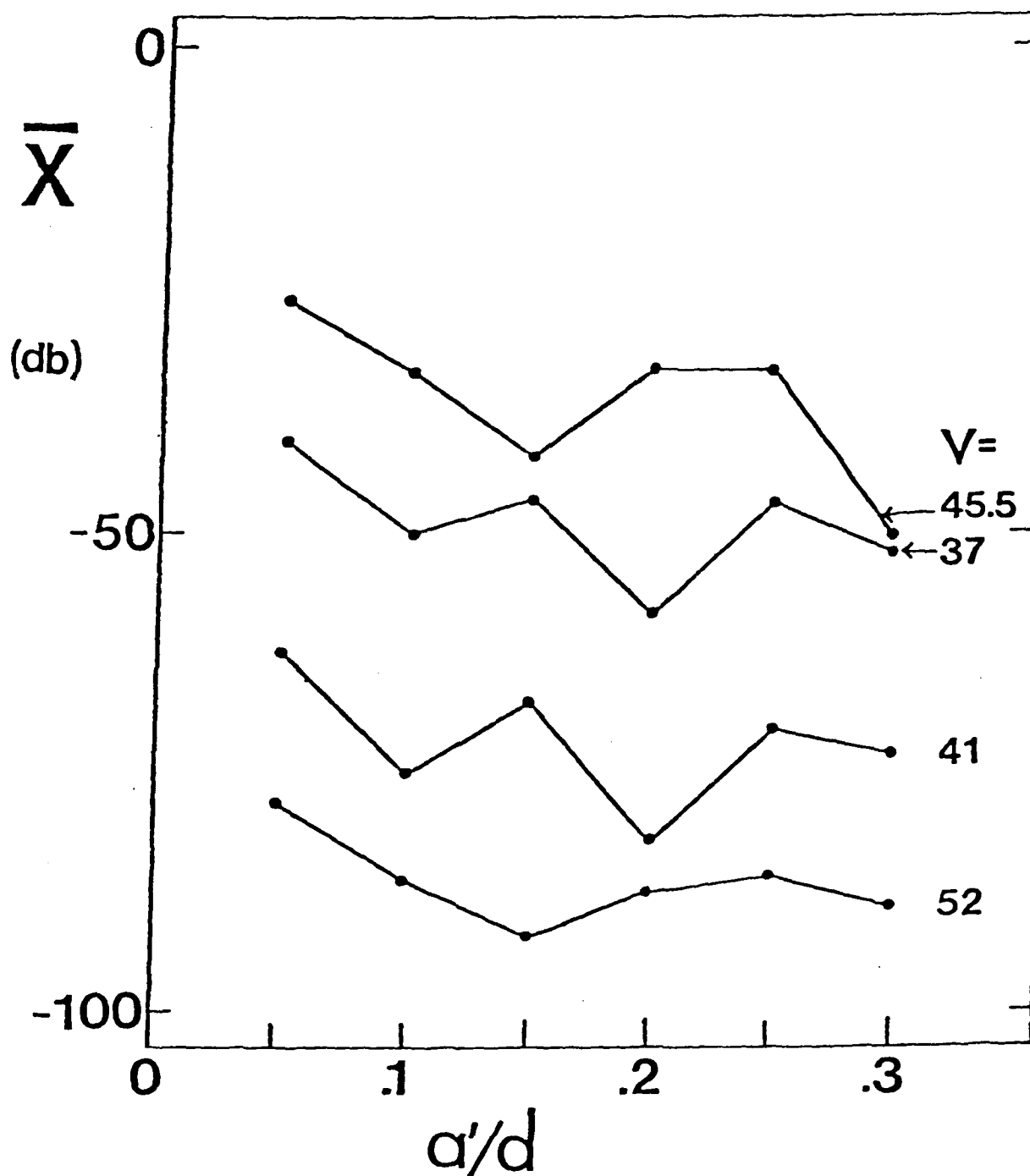


Fig. 11.35 Upper bound, \bar{X} , on the crosstalk due to evanescent-field coupling, as a function of the size a' , of the uniform spot excitation. Guide dimensions are $a/d=.3$, $c/d=.7$.

The only regions where these generalizations are not valid are in the two "resonance" regions ($V \sim 37.8$: see Fig. (33) and Sec. II-5.4.1; and $V \sim 52.6$) where the propagation constants of an isolated-core mode and an isolated-ring mode are nearly the same. The composite modes responsible for these resonances happen not to be the ones nearest cutoff. However, even though their evanescent fields do not overlap as strongly as those of the modes nearer cutoff, the near coincidence in their propagation constants allows a large power transfer to take place. The narrowness of these two peaks is another illustration of the sensitivity of the modal properties of the guide to the physical parameters contained in the normalized frequency. The fact that these resonance peaks fall short of 0 dB is due to the failure of either amplitude, D_q , to approach unity for these spot excitations.

It seems clear, intuitively, that the crosstalk estimate, \bar{X} , should be sensitive to the spot size. This is confirmed in Fig. (35), where \bar{X} is plotted against spot size for several values of V for the guide with $a/d=.3$, $c/d=.7$.

Two points about the numerical values of \bar{X} need to be stressed. First, even neglecting the resonance regions, there is a very strong V -dependence in the crosstalk, with variations over many decades. Not surprisingly, then, the crosstalk is very sensitive to how near the highest-order modes are to cutoff. For a given geometrical configuration, once one has calculated the isolated-guide modes of the core and ring—whose eigenvalues are very close to those of the composite modes—the regions of high or low crosstalk can be identified from the plot of these eigenvalues versus V . That is, high crosstalk occurs when two modes are close to cutoff, or when the isolated-guide eigenvalues coincide. Because of the great variations in \bar{X} , these regions can be determined simply by inspection.

The second point is that the crosstalk parameter, \bar{X} , is extremely low—in the range -60 to -80 dB—over a large portion of the curves of Fig. (34). For $V > 55$, there are regions where it goes even lower still. Even though these numerical values are estimates rather than exact results, one may be confident that the orders of magnitude for the evanescent-field crosstalk are correct, at least as an upper bound. Although there may be errors in the coefficients, D_q , as a result of neglecting the radiation modes, it is unlikely that these will be order-of-magnitude errors. Also, mode conversion may take place, with power transferred into nonazimuthally symmetric guided modes which have not been considered. In order to increase the overall crosstalk, however, the power would have to be scattered from lower-order $l=0$ modes to those few modes which might be nearer cutoff than the highest-order $l=0$ mode. If such preferential scattering into a new mode should occur quite strongly, one would expect a large increase in \bar{X} .

only if the new mode were much closer to cutoff or if (fortuitously) it were resonance with another composite mode with the same azimuthal symmetry.

These results have been presented to indicate what factors may influence crosstalk caused by evanescent-field coupling. In practical guides, this effect may be masked by crosstalk from competing mechanisms. Nonetheless, it is useful to have established an upper limit for it, and to indicate the kind of configurations for which it may contribute importantly to the total power transfer.

As we have mentioned, the sharp peaks in power transfer in the resonance regions are due to the near-coincidence of P_c^2 and P_r^2 . In realizable guides, the parameters determining these quantities cannot be expected to remain perfectly uniform over great distances. By introducing a model in which the propagation constants vary slightly with z , Arnaud <31> shows (for adjacent fibers) that a significant reduction in crosstalk can result. The same argument, applied to the problem at hand, suggests that the peaks in Fig. (34) could be severely diminished.

5.5 Adjacent Coupled Guides

We have applied the formulation introduced in Section II-5.2 to another composite system, consisting of adjacent identical circular waveguides. Insofar as accurate solutions for this problem have already been attained using the integral-equation technique (with program IDGS), the variational calculation was only carried far enough to demonstrate its viability.

Because of the symmetry of this configuration, the two unperturbed-mode field functions are the same, as are the eigenvalues. Rather than calling the latter P_A^2 and P_B^2 , we denote them by the single value P_0^2 . The integrals J_A and J_B in Eqns. (137) are also the same, as are K_A and K_B (and we drop the subscripts).

As a result, Eqns. (140) and (141) simplify considerably. It is easily shown that the two values of Γ are +1 and -1, corresponding to symmetric and antisymmetric modes respectively. The composite modes are

$$E_s = \frac{1}{\sqrt{2(1+\Delta)}} (\phi_A + \phi_B) \quad (171a)$$

$$E_a = \frac{1}{\sqrt{2(1-\Delta)}} (\phi_A - \phi_B) \quad (171b)$$

and the corresponding eigenvalues are

$$P_S^2 = P_0^2 - \frac{J+K}{1+\Delta} \quad (172a)$$

$$P_A^2 = P_0^2 - \frac{J-K}{1-\Delta}, \quad (172b)$$

which correlates with the results of Section II-3.3.4.2 when one determines that K and J are both negative, and $|K|$ is much greater than $|J|$. That is, the propagation constant for the symmetric mode lies above that of the unperturbed modes, while the antisymmetric one lies below. One can also see from Eqns. (172) that the variational calculation predicts an asymmetric splitting, which we observed earlier (e.g., Fig. (16)).

The comparison with coupled-mode theory (CMT), which predicts a symmetric splitting, is easily accomplished if we observe that the integral K in Eqns. (137) is proportional to the coupling constant C_{pp} which is defined in Eqn. (19) of Reference 20. In fact, the CMT result for the splitting between the symmetric and antisymmetric modes, and consequently for the beat-length, is reproduced if J and Δ are set equal to zero in Eqns. (172) and the normalized propagation constants are converted to $k_g^{(S)}$ and $k_g^{(A)}$. We thus are led to the conclusion that while CMT and this variational calculation are both approximate methods, the latter embodies features which make it more accurate. This conclusion is reinforced by recalling some of the discussion in Section II-3.5.2, in which we observed that the main weakness in the linear-array calculation of Meltz and Snitzer <23> was the failure of CMT (their starting point) to predict the asymmetric splitting in the two-guide case.

For the record, we record the values of J and K which we used to calculate the approximate composite modes. They are

$$K = -A_L^2 (-1)^L \pi \frac{J_L^2(\alpha)}{K_L^2(\beta)} \left[K_{L,2}(\beta \frac{d}{a}) + K_{2L}(\beta \frac{d}{a}) \right] \quad (173)$$

$$J = -A_L^2 V^2 \frac{\pi}{4} \frac{J_L^2(\alpha)}{K_L^2(\beta)} \sum_{k=0}^{\infty} \epsilon_k \left[K_{L,2}(\beta \frac{d}{a}) + K_{2L}(\beta \frac{d}{a}) \right]^2 \left[I_L^2(\beta) - I_{L-1}(\beta) I_{L+1}(\beta) \right] \quad (174)$$

where the Bessel function arguments α and β are the same as in Eqns. (142), V is defined in terms of the guide radius, a , the normalizing constant is

$$A_2^{-2} = -\frac{1}{2}\pi(1+\delta_{20})\alpha^2\frac{1}{p_0^2}J_{\ell-1}(\alpha)J_{\ell+1}(\alpha) \quad (175)$$

and d is the center-to-center separation of the guides. Since these integrals both require the integration of the external field representation of guide #2 over the area of guide #1, it is necessary to introduce basis-function transformations like those we used in the array problems (e.g., Eqn. (46)). This accounts for the presence, in Eqns. (173) and (174), of the Modified Bessel functions of the second kind with the arguments $\beta d/a$.

The full analytical evaluation of Δ is difficult, and was not deemed worth the effort for this example. An approximate result, involving the overlap integrated only over the areas of the two cores rather than all space, was used for such results as were obtained. In view of this approximation, however, and the scattered nature of the results, we choose to omit them from this report. The principal result we derive from this exercise is that the variational technique, like CMT, is a viable approximate approach to the coupled-guide problem.

6. Use of the Programs

6.1 General Comments

In this section we describe the means by which one may use the various FORTRAN IV programs relating to the modal properties of waveguides. That is, we describe the input parameters for each program and give the job control language required to run them on the CDC-6600 at AFGL, the machine on which they were developed. Many of the programs are quite similar in structure, a fact which is reflected in similar input and job-control requirements.

The program listings are given in Volume 2 of this report. The user may refer to comments found in the listings for supplemental information.

All of these programs require Bessel functions of one sort or another. To obtain them, we have selected a package of subroutines from the AMOSLIB library <26>. These subroutines were developed with the 60-bit CDC word in mind, and return values which are correct to at least twelve significant figures. Even with such great accuracy (which is unnecessary for our purposes; 5 or 6 figures is usually sufficient) they are faster than subroutines from other packages we have tried. They have been used in all programs except LIDGS, which has not been converted from the Scientific Subroutine Package (SSP) routines previously employed <27>.

6.2 Function

The purpose of all these programs is to solve for the modes of various guiding systems. The program output is therefore the values of the normalized propagation constants, P^2 , and the sets of coefficients which specify the field expansions. From this the power distributions can be obtained, as can the unnormalized propagation constants, k_g , and other quantities of interest.

Program TRUNCN solves for the modes of isolated two-medium step-index waveguides having reflection symmetry about the x- and y-axes.

Program IDGS solves for the modes of an array consisting of two identical guides having reflection symmetry about their common x-axis, and about their respective y-axes.

Program TWOGS solves for the modes of an array consisting of two guides of different sizes and shapes, having the same index of refraction, n_1 , reflection symmetry about their common x-axis, and reflection symmetry about their respective y-axes.

Program LIDGS solves for the modes of an array consisting of N identical equally-spaced guides oriented in a line, each with reflection symmetry about the common x-axis and about their respective y-axes.

Program COAX solves for the modes of the isolated cladded guide, assuming reflection symmetry about the x- and y-axes.

Program HICOAX solves for the modes of the isolated ring guide, assuming reflection symmetry about the x- and y-axes.

Program VAR solves for the modes of a four-region core-ring waveguide system with circular symmetry using a variational calculation. The index of refraction is assumed to be the same in the core and the ring.

6.3 Input Parameters for the Integral-Equation Technique Programs

6.3.1 Organization

Of the programs listed in the previous section, all but VAR perform calculations based on the integral-equation technique. As a result, many of the input parameters are similar or identical. The following discussion, which does not apply to VAR, identifies them and provides a brief description of them.

The input parameters are contained in a single data record which is part of the input stream. They can be loosely categorized either as program parameters (quantities which govern the numerical procedures utilized in the program) or as physical parameters (quantities needed to describe the physical configuration which is being considered). In each program the program parameters are read at the beginning of the code from the first data-card image in the data record. The physical parameters are read (at FORTRAN statement number 1) from the second card-image.

After these first two data cards are read, the problem specified by these parameters is solved. Control then returns to statement 1 and another

card-image containing physical parameters for another configuration is read. Each successive physical configuration is solved using the original program parameters.

When a blank card-image is encountered at statement 1, control skips to the end of the main program, where the previous results are tabulated. Then control returns to the original read statement at the beginning and the whole process repeats. A blank card at that point directs the program to cease execution. Thus, the programs can deal with any number of cases in one job. (Actually, only 20 separate configurations fit into the arrays reserved for tabulating results, so this limits the number of sets of physical parameters that can be treated before a new set of program parameters is read.) Note that the proper means of terminating execution is with two consecutive blank card-images in the data stream.

All the program parameters and physical parameters are input with formatted read statements.

6.3.2 Program Parameters

Table 12 lists the program parameters required for the six programs, and the format in which they are to be read.

NOT is the number of terms and equations taken before truncation of each submatrix. It is denoted by M in the text. The maximum values of NOT and the size of the determinant (using integer arithmetic) are given in Table 12. There is no default for NOT. Typical values range from 1 (circular cross-sections) to the maximum for isolated guide programs, and from 5 to the maximum for array programs.

NT2, which applies only to the array programs, is the number of terms in the sums over ℓ appearing in some matrix elements. It is denoted by M' in the text. (See the end of Section II-3.3.1.) Permissible values lie between NOT and 2*NOT. When all perimeters are circular, NOT should be chosen; otherwise NOT+4 is typical. Default value is NOT.

I (S in several programs) specifies the minimum accuracy, 10^{-I} , to within which each root is to be determined. The root-finding algorithm is good enough that the uncertainty which actually results (and which is printed) is often considerably less than this. Default for I is 3.

NP2 is the number of entries in the initial table of determinantal values. (See Section II-2.4.) Permissible values range between 2 and 50.

Default is 10. Larger values should be used if roots are likely to be closely-spaced, to prevent two or more roots from falling between consecutive table entries.

NOP is the number of points used to do numerical integrations. Maximum value is 200 points. The default value is 50, and this is generally sufficient unless very high accuracy is required. For cases in which all cross-sections are circular the numerical integrations can be done analytically. In such cases NOP can be set equal to 1, and the programs will compute the matrix elements properly.

IDIAG is a diagnosis code, used mostly for troubleshooting, which activates or inhibits the printing of quantities calculated at various stages of the computations. These quantities are different for different programs. Permissible values are 0 to 5. Program listings should be consulted for details.

NOG (LIDGS only) is the number of guides in the linear array. Permissible values are 2 through 6. There is no default.

K (LIDGS only) gives the accuracy, 10^{-K} , to which the Bessel functions are calculated in the SSP subroutines. Default value, which is usually sufficient, is 5.

6.3.3 Physical Parameters

Table 13 lists the physical parameters read at FORTRAN statement 1, and the required format, for each integral-equation technique program.

SC (integer) determines whether cosine (1) or sine (2) solutions are sought.

L (isolated-guide programs only) is the index of the first term in the field expansion to be used. For example, with NOT=3 and SC=1, the odd cosine expansion with indices 1, 3, and 5 will be obtained if L=1. If L=0 the even cosine expansion with indices 0, 2, and 4 will be obtained (unless the aspect ratio is unity; then the indices are 0, 4, and 8).

D (array programs only) is the center-to-center separation between adjacent guides, denoted by d in the text and given in units of b_1 . The smallest reasonable separation is the touching distance, which depends on the aspect ratio(s). This distance, the default, is given by $R1+SZ*R2$ in TWOGS and $2*R$ in IDGS and LIDGS. (See below.)

N (N1, N2) (real) is the superellipse index, \tilde{N} (\tilde{N}_1, \tilde{N}_2 for programs with two different cross-sections) appearing in Eqn. (31). See Section II-2.4

or Reference 2 for a discussion of useful values. Also see Table 14. Default values are unity, resulting in elliptical (or circular) cross-sections.

R (R1, R2) is the aspect ratio \tilde{R} (\tilde{R}_1, \tilde{R}_2 for programs with two different cross-sections) appearing in Eqn. (31). The distance from the origin to the edge along the x-axis is \tilde{R} , in units of the characteristic distance. Default values are unity.

SZ is the ratio of the "characteristic dimensions", b, for two dissimilar cross-sections. In TWOGS this is the quantity denoted by r_2 in Eqn. (59). Default is 1. In COAX it is the ratio of the outer semiminor axis (b_{23}) to the inner (b_{12}) and as such is always greater than unity. In COAX, default is 10 or some value smaller enough than 10 to prevent underflow in certain functions. In HICOAX, SZ is the ratio of the inner to the outer semiminor axis and is less than unity. Default is zero in HICOAX.

B is the normalized frequency and must be positive. Default is unity. Values of B greater than 15 or so may cause underflow or overflow problems, but this depends on the program and several other parameters (e.g., NOT).

PMAX, PMIN is the range of values of P^2 over which the initial table is computed. That is, values of the determinant are calculated at NP2 equally-spaced points between PMIN and PMAX. Default values are 1 and 0.

DST (array programs only) is a vector whose first element is D and which gives different interguide spacings. That is, if one wishes to solve several configurations which differ only in the spacing, one can put several values of d on a single card-image. This is done for the sake of program efficiency as well as convenience because during the initial table calculations those components of the matrix elements which do not depend on d are used for all cases. As a result, they are not recomputed as they are when a new card-image is read. If there are zeroes or blanks in one or more of these fields the program ignores them.

QQ (COAX only) is the ratio of the numerical apertures, and is equal to δ_{13}/δ_{12} (See Eqns. (104) and (107).) Default value is 40, which is appropriate for $n_3=1$ (air) if $n_1=1.475$ and $n_2=1.465$. QQ=1 implies $n_2=n_3$, or an infinite cladding.

6.4 Job Control Language

All of the programs described above require input data on TAPE5, which is equivalent to INPUT. A data record is therefore required in the input stream. Results are written to TAPE6, which is equivalent to OUTPUT.

Each of these programs resides on a file in UPDATE format. These files also contain most of the subroutines which are required for the respective programs. The exceptions are the Bessel function subroutines, which are stored on their own separate UPDATE file. (The exception to the exception is LIDGS, whose file contains its own Bessel function subroutines.) These files have been provided on magnetic tape to the technical personnel at RADC.

The format allowed by UPDATE, which is a CDC utility, is useful because it allows one to make changes in the program or in one or more of the subroutines without recompiling the rest. It does require, however, another record in the input stream. In the example given in Table 15 which is appropriate for TRUNCN, we assume that TRUNCN and its subroutines in UPDATE format reside on a mass-storage file called TRUN. Moreover, we assume that the entire contents of this file and also the contents of the file containing the AMOSLIB Bessel function routines have been compiled and submitted to the CDC utility EDITLIB, which creates a special binary or library image of all the routines. The files containing these libraries are assumed to be on mass storage, as TRUNLIB and BESSELFUNCT.

In Table 15 the record following the first end-of-record mark (7/8/9) directs UPDATE to pick the main program from the original file and write it to COMPILE. Program alterations could be specified in this record, if necessary. The record following the second 7/8/9 is the data record.

In the example given, three single-guide configurations are to be solved. The first is for the even cosine modes of a square guide ($\tilde{N}=30$, $\tilde{R}=1$) with propagation constants less than .5, for $B=2$. The second is for all the odd cosine modes of a square with $B=2$. The third is for all the sine modes of a 2:1 ellipse ($\tilde{N}=1$, $\tilde{R}=2$) with $B=2$. In each case a 4-term truncation is used, 4-place accuracy is demanded for each root, 10 initial table entries are specified, 50 integration points are used for each integral, and no special diagnostics are printed.

To run programs other than TRUNCN the UPDATE directive specifying the program name and the data record must be different. Also, of course, the correct permanent files must be attached. For LIDGS it is not necessary to use LIB1 because the necessary Bessel functions are all on the original program file.

In Table 16 a possible data record for IDGS is given. Four cases are solved. They all seek all the cosine modes of an array of two square guides, the center-to-center distances being 2, 2.25, 2.50, and 3. The first of these is the touching distance and therefore results in the modes of a 2:1 rectangle. (Note that one does not specify even or odd expansions for array programs.) The matrix is 5 by 5, and internal series are truncated at 9 terms. Some diagnostics are printed.

Memory requirements for each program in octal words are given in Table 12. The time requirements depend on the number of cases and the truncation order, but single cases can usually be run in a few seconds on the CDC-6600.

6.5 Program VAR

Program VAR solves for the modes of a four-region concentric core-ring waveguide system with circular symmetry, using a variational approach. The input parameters are L, A, C, B, PS1, PS2, and IDIAG, and are described in the following paragraphs. They are read at FORTRAN statement number 1. The format specification is (I5,2F5.2,F7.4,2F9.7,I5). One card-image specifies all the information needed to solve a single physical configuration. Up to 40 cases can be treated in one job. The record containing the data card(s) is part of the input stream. A blank card terminates program execution.

L, a non-negative integer, specifies the order of the unperturbed modes.

A (a in the text) is the radius of the core (see Fig. (31)). This is given as a fraction of the outer radius of the ring, d.

C (c in the text) is the inner radius of the ring, also given in units of d. Obviously $0 < A < C < 1$.

B is the normalized frequency, equal to V/π .

PS1, PS2 are the normalized propagation constants, P_c^2 and P_r^2 , of the two unperturbed modes which contribute to the composite modes being sought. They must be determined by some procedure such as boundary matching or by use of TRUNCN and HICOAX.

IDIAG is a diagnosis code which can take on the values 0, 1, or 2. It activates or inhibits the printing of various quantities which are calculated at different stages of execution.

Program VAR has been delivered in UPDATE format, so the procedures for using it are practically identical to those given in Section II-6.4. The Bessel functions are from AMOSLIB. In fact, Table 15 is a completely satisfactory example, except that permanent files containing the UPDATE source and EDITLIB binary versions of VAR (e.g., VAR and VARLIB) must be attached, the UPDATE directive is *COMPILE VAR, and the data record is different. Table 17 gives an appropriate data record for three configurations involving the unperturbed fundamental modes of the core and ring guides ($l=0$). In each case the core radius is .3 and the ring inner radius is .7. Separate values of B are selected in each case, and different intermediate quantities are printed in each case.

PROGRAM	PROGRAM PARAMETERS	FORMAT	MEMORY (OCTAL WORDS)	MAXIMUM NOT	MATRIX DIMENSION
TRUNCN	NOT, I, NP2, NOP, IDIAG	5I5	65,000	7	NOT
IDGS	NOT, NT2, I, NP2, NOP, IDIAG	6I5	110,000	10	NOT
TWOGS	NOT, NT2, I, NP2, NOP, IDIAG	6I5	110,000	10	2*NOT
LIDGS	NOG, NOT, NT2, K, I, NP2, NOP, IDIAG	8I5	105,000	10	NOG*NOT/2
COAX	NOT, I, NP2, NOP, IDIAG	5I5	75,000	12	2*NOT
HICOAX	NOT, I, NP2, NOP, IDIAG	5I5	75,000	12	2*NOT

Table II.12. Program Parameters and Other Information for the Integral-Equation Technique Programs. (See text.)

PROGRAM	PHYSICAL PARAMETERS	FORMAT
TRUNCN	SC, L, N, R, B, PMAX, PMIN	2I5, 5F5.2
IDGS	SC, D, N, R, B, PMAX, PMIN, (DST(J), J=2, /)	I5, 9F5.2
TWOGS	SC, D, N1, R1, N2, R2, SZ, B, PMAX, PMIN, (DST(J), J=2, 6)	I5, 14F5.2
LIDGS	SC, D, N, R, B, PMAX, PMIN, (DST(J), J=2, 4)	I5, 9F5.2
COAX	SC, L, N1, R1, N2, R2, SZ, B, PMAX, PMIN, QQ	2I5, 9F5.2
HICOAX	SC, L, N1, R1, N2, R2, SZ, B, PMAX, PMIN	2I5, 8F5.2

Table II.13. Physical Parameters for the Integral-Equation Technique Programs

	$\tilde{R} = 1$	$\tilde{R} \neq 1$
$\tilde{N} < .5$	Cusped	Cusped
$\tilde{N} = .5$	Square	Parallepiped
$.5 < \tilde{N} < 1$	Subcircle	Subellipse
$\tilde{N} = 1$	Circle	Ellipse
$\tilde{N} > 1$	Supercircle	Superellipse
$\tilde{N} = \infty$	Square	Rectangle

Table II.14. Cross-Sectional Shapes Resulting from Different Choices of the Superellipse Index, \tilde{N} , and the Aspect Ratio, \tilde{R} .

JOB01. 1234 USER
 ATTACH(OLDPL,TRUN,ID=USER,MR=1)
 UPDATE(P,C,D)
 FTN(I,SL,R=3)
 ATTACH(LIB1,BESSELFUNCT,ID=USER,MR=1)
 ATTACH(LIB2,TRUNLIB,ID=USER,MR=1)
 LIBRARY(LIB1,LIB2)
 LGO.
 7/8/9
 *COMPILE TRUNCN
 7/8/9

4	4	10	50		
1	0	30.0	1.00	2.00	0.50
1	1	30.0	1.00	2.00	
2	1	1.00	2.00	2.00	

6/7/8/9

Table II.15. JCL for Program TRUNCN

7/8/9

5	9	4	10	50	3				
1	2.00	30.0	1.00	1.50	1.00	0.00	2.25	2.50	3.00

7/8/9

Table II.16. A Data Record for IDGS

7/8/9

0	0.30	0.70	1.0000	.0273	.1959	0
0	0.30	0.70	1.5000	.1934	.3271	1
0	0.30	0.70	2.0000	.3774	.4384	2

7/8/9

Table II.17. A Data Record for VAR

7. REFERENCES

1. Eyges, L., Gianino, P., and Wintersteiner, P., "Modes of Dielectric Waveguides of Arbitrary Cross-Sectional Shape", J. Opt. Soc. Am. 69, 1226 (1979).
2. Eyges, L., Gianino, P., and Wintersteiner, P., "Modes of Dielectric Waveguides of Arbitrary Cross-Sectional Shape", RADC-TR-79-197 (June 1979).
3. Eyges, L., and Wintersteiner, P., "Modes of an Array of Dielectric Waveguides", J. Opt. Soc. Am. 71, 1351 (1981).
4. Eyges, L., and Wintersteiner, P., "Variational Approach to Modes and Crosstalk in Core-Ring Guides", J. Opt. Soc. Am. 72, 1597 (1982).
5. Gianino, P., Bendow, B., and Wintersteiner, P., "Propagation Characteristics of Irregularly Shaped Step-Index Fiberguides", in Physics of Fiber Optics (Advances in Ceramics, Vol. 2, B. Bendow and S. Mitra, eds.) American Ceramic Society, 1981, p. 330.
6. Abramowitz, M., and Stegun, I. A., eds., Handbook of Mathematical Functions, NBS Applied Mathematics Series, 55 (1964) p. 363.
7. Globe, D., "Weakly-Guiding Fibers", App. Opt. 10, 2252 (1971).
8. Allard, J., "Note on Squares and Cubes", Math. Mag. 37, 210 (1964).
9. Gardner, M., "Mathematical Games", Sci. Am. 213, 222 (1965).
10. Hildebrand, F. B., Introduction to Numerical Analysis, 2nd ed., McGraw-Hill, N.Y., (1974), p. 398.
11. Hildebrand, F. B., Introduction to Numerical Analysis, 2nd ed., McGraw-Hill, N.Y., (1974), p. 552.
12. Hornbeck, R. W., Numerical Methods, Quantum Publishers, N.Y., (1975), p. 65.
13. Muller, D. E., "A Method for Solving Algebraic Equations using an Automatic Computer", M.T.A.C. 10, 208 (1956).
14. Hildebrand, F. B., Introduction to Numerical Analysis, 2nd ed., McGraw-Hill, N.Y., (1974), p. 578.

7. REFERENCES (Continued)

15. Kunz, K. S., Numerical Analysis, McGraw-Hill, N.Y. (1957) p. 4.
16. Goell, J. E., "A Circular-Harmonic Computer Analysis of Rectangular Dielectric Waveguides", Bell Sys. Tech. J. 48, 2133 (1969).
17. Marcatili, E. A. J., "Dielectric Rectangular Waveguide and Directional Coupler for Integrated Optics", Bell Sys. Tech. J. 48, 2071 (1969).
18. Eyges, L., Appl. Opt. 17, 1673 (1978).
19. Yeh, C., "Modes in Weakly Guiding Elliptical Optical Fibres", J. Opt. Qu. Elect. 8, 43 (1976).
20. Snyder, A. W., "Coupled-mode Theory for Optical Fibers", J. Opt. Soc. Am. 62, 1267 (1972).
21. McIntyre, P. D., and Snyder, A. W., "Power Transfer Between Optical Fibers", J. Opt. Soc. Am. 63, 1518 (1973).
22. Wijngaard, W., "Guided Normal Modes of Two Parallel Circular Dielectric Rods", J. Opt. Soc. Am. 63, 944 (1973).
23. Meltz, G., and Snitzer, E., "Thermal and Dispersive Characteristics of Multicore Fibers", URSI Symposium on Electromagnetic Waves, Munich, Federal Republic of Germany, 1979.
24. Eyges, L., and Gianino, P. D., "Modes of Multilayered Guides", in Physics of Fiber Optics (Advances in Ceramics, Vol. 2, B. Bendow and S. Mitra, eds.) American Ceramic Society, 1981, p. 325.
25. Eyges, L., and Gianino, P., "Modes of Cladded Guides of Arbitrary Cross-Sectional Shape", J. Opt. Soc. Am. 72, 1606 (1982).
26. Amos, D. E. and Daniel, S. L., "AMOSLIB, A Special Function Library", Sandia Labs, SAND 77-1390 (1977).
27. IBM System 360 Scientific Subroutine Package, Publication No. H20-0205-3.
28. Pauling, L., and Wilson, E., Introduction to Quantum Mechanics, McGraw-Hill, New York (1935).
29. Snyder, A. W., "Asymptotic Expressions for Eigenfunctions and Eigenvalues of Dielectric or Optical Waveguides", IEEE Trans. MTI, 17, 1130 (1969).

7. REFERENCES (Continued)

30. Chan, C., and Steensma, P., "Crosstalk Analysis in Multiple-Layered Fibers", in Physics of Fiber Optics (Advances in Ceramics, Vol. 2; B. Bendow and S. Mitra, eds.) American Ceramic Soc., 1981, p. 227.
31. Arnaud, J. A., "Transverse Coupling in Fiber Optics, Part IV: Cross-talk", Bell Sys. Tech. Journal, 54, 1431, (1975).

III. QUANTITATIVE STUDY OF A MECHANISM FOR PRODUCING DIFFRACTION GRATINGS IN CRYSTALS EXHIBITING PHOTOREFRACTIVITY

1. Introduction

The following report summarizes the work which was done on the photorefractive effect problem during the summer of 1982. The first section outlines the physical problem in a qualitative manner. The second gives the mathematical formulation, while the third describes (briefly) the software, the implementation of the boundary conditions, and various procedures used in the program. The last section gives some of the results obtained. How to use program GRATING is described in the program listing; examples and listings have been furnished under separate cover.

The physical problem and the beginning of the mathematics involved is presented in Reference 1. An attempt has been made to avoid repeating contents of that report, except in a cursory manner when necessary.

The problem involves the "writing" of a permanent diffraction grating in an electro-optically active crystal by imposing a laser-beam interference pattern upon it. The grating can also be "erased" by imposing a constant illumination upon the crystal. We assume that the material under consideration has both occupied and unoccupied optical donor levels well-isolated within a forbidden gap. Electrons can be excited from occupied levels to the conduction band by the incident light. The conduction-band electrons can diffuse through the crystal, migrate under the influence of an electric field, and recombine with empty donor levels. The problem is one dimensional: no spatial variation occurs except in the z direction. The photovoltaic effect is not considered here.

A simple picture of the processes occurring is as follows. At time zero, when there are no conduction electrons, light with a certain spatial intensity pattern begins to shine on the crystal. This produces conduction electrons due to photoexcitation, with a greater density building up at places where the light is more intense. These electrons drift (under the influence of an applied field) or diffuse away, and also recombine with empty donor levels. Because the net effect of the drift is to remove electrons from the regions of higher density, recombination occurs preferentially at points of low light intensity. This upsets the initial charge neutrality of each local region, causing a net negative charge density in regions where recombination occurs faster than photoexcitation, and a net positive charge density in the other regions. The distribution of "space-charge" which is thus built up modifies the local electric field and the

resultant drift of the electrons. Eventually an equilibrium is attained, with a large z -dependent electric field existing inside the crystal. This slightly modifies the refractive index of the crystal, due to the electro-optic effect.

The stated problem is to evaluate the local electric field in the crystal as a function of space and time, so as to be able to determine the modification of the refractive index. This is to be done by setting up and solving the nonlinear differential equations for the conduction-electron density, and the occupied donor-level density. The solutions are to be determined numerically for various values of the physical parameters.

2. Formulation

2.1 Definitions of fields

$n(z,t)$	= number of conduction electrons per unit volume
$N_e(z,t)$	= number of occupied donor levels per unit volume
$N_+(z,t)$	= number of empty donor levels per unit volume
$\rho(z,t)$	= space-charge density
$E(z,t)$	= local electric field
$J(z,t)$	= local current density
$I(z)$	= light intensity pattern

2.2 Initial Conditions

$n(z,0)$	= 0	(no thermal excitation of conduction band)
$N_e(z,0)$	= N_{eo}	(independent of z)
$N_+(z,0)$	= N_{+o}	(independent of z)
$\rho(z,0)$	= 0	
$E(z,0)$	= E_{app}	= constant applied electric field
$J(z,0)$	= 0	

2.3 Basic Equations (see Reference 1; z and t -dependence are assumed for all fields)

$$N_e + N_+ = N_{e0} + N_{+0} \quad (\text{donor levels do not migrate}) \quad (1)$$

$$\rho = e(N_+ - N_{+0} - n) = e(N_{+\Delta} - n) \quad (\text{definition of space-charge}) \quad (2)$$

$$\epsilon \frac{\partial E}{\partial z} = 4\pi\rho \quad (\text{Gauss' law; } \epsilon = \text{dielectric constant}) \quad (3)$$

$$\frac{\partial n}{\partial t} = \frac{\partial N_+}{\partial t} + \frac{dJ}{dz} \frac{1}{e} \quad (\text{charge-continuity}) \quad (4)$$

$$J = +e\mu nE + eD \frac{\partial n}{\partial z} \quad (5)$$

$$\frac{\partial N_+}{\partial t} = - \frac{\partial N_e}{\partial t} = \gamma_I N_e - \gamma_r n \frac{N_+}{N_{+0}} \quad (6)$$

The last of these equations (6) represents changes in donor-level densities due to photoexcitation and recombination; $\gamma_I(z)$ and γ_r are the respective rates for these processes. The next-to-last equation (5) gives the current due to drift and diffusion. D is the diffusion constant and μ is the electron mobility, also a constant.

2.4 Differential Equations

Combining the basic equations leads to

$$\frac{\partial n}{\partial t} = \underbrace{D \frac{\partial^2 n}{\partial z^2}}_{\text{diffusion}} + \underbrace{\mu E \frac{\partial n}{\partial z} + \left(\frac{4\pi\mu e}{\epsilon} \right) (nN_{+\Delta} - n^2)}_{\text{drift}} + \underbrace{\gamma_I N_e}_{\text{photoexcitation}} - \underbrace{\gamma_r \left(\frac{1}{N_{+0}} \right) nN_+}_{\text{recombination}} \quad (7a)$$

$$\frac{\partial N_e}{\partial t} = - \gamma_I N_e + \gamma_r \left(\frac{1}{N_{+0}} \right) nN_+ \quad (7b)$$

The photoexcitation rate, $\gamma_I(z)$, is proportional to the light intensity. Assuming $I(z)$ is an interference pattern,

$$\gamma_I(z) = \langle \gamma_I \rangle \left(1 + M \cos k_g z \right) = \langle \gamma_I \rangle \bar{F}(z) \quad (8)$$

The photoexcitation process leaves its imprint on the final spatial distributions, so ultimately we will take $2\pi/k_g$ as "unit distance". Similarly, the dielectric relaxation time characterizes the duration of the process, so the inverse relaxation rate $(\gamma_{d1})^{-1}$ will eventually be taken as "unit time". (See Reference 1, and below.) Meanwhile it is necessary to eliminate N_+ in favor of N_e , and evaluate the electric field due to space-charge. The dependent variables are normalized by taking

$$u = \frac{n}{\langle n \rangle} \quad (9a)$$

$$v = \frac{N_{e0} - N_e}{\langle n \rangle} \quad (9b)$$

where $\langle n \rangle$ is defined in the list of quantities given below. Then the space-charge field at z can be found by integrating $\frac{\partial E}{\partial z}$, or ρ , from $-\infty$ to z . The result for the total field (t-dependence understood) is

$$E(z) = E_{app} + \frac{4\pi e \langle n \rangle}{\epsilon} X(z) = E_{app} + \frac{4\pi e \langle n \rangle}{\epsilon} \int_{-z_0}^z (v(z') - u(z')) dz' \quad (10)$$

where $-z_0$ is the left boundary. This makes the first equation into a non-linear integro-differential equation. To avoid the difficulties accompanying a complete treatment of the space-charge contribution to E , we will merely write it as X and evaluate it at each step based on information from the previous steps. This approximation will be discussed in III.3.5. The equations become

$$\frac{\partial u}{\partial t} = D \frac{\partial^2 u}{\partial z^2} + (E_{app} + \gamma_{d1} \bar{X}) \frac{\partial u}{\partial z} + \gamma_{d1} (uv - u^2) + \bar{F}(z) (\gamma_r - \langle \gamma_I \rangle v) - \gamma_r u (1 + R \frac{\langle \gamma_I \rangle}{\gamma_r} v) \quad (11a)$$

$$\frac{\partial v}{\partial t} = \bar{F}(z) (\gamma_r - \langle \gamma_I \rangle v) - \gamma_r u (1 + R \frac{\langle \gamma_I \rangle}{\gamma_r} v) \quad (11b)$$

$$\text{where } \gamma_{d1} = \frac{4\pi e \mu}{\epsilon} \langle n \rangle \quad (12a)$$

$$\langle n \rangle = \frac{\langle \gamma_I \rangle}{\gamma_r} N_{e0} \quad (12b)$$

$$R = \frac{N_{e0}}{N_{+0}} \quad (12c)$$

The mean excitation rate, $\langle \gamma_I \rangle$ can be written in terms of the mean intensity $\langle I \rangle$ plus the optical cross-section and wavelength, but for the purposes at hand it is sufficient to specify it independently (in units of γ_{di} , of course).

The same is true of the recombination rate γ_r . It is also convenient to specify E_{app} and D in terms of drift and diffusion distances, Λ_E and Λ_D respectively (defined below). Then, letting z and t go into $\frac{k_g z}{2\pi}$ and $\gamma_{di} t$,

and thereby scaling distance and time to the units given above, the final equations become

$$\frac{\partial u}{\partial t} = A^2 G_1 \frac{\partial^2 u}{\partial z^2} + (G_1 B + X(z)) \frac{\partial u}{\partial z} + uv - u^2 + F(z) \left[G_1 - G_2 v \right] - G_1 u \left[1 + R \frac{G_2}{G_1} v \right] \quad (13a)$$

$$\frac{\partial v}{\partial t} = F(z) \left[G_1 - G_2 v \right] - G_1 v \left[1 + R \frac{G_2}{G_1} v \right] \quad (13b)$$

where

$$G_1 = \frac{\gamma_r}{\gamma_{di}} \quad (14a)$$

$$G_2 = \frac{\langle \gamma_I \rangle}{\gamma_{di}} \quad (14b)$$

$$A = \frac{k_g \Lambda_D}{2\pi} \quad (14c)$$

$$B = \frac{k_g \Lambda_E}{2\pi} \quad (14d)$$

$$X(z) = \int_{-z_0}^z dz' (v(z') - u(z')) \quad (14e)$$

$$F(z) = 1 + M \cos 2\pi z \quad 0 \leq M \leq 1 \quad (14f)$$

The diffusion and drift distances have been introduced through the use of ⁽¹⁾

$$\gamma_r \Lambda_E = \mu E_{app} \quad (14g)$$

$$D = \Lambda_D^2 \gamma_r \quad (14h)$$

One can see that the coupled equations can be solved if the constants G_1 , G_2 , A , B , M , and R are specified, if the boundary conditions and initial conditions are given, and if adequate provisions are made for incorporating the space-charge contribution, $X(z)$. These six normalized input parameters are the only physical parameters the program will need for input, except for those defining the boundaries.

3. Software and Numerical Procedures

3.1 GRATING

The complete software package consists of program GRATING and associated subroutines which were written during the term of the contract, and packages PLOTN and PDECOL. PLOTN is a general-purpose line-printer plot subroutine written by ARCON personnel some time ago. PDECOL (described below) is a general-purpose partial-differential-equation package obtained from the International Mathematical and Statistical Library (IMSL). It consists of subroutine PDECOL and 18 other subprograms. PLOTN and PDECOL have been incorporated into the overall program structure with as few changes as possible. In fact, the only changes in the IMSL routines appear near line 825 of subroutine PDECOL and are surrounded by comment-cards consisting of "\$" symbols.

Instructions for the use of GRATING, PLOTN, and PDECOL are included in comments in the program listings. Listings and examples have been provided under separate cover.

3.2 PDECOL

The package PDECOL is being used to solve the coupled nonlinear equations. This package, written so as to take advantage of the 60-bit word-size in CDC computers, is described in Reference 2. The class of problems amenable to solution through its use are those with N coupled equations in

the form

$$\frac{\partial \vec{u}}{\partial t} = \vec{f}(t, z, \vec{u}, \vec{u}_z, \vec{u}_{zz}) \quad (15)$$

with boundary conditions which can be written as

$$\vec{b}(\vec{u}, \vec{u}_z) = \vec{Z}(t) \quad (16)$$

for each boundary. In these equations, \vec{u} stands for the dependent variables to be determined:

$$\vec{u} = (u_1, u_2, \dots, u_N) \quad (17)$$

\vec{u}_z stands for the space-derivative of each component of \vec{u} , and \vec{u}_{zz} is the second space derivative. Initial conditions are of course also required, and they must be consistent with the boundary conditions.

In the problem at hand, $N = 2$ and $\vec{u} = (u, v)$. The two equations at the end of the last section are clearly of the required form.

PDECOL is a package designed to take advantage of some very general and successful algorithms which have been developed to solve ordinary differential equations (ODEs), to solve the general class of partial differential equations (PDEs) described above. A very much-simplified description is as follows. The user defines a spatial discretization appropriate to his problem. Certain spline basis functions, with an order which the user may select, are used to approximate the dependent variables in each of these intervals, separately. That is, each component of \vec{u} is written as the product of certain coefficients, c , which depend only on time, and the known basis functions which depend only on z . These approximate solutions are required to satisfy the original differential equations at certain "collocation points". The result is a set of ODEs in the form

$$(A) \frac{d\vec{c}}{dt} = \vec{g}(t, \vec{c}) \quad (18)$$

The number of these equations is proportional to both N and the number of spatial intervals chosen. The coupled ODEs are solved by integrating in time, using well-established procedures. One thus obtains, for a single output time, a set of coefficients, c . These are used to evaluate the actual solutions, \vec{u} . One then advances the output time to a larger value and repeats the process as often as is desired. The end result is sets

of solution values (u, v , in our case) evaluated at whatever points, z , the user chooses, with each set corresponding to a user-selected instant in time. In the present case, it is necessary to utilize well-chosen sets of solution values at the end of each step (at least) in order to perform the integration for the space-charge field which is indicated in Eqn. (14e).

We refer to the user-selected times as "output times" to distinguish them from the "working times" selected by the package. Further discussion of these appears in III.3.7.

3.3 Boundary Conditions

In the present formulation of our problem, we assume a periodic illumination function $F(z)$ which is symmetric or antisymmetric about zero. The initial thought is therefore to impose periodic boundary conditions at the endpoints $(-z_0, z_0)$. These are four separate equations represented by

$$\vec{u}(-z_0) = \vec{u}(z_0) \quad (19a)$$

$$\vec{u}_z(-z_0) = \vec{u}_z(z_0) \quad (19b)$$

So long as z_0 is (at least) half integer and $F(z)$ has the form given in Eqn. (14f), such conditions will properly describe the physical situation. The asymmetry introduced by the applied field may cause physical distributions (e.g., ρ) to be shifted in phase with respect to the illumination. (See Fig. 1). However, for half-integer or integer values of z_0 , these distributions will still satisfy Eqns. (19). We note that closed circuit conditions prevail so that currents flowing out one end enter again at the opposite boundary.

Unfortunately the equations above do not fit the form demanded by PDECOL, Eqn. (16), since they combine the requirements at the left and right boundaries. There are no known solutions or constraints valid for all time at any point where the illumination varies with z , unless diffusion and drift are absent. Indeed, the whole objective is to obtain solutions resulting (primarily) from the combination of drift and a spatial variation in illumination. Therefore, in order to use this package, it is necessary to specify the problem a little differently. We may modify the illumination function so that it

hardly varies in the region adjacent to the two boundaries, as shown in Fig. 2 and in this equation:

$$F(z) = \begin{cases} 1 + M \cos (2\pi z + \phi) & |z| \leq z_B \\ 1 \pm M \exp (-\pi^3 |z - z_B|^2) & z_B \leq |z| \leq z_0 \end{cases} \quad (20)$$

In Eqn. (20), ϕ , z , and the signs in the lower expression must be chosen so that $F(z)$ is continuous and $F'(z)$ is zero at $\pm x_B$. ϕ may take on the values zero and $\pm \pi/2$. In the former case, the pattern is symmetrical about zero; in the latter, antisymmetrical. The argument of the exponential is such that the integral of $F(z)$ from z_B to ∞ equals the integral of a quarter-cycle of the sinusoidal portion of the curve.

With the use of this light-intensity pattern, it becomes logical to stipulate that Neumann conditions hold at the boundaries; that is, the space-derivatives of all the fields must be zero. This supposes that the boundary is "far enough" away from any region where spatial variations do exist for an equilibrium to be attained. To establish just how far is "far enough" it is necessary to ask what process could cause a gradient in the electron or donor-level densities in the first place. The photoexcitation and recombination processes depend on the populations themselves, but not on their gradients. (If gradients already exist, these processes may change the populations at rates which depend on z —for example, recombination occurs faster where n is greater—but if the illumination is constant they will not produce gradients by themselves.) On the other hand, diffusion and drift do have a directional preference. For example, if there is a high concentration of electrons at $z \leq z_B$, they will diffuse preferentially toward the right boundary. As they do some of them will recombine with empty donor levels. The resultant electron population will therefore decrease with increasing z . The diffusion distance Λ_D can be seen, from its definition, to incorporate the recombination rate. Only if the recombination time is small compared to the time required for electrons to migrate to the boundary will the effect of the higher concentration be dissipated. Therefore, if the diffusion distance is much less than $(z_0 - z_B)$, the gradients will be small at the boundaries. As similar considerations apply to electron drift under the influence of the electric field, the conditions

$$\Lambda_D \ll (z_0 - z_B) \quad (21a)$$

$$\Lambda_E \ll (z_0 - z_B) \quad (21b)$$

are sufficient to establish the validity of the boundary conditions at $\pm z_0$:

$$\frac{\partial u}{\partial z} \approx 0 \quad \frac{\partial v}{\partial z} \approx 0 \quad (22a)$$

$$(22b)$$

The preceding considerations suggest a different formulation of the boundary constraints. The existence of a nonzero net charge density, ρ , at any point in the crystal depends on the possibility of the migration of electrons from a region where the photoexcitation rate is higher to one where it is lower. Since the photoexcitation rate does not vary with z near the boundaries, it follows that $\rho \approx 0$ at the boundaries. This can be expressed as

$$u(z_0) - v(z_0) \approx 0 \quad (23a)$$

with a similar requirement at $-z_0$. In addition, however, we can specify that the gradient of either u or v be zero at $\pm z_0$, e.g.

$$\left. \frac{\partial u}{\partial z} \right|_{z_0} \approx 0 \quad (23b)$$

This (Eqns. 23) is the form in which we will write the boundary conditions. Referring to Eqn. (16), we find

$$b_1 = u - v \quad (24a)$$

$$b_2 = u_z \quad (24b)$$

and $\vec{z} = (0,0)$.

3.4 Initial Conditions

From the definitions of u and v , and the conditions listed in III.2.2, one can easily see that at the initial time, $t = 0$, the requirements

$$u(z,0) = 0 \quad (25a)$$

$$v(z,0) = 0 \quad (25b)$$

must be satisfied.

3.5 Evaluation of the Space-Charge Field

We have pointed out, in the discussion prior to Eqns. (11), that it is necessary to evaluate the space-charge field at the n^{th} step (corresponding to time t) based on information from previous steps. That is, $X(z,t)$ appearing in Eqns. (11a) and (13a) is the integral of $\rho(z,t)$, but ρ is known only at previous steps corresponding to earlier times. The manner in which values of $X(z,t)$ are selected is very important because these values affect the convergence of the PDE package results. In fact, poor estimates of $X(z,t)$ cause an accumulation of errors which either degrades the solutions directly or causes the time increment selection procedure to use inappropriate jumps. In either case, execution terminates with an error flag.

At the beginning of the n^{th} step, an array of "anticipated" values of $X(z,t)$ is used in Eqn. (13a). After the n^{th} step is complete, an array of "actual" values is determined by numerical integration of the newly-obtained $\rho(z,t)$. (The different elements of the array correspond to different values of z .)

The anticipated array at step n is obtained from the actual arrays at steps $n-1$, $n-2$, and $n-3$ by simple polynomial extrapolation. The results, as measured by the average absolute difference between the actual and anticipated values, are significantly better with quadratic extrapolation (three points) than with linear extrapolation (two points) and much better than with no extrapolation (one point). More importantly, the program operates more efficiently when more points are used for extrapolation. That is, fewer time increments are needed to satisfy a given error threshold, and the program runs faster. Conversely, with no extrapolation, convergence may simply not be obtained.

This is a point which is important enough that one should consider making improvements in the extrapolation procedure even beyond what has already been done. As we shall see, the time-dependence of the space-charge field during both the write and erase modes can often be approximated quite well by an exponential for all values of z . For short times, even a linear approximation is quite good, but the largest errors come for later times when (1) the program is automatically selecting larger time increments and (2) the "true" exponential time-dependence is less well approximated by the extrapolation procedure used here. Therefore, it might be advantageous to build in alternative schemes for anticipating the space-charge field arrays. At least one of these schemes should assume an exponential time-dependence for $X(z)$. It would be a simple matter to compare the various methods as the program proceeds and select whichever of them is most successful in predicting the space-charge field.

3.6 Erase Mode

The simple illumination pattern given in Eqn. (20) is assumed to have been turned on at time zero and left unchanged thereafter while the grating is being written. Ultimately a steady-state condition is reached. It is possible, by changing M , ϕ , or the baseline intensity (unity) to instantly alter this pattern and thereby begin a new mode of operation. In the program, the intensity pattern is defined in function LGT.

In GRATING, the erase mode is modelled by setting M equal to zero after the grating has already been written. Physically, the constant illumination preferentially excites electrons to the conduction band in the regions where they are most numerous ($\rho < 0$). The electric field removes them from these regions, the ultimate effect being the neutralization of the space-charge and the consequent erasure of the grating.

Numerically, the solution arrays obtained in the write cycle are accurate to 4, 5, or even 6 significant figures at any time. (This depends upon the program parameters and the physical parameters which have been selected.) Since the field and the charge distribution are increasing monotonically in time, the accumulating error reflects only the most recent steps. In the erase mode, the opposite is true: the overall decrease in these amplitudes causes the relative errors to increase considerably, even if the absolute errors, which are mostly built in during the write cycle, remain approximately constant. The end result is that, by the time the space-charge and the space-charge field have dropped off by 3 or 4 orders of magnitude, the program results for the details of their z -dependence become questionable. Nevertheless, despite the appearance of this noise in the late-time erase results, the overall picture of the erase mode is quite accurate.

It would also be possible to "rewrite" rather than simply erase the grating. This could be accomplished by any number of means. One simple way would be to change ϕ , in Eqn. (20), by $\pi/2$ or π so that the bright and dark regions are shifted from their original positions. This facility has not been built in to GRATING, however.

3.7 Working-time Increments

The process of integrating the ODEs in Eqn. (18) is done in discrete steps of working time, which are usually selected by PDECOL. These increments are chosen to be as large as possible subject to accuracy constraints imposed at the beginning by the user. In normal operation, they never decrease; rather, they remain fixed for several steps until certain criteria

are met, at which time a larger step size is tried. The fastest operation occurs when PDECOL is allowed to run freely with its own choice of increments. In such cases, the working time and output time never coincide. Once the working time skips past the current output time the program pauses to obtain the solution arrays by interpolation, and then proceeds as before upon assignment of a new output time.

It is possible (by use of the input variable INDEX - see PDECOL listing) for the user to cause the working time to coincide with the output time at the end of each output time step. The difficulty here is that the last working time step is then simply what is required to hit the output time exactly. This may happen to be a very small increment, and in such cases the succeeding working time steps are scaled upward from this rather than from the much larger previous increment. An unnecessarily large number of working time steps can therefore be used to reach the same conclusion in the end.

It could be desirable to do this if certain difficulties are being encountered—for example, if the anticipated values of the space-charge field at certain steps are sufficiently in error to cause degradation of the results. Then, because of the smaller steps in time, the results of the extrapolation procedure described in Sec. III.3.5 would be improved. For cases tested so far, it has not been necessary to use such a scheme.

As will be seen in Sec. III.4.2, the initial buildup of the conduction-electron density is very rapid. It occurs on a time scale on the order of 10^{-8} , so the initial working-time steps, DT, must be very small (a couple orders of magnitude below this, at least). If the user does not set DT small enough, the program may be able to correct for it but will waste time doing so.

The final steady state is not reached until $t \gg 1$, so it is an essential requirement that the program be able to automatically graduate from small steps to much larger steps as conditions dictate. Even when PDECOL steps up the time increments freely, 100 to 300 steps may be required. Since these working-time steps are normally independent of the choice of output times, the latter can be set only for large values ($t \geq 1$) if desired. By so doing, however, one loses the ability to study the early-time evolution of the fields.

At the beginning of the erase mode, the working-time steps must once again be constrained to be small. (The reason is the same as at the beginning of the write mode—the conduction-electron density is changing rapidly.) This is accomplished by use of INDEX. (See comments in the program listing.)

4. Results

4.1 Introduction

The main results which were derived from GRATING during its testing phase are presented in this section, mostly in graphical and tabular form. The physical distributions of primary interest are the space-charge and the space-charge field, which are given as functions of z for various values of t and different values of the input parameters. Many although not all of the results are for the zero-diffusion case ($A = 0$) because for large t the final distributions can be checked against analytical results. The growth of the field in time is also shown for certain parameters to illustrate the time scales involved.

An overview of the essential results can be derived from Figs. 3, 6, and 8. They give, respectively, the growth of the space-charge field as a function of time for different modulation factors; the space-charge field as a function of z for different times; and the space-charge itself as a function of z for different modulation factors.

The results given in this section are derived using an illumination function with $\phi = 0$, $z_B = 2$ and $z_0 = 5$ (see Eqn. (20) and Fig. 2). The values of the input parameters used were---unless otherwise stated--- $A = 0$, $B = .016$, $R = 1$, $G_1 = 2.5 \times 10^7$ and $G_2 = .01625$. These are referred to as the "standard parameter set". Except for the assumption of no diffusion, these values were derived by assuming initial concentrations of 100 ppm for full and empty optical donor levels and an applied field of 10 kV/cm and then using formulas given in Appendix B of Ref. 1. Later we demonstrate some of the effects of separately varying the diffusion length, the drift length (the applied field), and the initial ratio of filled to empty traps. The results reported here do not in any sense constitute an exhaustive study of the parameter sets which are physically reasonable for crystals of interest, or even for any single type of crystal. They are presented to show the simplest dependences on the various parameters.

There are several input quantities, required to run the program, which are not physical parameters but rather are program parameters. These are discussed in the comments in the program listing. Default values, given there, were used for all of these for the results given below---except NINT, which is the number of spatial intervals between $-z_0$ and $+z_0$. We found that for the standard parameter set and $M \leq .6$, NINT = 100 was adequate. For $M > .7$ larger values of NINT (e.g., 200) were required.

All results reported below were done with either 100 or 200 intervals. If more cycles are specified in the interference region, of course, larger values of NINT will again be required.

Variations of the other program parameters did not materially affect the results for those cases tested.

4.2 Time Scales

There are two time scales which must be considered during the buildup of the charge distributions from their initial values. This results from the fact that the times required for the transport of electrons over significant distances is much greater than the time the individual electrons remain in the conduction band before recombining with empty traps.

The buildup of the conduction-electron density from zero to a more or less steady state is reached very quickly. The competing mechanisms which balance each other out are photoexcitation and recombination. (At any instant, the transport mechanisms which serve to redistribute the charge are a minor perturbation.) This time scale is on the order of $(G)^{-1} \sim 0(10^{-8})$, as can be seen from the following short-time approximation which is valid for many situations (see Sec. III.4.6):

$$u(z,t) = F(z)[1 - \exp(-G_1 t)] \quad t \ll 1 \quad (26)$$

After this initial rapid buildup is achieved, the effect of the gradual net movement of electrons into the dark regions eventually becomes felt. The conduction electron density, u , remains approximately fixed at $F(z)$, but the positive charge density, v , is being altered continuously by the steady transport of electrons until it reaches values much greater in magnitude than unity. The time scale on which this buildup of the space charge ($v-u$) occurs is that of the dielectric relaxation time---which is, by our definition, unity and therefore vastly greater than the time scale on which the conduction-electron density buildup occurs.

In the time range $(G_1)^{-1} \ll t \ll 1$ the space-charge field is still swamped by the applied field and the conduction-electron density is nearly constant in time, so the conditions which control the transport mechanisms (drift and diffusion) are time-invariant. The charge buildup therefore proceeds at a constant rate. The charge distribution and field pattern reflect the sinusoidal space-dependence of the illumination function.

When the space-charge field becomes comparable to the applied field ($t \sim 1$), the drift mechanism is altered and the preceding comments do not apply. The ultimate z -dependence of the space-charge (and the space-charge field) depends on the physical parameters used, but it is generally not sinusoidal.

These considerations will be discussed and exemplified in some of the following sections.

4.3 Time Development of the Space-Charge Field

Figures 3 and 4 show the buildup of the space-charge field as a function of time for cases with no diffusion. What is plotted in these two figures is the amplitude of E_{sc} and the maximum value of E_{sc} , respectively, in units of applied field. (The amplitude of E_{sc} is defined as the difference between the maximum and minimum values.) These quantities are given for various values of the modulation factor to illustrate the dependence on the "strength" of the interference pattern. Clearly, for a given material, the steady-state condition is reached more quickly for small values of M . Also the field strengths ultimately attained are much smaller for smaller M .

For large values of M , the maximum field attains values many times greater than E_{app} . It should be recognized, however, that for these cases the assumption of zero diffusion is more critical because of the extremely sharp peaks in the charge density which are the cause of these large values for E_{sc} . Also, for the same reason, convergence of the algorithm is more tenuous and, as mentioned earlier, a finer spatial discretization (determined by NINT) is required.

For the case of zero diffusion, the steady-state values of E_{sc} can be derived easily from the basic equations. Since all the time derivatives are zero, and $D = 0$, one can see from Eqns. (4) and (5) that the current density has a constant value equal to $J_o = e\mu n(z)E(z)$. But, assuming no saturation takes place ($N_+/N_{+o} \sim N_e/N_{eo} \sim 1$ for all z), Eqns. (7b), (8), and (12b) establish that $n(z) = \langle n \rangle F(z)$, so that

$$E(z) = E_{app} + E_{sc}(z) = \frac{1}{F(z)} \left(\frac{J_o}{e\mu \langle n \rangle} \right) \quad (27)$$

This holds everywhere, including places where $E_{sc} = 0$ and $F(z) = 1$, so the quantity in parentheses in Eqn. (27) is simply E_{app} and the space-charge field is given by

$$E_{sc}(z) = -E_{app} \left(\frac{1}{F(z)} - 1 \right) = -E_{app} \left(\frac{M \cos k_g z}{1 + M \cos k_g z} \right) \quad (28)$$

From Eqn. (28) the minimum value of E_{sc} , the maximum value, and the amplitude can easily be found by using appropriate values of $k_g z$. The analytical and numerical results for these values are compared in Table 1 for various values of M , with $t = 10$ chosen to represent the steady state for the numerical calculations. Agreement is excellent except for $M > .6$ where a larger value of t is needed.

Another useful result has been obtained empirically for the zero-diffusion case. This result is expressed as

$$(E_{sc})_{max} = \frac{M}{1-M} E_{app} (1 - e^{-\gamma_1 t}) \quad (29a)$$

$$(E_{sc})_{min} = -\frac{M}{1+M} E_{app} (1 - e^{-\gamma_2 t}) \quad (29b)$$

where $\gamma_1 = 1 - M$ and $\gamma_2 = 1 + M$, and can be used to calculate curves such as are drawn in Figs. 3 and 4.

For the erase mode, the time-dependence of the decaying space-charge field is given in Fig. 5, where the ratio of the maximum values of E_{sc} at time t and at time t_0 is plotted. (t is measured from t_0 , the moment the interference pattern is destroyed and erasure of the grating commences.) Unlike the circumstances during field buildup the time constant is not a function of the modulation factor. In fact, the time dependence is given almost exactly by $\exp(-t)$ for most cases. For values of R considerably greater than unity, however, the decay proceeds slightly faster.

4.4 Spatial Distributions

Figures 6-10 show the space-charge field and the space charge itself as a function of z for several different cases. Fig. 6 gives the distribution (for the standard parameter set) at $t = .1, 1$, and 10 . At the first of these three times the space-charge field is still much smaller

than the applied field and the charge buildup is proceeding at a constant rate (see III.4.2). The field pattern is almost exactly sinusoidal, like the illumination pattern. At $t = 1$, the space-charge field is beginning to influence the electron transport. At $t = 10$ the steady state has been attained and the field pattern bears no resemblance to a sinusoid.

Figures (7a)-(7c) show, for different modulation factors, the space-charge field for $t = 10$, which represents the steady state or (in the cases of $M \geq .7$) a nearly-steady state. Clearly the greater modulation factors cause larger maxima.

The curve with $M = .7$ was derived using 200 spatial intervals. The x appearing above each maximum represents numerical values obtained with $NINT = 100$, which gives too few intervals. The resulting discrepancies are all less than 2% (the worst cases are at the maxima) but close inspection reveals that they increase as one goes from negative to positive values of z . This increasing error occurs because the charge density is not determined on a fine enough grid in areas where its space derivative is very large (see Fig. (8b)). This in turn degrades the values of ρ which are obtained and, additionally, causes the numerical integration of ρ , which gives the space-charge field, to be inaccurate. The result is that the charge density in the negative and positive portions of the periodic distribution do not exactly cancel, as they should when integrated. Then as one integrates from $-z_0$ to z an accumulating error builds up with each period. Thus, maxima which attain successively higher values are indication of a need for a larger number of intervals. Another clear indication of such an occurrence is that the space-charge field at $z \sim +z_0$ (the "residual field"--see Sec. III.4.6) not only be nonzero (because machine roundoff will inevitably produce some "field") but also be a significant fraction of the maximum field.

Figures (8a)-(8c) give the space-charge distribution as a function of z for the same conditions as prevailed for Figs. (7a)-(7c). The charge is given in units of $\langle n \rangle$. The differences between these distributions result from the different modulation factors and can be explained by the differences in the gradient of the light intensity, which is much greater for larger values of M . That is, when $M = .1$ the contrast in intensity between the "light" and "dark" regions is small, whereas when $M = .9$ it (and the consequent difference in the photoexcitation rates) is much greater.

Consider the $M = .1$ curve in Fig. (8a). The peaks of the light intensity are at $z = 0, \pm 1$, and ± 2 and the minima are at $\pm .5$ and ± 1.5 . The drift distance is small compared to the interference-pattern spacing (unity). The applied field is positive so electrons are drawn to the left.

At the intensity maxima (and minima), just as many electrons are drawn into these regions as are drawn out of them, so the net charge there remains zero. To the left of each maximum, the net result of the transport is to draw electrons into the region; to the right, the effect is to draw electrons from it. Both differences result because of the gradient in the light intensity, which produces greater or lesser numbers of photoelectrons in the regions from which they are being drawn by the applied field than in the regions into which they are being drawn. (The peaks at +2.15 represent the net movement of negative charge to the left.)

For the larger values of M in Figs. (8a)-(8c), the striking result is how the positive and negative charge peaks build up on either side of the light-intensity minima, and how these peaks are so much closer together for the larger modulation factors. This spatial distribution of course explains the large peaks in the space-charge field, and the shallow troughs. The extremely sharp dropoffs in ρ near the light-intensity minima for $M \geq .7$ also explain the need for greater spatial discretization for these cases.

Figures (9) and (10) compare, for $M = .5$, the zero-diffusion case with a case in which $A = .064$. This assumed diffusion distance is thus four times greater than the drift distance due to the applied field. As one would expect, it causes the charge distribution beyond the ends of the interference pattern to be more negative than before. It also shifts the positions of the maxima and minima of the charge distribution and augments the magnitudes of these extrema. In general, for large diffusion rates the space charge distributions become quite complicated.

4.5 Effect of Varying R

The limited number of runs in which R was varied showed that no differences from the standard cases resulted from taking R less than unity (down to 10^{-3}). For $R > 100$, however, differences do show up. Apparently for large values of R most traps are filled and recombination is inhibited, at least in comparison to the $R = 1$ case. Preferential recombination must occur significantly more strongly where the traps have been emptied already, which leads to a diminished field. The charge shifts to the left more for larger R , reflecting the difficulty of finding empty traps after migration from the intensely-lit regions. As a consequence, very careful consideration must be given to the assumptions relating to the boundary conditions, because for these cases a significant nonzero charge distribution may extend into the constant-illumination region. In fact, future testing procedures should be devised to assess the validity of the program results for this limit.

Figures (11)-(13) show some of the effects of varying R . Except for R , the standard parameter set is assumed, with $M = .5$. Fig. (11) shows the growth, in time, of the amplitude of the space-charge field. Fig. (12) shows the space-charge field for $R = .001, 1$, and 1000 , and Fig. (13) gives a portion of the space charge distribution for many values of R between 1 and 2000 . In each case the largest values of R cause E_{sc} and ρ to have nonnegligible values farther out into the constant-illumination region than in the standard case.

4.6 Miscellaneous Results; Limiting Case

One important assessment of the efficacy of the program is found by calculating what we call the "residual field" at $+z_0$. Our assumption has been that at the edge of the crystal all influences of the varying light pattern have dissipated, and both ρ and E_{sc} are zero. Since $E_{sc}(z)$ is obtained by numerically integrating $\rho(z)$ from $-z_0$ to z , and since physically the charge must be conserved within the crystal, an estimate of the errors introduced by the numerical procedures we employ can be obtained by calculating the residual field, or the space-charge field at $+z_0$, and seeing how it differs from zero. For most cases tested, the ratio of $E_{sc}(z_0)$ to the maximum value attained by E_{sc} within the crystal was less than 10^{-3} .

Table 2 gives some information about the effect of varying the parameters on the program's performance. The column labelled E_{res}/E_{max} is the residual-field ratio discussed above, evaluated at $t = 10$ which is nominally the steady state. "CPT" refers to the execute time, in seconds, required for the write mode of the program to run from $t = 0$ to $t = 10$. (The program was run on a CDC-6600.) In general, the erase mode took about as much time as the write mode.

With any complicated set of equations, it is useful to be able to reduce them to special cases for which the solutions can be found analytically, as a check on the program and the overall procedure. In this case, one can eliminate the drift and diffusion terms by striking out the first four terms of Eqn. (13a). The right-hand sides of Eqn. (13) then become identical, and it is easy to see, by using the initial conditions, that u and v are also identical. Of course, since those terms are exactly the ones responsible for the migration of negative charge, it follows that there ought to be no separation of positive and negative charge - a condition represented by $\rho \equiv 0$, or $u - v \equiv 0$. Nevertheless, as a check on the program it is useful to find the solution for u . This check is useful only for the short time-scale discussed in Sec. III.4.2.

Substituting u for v in the second equation leads to

$$\frac{du}{dt} = -au^2 - bu - c \quad (30)$$

which can be integrated directly:

$$\int_{u(0)}^{u(t)} \frac{du'}{au'^2 + bu' + c} = - \int_0^t dt' = -t \quad (31)$$

We have defined a , b , and c , which are constants with respect to time, as

$$a = RG_2 \quad (32a)$$

$$b = G_1 + F(z)G_2 \quad (32b)$$

$$c = -F(z)G_1 \quad (32c)$$

Since R , G_1 , G_2 and $F(z)$ are all positive, $b^2 - 4ac > 0$ and the indefinite integral is⁽³⁾

$$(b^2 - 4ac)^{-\frac{1}{2}} \ln \left| \frac{2au' + b - (b^2 - 4ac)^{\frac{1}{2}}}{2au' + b + (b^2 - 4ac)^{\frac{1}{2}}} \right|$$

After applying the initial condition ($u = 0$), making some convenient definitions, and doing a little algebra, one arrives at

$$\ln \left| \frac{-1 + c'u}{1 + c''u} \right| = -(b^2 - 4ac)^{\frac{1}{2}} t \quad (33)$$

where

$$c' \equiv \frac{2a\alpha}{b(1-\alpha)} > 0 \quad (34a)$$

$$c'' \equiv \frac{2a\alpha}{b(1+\alpha)} > 0 \quad (34b)$$

$$\alpha \equiv b(b^2 - 4ac)^{-\frac{1}{2}} < 1 \quad (34c)$$

If $0 \leq c'u \leq 1$, this reduces to

$$\dot{u}(z,t) = \frac{1 - f(t)}{c' + c'' f(t)} \quad (35)$$

where

$$f(t) = \exp \left[-(b^2 - 4ac)^{1/2} t \right] \quad (36)$$

and, of course, c' and c'' contain the z -dependence.

One special case of interest occurs when $G_1 \gg G_2$ and $G_1 \gg RG_2$.

These conditions are typical of the crystals discussed in Ref. 1. In this case, the square roots which appear can all be approximated with a Taylor expansion. Eventually one obtains

$$u(z,t) \approx F(z) \left(1 - \exp(-G_1 t) \right) \quad (37)$$

which is accurate to $O(G_2/G_1)$ or $O(RG_2/G_1)$, whichever is larger.

Program GRATING produced results agreeing with Eqn. (37) to at least five significant figures for each case tested.

M	$\frac{\text{MAX}(E_{sc})}{E_{app}}$	$\frac{M}{1-M}$	$\frac{\text{MIN}(E_{sc})}{E_{app}}$	$\frac{-M}{1+M}$	$\frac{\text{MAX-MIN}}{E_{app}}$	$\frac{2M}{1-M^2}$
$\frac{1}{3}$.5000	.5	-.2500	-.25	.7500	.75
.40	.6665	.6667	-.2860	-.2857	.9523	.9524
.50	.9975	1	-.3338	-.3333	1.331	1.333
.60	1.482	1.5	-.3758	-.375	1.857	1.875
2/3	1.943	2	-.4005	-.4	2.344	2.4

Table III-1. Numerical and analytical results for the steady-state space-charge field for the zero-diffusion case and various values of the modulation factor. Numerical values were derived using the standard parameter set and $t = 10$.

NINT	M	A	B	R	CPT (sec)	E_{res}/E_{max}
100	.1	0	.016	1	140	1×10^{-7}
	.3				140	7×10^{-6}
	.5				140	2×10^{-4}
	.7				150	1×10^{-3}
	.9				155	8×10^{-2}
200	.7	0	.016	1	300	3×10^{-4}
	.9				310	4×10^{-3}
100	.5	.016	.016	1	150	4×10^{-5}
		.032			150	2.4×10^{-4}
		.048			165	
		.064			165	3×10^{-3}
		.080			165	4×10^{-3}
200		.080			290	4×10^{-4}
100	.5	0	.016	1	140	2×10^{-4}
				100	140	4×10^{-5}
				500	180	1×10^{-5}
				1000	230	3×10^{-6}
				2000	315	3×10^{-3}
200				1000	490	1×10^{-6}

Table III-2. Performance of program GRATING for various parameter sets, as measured by execution time required to reach $t = 10$ (CPT) and by the residual field ratio (See III.4.6).

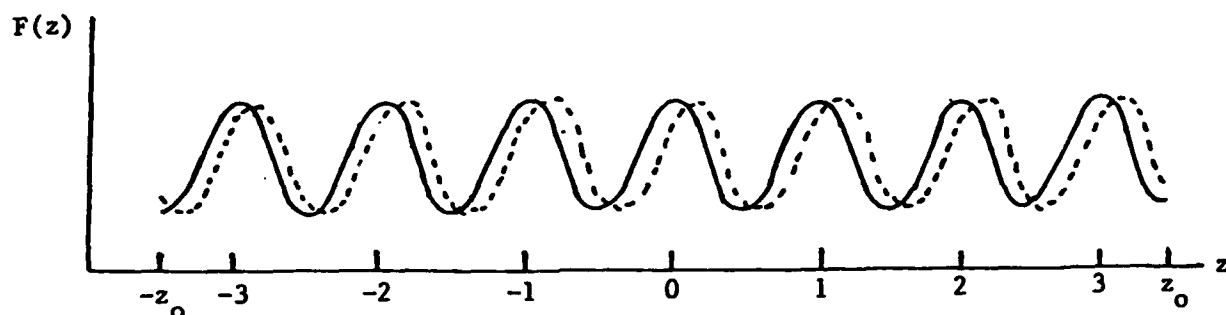


Fig. 1 Ideal illumination function $F(z)$ with $M = .5$ (solid line) and with a phase-shifted distribution (e.g., $\rho(z)$) superposed.
 $z_0 = 3.5$.

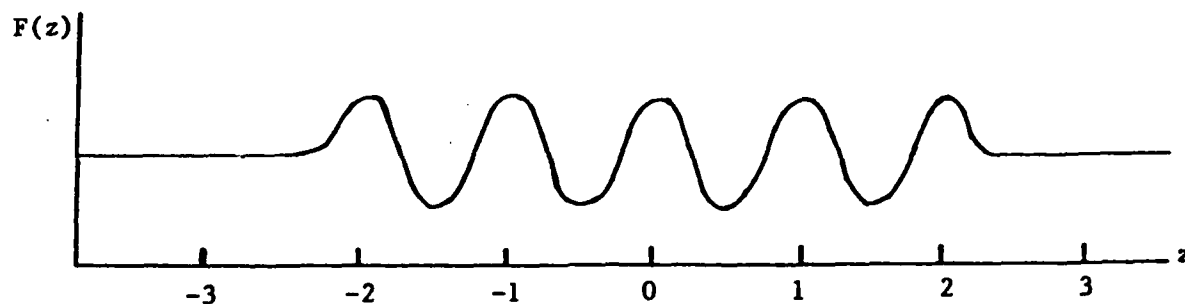


Fig. 2 Illumination function $F(z)$ used in the program, with $M = .5$, $\phi = 0$, $z_B = 2$, and $z_0 = 5$ (off scale). $F(z)$ is given in Eqn. (20).

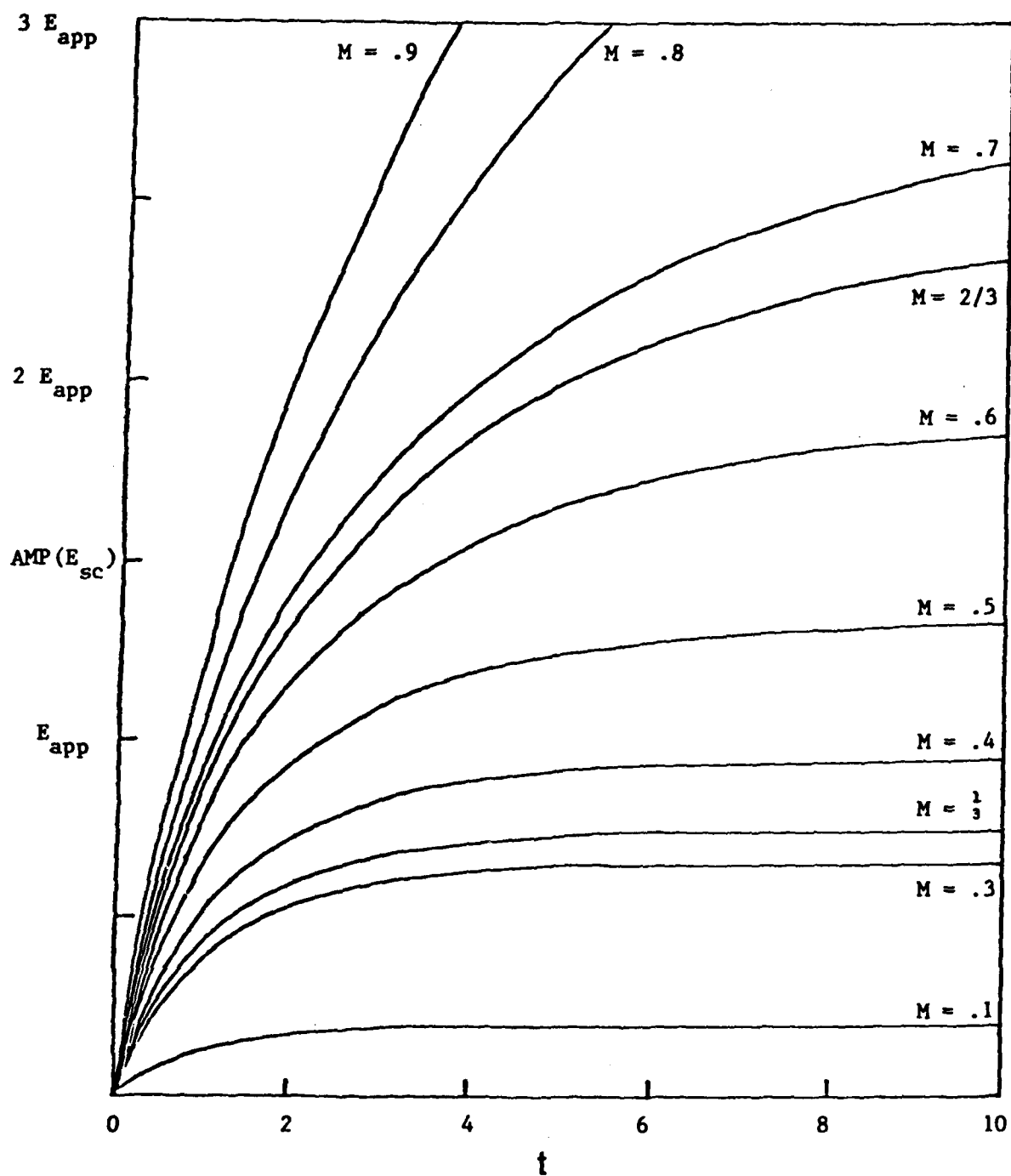


Fig. 3 Amplitude of the space-charge field as a function of t for various modulation factors, M .

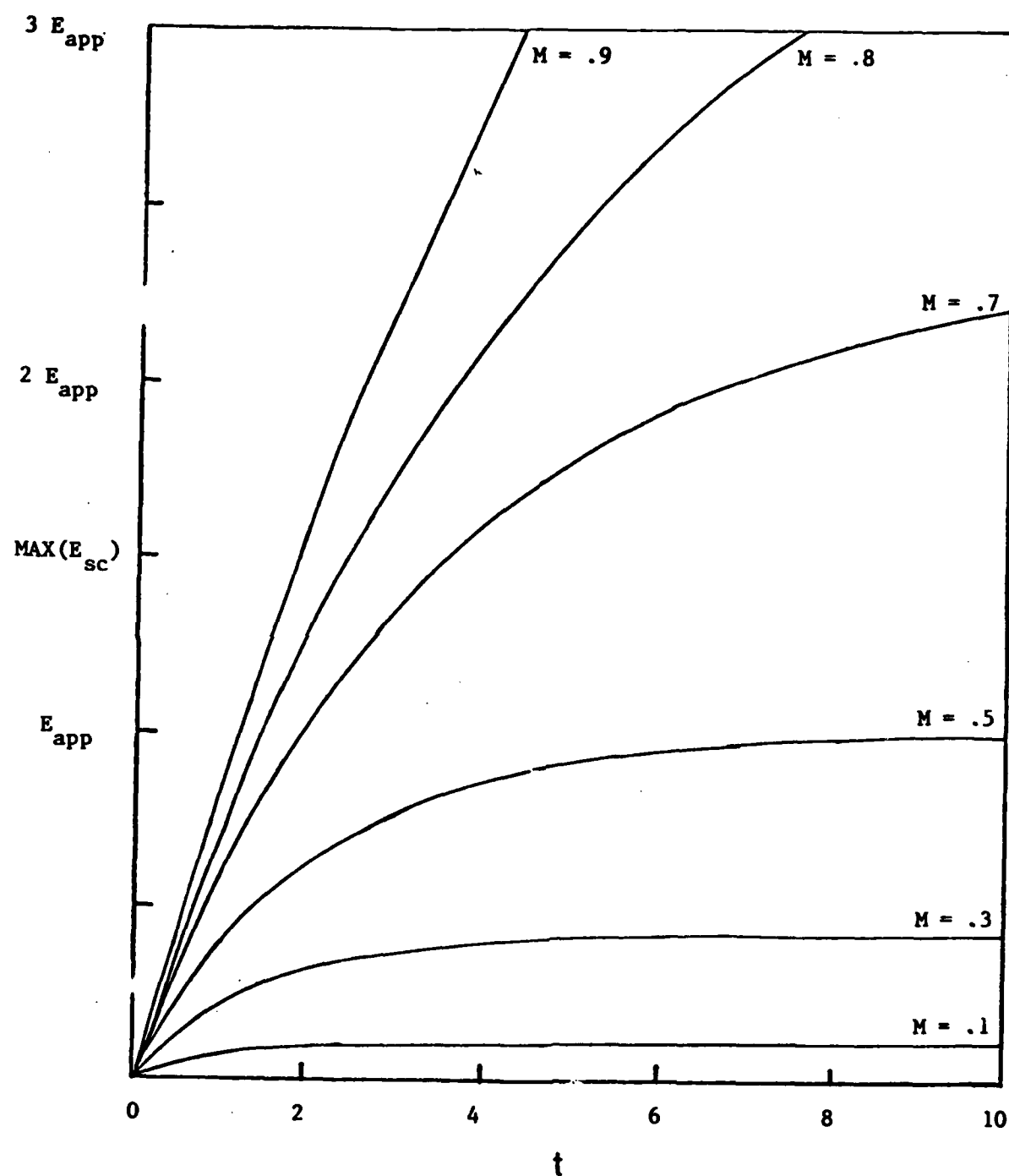


Fig. 4 Maximum value of the space-charge field as a function of t for various modulation factors, M .

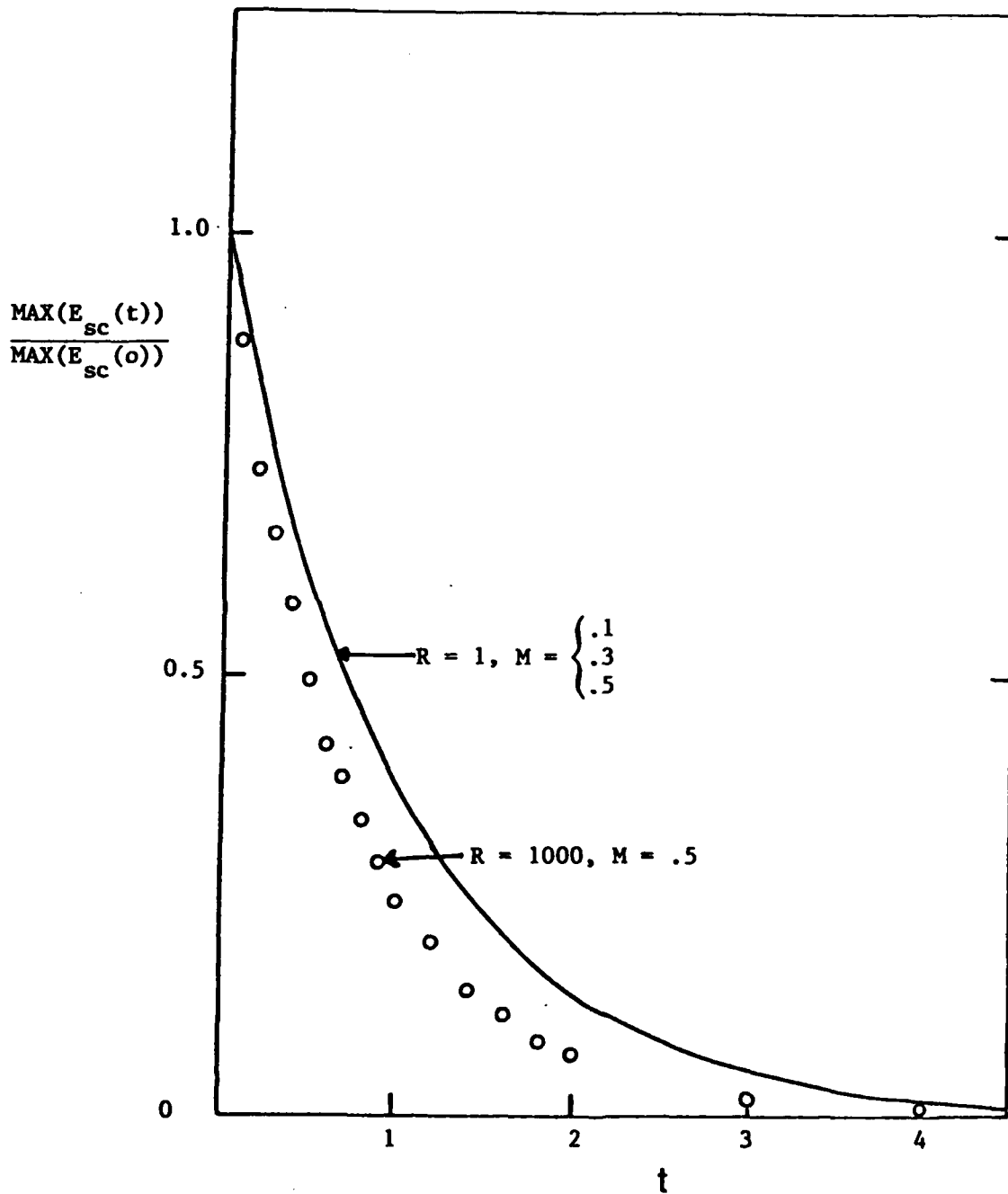


Fig. 5 Maximum value of the space-charge field during the erase mode, as a function of t . Time is measured from the moment the erase mode is initiated.

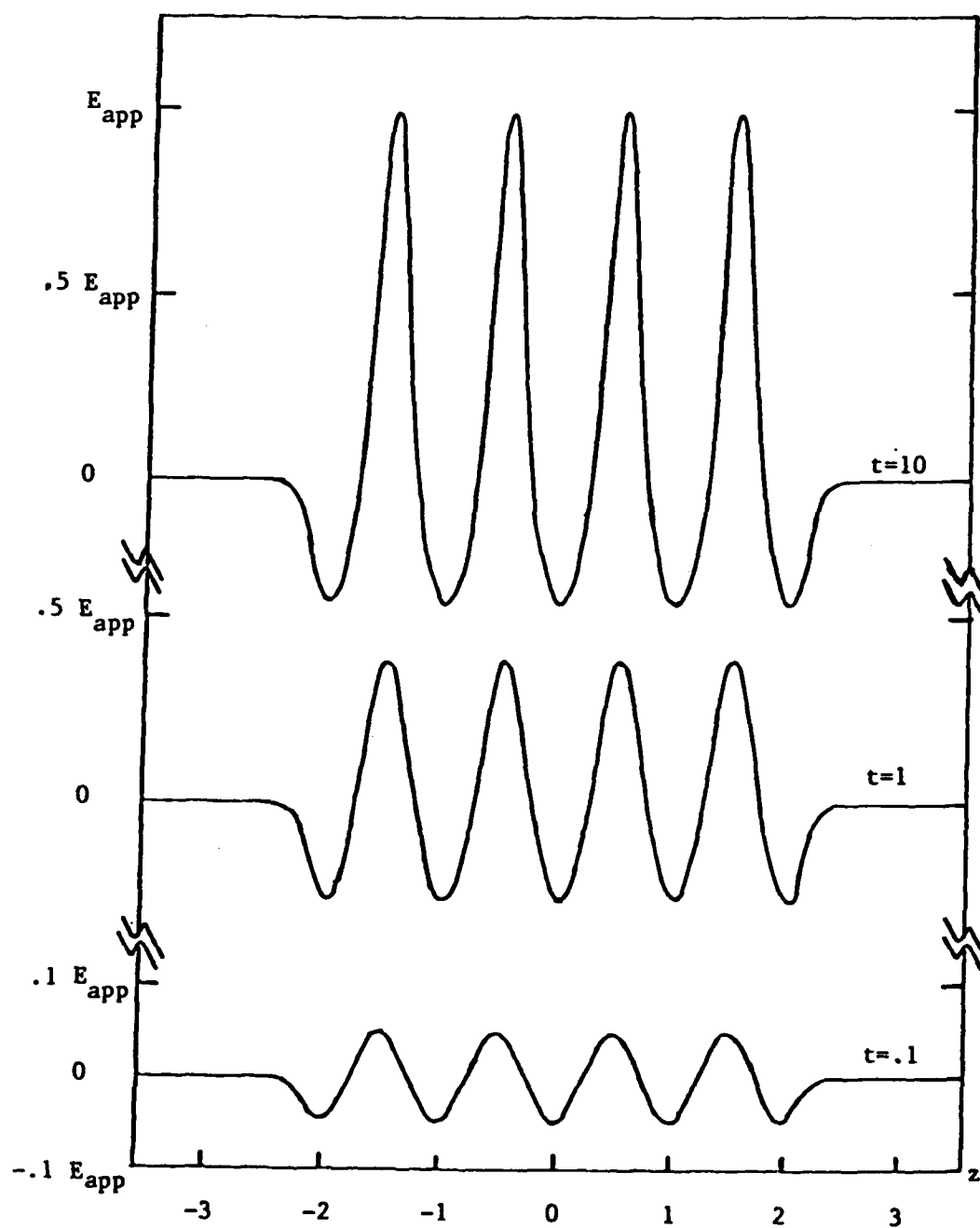


Fig. 6 The space-charge field, E_{sc} as a function of z for three times. Note that the scales differ.

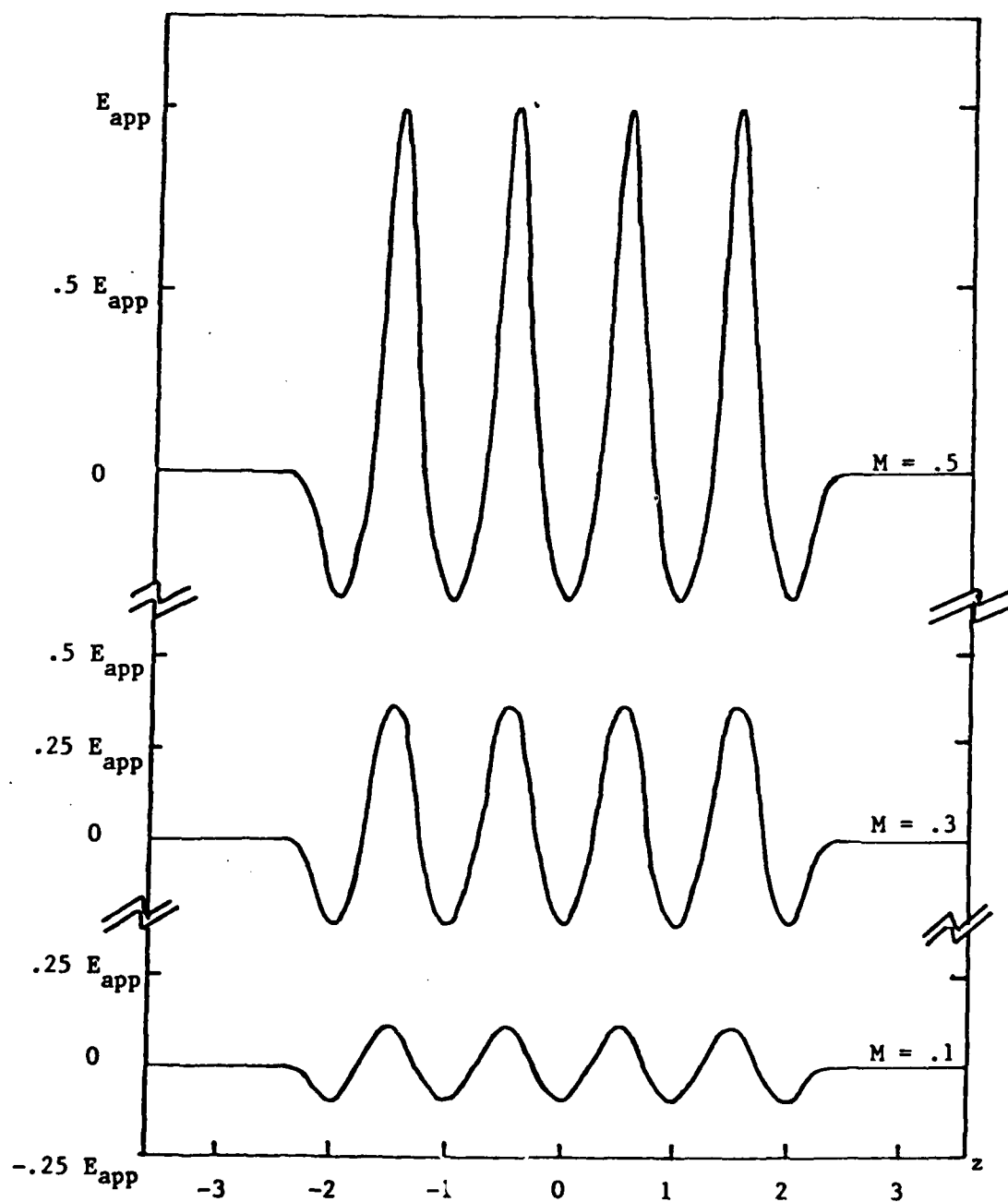


Fig. 7(a) The space-charge field as a function of z for the steady-state. Modulation factors are .1, .3, and .5.

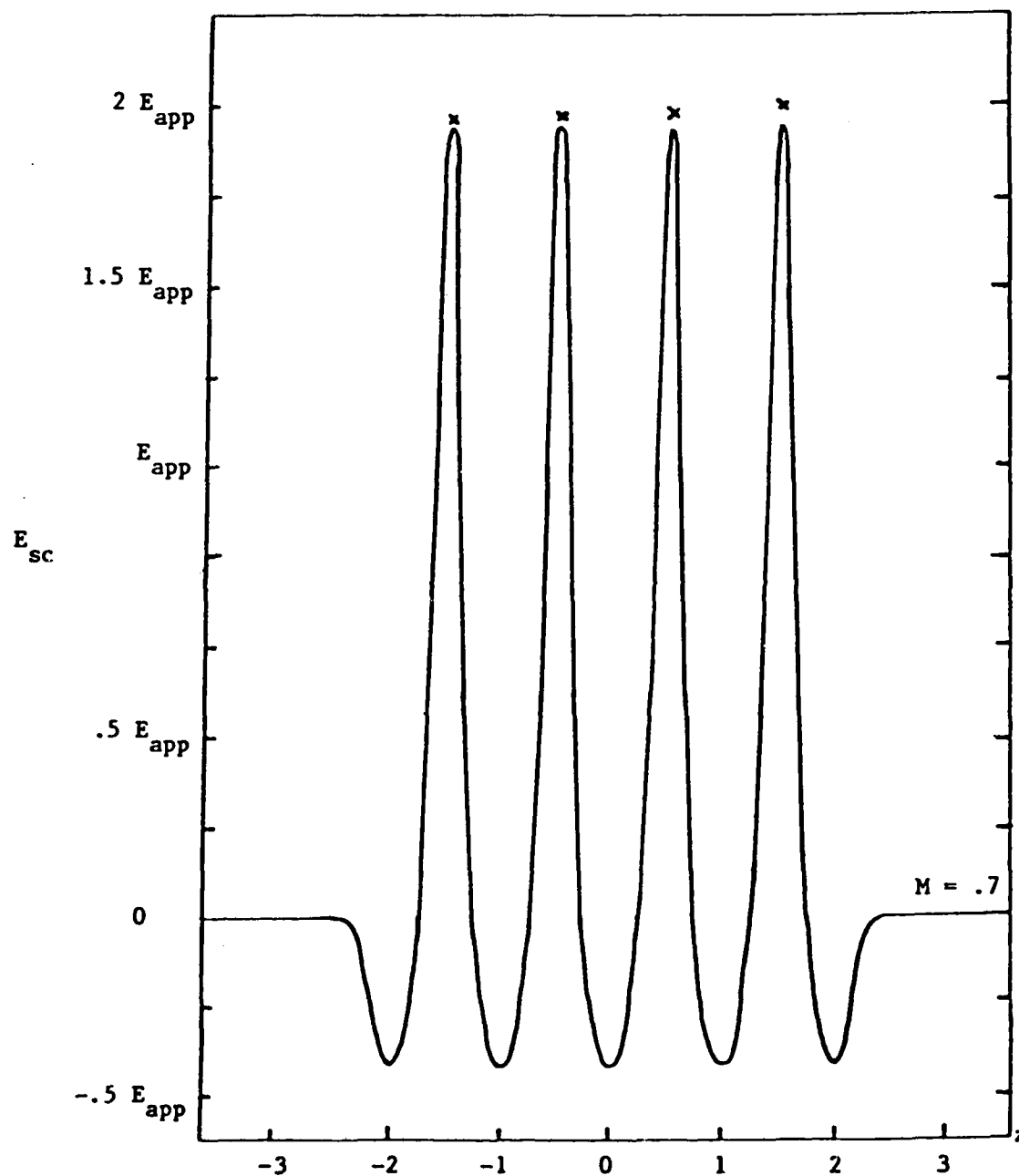


Fig. 7(b) The space-charge field as a function of z for the steady-state. Modulation factor is .7. These results were obtained with $NINT = 200$. The x marks above each peak give the maxima obtained with $NINT = 100$ and represent the most extreme deviations in the curves obtained in these two ways.

AD-A139 603

MATHEMATICAL MODELLING OF WAVEGUIDING TECHNIQUES AND
ELECTRON TRANSPORT VOLUME 1(U) ARCON CORP WALTHAM MA
S WOOLF ET AL. JAN 84 RADC-TR-83-313-VOL-1

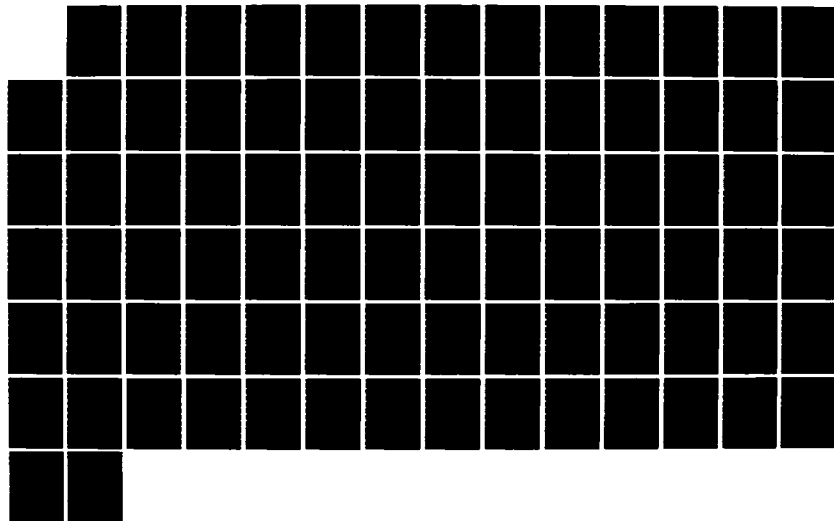
3/3

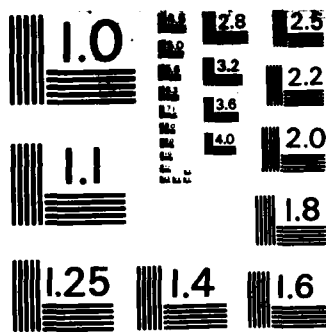
UNCLASSIFIED

F19628-78-C-0188

F/G 12/1

NL





MICROCOPY RESOLUTION TEST CHART
NATIONAL BUREAU OF STANDARDS-1963-A

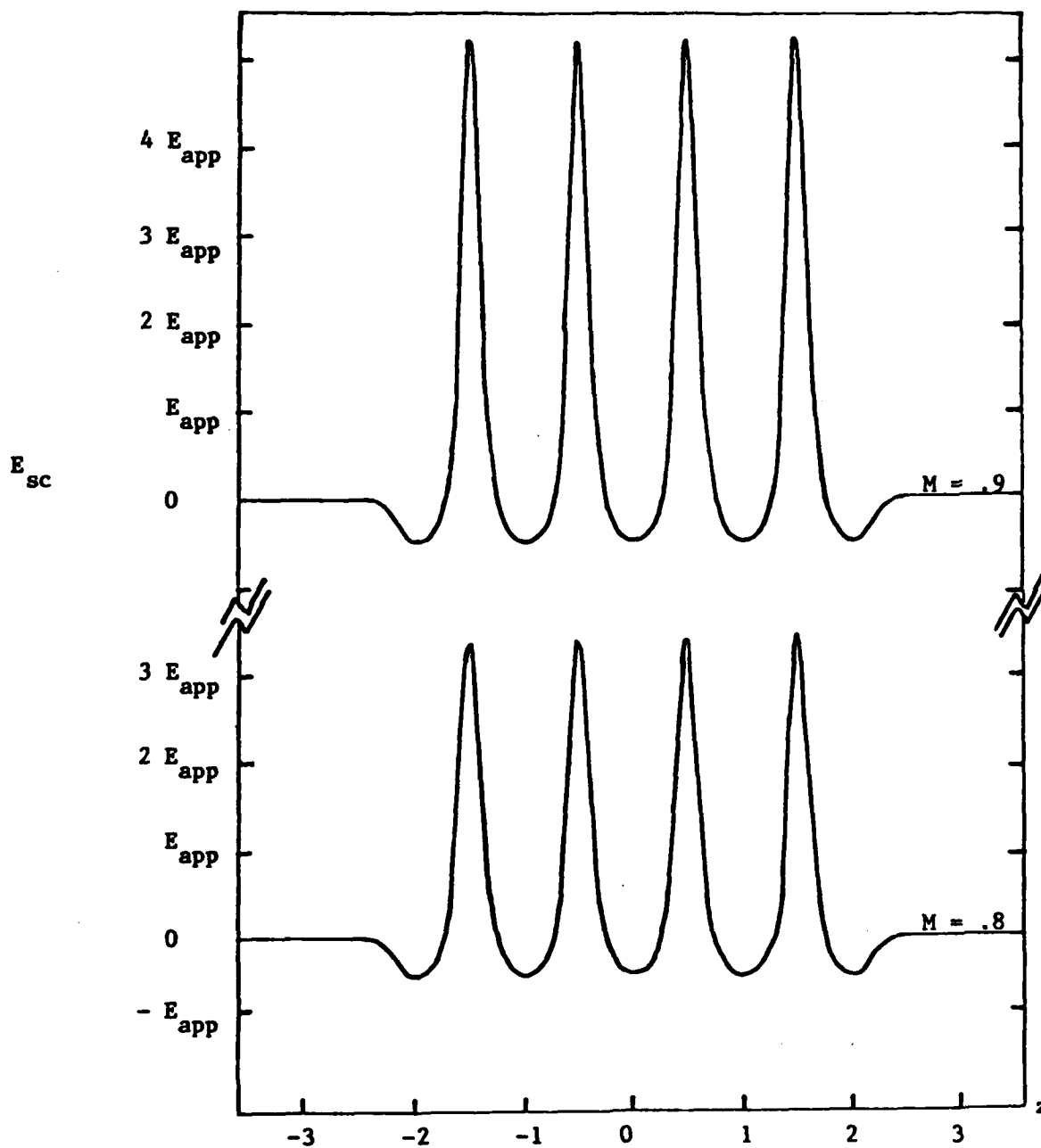


Fig. 7(c) The space-charge field as a function of z for the steady-state. Modulation factors are .8 and .9. Note that the scales are different from (a) and (b).

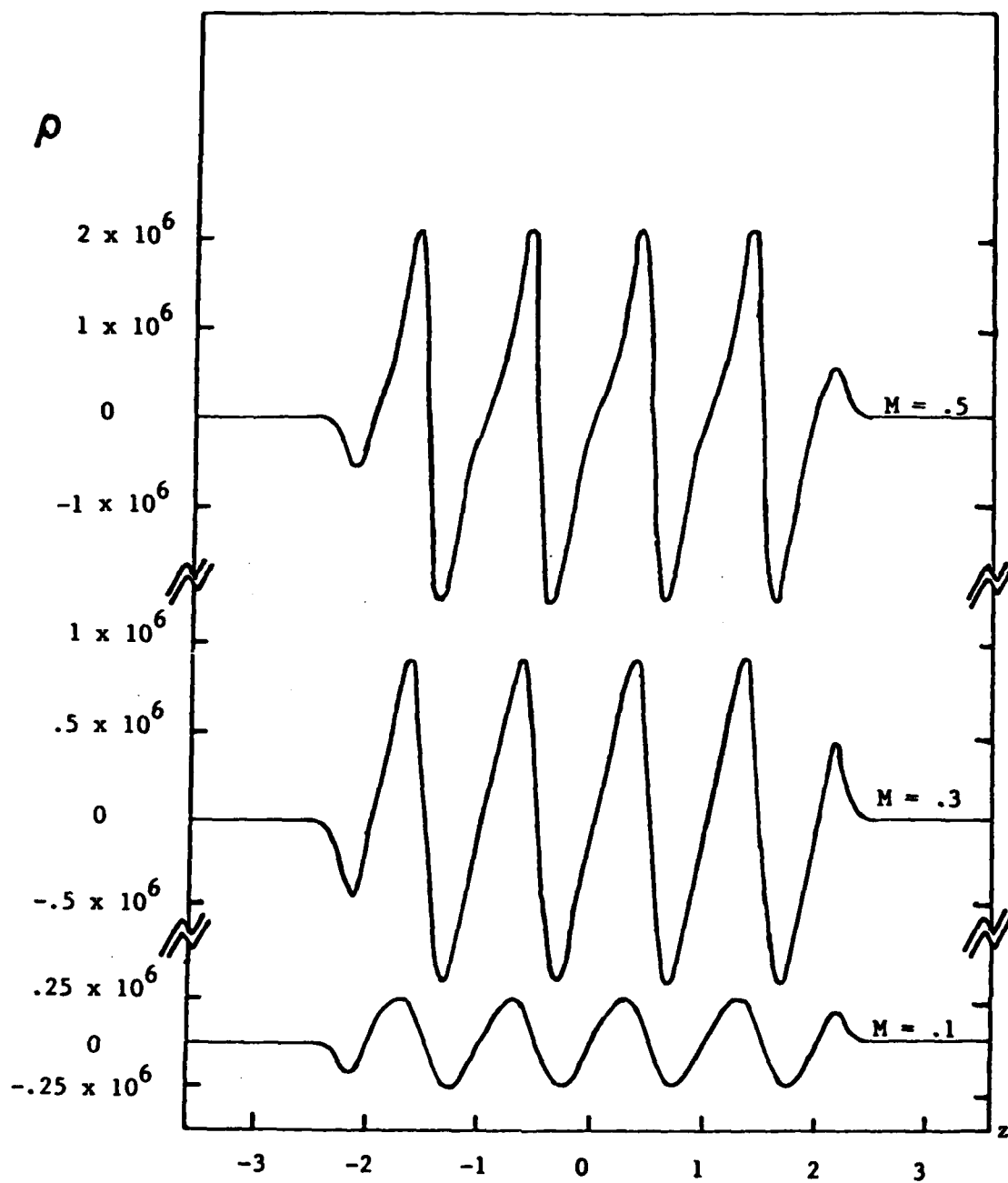


Fig. 8(a) The space-charge, ρ , as a function of z for the steady-state, in units of $\langle n \rangle$. Note the different scales used for each curve. Modulation factors are .1, .3, and .5.

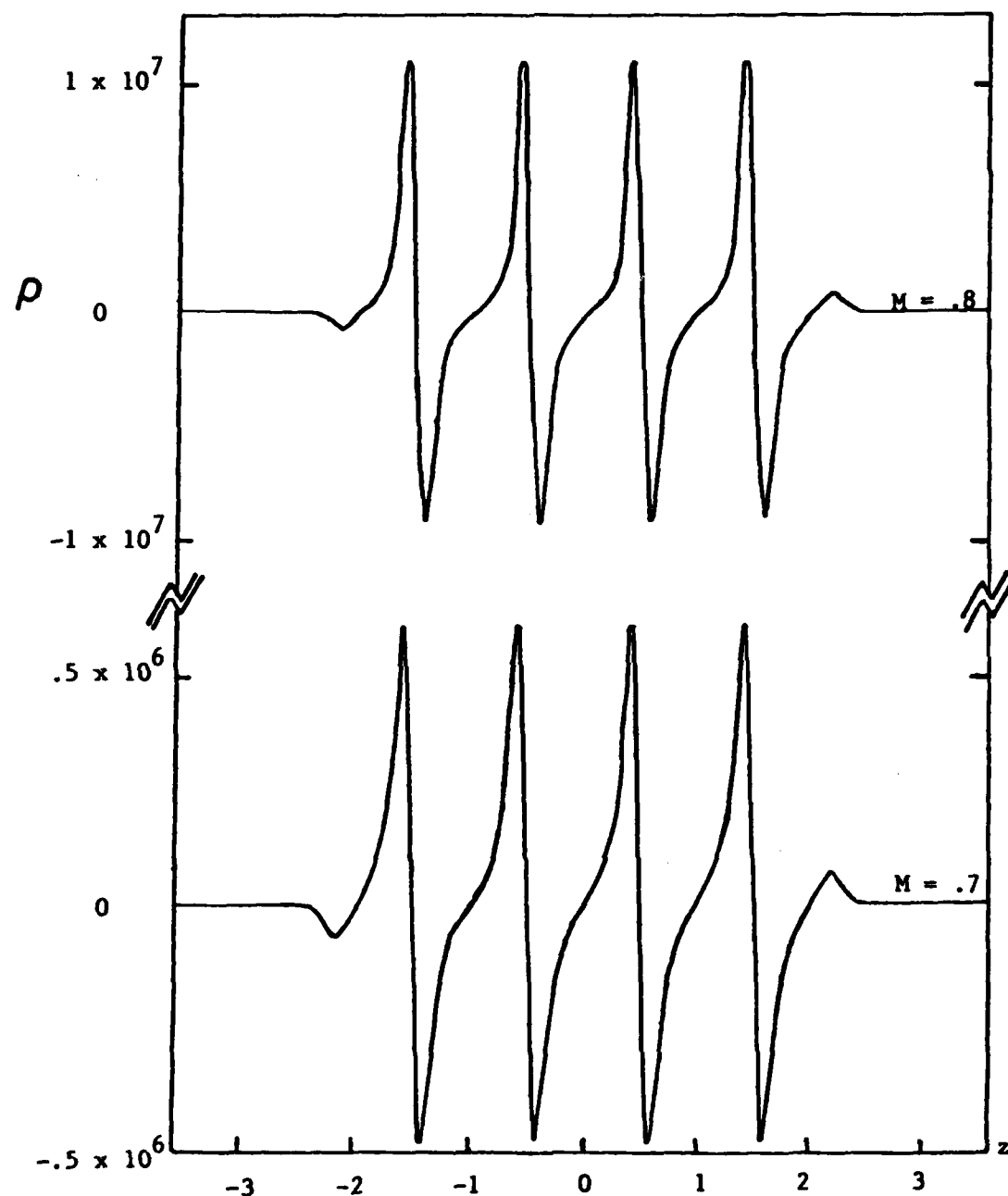


Fig. 8(b) The space-charge, ρ , as a function of z for the steady-state, in units of $\langle n \rangle$. Note the different scales used for each curve. Modulation factors are .7 and .8.

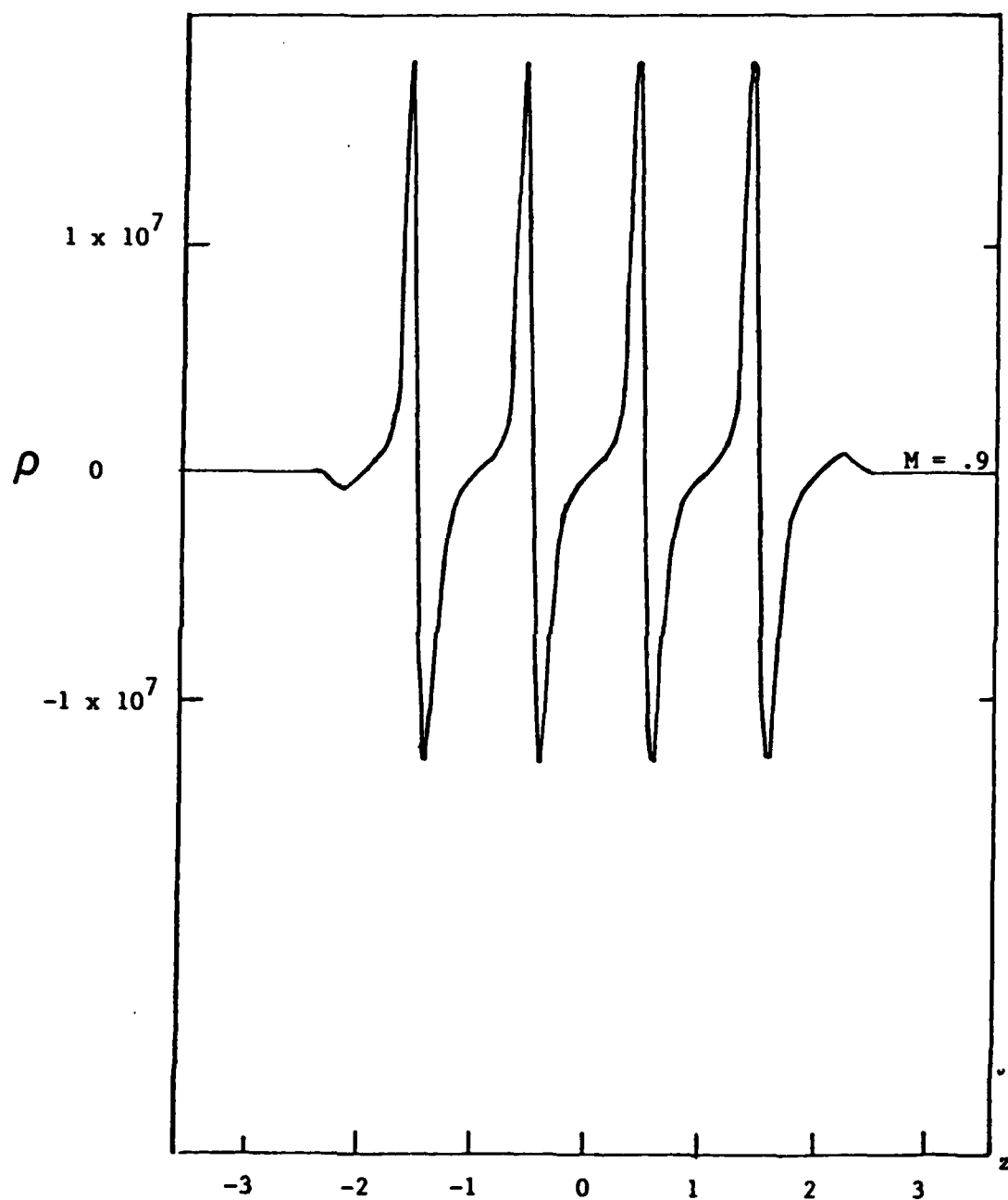


Fig. 8(c) The space-charge, ρ , as a function of z for the steady-state, in units of $\langle n \rangle$. Modulation factor is .9.

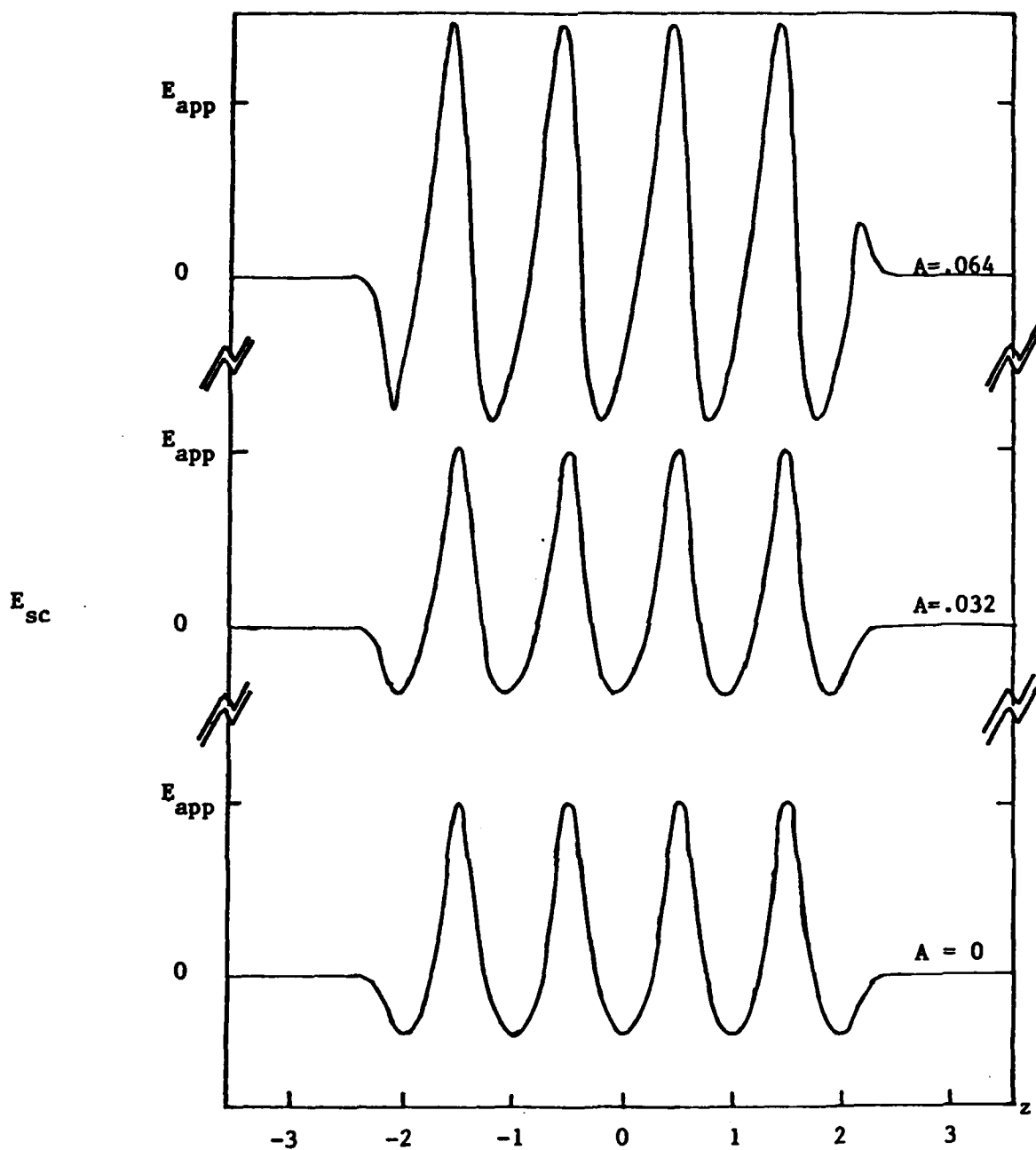


Fig. 9 The space-charge field as a function of z for the steady-state for two different diffusion-drift distances. Except for A , the standard parameter set is assumed with $M = .5$.

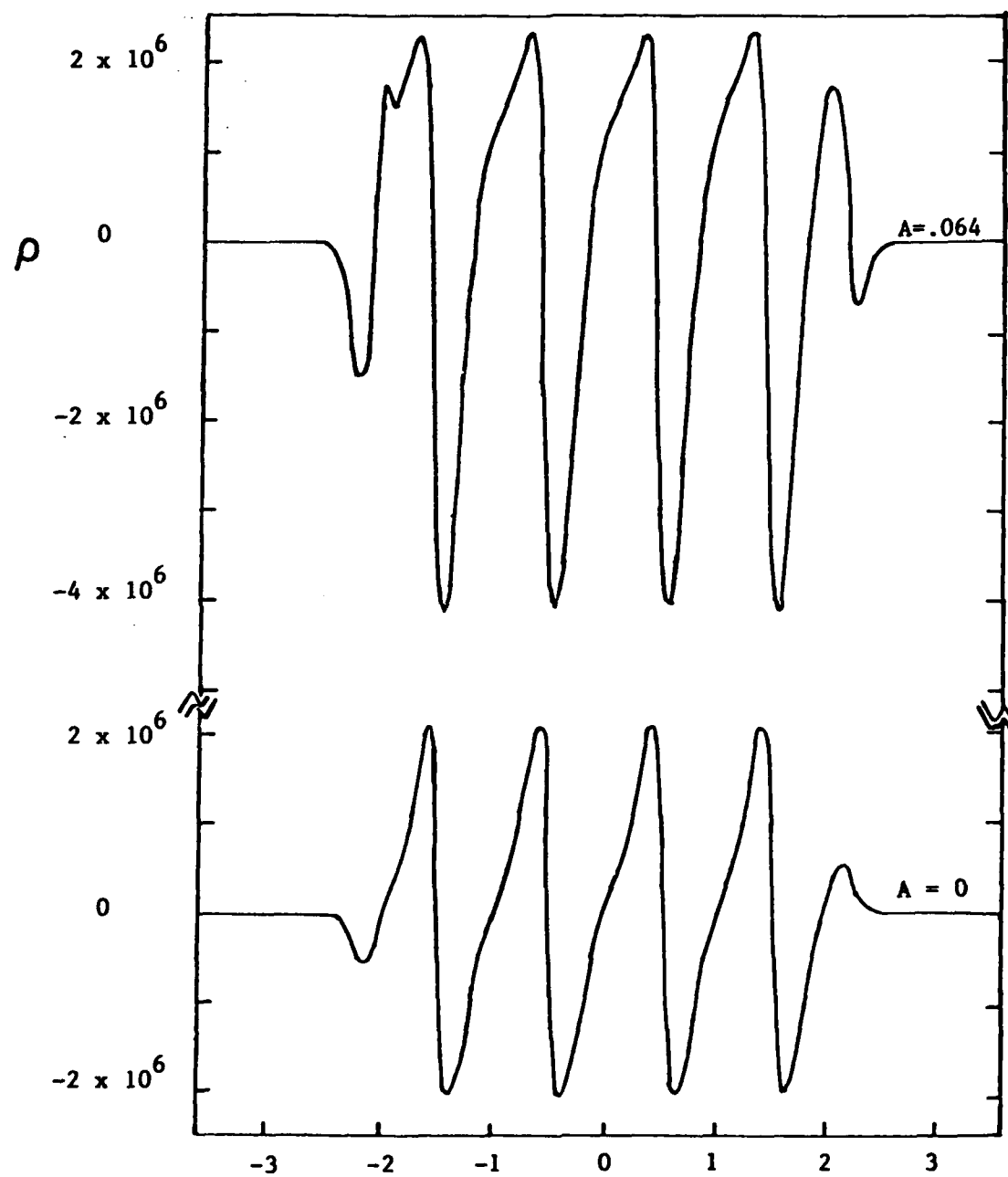


Fig. 10 The space-charge, ρ , as a function of z for the steady-state for two different diffusion-drift distances. Except for A , the standard parameter set is assumed, with $M = .5$.

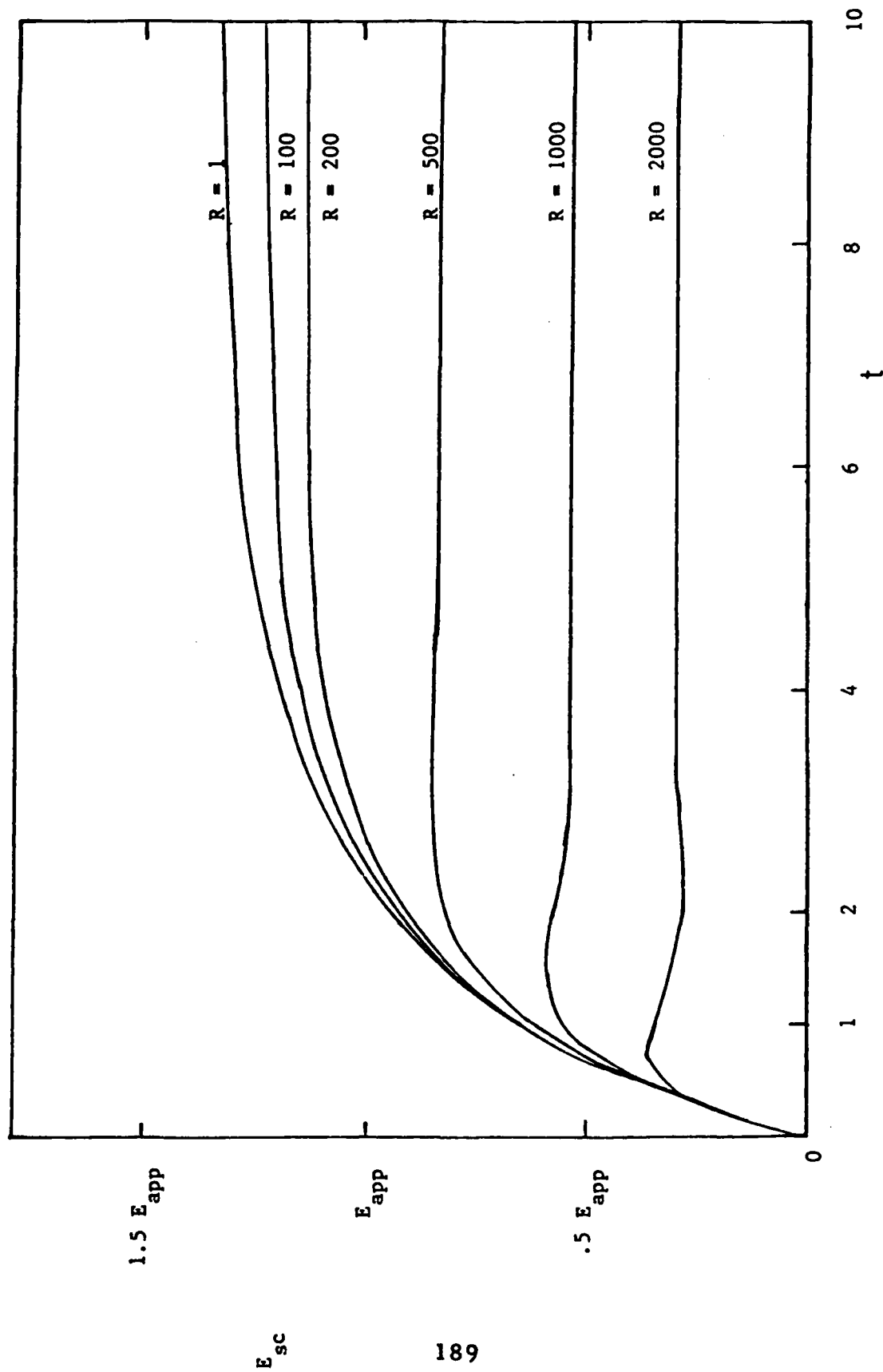


Fig. 11 The amplitude of the space-charge field as a function of time for values of R greater than or equal to unity. For $R < 1$, the $R = 1$ curve is replicated. Except for R , the standard parameter set is assumed with $M = .5$.

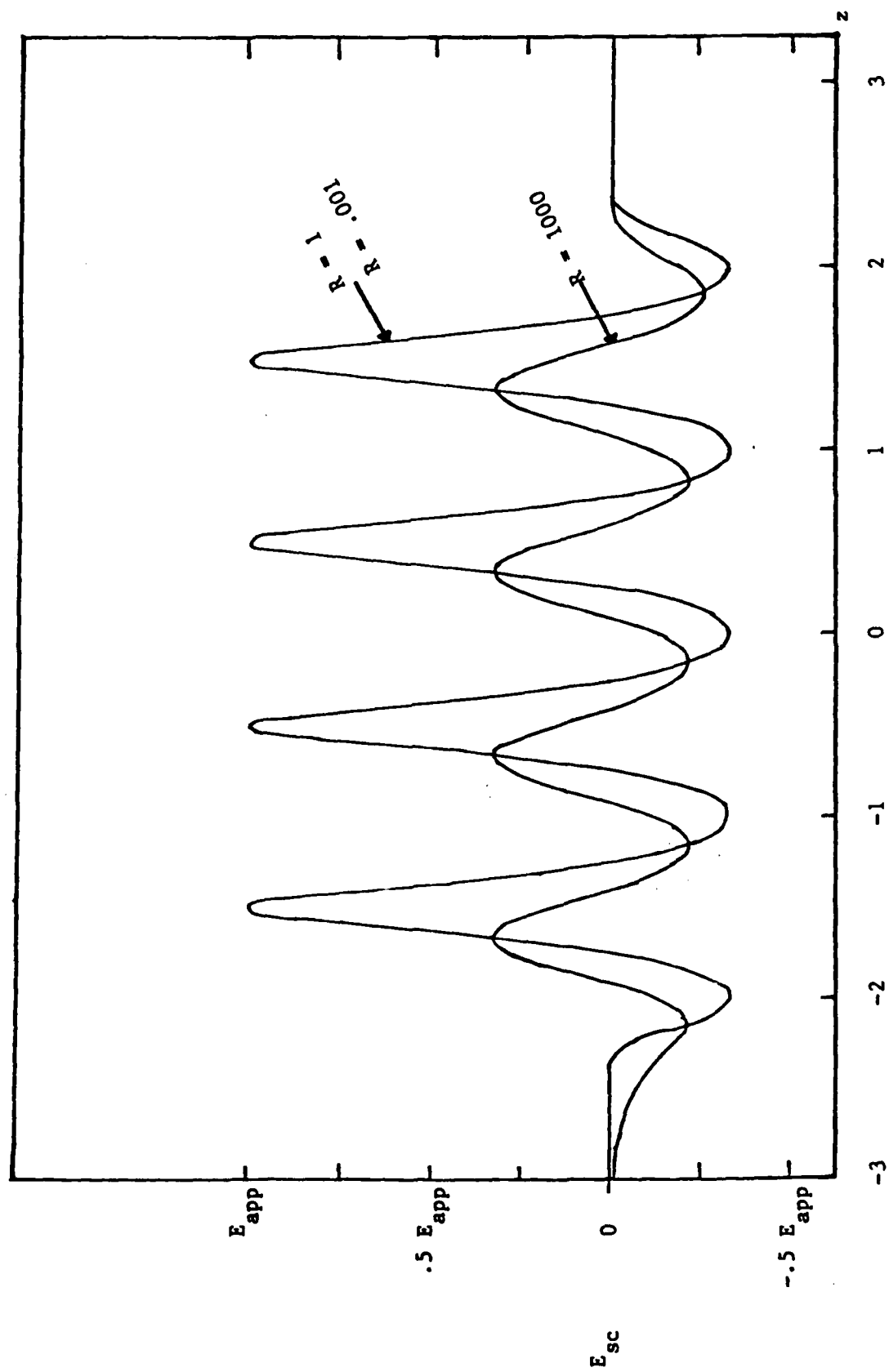


Fig. 12 The space-charge field as a function of z for the steady-state, for $R = .001$, 1, and 1000. Except for R , the standard parameter set is assumed with $M = .5$.

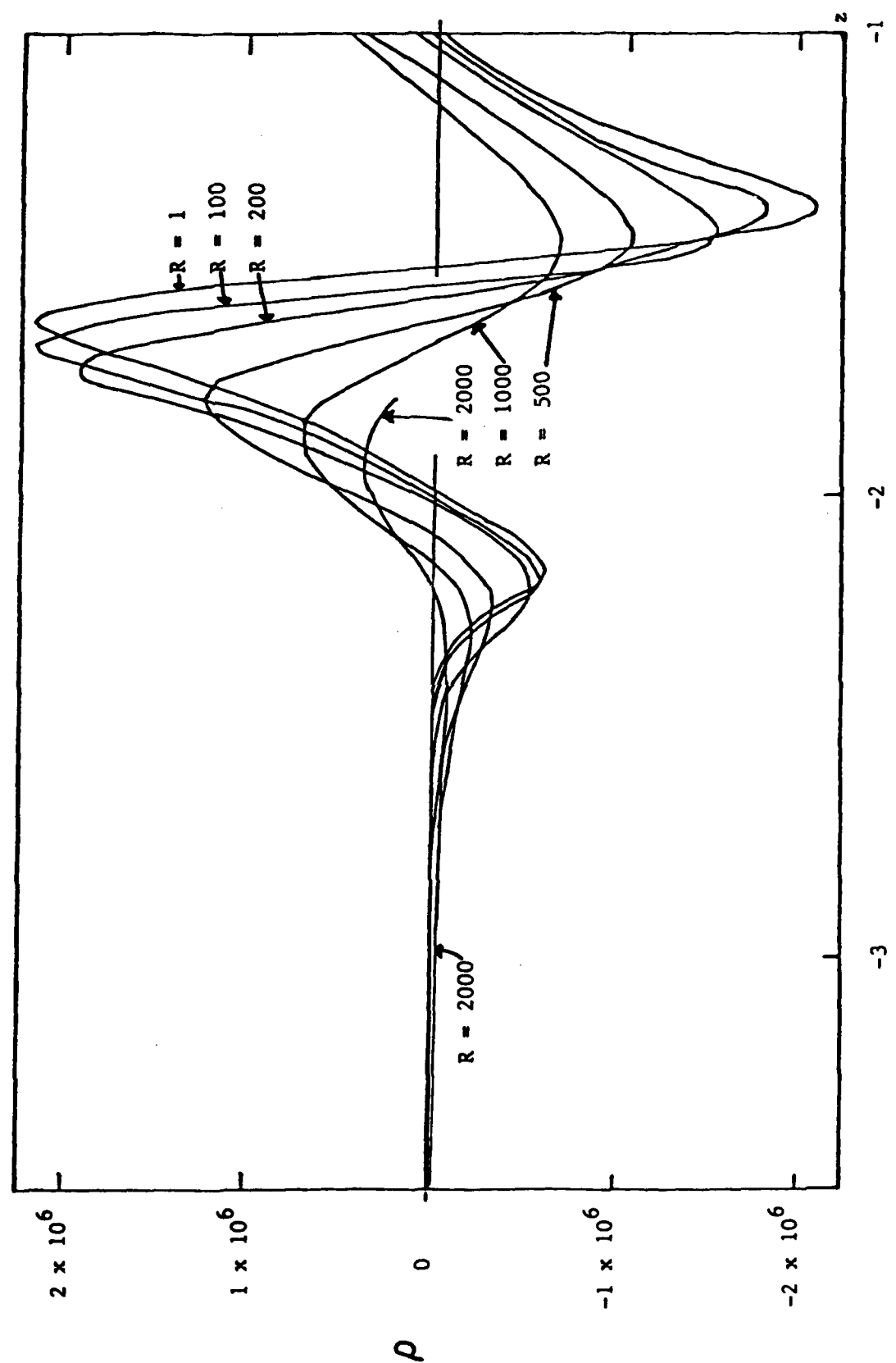


Fig. 13 The space-charge as a function of z near the leftmost edge of the interference pattern, for the steady-state and various values of R . Except for R , the standard parameter set is assumed with $M = .5$.

5. REFERENCES

1. M. Sparks, "Preliminary Report on the Mathematics of Photo-refractivity", Appendices A and B in Phase Conjugate Optics (G. J. Dunning, et al), Hughes Research Laboratories, AFSC Annual Report, 1981, F19628-80-C-0185.
2. N. K. Madsen and R. F. Sincovec, "PDECOL, General Collocation Software for Partial Differential Equations", ACM Trans. on Math Software, 5, 326 (1979).
3. H. B. Dwight, Tables of Integrals and Other Mathematical Data, 4th ed., Macmillan, N. Y., 1962.
4. C. Kittel, Introduction to Solid State Physics, 3rd ed., Wiley, N. Y., 1966.

IV. ELECTRON TRANSPORT

A. SOLUTION OF THE ELECTRON TRANSPORT EQUATION BY THE METHOD OF DISCRETE ORDINATES

1. Introduction

Solutions of electron transport problems were obtained by the method of discrete ordinates (S_N) using both computer codes written by ARCON personnel and discrete ordinates codes originally written for the solution of neutron transport problems in nuclear reactors. It was found that developing and using our own discrete ordinates codes provided us with the means and insight to take advantage of the powerful S_N transport codes available from the nuclear engineering field. Development of the ARCON S_N codes led to our adaptation of ONETRAN⁽¹⁾, the finite element, multigroup, discrete ordinates computer code (developed at Los Alamos National Laboratory), to the solution of electron transport problems. With both the ARCON codes and ONETRAN we were able to obtain electron energy and charge deposition profiles in metals which compared very well with other methods of transport calculation, Monte Carlo and semi-analytical approximation, as will be shown. We begin this discussion with an outline of the method of discrete ordinates (S_N).

2. The Method of Discrete Ordinates-General Discussion

The basic discrete ordinates (S_N) algorithm was originated by Carlson and Lathrop⁽²⁾. The original work was performed to solve neutron transport problems. Indeed all major efforts in S_N have been directed toward neutral particle transport (this includes photons) due to the high level of interest in nuclear reactor flux calculations and shielding studies. Since electron and photon transport in plane geometry are of interest here, we shall consider the one-dimensional version of the discrete ordinate form of the transport equation. This restriction facilitates illustration and does not impose severe limitations on applicability since many experimental situations involve infinite or semi-infinite slab geometry.

In plane geometry, the time-independent transport equation for the particle flux is

$$\mu \frac{\partial \phi}{\partial x} + \sigma(E) \phi(x, \mu, E) = \int_{-1}^1 \sigma_s(\mu', \mu, E) \phi(x, \mu', E) \frac{d\mu'}{\mu'} + q(x, \mu, E), \quad (1)$$

where $\phi(x, \mu, E)$ is the particle flux (particle number density times their speed; in the formulation of the electron transport equation, ϕ is the number density), x is the position coordinate in the transport medium (see Fig. 1), μ is the direction cosine of the particle trajectory with respect to the x -axis, and E is the particle energy. The total interaction cross section is denoted by $\sigma(E)$, while the cross section for scattering from direction μ' to direction μ is denoted by $\sigma_s(\mu', \mu, E)$. The last term, $Q(x, \mu, E)$ is the inhomogeneous source term to account for particle sources which are independent of ϕ .

In the method of discrete ordinates (or S_N method) the angular variable, μ , is discretized into a small number of directions or rays. The transport equation is then written for each ray. Each of these equations, which includes the scattering or re-direction terms for ray-to-ray transfer, can then be solved by either a finite difference approximation scheme for the spatial derivative terms. (An alternative, discrete ordinate method other than S_N involves the treatment of the spatial dependence by a procedure in which the set of discrete ordinate differential equations is solved directly by the matrix eigenvalue method.

Discretization of the angular variable is accomplished by selecting a set of, say, K discrete directions or rays, μ_k , $k=1, 2, \dots, K$ and corresponding quadrature weights w_1, w_2, \dots, w_K , which will be used for numerical integrations over angle. (The most frequent choice for this set of directions and weights is the Gaussian quadrature set since the angular integrations are exact for the order of Legendre series expansion of the flux. The transport equation, (Eqn. 1) is then evaluated at each of the discrete directions, μ_k , so that the K discrete ordinate equations are

$$\begin{aligned} \mu_k \frac{\partial}{\partial x} \phi(x, \mu_k, E) + \sigma(E) \phi(x, \mu_k, E) = & \quad (2) \\ \sum_{j=1}^K w_j \sigma_s(\mu_j, \mu_k, E) \phi(x, \mu_j, E) + & \\ Q(x, \mu_k, E), \quad k=1, 2, \dots, K. & \end{aligned}$$

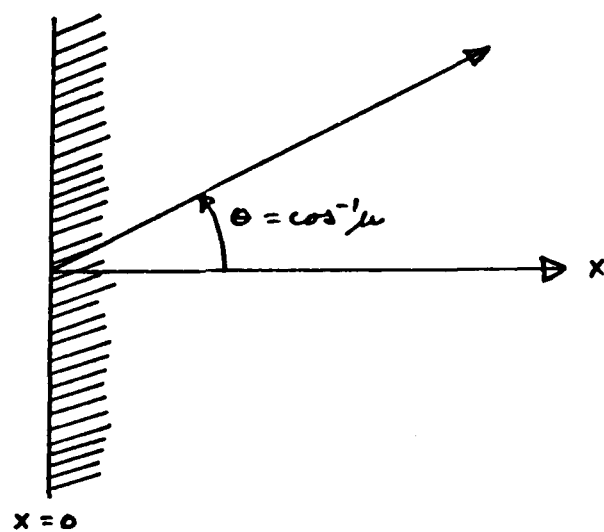


Figure 1. One-dimensional slab geometry

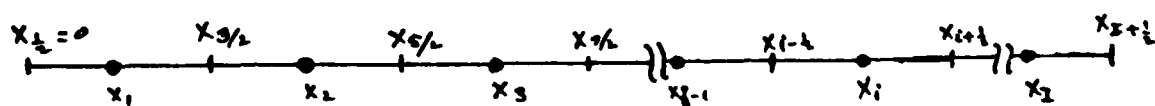


Figure 2. Spatial mesh for discretization of discrete ordinates equations

At this point it is opportune to suppress the energy dependence of the variables in Eqn. 2. In fact, energy dependent problems are solved using the multigroup approach in which the range of particle energies is divided into a number of energy groups and the discretized transport equation is then solved using "group-averaged" quantities (flux, cross sections and sources) for each group. The down-scatter or up-scatter of particles from one energy to a state of lower or higher energy is accounted for by the inclusion of group-to-group transfer terms which are treated as effective absorptions in the transport equation for a particular group from one group and reappear as source terms (in accordance with particle conservation considerations) in one or more of the other group transport equations. Multigroup S_N computer codes are structured in such a way that the sweep through all energy groups is called "outer iteration" while the iterative process for the solution of the spatial dependence of the flux (to be discussed next) is known as "inner iteration". If only down-scattering is present, i.e. scattering from a group of higher energy to a group of lower energy, as is the case for electrons and photons, only one outer iteration is necessary. It is by this method of energy discretization that explicit energy dependence is removed from the discrete ordinate equations.

This multigroup approximation method then allows us to focus our attention on the numerical solution of the one-speed or "in group" transport equation. If for simplicity we omit an index denoting the energy group under consideration, Eqn. 2 now takes the form

$$\mu_k \frac{d}{dx} \phi(x, \mu_k) + \sigma \phi(x, \mu_k) = \sum_{j=1}^K w_j \sigma_s(\mu_j, \mu_k) \phi(x, \mu_j) + Q(x, \mu_k), \quad (3)$$

$$k = 1, 2, \dots, K$$

where it is to be understood that the notation ϕ, σ, Q now refer to quantities for a particular energy group, and the source term Q includes "in-scatter" sources from other groups.

The spatial discretization of Eqn. 3 is accomplished by the introduction of a spatial mesh x_1, x_2, \dots, x_I , where x_I is the midpoint of the i -th mesh cell (see Fig. 2). The boundaries of the i -th cell are denoted by $x_{I+\frac{1}{2}}$. These must also be made to coincide with material boundaries, for obvious reasons (i.e. variation of cross section values with material; imposition of boundary

conditions). If the spatial cell width is defined for the i -th cell as

$$\Delta x_i = x_{i+\frac{1}{2}} - x_{i-\frac{1}{2}}, \quad (4)$$

then the finite differenced form of Eqn. 3 can be written as

$$\begin{aligned} \mu_k \frac{(\phi_k^{i+\frac{1}{2}} - \phi_k^{i-\frac{1}{2}})}{\Delta x_i} + \sigma \phi_k^i = \\ \sum_{j=1}^K w_j \sigma_s(\mu_j, \mu_k) \phi_j^i + S_k^i, \end{aligned} \quad (5)$$

where the superscripts refer to quantities in the i -th spatial cell, and the subscripts refer to the k -th angular ordinate. The quantities $\phi^{i+\frac{1}{2}}$ are the flux values at the edges of cell i , while the quantities ϕ and Q are the average values of the flux and source terms for cell i . Clearly Eqn. 5 cannot be solved without further information, since it is a system of IK equations with $(2I+1)K$ unknowns [$(I+1)K$ values of the cell edge fluxes plus IK values of the cell average fluxes]. What is needed here is a means for relating cell-edge fluxes to cell-average fluxes.

2.1 The Diamond Difference Approximation

The simplest scheme for reducing the number of unknowns is given by the "diamond difference" (2) approximation in which the cell-center flux is taken to be the simple average of the cell-edge fluxes, or

$$\phi_k^i = \frac{1}{2} (\phi_k^{i+\frac{1}{2}} + \phi_k^{i-\frac{1}{2}}) \quad (6)$$

Then Eqn. (5) becomes

$$\mu_k \frac{(\phi_k^{i+\frac{1}{2}} - \phi_k^{i-\frac{1}{2}})}{\Delta x_i} + \sigma \frac{(\phi_k^{i+\frac{1}{2}} + \phi_k^{i-\frac{1}{2}})}{2} = S_k^i, \quad (7)$$

where the source term on the right, S_k^i , is the sum of the in-scattering source term plus the fixed source term; that is

$$S_k^i = \sum_{j=1}^K w_j \sigma_s(\mu_j, \mu_k) \phi_j^i + Q_k^i. \quad (8)$$

The solution process of Eqn. 7 is an iterative one. It is assumed that S_k^i is known. Eqn. 7 is solved for the edge fluxes with either a forward or backward sweep through the spatial mesh, depending on the boundary conditions and direction of μ_k . The diamond difference approximation is then applied to obtain the cell center flux values from which an updated estimate of S_k^i is obtained. Then the entire process is repeated as many times as is necessary for convergence of the flux to be achieved. The convergence criterion is usually of the following type:

$$\max \left| 1 - \frac{\phi^{i+\frac{1}{2},n}}{\phi^{i+\frac{1}{2},n-1}} \right| < \epsilon, \quad (9)$$

where, for the n-th iteration, $\phi^{i+\frac{1}{2},n}$ is the cell edge scalar flux given by

$$\phi^{i+\frac{1}{2},n} = \sum_{k=1}^K w_k \phi_k^{i+\frac{1}{2},n}, \quad (10)$$

and ϵ is a small number, usually in the range 10^{-3} to 10^{-5} .

Because of the spatial differencing approximation (Eqn. 6), there are now $(I+1)K$ unknowns in the set of IK equations given by Eqn. 7. This together with K boundary conditions (values of the angular flux at the boundaries) provides sufficient information for a solution. One may solve Eqn. 7 explicitly for either $\phi_k^{i+\frac{1}{2}}$ or $\phi_k^{i-\frac{1}{2}}$:

$$\phi_k^{i+\frac{1}{2}} = \left(\frac{2\mu_k - \sigma \Delta x_i}{2\mu_k + \sigma \Delta x_i} \right) \phi_k^{i-\frac{1}{2}} + \frac{2\Delta x_i S_k^i}{2\mu_k + \sigma \Delta x_i}, \quad (11a)$$

$$\text{or } \phi_k^{i-\frac{1}{2}} = \left(\frac{2\mu_k + \sigma \Delta x_i}{2\mu_k - \sigma \Delta x_i} \right) \phi_k^{i+\frac{1}{2}} + \frac{2\Delta x_i S_k^i}{-2\mu_k + \sigma \Delta x_i}. \quad (11b)$$

The choice of which of these equations to use, the positive sweep, Eqn. 11a, or the negative sweep, Eqn. 11b, depends on whether the particular angle μ_k is forward or back directed. That is, if one knows the value of the incoming flux, $\phi_k^{1/2}$, ($\mu_k > 0$) at the left boundary of the slab ($x=0$), then it is necessary to use Eqn. 11a to obtain $\phi_k^{3/2}$, $\phi_k^{5/2}$, ..., $\phi_k^{I+1/2}$ for $\mu_k > 0$. Then on the reverse sweep ($\mu_k < 0$) the known flux value on the right boundary, $\phi_k^{I+1/2}$, is used to initiate this sequential calculation for $\phi_k^{I-1/2}$, $\phi_k^{I-3/2}$, ..., $\phi_k^{1/2}$. In general, it may be said that Eqns. 11a, 11b are used on an alternating basis, the first for $\mu_k > 0$ and the second for $\mu_k < 0$.

The above solution scheme, utilizing the diamond difference approximation, is the basis for many discrete ordinates computer codes. The ARCON transport code, BEAMSRC, makes use of it in calculating charge distributions, backscatter and transmission current fractions, and energy deposition profiles resulting from an electron beam incident on Aluminum. Another ARCON S_N code, UNISORC, also utilizes the diamond difference approximation to calculate particle fluxes resulting from distributed sources in one and two material region slab geometry. Some results obtained with these codes will be shown in a later section.

2.2 Coarse Mesh Rebalance

ARCON discrete ordinates codes as well as most standard S_N codes make use of a convergence acceleration device known as coarse mesh rebalance. The principle employed here is that of invoking particle conservation at coarse spatial mesh intervals to correct for accumulated spatial discretization and flux extrapolation errors. The rebalance computation is usually done after every iteration early in the S_N calculation and then on an intermittent basis, perhaps every five or ten iterations, for the remainder of the calculation. We have found that solution convergence speed can be increased by as much as a factor of two when this procedure is employed.

The particle conservation equations for coarse mesh rebalance are obtained as follows⁽³⁾: the fine mesh grid is divided into a number, M , of coarse mesh intervals of equal size δx such that (see Fig. 3)

$$\delta x = \frac{I}{M} \Delta x, \quad (12)$$

where, as before, I is the total number of fine mesh cells of width Δx (for the sake of simplicity we restrict ourselves to a one-material medium

of constant fine mesh width Δx - extension to multilayered media is straightforward). The particle

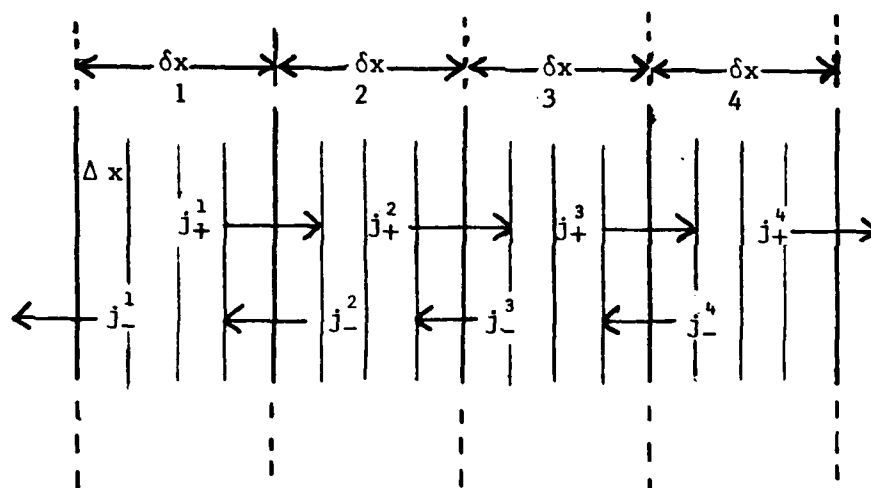


Figure 3. Coarse mesh overlay configuration
I=16, M=4

currents crossing the m -th coarse mesh cell boundaries are given as j_{\pm}^m where the (\pm) denotes crossing the right (+) and left (-) boundaries, respectively. The j_{\pm}^m are defined in terms of the angular fluxes at these boundaries by

$$j_{+}^m = \int_0^1 \mu \phi(\mu)^{m+\frac{1}{2}} d\mu \quad , \text{ and } j_{-}^m = \int_{-1}^0 \mu \phi(\mu)^{m-\frac{1}{2}} d\mu \quad (13)$$

In our S_N programs, these integrals are evaluated by Gaussian quadrature. Then for the configuration of Fig. 3 the particle balance equations are

$$\begin{aligned} (j_{+}^1 - j_{-}^1) + j_{-}^2 + \sigma_a \phi^1 \delta x &= S^1 \delta x & (\text{cell 1}) \\ (j_{+}^2 - j_{-}^2) - (j_{+}^1 - j_{-}^3) + \sigma_a \phi^2 \delta x &= S^2 \delta x & (\text{cell 2}) \\ (j_{+}^3 - j_{-}^3) - (j_{+}^2 - j_{-}^4) + \sigma_a \phi^3 \delta x &= S^3 \delta x & (\text{cell 3}) \\ (j_{+}^4 - j_{-}^4) - (j_{+}^3) + \sigma_a \phi^4 \delta x &= S^4 \delta x & (\text{cell 4}) \end{aligned} \quad (14)$$

net flow across
removal
sources
cell boundaries
term
(scattering

plus fixed)

were, in the above equations, σ_a is the absorption cross section and the ϕ^m and S^m are the sums, over all fine mesh cells in coarse mesh cell m , of the cell - center scalar fluxes and sources. These balance equations would be exact if the $\phi^m \delta x$ and $S^m \delta x$ were defined as true integral quantities $\int_{\delta x} \phi dx$ and $\int_{\delta x} s dx$, but since spatial discretization is inherent in the flux and source computations on the fine mesh, such integrations would not significantly improve the calculation.

In actual fact, the j_+^m do not satisfy Eqn. (14) due to discretization errors. They can however be forced to satisfy a similar set of relations if they are multiplied by a set of rebalance factors, f_m , which are actually measures of the extent to which deviation from particle conservation is present. When this is done, the balance equations become

$$\begin{aligned}
 f_1(j_+^1 - j_-^1) + f_2 j_-^2 + \sigma_a f_1 \phi^1 \delta x &= S^1 \delta x \\
 f_2(j_+^2 - j_-^2) - f_1 j_+^1 + f_3 j_-^3 + \sigma_a f_2 \phi^2 \delta x &= S^2 \delta x \\
 f_3(j_+^3 - j_-^3) + f_2 j_+^2 + f_4 j_-^4 + \sigma_a f_3 \phi^3 \delta x &= S^3 \delta x \\
 f_4(j_+^4 - j_-^4) - f_3 j_+^3 + \sigma_a f_4 \phi^4 \delta x &= S^4 \delta x
 \end{aligned}
 \tag{15}$$

In these equations the unknowns are the rebalance factors f_m , and the solution is readily obtainable via matrix inversion. The next step is to multiply the fine mesh angular flux values by their appropriate rebalance factor. The S_N calculation then continues using these "corrected" flux values.

In the ARCON S_N codes one has the choice of using or not using the coarse mesh rebalance option. If it is used, one may then choose the number of coarse mesh intervals desired as well as the number of iterations between rebalances. An interesting consequence of using coarse mesh rebalance is the following: the iterative solution of Eqn. (5) can be thought of as an order-of-scattering development. That is, each iteration corresponds to an order of scattering. This, however, is no longer true when coarse mesh rebalance is used, and while convergence of the solution will in general be obtained more quickly with it, the converged solution itself may be slightly different (4th place and beyond) as a result.

The Los Alamos code, ONETRAN, implements coarse mesh rebalance only by specifying the coarse mesh cell boundaries to be coincident with the material boundaries of the scattering medium. Thus, for a one material medium, coarse mesh rebalance actually amounts to whole system rebalance.

2.3 The Finite Element or Linear Discontinuous Flux Extrapolation Scheme

There are, in addition to diamond difference, several flux extrapolation schemes of higher order approximation. The principal advantage in using these schemes is that converged, stable flux solutions may be obtained using a coarser spatial mesh than that required for the diamond difference solution of the same accuracy. Another advantage is that the computation of negative fluxes (an obviously non-physical numerical artifact), while not uncommon in the diamond difference case, occurs with much less frequency when a higher order scheme is used. When negative fluxes do occur, in diamond difference codes the standard fix-up procedure is to reset the negative flux values to zero and then proceed to the next iteration. The number of iterations required to achieve convergence is increased accordingly, thus prolonging the length of the overall computation time. This problem can be particularly severe when the flux is sharply increasing or decreasing over a short distance, such as may occur at or near a material interface.

Since we make extensive use of ONETRAN in our electron transport calculations, the linear discontinuous scheme, implemented in ONETRAN, is briefly discussed here. The flux and source functions within a mesh cell are expanded in terms of a set of piecewise linear basis functions. It is also assumed that the flux and source functions are discontinuous at the mesh cell boundaries. Eventually, in practice after a sufficient number of iterations, the magnitude of the discontinuity becomes small as the problem converges and is in fact inconsequential particularly if cell center rather than edge fluxes are of interest. The explicit equations for the cell edge fluxes as they are coded in ONETRAN are (for $\mu_k > 0$)

$$\phi_k^{i+\frac{1}{2}} = \frac{(6\mu_k^2 - 2\mu_k\sigma\Delta x_i)\phi_k^b + \sigma(\Delta x_i)^2 S_k^{i+\frac{1}{2}} + 3\mu_k\Delta x_i(S_k^{i+\frac{1}{2}} + S_k^{i-\frac{1}{2}})}{(6\mu_k^2 + 4\mu_k\sigma\Delta x_i + \sigma^2(\Delta x_i)^2)}, \quad (16)$$

$$\phi_k^{i-\frac{1}{2}} = \frac{(6\mu_k^2 + 4\mu_k\sigma\Delta x_i)\phi_k^b + \sigma(\Delta x_i)^2 S_k^{i-\frac{1}{2}} - \mu_k\Delta x_i(S_k^{i+\frac{1}{2}} - S_k^{i-\frac{1}{2}})}{(6\mu_k^2 + 4\mu_k\sigma\Delta x_i + \sigma^2(\Delta x_i)^2)}, \quad (17)$$

where the quantities $\phi_k^{i+\frac{1}{2}}$, ϕ_k^b , are as shown in Fig. 4,

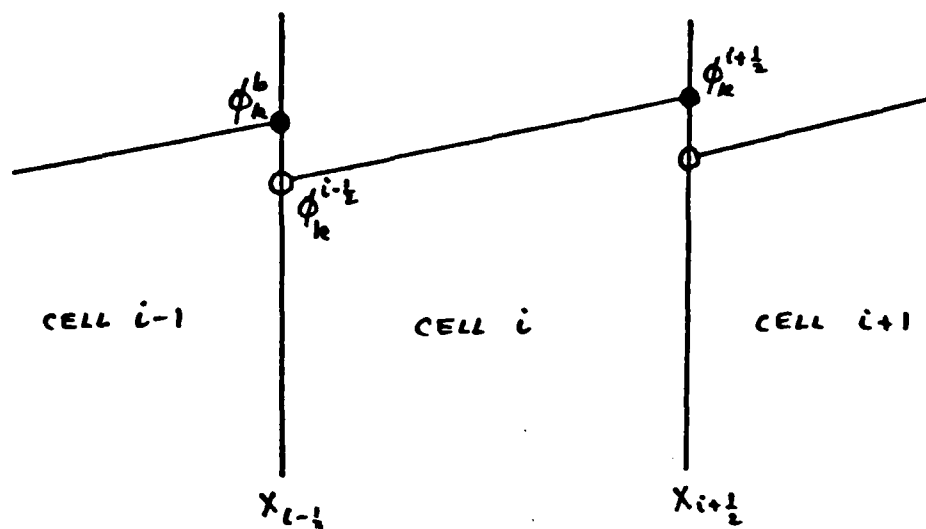


Figure 4. Linear discontinuous representation of the angular flux in the i -th mesh cell. The \bullet indicates actual value of angular flux on the mesh cell boundary. ϕ_k^b is the angular flux from the previous mesh-cell boundary.

with ϕ_k^b being the cell edge flux (right edge) calculated for the $(i-1)$ th cell and $S_k^{i+\frac{1}{2}}$, $S_k^{i-\frac{1}{2}}$ are obtained from their corresponding ϕ values as in Eqn. 8. Similar expressions apply for the left-directed sweep ($\mu_k < 0$).

In general, higher order flux extrapolation schemes are either positive (negative fluxes never occur) or near-positive (negative fluxes very seldom occur). Thus negative flux fixup is unnecessary. Since the linear discontinuous scheme is near positive, ONETRAN does not perform negative flux fixup. (There is an option in ONETRAN where diamond difference is used in which case negative flux fixup is done.)

2.4 The ARCON Discrete Ordinates Code Collection-SNARC

Discrete ordinates codes were written at ARCON for the purpose of testing discrete ordinates algorithms and investigating the feasibility of applying S_N techniques to electron transport problems. Since most, if not all, pre-packaged S_N codes such as DTF69⁽⁹⁾ and ONETRAN⁽¹⁾ were written to incorporate a high degree of flexibility (i.e. the inclusion of plane, spherical and cylindrical geometries, elaborate cross section mixing packages) for use in a large number of neutron applications, it was found

that these codes were unnecessarily large and complicated to use (for rapid job turn-around) as a test bed for electron transport algorithms. For this reason, a collection of smaller codes, SNARC, was written. This set of codes can be classified into three general categories, a code for handling problems involving particle beam sources (BEAMSRC), boundary sources with specifiable angular distributions (ONEDSN) and uniformly distributed sources (UNISORC). The beam source code is constructed to perform multigroup calculations. All three codes employ the diamond difference approximation and apply only to plane or slab geometry. These codes can accept as input either a scattering or redistribution probability function in analytic form or Legendre coefficients of series approximations to the redistribution function. Validity of implementation of the S_N algorithm by these codes has been tested against published benchmark solutions. We will now show examples of the results obtained.

2.4.1 Program ONEDSN

Our first example is a comparison of the results of ONEDSN with the analytical calculations of Ishiguro⁽⁴⁾ who obtained transmission fractions and flux distributions through single and double slabs for isotropic and anisotropic scattering using Case's method.⁽⁵⁾ Table 1 shows our results alongside those of Ref. 4 for the case of anisotropic scattering in two adjacent slabs, each of unit thickness, with unit incident flux whose angular distribution is given by

$$\phi(\mu) = 4\mu^2 \quad (18)$$

on the vacuum surface of the left slab (Fig. 5)

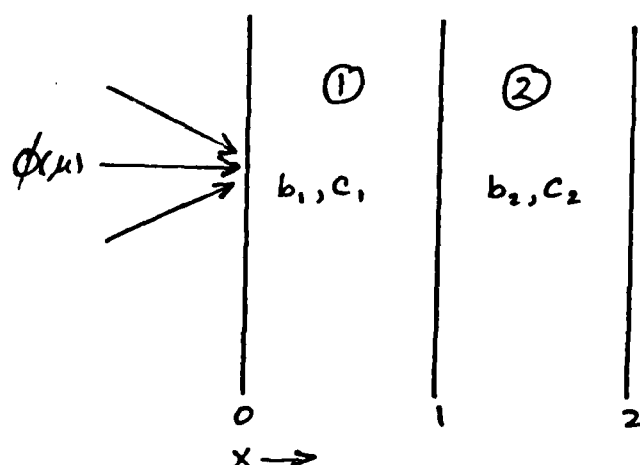


Figure 5. Problem geometry for comparison of ONEDSN calculations with Ref. 4.

The two media are characterized by their different albedos, $c_1=0.9$, $c_2=0.8$ and coefficients of scattering anisotropy, b_1 and b_2 . Our angular redistribution function is given by

$$f(\mu, \mu') = \frac{1}{2} (1 + b \mu \mu') \quad (19)$$

Four cases were studied: $b_1=b_2=0.0$ (isotropic scattering); $b_1=0.0$, $b_2=0.5$; $b_1=0.5, b_2=0.0$; $b_1=0.5, b_2=0.5$.

TABLE I

Comparison of ONEDSN calculations with those of Ishiguro (Ref. 4)

		$b_1=0.0, b_2=0.0$		$b_1=0.0, b_2=0.5$		$b_1=0.5, b_2=0.0$		$b_1=0.5, b_2=0.5$	
	X	ONEDSN	REF. 4.	ONEDSN	REF. 4.	ONEDSN	REF. 4.	ONEDSN	REF. 4.
FLUX	0.0	2.1624	2.1635	2.1450	2.1461	2.1118	2.1129	2.0921	2.0932
	0.4	2.0042	2.0046	1.9720	1.9724	2.0163	2.0167	1.9819	1.9823
	0.8	1.5686	1.5690	1.5218	1.5222	1.6346	1.6350	1.5862	1.5866
	1.2	1.1113	1.1117	1.0805	1.0809	1.1842	1.1846	1.1532	1.1537
	1.6	0.7527	0.7529	0.7560	0.7563	0.8006	0.8009	0.8054	0.8057
	2.0	0.4131	0.4131	0.4393	0.4393	0.4389	0.4389	0.4675	0.4675
TRANSMISSION FRACTION		0.2609	0.2609	0.2763	0.2763	0.2767	0.2767	0.2935	0.2935

The transmission results are identical to the fourth decimal place. The flux error tolerance used in the ONEDSN calculations was 10^{-6} .

In addition to these cases, ONEDSN results were also obtained for a plane isotropic flux source and a plane cosine flux source on the left surface of both single and two slab media. The flux and emergent currents were compared with Ref. 4, and agreement was found to be excellent. It should also be pointed out here that neither coarse mesh rebalancing nor negative flux fixup was employed here. ONEDSN represents our simplest S_N code version. A code listing is provided in Vol. II.

2.4.2 Application of Program BEAMSRC to Henyey-Greenstein Scattering

The next example of the performance of the ARCON S_N code is a comparison of results obtained using BEAMSRC for a monodirectional particle beam incident on a slab with published data (Van de Hulst, Ref. 6) obtained with Case's eigenfunction method. The angular redistribution function is given by the Henyey-Greenstein formula (6)

$$f(\mu, \mu') = \frac{2}{\pi} \left[\frac{(1-g^2)}{\sqrt{\alpha+\beta}} (\alpha-\beta) \right] E(k^2), \quad (20)$$

where g is the asymmetry factor ($0 \leq g \leq 1.0$),

$$\alpha = 1 + g^2 - 2g\mu\mu',$$

$$\beta = 2g \sqrt{(1-\mu^2)(1-\mu'^2)},$$

$$k^2 = \frac{2\beta}{\alpha+\beta},$$

and $E(k^2)$ is the complete elliptic integral.

In Table 2 we present comparisons of transmission and backscatter fractions for the cases of a normally incident beam on two slabs of thickness $T=1.0$ and $T=2.0$ mean full paths, for two g values (0.5 and 0.75), and two albedo values ($c=1.0$, $c=0.4$). The notation (a,b,c,d) in this table refer to the following four cases of spatial and angular discretization:

- a) $I=50$, $K=12$
- b) $I=50$, $K=24$
- c) $I=100$, $K=12$
- d) $I=100$, $K=24$

where I and K are the total number of spatial mesh cells and discrete angular ordinates, respectively (as defined earlier in Sec. 1.1). In these, as in all BEAMSRC calculations, coarse mesh rebalance and negative flux fixup were used.

TABLE 2.

Comparison of BEAMSRC transmission and backscatter fractions for Henyey-Greenstein scattering with those of Van de Hulst (Ref. 6) for a normally incident beam.

		ALBEDO = 1.0		ALBEDO = 0.4	
		TRANSMISSION	BACKSCATTER	TRANSMISSION	BACKSCATTER
SLAB THICKNESS = 1.0 mfp	g = 0.5	BEAMSRC REF. 6	BEAMSRC REF. 6	BEAMSRC REF. 6	BEAMSRC REF. 6
		a) 0.82596	a) 0.17404	a) 0.48875	a) 0.02769
		b) 0.82597	b) 0.17403	b) 0.48865	b) 0.02751
		0.82389	0.17612	0.48244	0.02688
		c) 0.82491	c) 0.17509	c) 0.48862	c) 0.02789
		d) 0.82492	d) 0.17508	d) 0.48853	d) 0.02770
SLAB THICKNESS = 1.0 mfp	g = 0.75	a) 0.92292	a) 0.07708	a) 0.52289	a) 0.01074
		b) 0.92325	b) 0.07675	b) 0.52300	b) 0.01060
		0.92126	0.07874	0.51656	0.01050
		c) 0.92194	c) 0.07806	c) 0.52297	c) 0.01083
		d) 0.92227	d) 0.07773	d) 0.52308	d) 0.01069
SLAB THICKNESS = 2.0 mfp	g = 0.5	a) .68367	a) .31633	a) .22850	a) .032160
		b) .68375	b) .31625	b) .22844	b) .031963
		.67970	.32030	.22021	.03100
		c) .68163	c) .31837	c) .22805	c) .032514
		d) .68170	d) .31830	d) .22800	d) .032314
SLAB THICKNESS = 2.0 mfp	g = 0.75	a) .84140	a) .15860	a) .26738	a) .012605
		b) .84196	b) .15804	b) .26754	b) .012451
		.83682	.16318	.25710	.01228
		c) .83885	c) .16115	c) .26718	c) .012778
		d) .83940	d) .16060	d) .26734	d) .012622

The listing of BEAMSRC provided in Vol. II is the final version and contains screened-Rutherford rather than Henyey-Greenstein cross sections.

2.4.3 Application of Program BEAMSRC to Electron Transport Problems

In the treatment of electron transport problems, program BEAMSRC was run in both the one-group and multigroup modes. The one-group calculations were performed for two reasons. The first of these is that a set of calculations by Morel(7) exists in the literature for the case of an electron beam normally incident on Aluminum, so that direct comparisons of flux and transmission fractions are possible, thus further validating the S_N algorithm used in the ARCON codes. Secondly, the successful operation of a multigroup electron transport code depends in large measure on the validity of the one-group algorithm.

2.4.3.1 One-Group Calculations

The model assumed for electron scattering is given by the following expression for the screened Rutherford cross section for elastic nuclear scattering(8).

$$\sigma_s(T, \omega) = 2\pi \frac{Z(Z+1)N_a r_o^2}{A} \left[\frac{(T+1)}{T(T+2)} \right]^2 \cdot \frac{1}{(1+\eta-\omega)^2} \quad (21)$$

where

- T = kinetic electron energy in mc^2 (electron rest-mass) units
- Z = atomic number of the transport medium
- N_a = Avogadro's number
- r_o = e^2/mc^2 (classical electron radius)
- A = atomic weight of the transport medium
- η = atomic screening constant
- ω = cosine of the scattering angle.

The units of the cross section are (cm^2/g) . The screening constant η is given by the Moliere formula(7)

$$\eta = 0.5 \left[\frac{z^{1/3}}{.885(137)} \right]^2 \cdot \frac{1}{T(T+2)} \cdot \left[1.13 + 3.76 \left(\frac{z}{137} \right)^2 \frac{(T+1)^2}{T(T+2)} \right]. \quad (22)$$

The angular dependence of the scattering cross section has an anisotropic character which increases with electron energy. This anisotropy is severe enough to cause either numerical instability or very slow convergence in S_N calculations. In order to circumvent this difficulty, a device for removing the anisotropy known as the "extended transport correction" is used.⁽⁷⁾ Briefly, the effect of the transport correction is to separate out the delta function component (no angular deflection) from the scattering cross section, leaving behind a more manageable (weak anisotropy) angular behavior for the cross section. To demonstrate this, we expand the angular part of the scattering cross section in a Legendre series as follows:

$$\sigma_s(\mu, \mu') = \sum_{l=0}^{\infty} (l + \frac{1}{2}) \sigma_l P_l(\mu) P_l(\mu'), \quad (23)$$

where the σ_l are the Legendre coefficients of $\sigma(\mu, \mu')$ given by

$$\sigma_l = \int_{-1}^1 d\mu \sigma(l, \mu) P_l(\mu) \quad (24)$$

and the P_l are Legendre polynomials. Then if we resolve the series in three terms such as

$$\begin{aligned} \sigma_s(\mu, \mu') &= \sum_{l=0}^{L-1} (l + \frac{1}{2}) (\sigma_l - \sigma_0) P_l(\mu) P_l(\mu') \\ &+ \sum_{l=L}^{\infty} (l + \frac{1}{2}) (\sigma_l - \sigma_L) P_l(\mu) P_l(\mu') \\ &+ \sigma \sum_{l=0}^{\infty} (l + \frac{1}{2}) P_l(\mu) P_l(\mu') \end{aligned} \quad (25)$$

we find that if the value of L is chosen such that $(\sigma_0 - \sigma_L)$ is sufficiently small for $l > L$, a condition not difficult to satisfy, then the second term is negligible compared with the first. The third term is identically $\sigma_L \delta(\mu - \mu')$, and we have

$$\sigma_s(\mu, \mu') \approx \sum_{l=0}^{L-1} (l + \frac{1}{2}) (\sigma_l - \sigma_L) P_l(\mu) P_l(\mu') + \sigma_L \delta(\mu - \mu'). \quad (26)$$

Since the δ function does not contribute to the scattered flux (this can be verified by substituting the above expression into the transport equation), it need not be considered further. If we then define the transport corrected cross section coefficients as

$$\sigma_l^* = \sigma_l - \sigma_L, \quad (27)$$

then

$$\sigma_s(\mu, \mu') \approx \sum_{l=0}^{L-1} (l + \frac{1}{2}) \sigma_l^* P_l(\mu) P_l(\mu') + \sigma_L \delta(\mu - \mu'). \quad (28)$$

The Legendre coefficients for the screened Rutherford cross section are most easily evaluated using the following expressions⁽⁷⁾

$$\sigma_l = \sigma_0 [1 - \eta(1 + \eta/2) c_l] \quad (29)$$

where the total scattering cross section σ_0 is given by

$$\sigma_0 = \int_{-1}^1 \sigma(l, \mu) d\mu \quad (30)$$

η is the screening constant (energy dependent), and the C_l are related by the recursion equations

$$\begin{aligned} C_0 &= 0, \\ C_1 &= \ln(1 + \eta/2) - (1 + \eta/2), \\ &\vdots \\ C_{l+1} &= (2 + \frac{1}{l})(1 + \eta)C_l - (1 + \frac{1}{l})C_{l-1} - \frac{(2 + \frac{1}{l})}{(1 + \eta/2)} \end{aligned} \quad (31)$$

The expression for the σ_l^* is then

$$\sigma_l^* = \sigma_0 \eta (1 + \eta/2) (C_l - C_{l-1}). \quad (32)$$

Given that the anisotropy of the scattering cross section can be handled in a feasible manner as shown above, the problem of dealing with a monodirectional beam source requires attention. The difficulty arises when one tries to relate the purely mathematical representation of a delta function in angle to a numerical representation suitable for incorporation into the S_N discrete angle formulation. In fact, the delta function requires an impractically long (if not infinite) Legendre in angle for an adequate representation. To circumvent this difficulty, the unscattered beam source is replaced by a once-scattered source, spatially distributed across the scattering medium, thus removing the problem of having to devise a numerical method for handling delta functions. The once-scattered source is introduced into the S_N calculation as any other

spatially distributed source would be, and the unscattered flux due to the incident beam is treated separately analytically. The expression for the once-scattered source distribution, $Q_1(x, \mu)$, is obtained by direct substitution of the unscattered flux, $\phi_u(x, \mu)$, into the collision density kernel integral. That is

$$Q_1(x, \mu) = \int_{-1}^1 \sigma^*(\mu, \mu') \phi_u(x, \mu') d\mu', \quad (33)$$

where $\sigma^*(\mu, \mu')$ is the transport-corrected scattering cross section. (The subscript 'u' is intended to denote "unscattered".)

The expression for the unscattered flux resulting from a monodirectionally incident beam along direction $\mu_0 (= \cos \theta_0)$ is (see Fig. 6)

$$\phi_u(x, \mu) = e^{-x/\lambda^* \mu_0} \delta(\mu - \mu_0) \quad , \quad (34)$$

where λ^* is the total transport-corrected electron mean free path given by

$$\lambda^* = \frac{1}{\sigma_0^* + \sigma_a} = \frac{C}{\sigma_0^*} \quad , \quad (35')$$

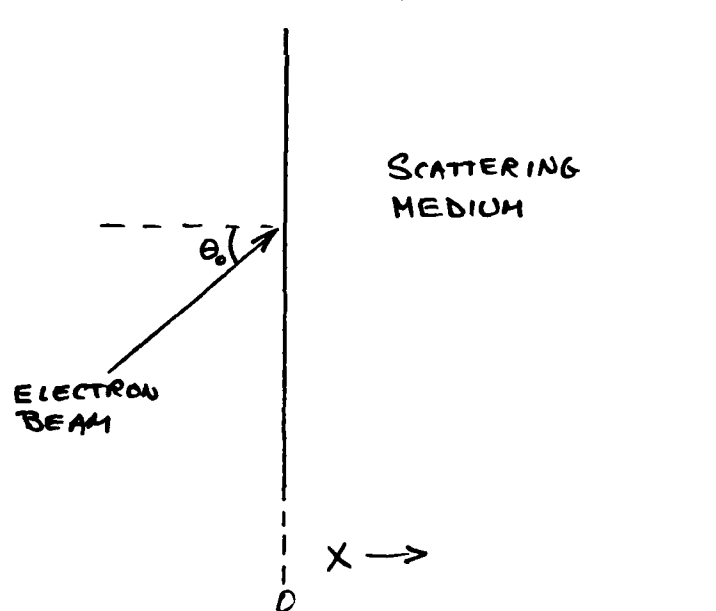


Figure 6. Geometry for electron beam discrete ordinates transport calculation

where σ_a and C are the electron absorption (actually energy downscatter) cross section and albedo, respectively.

Then

$$Q_1(x, \mu) = e^{-x/\lambda^* \mu} \sum_{l=0}^L (l + \frac{1}{2}) \sigma_e^* P_l(\mu) P_l(\mu_0) , \quad (36)$$

where the Legendre expansion

$$\sigma^*(\mu, \mu') = \sum_{l=0}^L (l + \frac{1}{2}) \sigma_e^* P_l(\mu) P_l(\mu') , \quad (37)$$

has been substituted for the scattering cross section. The expression, Eqn. 36, for the once-scattered source is not difficult to evaluate. Furthermore, the unscattered flux expression as given by Eqn. 34 is already in a useful form for obtaining the dose contribution due to direct radiation. The once-scattered source formulation for handling monodirectional beam sources is not only used in program BEAMSRC. We also employ it in conjunction with ONETRAN. In fact one of the principal functions of BEAMSRC is that sections (or subroutines) of it provide pieces of code that serve as input data preparation modules for our ONETRAN electron transport calculations.

A set of nine BEAMSRC runs were made for three electron source energies, 0.01, 0.1, and 1.0 Mev, normally incident on three thicknesses of Aluminum. These runs correspond exactly to the set of runs reported in Ref. 7. Comparisons of scalar flux values calculated using BEAMSRC with Morel's results are shown in Figs. 7, 8, 9. The agreement is excellent for all three source energies.

2.4.3.2 Multigroup Calculations

In multigroup S_N calculations the energy group widths, ΔE , are usually obtained by dividing the total energy range of the particle by the number of groups. This simple criterion need not necessarily apply in the

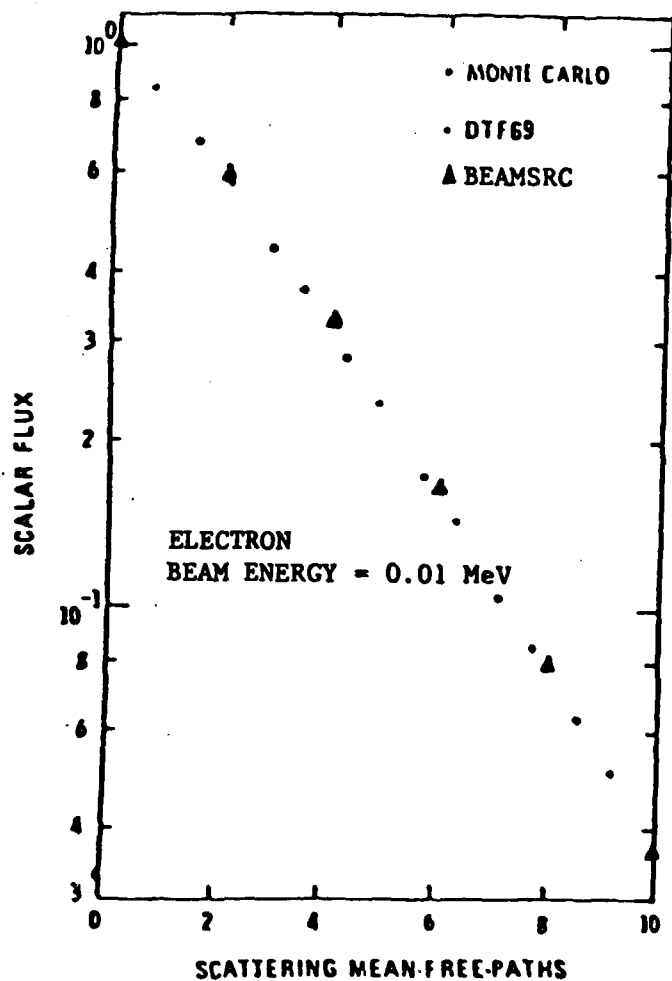


Figure 7.

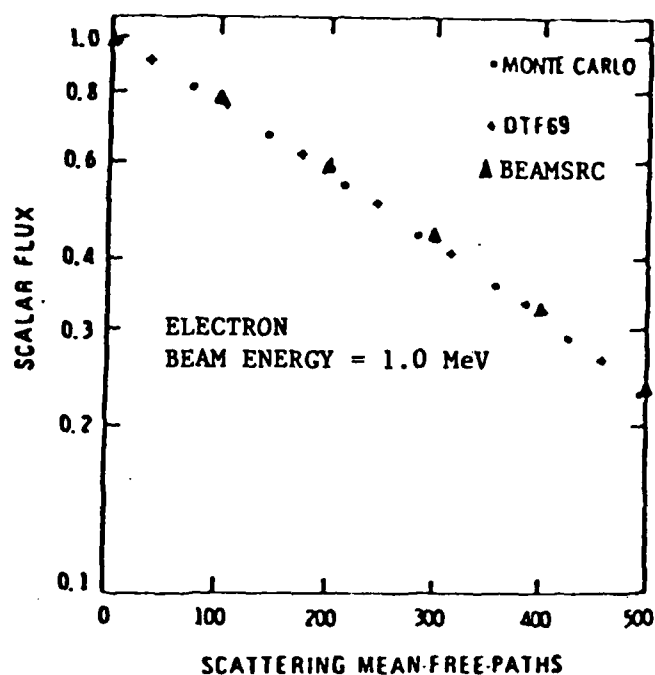


Figure 8.

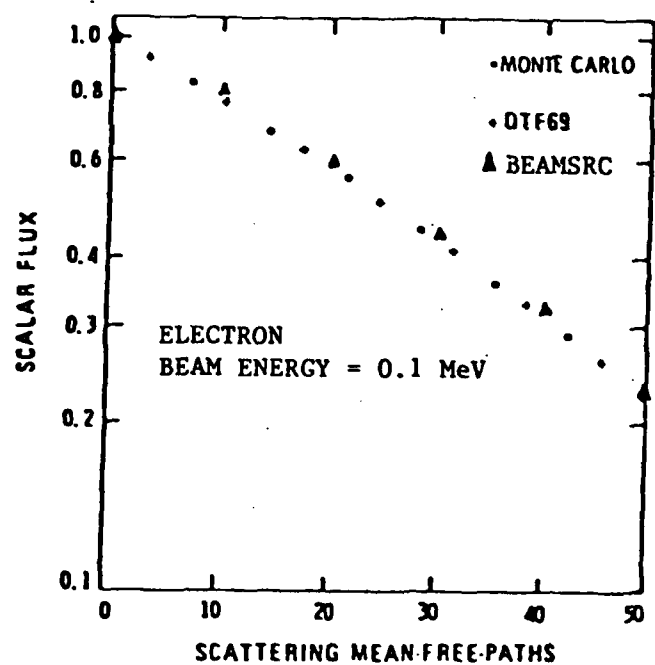


Figure 9.

Figs. 7, 8, 9 (From Ref. 7). Scalar Flux comparisons for normally incident electron beams (Energy = 0.01 MeV, Fig. 7; 0.1 MeV, Fig. 8; 1.0 MeV, Fig. 9) on Aluminum slabs. The •'s and + 's correspond to Monte Carlo and S_N (DTF69) calculations of Ref. 7. The Δ 's represent the BEAMSRC results.

case of the electron transport. For a given change ΔE in electron energy, the average distance or change in pathlength that the electron travels within that energy interval can differ by as much as a factor of 20 in Aluminum over the electron energy range 200 keV down to about 3 keV. This is due to the variation of the material stopping power with energy.

Program BEAMSRC was used as a test bed to determine whether or not adoption of a variable energy group width would be of significant advantage. A criterion was devised for determining the energy group widths in BEAMSRC for which the probability of absorption was the same for all groups (i.e., a constant albedo). Results are shown in Figure 10 for a 20 group test run of BEAMSRC. A 200 keV electron beam was assumed normally incident on an Aluminum slab approximately one electron range in thickness (0.04 g/cm^2). A Gaussian quadrature set of 12 angles (S_{12} calculation) and a 50 mesh cell spatial discretization were used. The curve shows the BEAMSRC results for the energy deposition profile, while the histogram was obtained with the Monte Carlo code, TIGER of the Halbleib and Vandevender⁽¹⁰⁾. The TIGER calculation was made using 10000 electron case histories. The maximum estimated standard error was 4 percent.

It can be seen from Fig. 10 that the energy disposition profiles obtained by the two methods, S_N and Monte Carlo, agree fairly well until about 0.15 g/cm^2 penetration depth. Beyond this point, the S_N curve is consistently higher than the Monte Carlo histogram. This seems to indicate that the variable energy group width scheme may not be optimal at least when used in conjunction with the diamond difference and coarse mesh rebalance of BEAMSRC. As will be shown in section 2.5 a constant energy group width used in conjunction with the finite element spatial differencing scheme of ONETRAN produces better agreement with the Monte Carlo result.

In addition to energy disposition profiles, it is also possible to obtain flux curves as a function of electron energy with the S_N method. An example of a BEAMSRC multigroup flux calculation is shown in Fig. 11 where a 20 keV electron beam was assumed normally incident on a gold target of thickness 0.75 g/cm^2 . The calculation was performed with 20 energy groups, each group having the same albedo. The direct, or unscattered, flux, a decaying exponential is not shown. It can be seen that as the electron energy decreases, the flux asymmetry also decreases, a consequence of multiple scattering.

Program listings of ONEDSN, BEAMSRC and UNISORC, an S_N code for spatially distributed sources, are given in Vol. II.

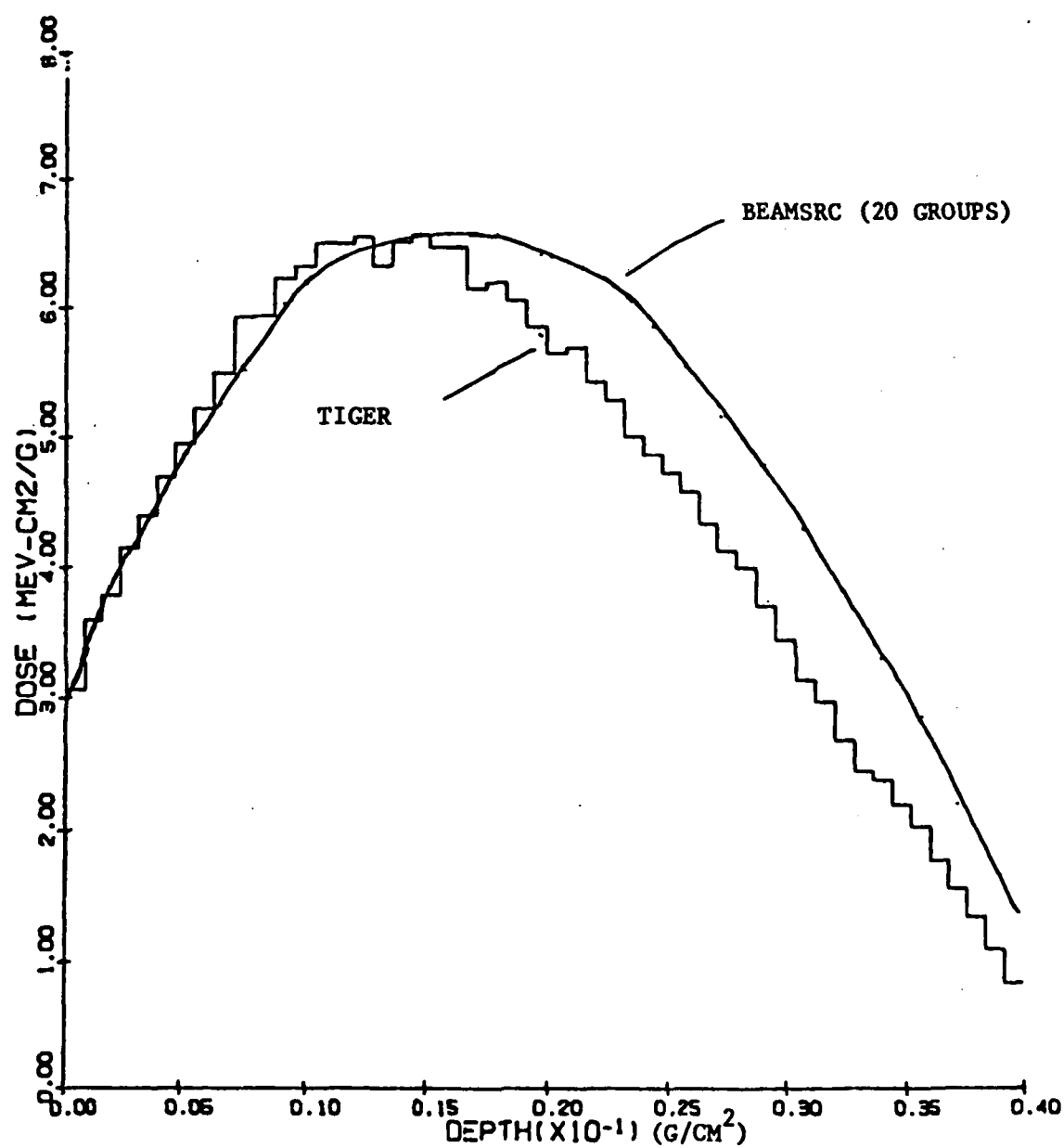


Figure 10. Comparison of Energy Deposition Profiles as Calculated by BEAMSRG and TIGER for 200 keV Electron Beam normally incident on Aluminum.

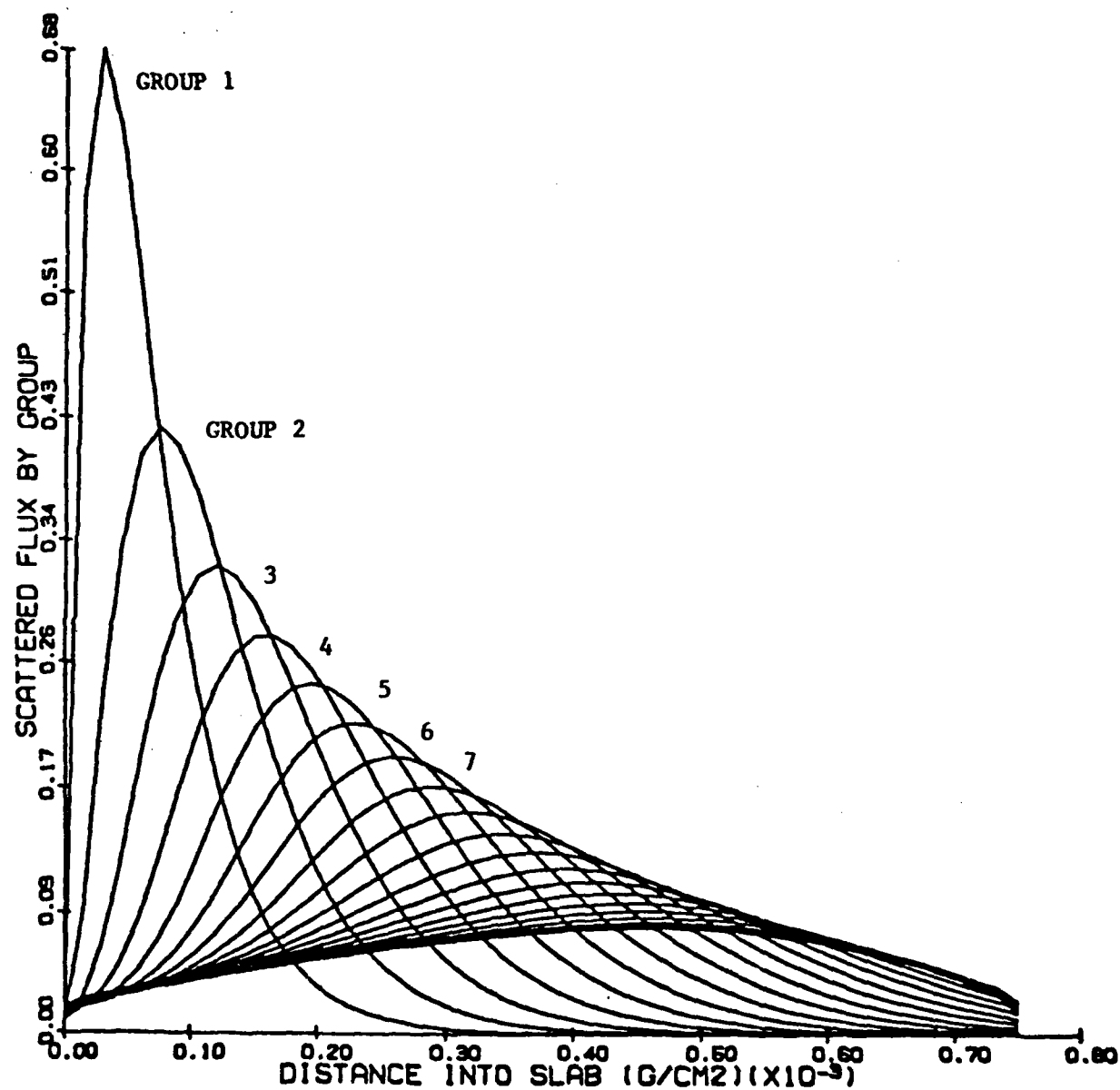


Figure 11. Group Fluxes as Calculated by BEAMSRC
for 20 keV Electron Beam Normally
Incident on Gold.

2.5 Electron Transport Calculations with ONETRAN ⁽¹⁾

Perhaps the most important benefit that was derived from the writing of the SNARC programs (BEAMSRC in particular) was that it greatly aided us in applying ONETRAN to electron transport problems. The process of writing and debugging our own S_N code enabled us to decipher workings of the ONETRAN code by comparing, iteration-by-iteration, the results of ONETRAN (using the diamond difference option) and BEAMSRC for the same problem. Furthermore, the BEAMSRC code provided us with a set of routines for calculating cross sections and source distributions, which we have combined with a set of interface routines to translate these quantities into a ONETRAN compatible input data form. Thus, we have the capability of running ONETRAN for electron transport problems with a minimum of complication. For example, to run a single slab beam problem, the only input data required are the incident beam energy and angle, slab thickness and material, the number of energy groups, the number of spatial mesh cells, and the order of the angular discrete ordinate approximation. With slight variations of this "front-end" code (which we have named ONETRIN) for ONETRAN, we are able to run spatially distributed electron source problems, problems with electron sources with uniform and non-uniform angular distributions located on slab surfaces, and two material interface problems. A program listing of ONETRIN is provided in Vol. II.

Minor modifications were made to the ONETRAN output routines to print out the results in compact form and to generate data files suitable for CRT plots, printer plots and energy deposition calculations.

Examples of energy deposition profile results obtained with ONETRAN for electron beams normally incident on Aluminum slabs are shown in Figures 12-16. The incident beam energies are 0.01 MeV (Fig. 12), 0.05 MeV (Fig. 13), 0.20 MeV (Fig. 14), 0.50 MeV (Fig. 15) and 1.0 MeV (Fig. 16). In all cases there are three curves shown corresponding to 10 group, 20 group and 40 group ONETRAN calculations. The histograms are Monte Carlo results obtained with TIGER⁽¹⁰⁾. The Monte Carlo program was run with 10,000 electron case histories. The slab thicknesses were chosen to correspond to approximately 1.1 electron ranges. As can be seen, the agreement between the ONETRAN curves and the TIGER histograms is very good across the entire range of source energies, and as one might expect, increasing the number of energy groups results in improved agreement between the two methods of calculation. In all cases, extended S_{12} calculations were performed using the transport corrected screened Rutherford cross sections (Eqn. 32). The down-scatter or group-to-group cross sections were calculated using the stopping power formula of Rohrlich and Carlson⁽¹¹⁾. As can be seen, this choice of cross section and stopping power expression seems adequate for the Aluminum calculations. However, some of this success may be fortuitous for the following two reasons: 1) Aluminum is a low z

material, so that errors due to using the screened-Rutherford cross section rather than the Mott cross section are not as serious as would be the case for high z materials; and 2) the Monte Carlo calculations take straggling into account while the S_N calculations do not. A straggling effect is present in the S_N calculations, but it's presence is not legitimate. There is artificial straggling due to the energy discretization, an artifact of the S_N algorithm and has nothing to do with physical straggling.

Figure 17 shows this straggling effect. It is a plot of the energy spectrum of electrons transmitted through a slab of Aluminum of thickness 0.02g/cm^2 (~ 0.5 electron range units) resulting from a 200 keV slant beam ($\cos\theta_0 = .916667$, see Fig. 6) incident on the slab. The histogram represents the TIGER Monte Carlo result in which physical straggling due to inelastic collisions is accounted for. If straggling were not included in the Monte Carlo calculation, that is, if electron energy loss were accounted for only by continuous slowing down, the histogram upper limit would end abruptly at approximately 149 keV. There are five S_N transmission curves in the plot, corresponding to 10, 20, 40, 60 and 80 groups. As would be expected the artificial straggling effect due to energy discretization is reduced as the number of energy groups is increased.

Figures 18 and 19 show electron energy deposition profiles in gold for electron beams with slant incidence given by $\cos\theta_0 = 0.916667$. The source energies are 0.2 meV (Fig. 18) and 1.0 meV (Fig. 19). As in the Aluminum case, three curves are shown in Fig. 18, corresponding to 10, 20 and 40 groups. Also, as before, the S_N results are compared with a TIGER Monte Carlo run. The agreement here is not as good as was found in the Aluminum case. We feel that Mott cross-sections(12) rather than screened-Rutherford would improve the agreement. We plan to install a Mott cross-section package into our S_N electron transport code in the near future in order that high- z materials be treated more correctly.

The two curves in Fig. 19 were both obtained with 40 group calculations. The dotted curve is the energy deposition profile for an S_N calculation with the stopping power expression given by the Rohrlich and Carlson formula(11). The dot-dash curve was obtained using a stopping power corrected for radiative (bremsstrahlung) energy loss. Neither curve matches the Monte Carlo result in an entirely satisfactory manner. In fact, the addition of the radiative stopping power correction seems to exacerbate the problem. The discrepancies shown here clearly point out the necessity for adopting a more physically realistic model for the scattering cross section such as Mott, particularly for the higher electron energies (≥ 1 meV) in high- z materials.

Fig. 12

Electron energy deposition profile in Aluminum
for a normally incident electron beam of energy
0.01 MeV .

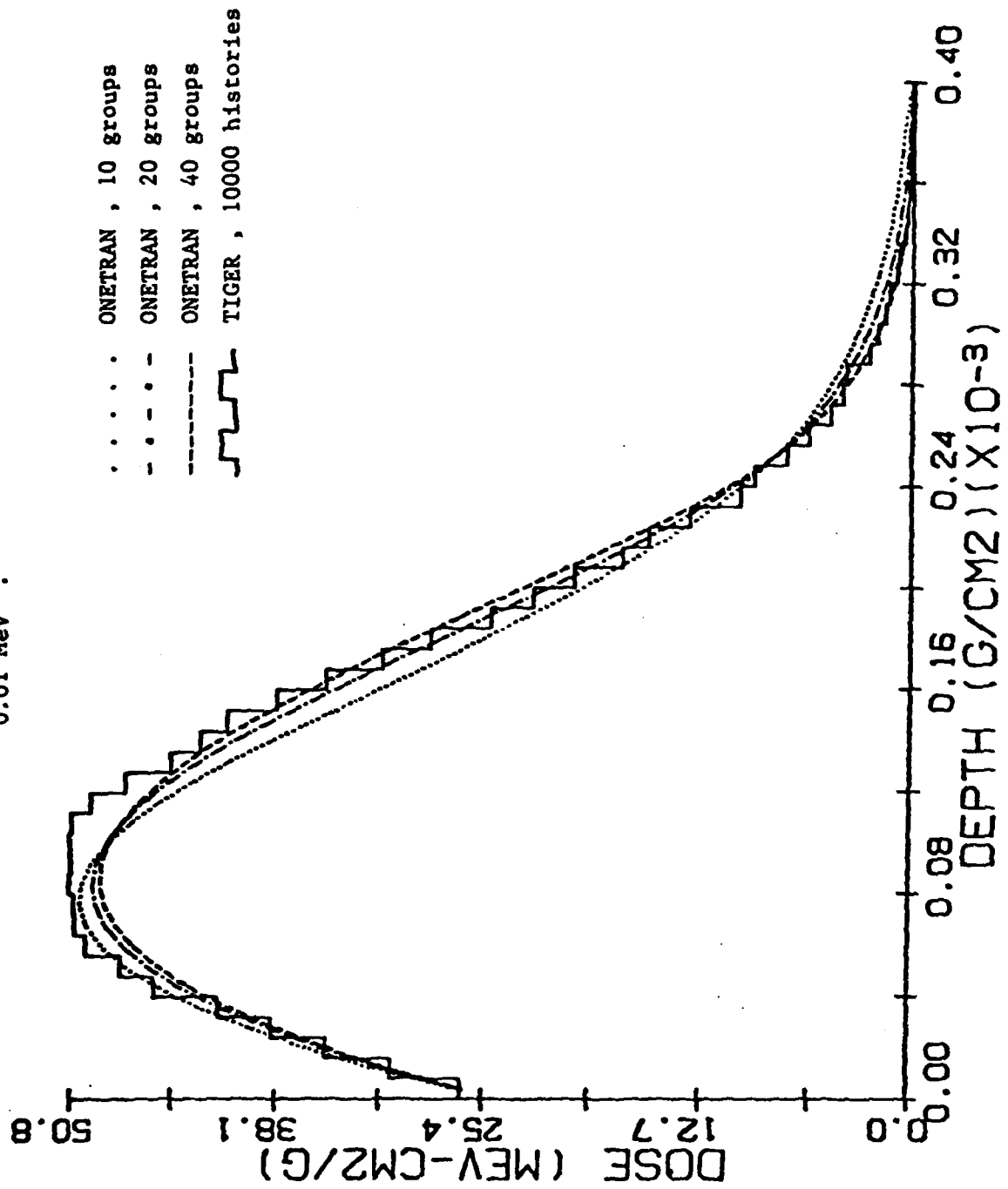


Fig. 13

Electron energy deposition profile in Aluminum
for a normally incident electron beam of energy
0.05 MeV .

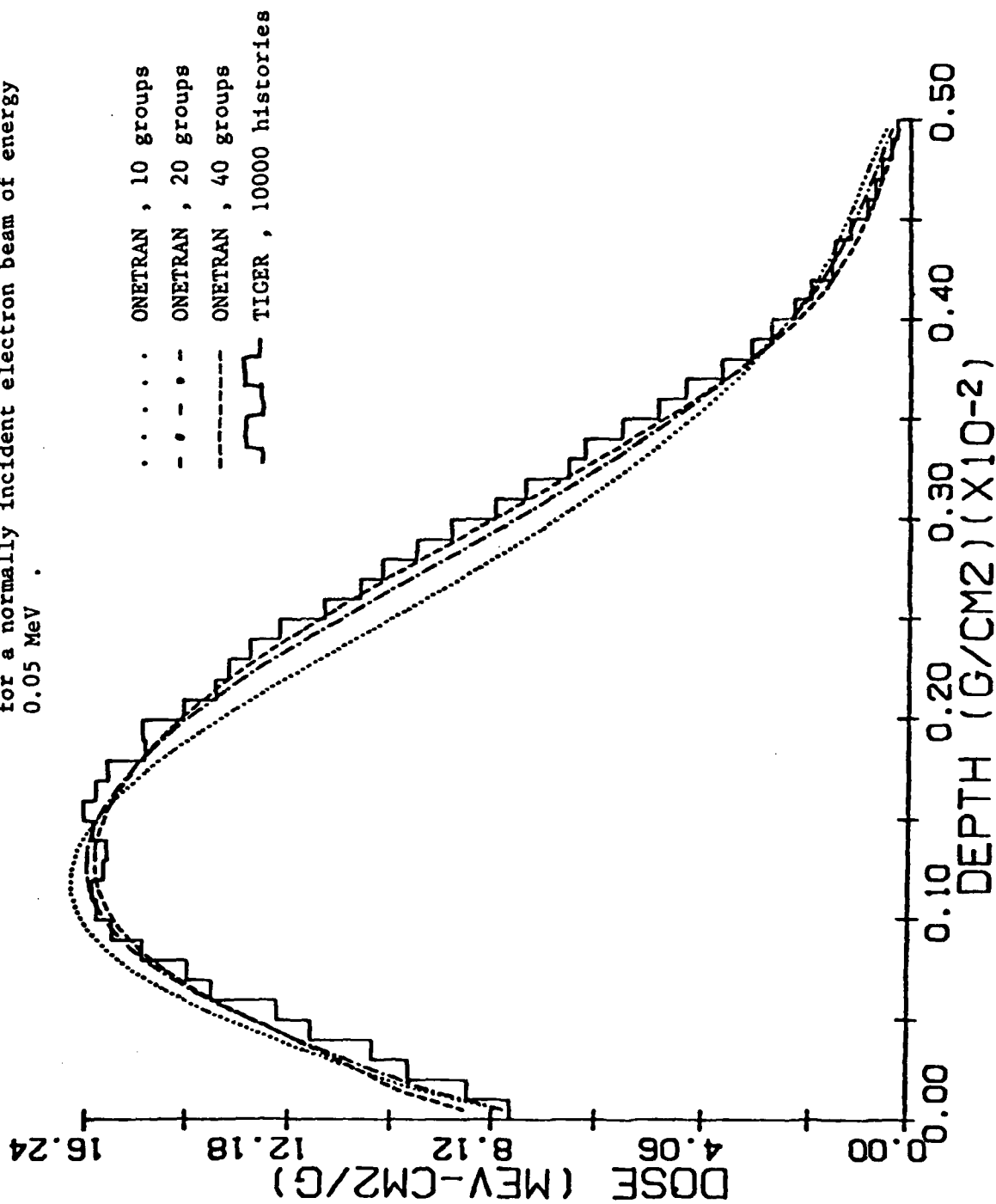


Fig. 14

Electron energy deposition profile in Aluminum
for a normally incident electron beam of energy
0.20 MeV .

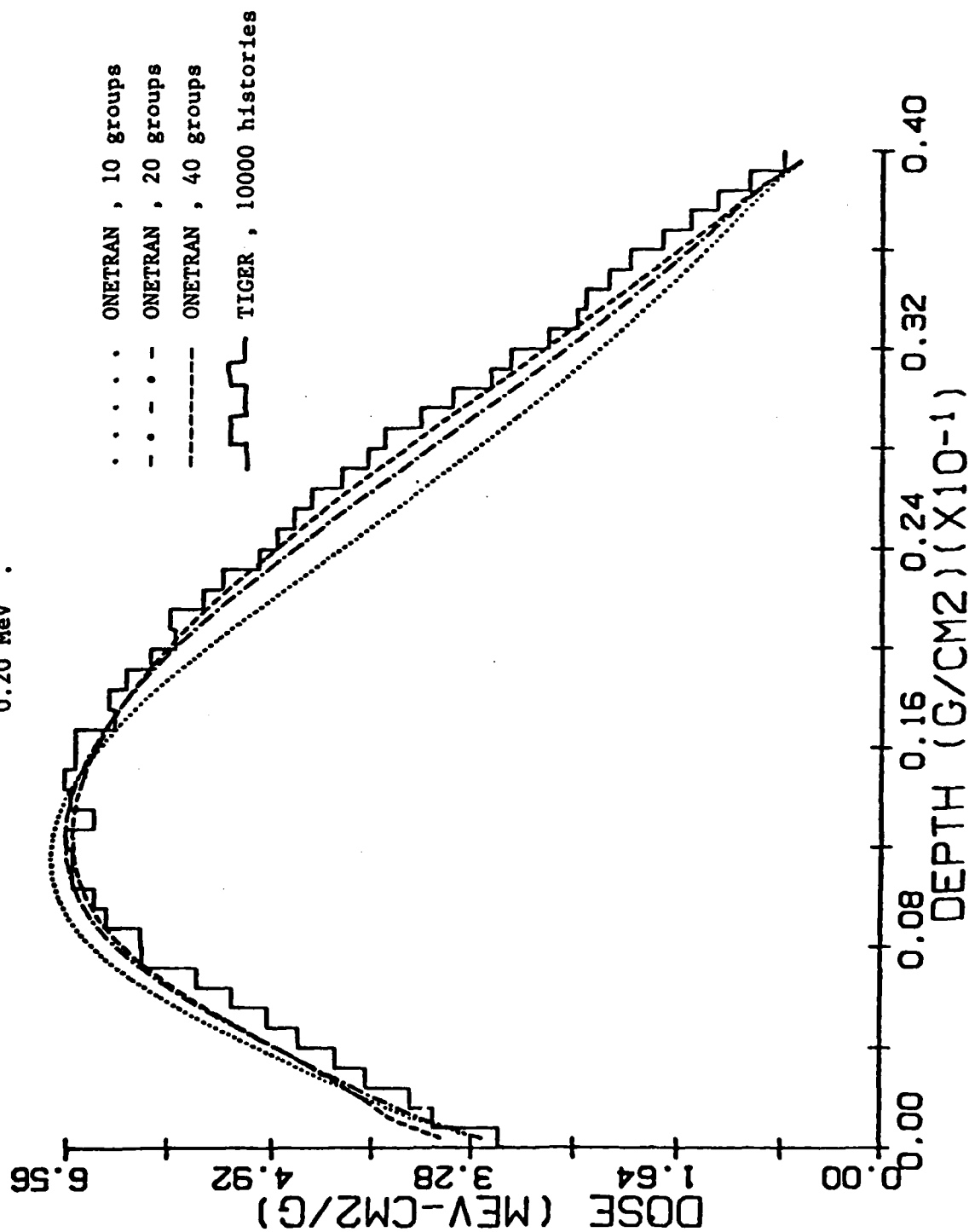


Fig. 15

Electron energy deposition profile in Aluminum
for a normally incident electron beam of energy
0.50 MeV .

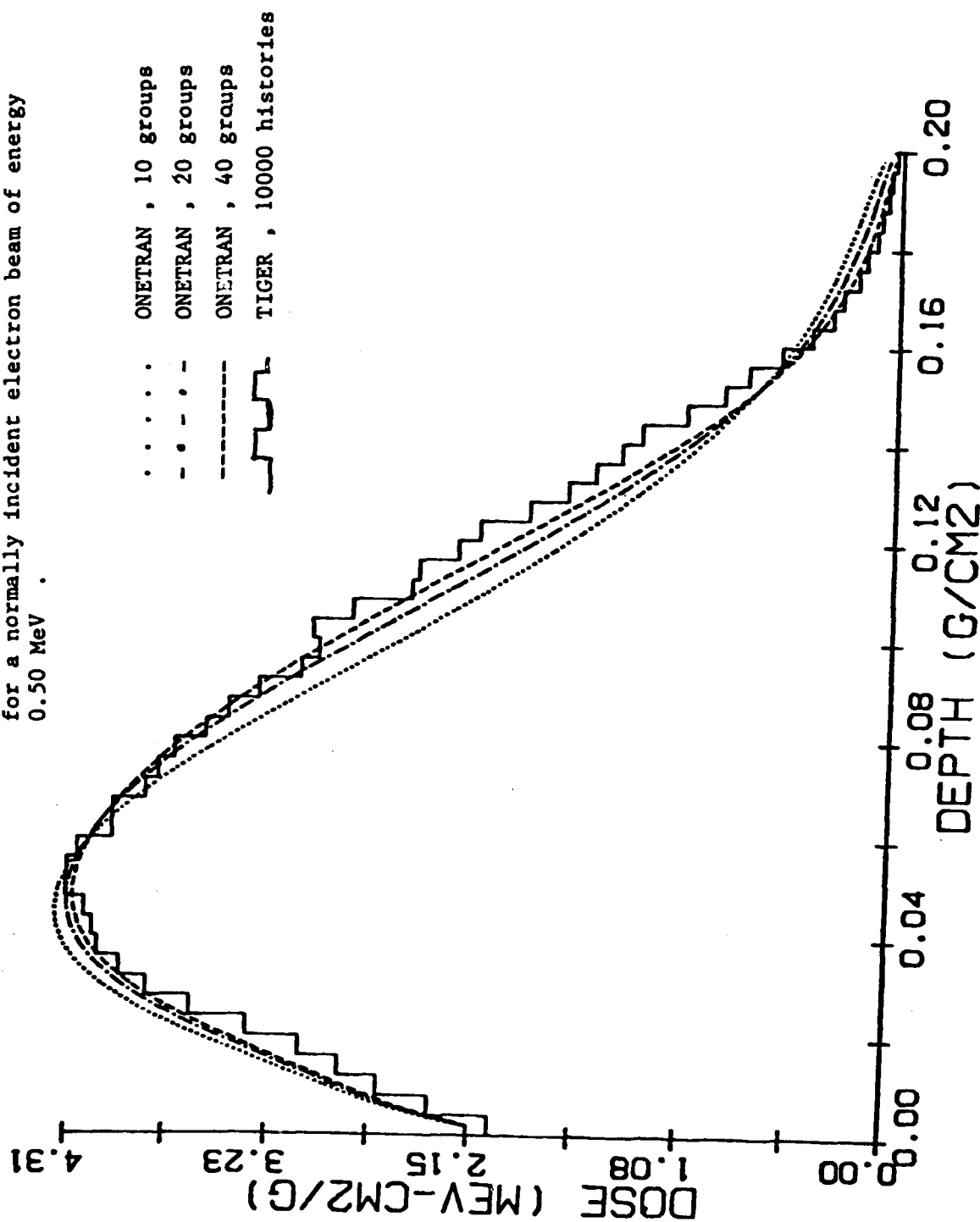


Fig. 16

Electron energy deposition profile in Aluminum
for a normally incident electron beam of energy
1.0 MeV .

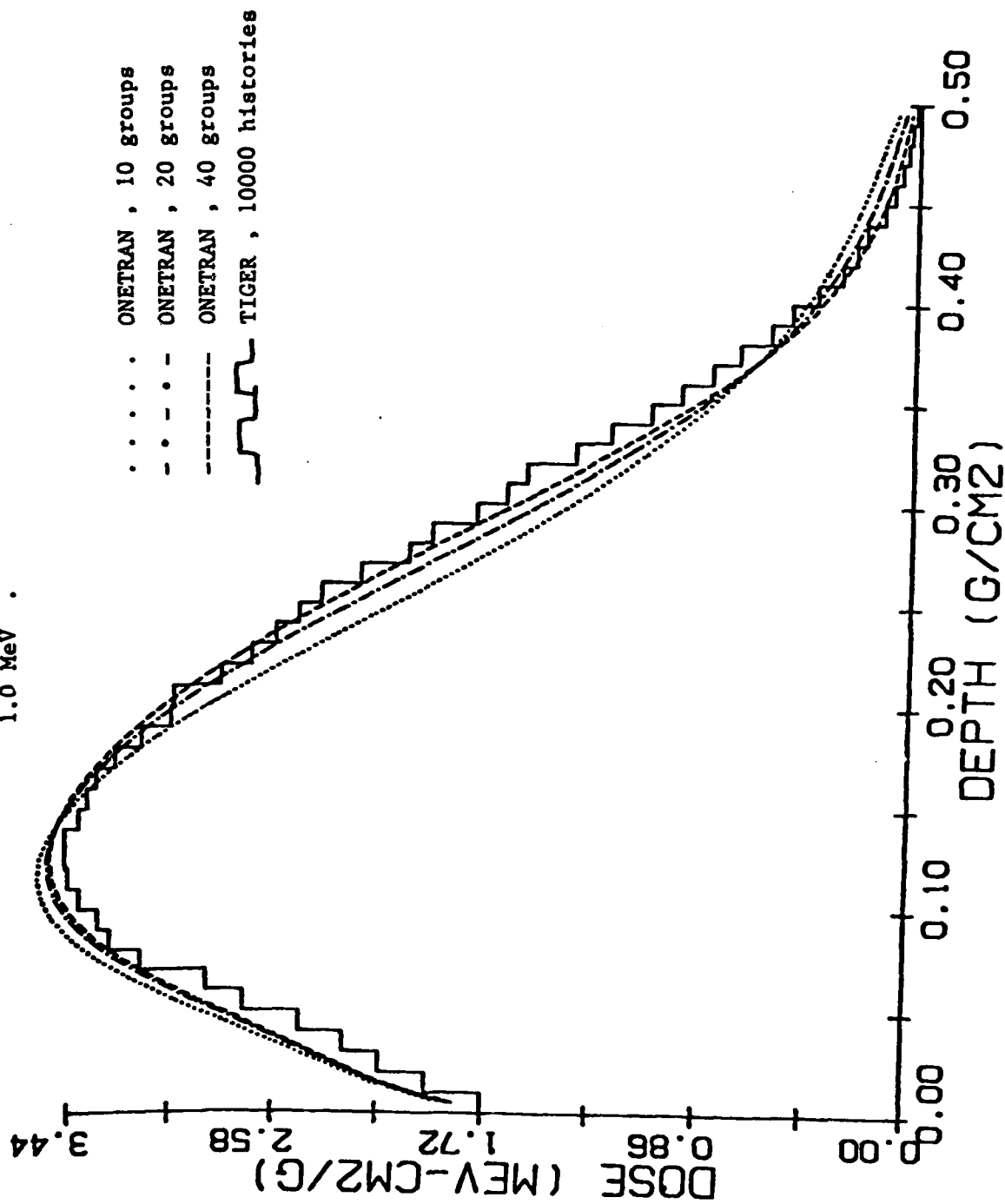


Fig. 17

Energy spectrum of transmitted electrons through Aluminum slab of thickness $0.02\text{g}/\text{cm}^2$.

Source energy, $E_0 = 0.20\text{ MeV}$

Incident direction, $\mu_0 = 0.916667$

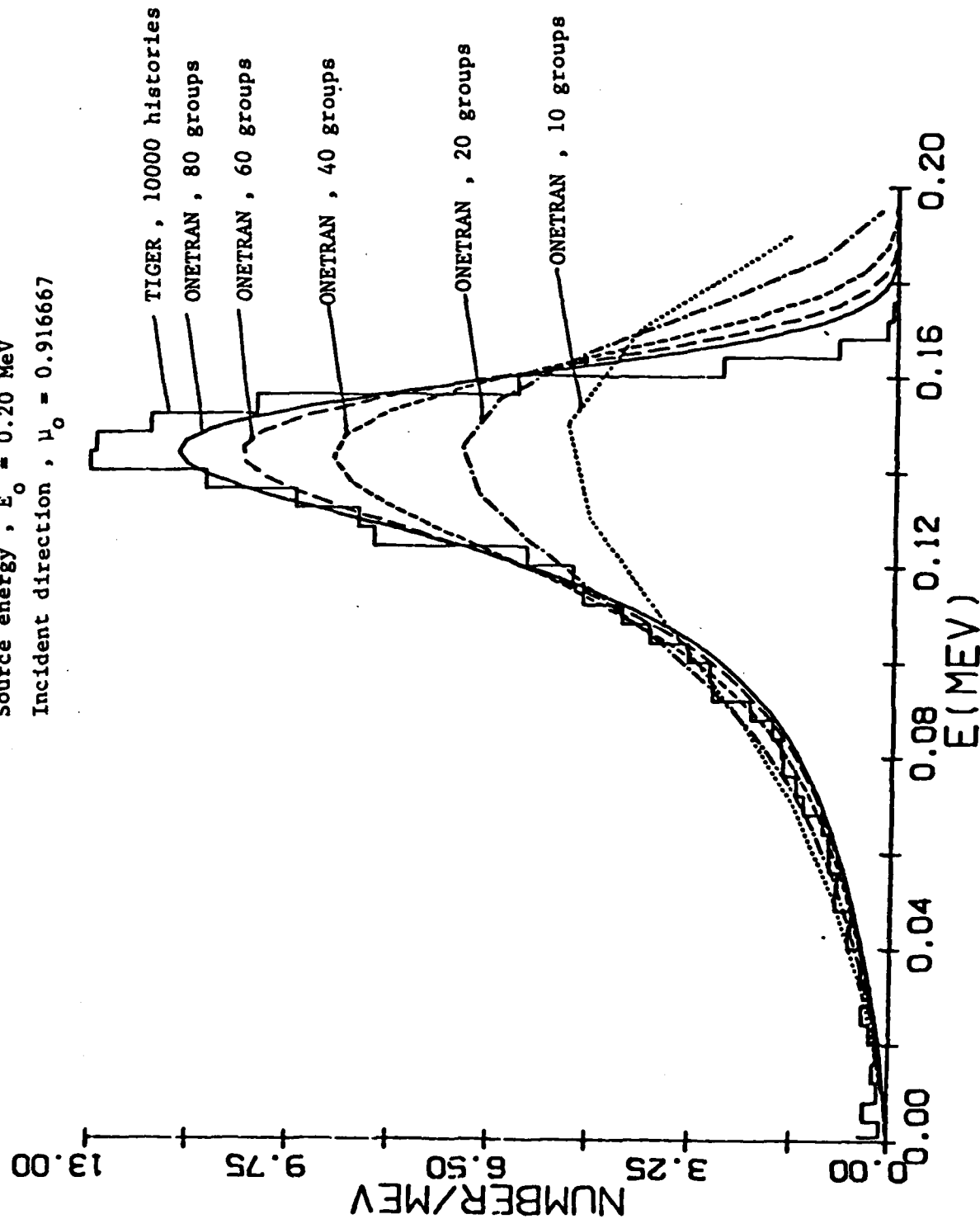


Fig. 18

Electron energy deposition profile in gold for an electron beam with slant incidence ($\mu_0 = .916667$) of energy 0.20 Mev .

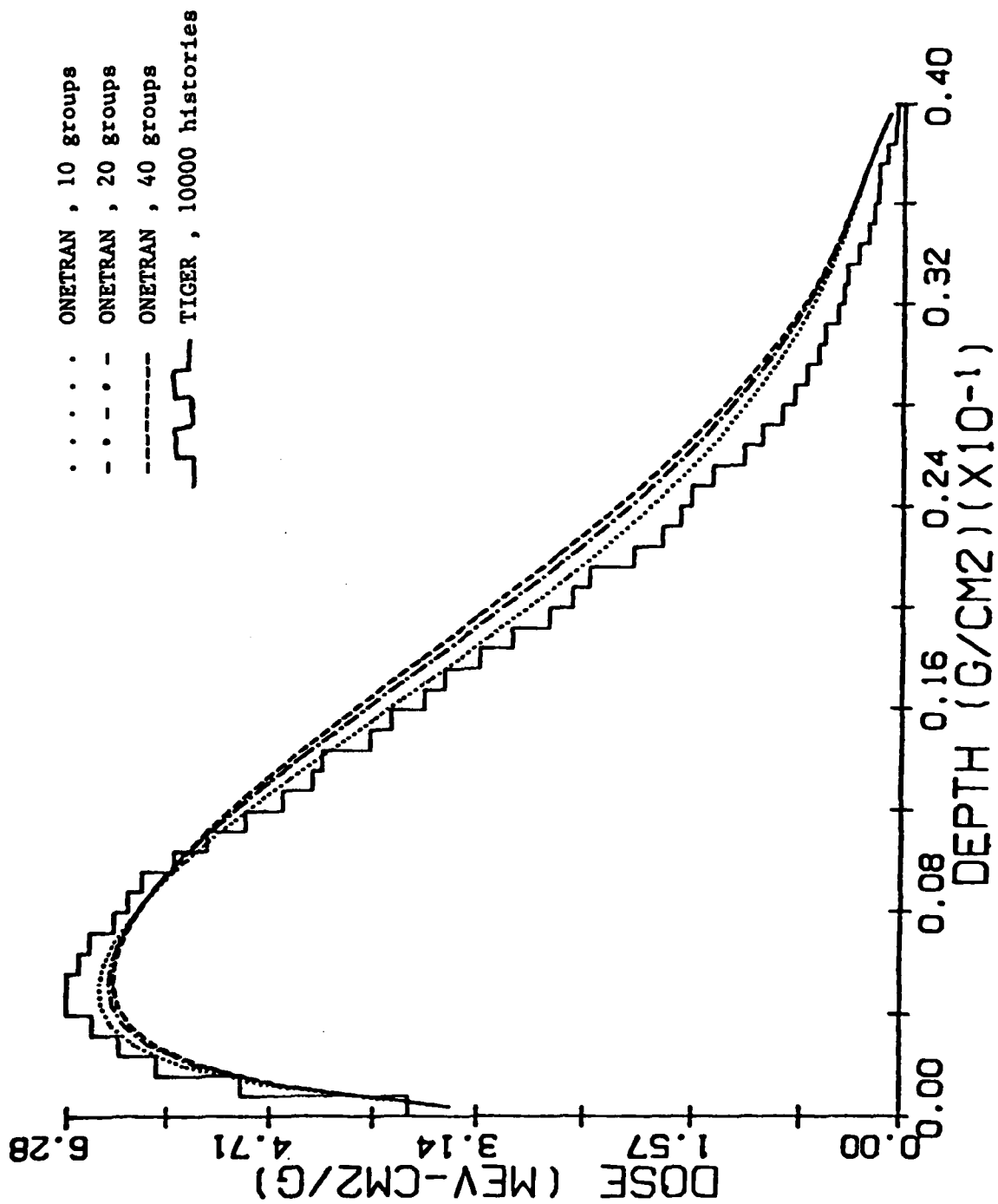
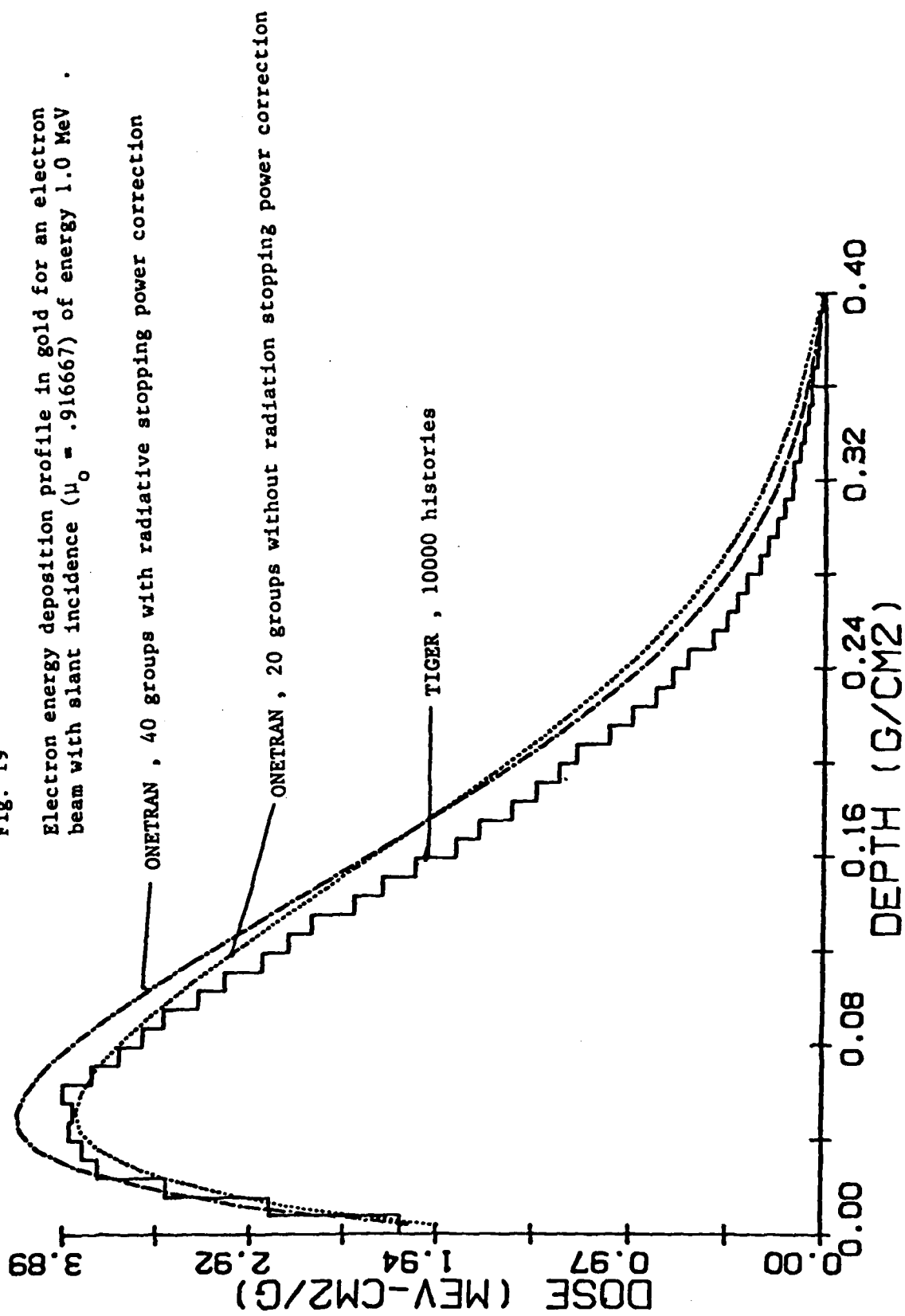


Fig. 19

Electron energy deposition profile in gold for an electron beam with slant incidence ($\mu_0 = .916667$) of energy 1.0 MeV .



IV. ELECTRON TRANSPORT

B. SOLUTION OF ELECTRON TRANSPORT PROBLEMS BY THE MONTE CARLO METHOD

1. Introduction

As was true in our discrete ordinates electron transport work (see Section A), solutions of electron transport problems were also obtained by the Monte Carlo method, again using computer codes written at ARCON as well as TIGER⁽¹⁰⁾, one of a series of computer programs written at Sandia National Laboratories to perform coupled electron-photon Monte Carlo calculations. We obtained electron transmission and backscatter fractions, energy deposition profiles and charge deposition profiles in metals and polymers with both the ARCON codes and TIGER. Sample comparisons of our Monte Carlo results with experimental measurements of transmission and backscatter fractions as well as TIGER energy deposition profiles are given in the following subsections. Also a description of a Monte Carlo code designed to calculate energy and charge deposition near material interfaces at deep penetrations (~ 10 mean free paths) in slab targets will also be described. Work on this program is incomplete, however we believe that there is some value in describing its structure and presenting code listings even in this developmental phase since parts of the program may be found suitable for incorporation into future Monte Carlo efforts.

We shall begin with a description of MCEL, the ARCON single scattering low energy electron Monte Carlo program. Then we shall proceed with an account of MULTSCAT, our multiple scattering Monte Carlo program which is applicable to low energy electron transport and has been found to yield valid results at 200 keV. The discussion will continue with a description of MCINTF, the Monte Carlo program intended for application to dose profiles at material interfaces deep inside thick slab targets. Finally, we shall show examples of charge deposition profiles calculated with the TIGER code for a polymer, C_6H_9O , and comparisons of these results with experimental results obtained at RADC.

2. Program MCEL - A Single Scattering Monte Carlo Code for KeV Electron Transport

2.1 Objective

To solve the transport problem for a beam of electrons (20-50 KeV) incident on a metal slab using the screened-Rutherford single scattering formula. A provision is made to include the effect of inelastic scatter, if necessary. A listing of MCEL is given in Vol. II.

2.2 Quantities Calculated

- 1) $T(t,E)$ - transmission fraction (or current normalized to unit particle incidence) as a function of slab thickness, t , and energy, E .
- 2) $B(t,E)$ - backscatter fraction (or current normalized to unit particle incidence) as a function of slab thickness, t , and energy, E .
- 3) $T(t)$ - transmission fraction as a fraction of slab thickness, t .
- 4) $B(t)$ - backscatter fraction as a fraction of slab thickness, t .
- 5) $F_T(t,E)$ - transmitted flux (normalized to unit particle incidence) as a function of slab thickness, t , and energy, E .
- 6) $F_B(t,E)$ - backscattered flux (normalized to unit particle incidence) as a function of slab thickness, t , and energy, E .

The above six items are calculated for 10 preset values of t over the ranges of 0 to 500 nm in Au and 0 to 1500 nm in Al. There is a provision for user selection of the t values. The energy dependence of these functions is given in histogram form. There are 20 energy bins of equal width ($0.05 \times E_0$, E_0 = source energy).

Every Monte Carlo output quantity listed above is accompanied by a one- or two-digit integer from 0 to 99 (estimates greater than 99 are shown as 99) which is the best estimate of the statistical standard error expressed as a percent of the final value.

2.3 Principles of Operation

This single scattering Monte Carlo algorithm for electron transport utilizes the screened Rutherford⁽⁸⁾ cross-section formula in conjunction with the continuous slowing down approximation. A beam of electrons of energy E_0 is assumed incident (at arbitrary obliquity) on a metal (Al or Au) target. The penetration distance, Δs , the point of first collision is calculated as

$$\Delta s = -\lambda(E) \ln \xi \quad (38)$$

where $\lambda(E)$ is the total mean free path of the electron with energy E , and ξ is a random number uniformly distributed on the interval (0, 1). The total mean free path, or rather its reciprocal, the total cross-section $\sigma(E)$ is given by the screened Rutherford⁽⁸⁾ formula

$$\frac{1}{\lambda(E)} = \sigma(E) = 2\pi(Z+1)N_a n_0^2 z/A \left[\frac{T(T+1)}{T(T+2)} \right]^2 = \frac{1}{\eta(1+\eta/2)} \quad (39)$$

where the quantities T , Z , A , N_a , r_0 , η are as previously defined in Eqn. 22 (Sec. A.2.4.3.1).

When the coordinates of the collision site have been determined, the new value of the electron energy and the scattering angle are computed. In the energy calculation the following stopping power formula of Rohrlich and Carlson⁽¹¹⁾ is used

$$\frac{dE}{ds} = \frac{2\pi N_a n_0^2 m c^2}{\beta^2} \frac{z}{A} \left\{ \ln \left[\frac{T^2(T+2)}{2(I/mc^2)} \right] + F(T) \right\} \quad (40)$$

where $m c^2$ = electron rest mass (.511 MeV),

$$\beta = [T(T+2)]^{1/2}/(T+1) = (\text{electron velocity})/C,$$

$$I = 10^{-6} Z(9.76 + 58.8 Z^{-1.19}) \text{ MeV}, \quad (41)$$

and

$$F(T) = 1 - \beta^2 + [\tau^2/8 - (2\tau+1)\ln 2]/(\tau+1)^2$$

Then the electron energy at the point of collision, E_f , is given approximately by

$$E_f \approx E_i - \left. \frac{dE}{ds} \right|_{E_i} \Delta s, \quad (42)$$

where E_i is the electron energy at the point of previous collision.

The scattering angle is computed by Monte Carlo sampling of the following screened-Rutherford angular distribution.

$$f_E(\mu, \rho) = \frac{\sigma(E, \mu)}{\sigma(E)} = \frac{1}{2\pi} \frac{\eta(1+\eta/2)}{(1+\eta-\mu)^2}, \quad (43)$$

where μ is the cosine of the polar scattering angle, ω , and ρ is the azimuthal scattering angle.

After the first collision, when the new electron energy and scattering angle have been determined, the electron is translated to the point of next collision using Eqn. 38 to determine the distance Δs , and the above procedure is repeated until the electron escapes from the medium, or the electron energy falls below a designated cut-off value, or the maximum allowed number of collisions (user specified) has been reached.

2.4 Description of Routines

2.4.1 MCEL (= Main Program)

This program calls the various subroutines necessary for the calculation and performs the timing function for each case history. Every case history is initiated by the main program, and after the user requested number of case histories (NMAX) is run, the main program halts the calculation. The time elapsed for each case history is noted. The average run time for (NMAX/10) case histories is updated every time another (NMAX/10) histories are completed. A test is performed after each average update to determine if enough time has been allowed (on the input card) by the user to complete the requested number of histories. If the time remaining is insufficient, the calculation is terminated, and the results obtained up to that point in the calculation are saved on a permanent file for processing at a later time.

2.4.2 SETRUN

This subroutine initializes the various parameters necessary for the Monte Carlo calculation. It consists of DATA statements specifying: 1) default values of the coordinates and angular orientation of the incident electron beam; 2) default values for the material thicknesses for Al and Au; 3) density values for Al and Au. Input data cards follow these DATA statements. The number of such cards is variable depending on whether some of the default values given in the data statement are to be overwritten. Basically, the information to be read in consists of a specification of the number of histories to be run (NMAX); the maximum allowed number of collisions per case history (MAXCOLL); a debug printout parameter (NPRNT : 0/1 = off/on); a flag parameter (INPUT : 0/1 = no/yes) to read the INCODE array (explained below); a flag parameter (NSLABS : 0/1 = no/yes) to read in the slab thickness array (THICK) and override the default values (the units of THICK are nm); the target material selector (MAT : 1/2 = Al/Au); a parameter to elect the inelastic scattering option (INEL : 0/1 = no/yes); time limit for the run in seconds (TLIM); incident beam polar angle cosine (CTHO); incident beam energy in KeV (EO); low energy cut-off value (ECUT) in KeV. The input code array, which is read in if INPT = 1, consists of the following; (INCODE (I) : 0/1 = off/on - I = 1, read random number generator seed; I = 2, read source point coordinates.

This subroutine also calls subroutine ESET to initialize the energy dependent parameters (i.e., scattering cross-section, stopping power, etc.). All of the input information is then printed out. This subroutine is called only once.

2.4.3 ESET

The purpose of this subroutine is to calculate the stopping powers, screening parameters and screened-Rutherford scattering cross-sections (see Eqns. 39-41) for a table of 100 energy values ranging from the source energy down to the cut-off energy. If the stopping power formula yields a positive value before the cut-off energy (ECUT) is reached, the table is truncated to the lowest energy value corresponding to a negative stopping power, and ECUT is reset to that value.

2.4.4 SETHIS

Each time a new case history is begun this subroutine is called to initialize the electron trajectory parameters such as coordinates (X, Y, Z), angles (CTH, STH, CPHI, SPHI), energy (EGY), collision counter NCOLL,

pointer index for trajectory characteristics table (LCHR), termination flag for history (IFLAG). A call to entry point CROSS is also made to initialize the total mean free path for the incident electron.

2.4.5 PENET

The primary function of this subroutine is that of translating the electron position to the point of next collision and calculation of the new electron position coordinates. For this Monte Carlo algorithm, the inter-collision distance is computed according to Eqn. 38. In addition, PENET also performs the function of checking to determine if the electron case history should be terminated. This condition can occur in either of two ways: 1) the electron can exit from the scattering medium (transmission or backscatter); or 2) the maximum allowed number of collisions (MAXCOLL) has been reached. In either case, the history termination parameter (IFLAG) is set equal to 1.

2.4.6 ENERGY

When a collision has taken place, the energy of the electron at the point of collision is calculated using the continuous slowing down approximation (Eqn. 42). If the effect of inelastic scattering is to be included, the inelastic cross section⁽¹³⁾ is calculated and added to the screened Rutherford cross-section. A determination is then made of whether elastic or inelastic scattering has occurred. This is done by comparing a random number, ξ , uniformly distributed on the interval (0,1) with the probability of elastic scattering, P_{el} as follows:

$$P_{el} = \frac{\sigma_{el}}{\sigma_{el} + \sigma_{inel}} \quad (44)$$

If $\xi < P_{el} \rightarrow$ elastic scattering,

$\xi \geq P_{el} \rightarrow$ inelastic scattering,

The total mean free path, λ , is then given by

$$\lambda = \frac{1}{\sigma_{el} + \sigma_{inel}} \quad , \quad (45)$$

if elastic scattering is considered (INEL = 1) in the calculation.
Otherwise

$$\lambda = \frac{1}{\sigma_{el}} \quad - \quad (46)$$

2.4.7 ANGLES

After the coordinates of a collision site have been computed by PENET, and the new electron energy and mean free path have been computed by ENERGY, the change in direction of motion of the electron is determined. The cosine and sine of the scattering angle, ω , are computed as follows:

Inelastic scatter⁽¹³⁾;

$$\text{Let} \quad E_{low} = \min [.02 \text{ KeV} , E_{cutoff}] \quad , \quad (47a)$$

$$k = \frac{E - E_{low}}{E - E_{low}} \quad , \quad (47b)$$

$$\text{then} \quad w = k \cdot E_{low} / (k - \xi \cdot E_{low}) \quad , \quad (47c)$$

$$\text{and} \quad \sin \omega = \sqrt{\frac{w}{E}} \quad , \quad (47d)$$

$$\cos \omega = \sqrt{1 - \frac{w}{E}} \quad , \quad (47e)$$

where ξ is a random number uniformly distributed on the interval (0,1).

Elastic scatter;
The probability density function for elastic scatter is given by

$$P(\omega) = \frac{\sigma(\omega)}{\sigma_{\text{TOT}}} = \frac{1}{2\pi} \frac{\eta(1+\eta/2)}{(1+\eta-\mu)^2}, \quad (48)$$

where $\mu = \cos\omega$.

Let the probability of an individual scattering event with scattering angle ω be a random number, ξ , uniformly distributed on (0,1).

$$\text{then } \xi = \int_{-1}^{\cos\omega} \frac{\eta(1+\eta/2)}{(1+\eta-\mu')^2} d\mu', \quad (49)$$

which results in the selection of ω as follows;

$$\cos\omega = \frac{2\xi(1+\eta) - \eta}{2\xi(1+\eta)}, \quad (50a)$$

$$\sin\omega = (1 - \cos^2\omega)^{1/2}, \quad (50b)$$

Inspection of Eqn. 50a shows a correspondence between $\cos\omega$ and ξ .
That is,

$\xi = 0.$	$\cos\omega = -1$ (total backscatter),
$\xi = 0.5$	$\cos\omega = \frac{1}{1+\eta},$
$\xi = 1.0$	$\cos\omega = 1$ (total forward scatter).

Since the scattering is assumed to be isotropic in azimuth, the azimuthal displacement ρ (RHO) is taken as

$$\rho = 2\pi\xi, \quad (51)$$

where ξ is uniformly distributed random number on (0,1). The post collision polar angle functions, $\cos \theta$, $\sin \theta$, (CTH, STH) are then computed from the pre-collision values $\cos \theta_1$, $\sin \theta_1$, (CTH1, STH1) as follows

$$\cos \theta = \cos \theta_1 \cos \omega + \sin \theta_1 \sin \omega \cos \rho, \quad (52a)$$

$$\sin \theta = (1 - \cos^2 \theta)^{1/2} \quad (52b)$$

The corresponding azimuthal values $\cos \phi$, $\sin \phi$, (CPHI, SPHI) are calculated from the pre-collision values $\cos \phi_1$, $\sin \phi_1$, (CPHI1, SPHI1) by

$$\cos \phi = (C1) \cdot (\cos \phi_1) - (S1) \cdot (\sin \phi_1), \quad (53a)$$

$$\sin \phi = (S1) \cdot (\cos \phi_1) + (C1) \cdot (\sin \phi_1), \quad (53b)$$

where

$$C1 = (\cos \omega - \cos \theta \cos \theta_1) / \sin \theta \sin \theta_1, \quad (53c)$$

$$S1 = \sin \rho \sin \omega / \sin \theta \quad (53d)$$

2.4.8 SCORE

After an electron undergoes a collision, the z-coordinates, incident polar angle cosine, post collision angle information, electron energy and collision number are recorded in the trajectory characteristics buffer array (STO). If the case history is to be terminated (IFLAG \neq 0), this fact is recorded by multiplying the collision number by -1.

2.4.9 PROC

This subroutine processes the electron trajectory characteristics. It is called after each case history is completed. Each time another (NMAX/10) histories are finished, all of the quantities itemized in section II are calculated. A running average of these quantities and a running tally of the statistical standard error associated with each of these quantities are maintained. After all NMAX histories have been completed, PROC prints out the final values and also writes them on a permanent file which can be used later on for plotting and analysis.

2.4.10 STATS

A computation of the statistical standard error for every Monte Carlo output quantity is performed by this subroutine. If the total Monte Carlo computation of the quantity x , is divided into N batches ($N = 10$ in this case), then the best estimate of the statistical standard error, expressed as a percent of the final value, is given as⁽¹⁰⁾.

$$(S.E.)_N = \frac{100}{|\langle x_N \rangle|} \left\{ \left| \frac{\langle x_N^2 \rangle - \langle x_N \rangle^2}{N-1} \right| \right\}^{\frac{1}{2}}, \quad (54)$$

where

$$\langle x_N \rangle = \frac{1}{N} \sum_{i=1}^N x_i, \quad (55)$$

and

$$\langle x_N^2 \rangle = \frac{1}{N} \sum_{i=1}^N x_i^2. \quad (56)$$

The x_i 's are the values of the quantity obtained from each batch.

2.5 Comparison of MCEL Results with other Calculations and Experimental Data

Several MCEL calculations were made for low energy electron beams incident on Aluminum and Gold slabs. A sample calculation is that of a 20 keV electron beam normally incident on Aluminum. The quantities $T(t, E)$ and $B(t, E)$, the transmission and backscatter fractions as functions of slab thickness t and electron energy E were calculated as well as their respective totals over all energies, $T(t)$ and $B(t)$. Figure 20 shows a comparison of the $T(t)$ calculated with MCEL, \odot , with the Monte Carlo data of Reimer and Krefting⁽¹⁴⁾ and the experimental data of Kulenkampff and Spyra⁽¹⁴⁾. Figure 21 shows the corresponding backscatter data. As can be seen, the agreement is good.

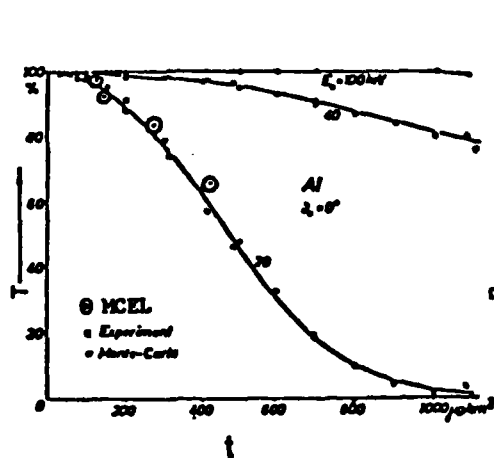


Figure 20.

Comparison of Electron Transmission Fractions for Aluminum Films (reproduced from Ref. 14).

Incident electron energy = 20 keV.

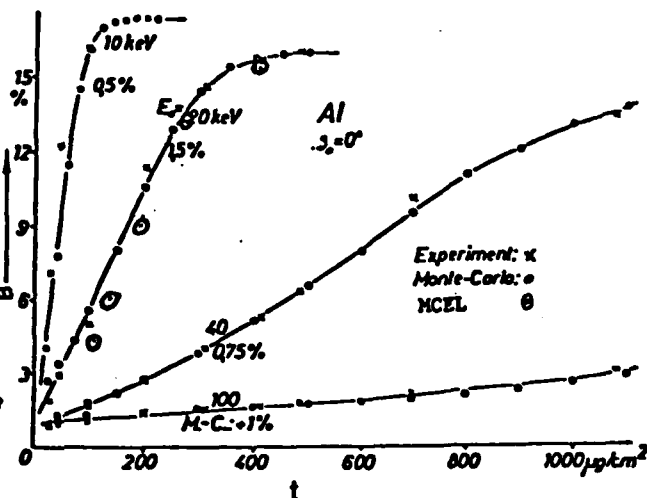


Figure 21.

Comparison of Electron Backscatter Fractions for Aluminum Films (reproduced from Ref. 14).

Incident electron energy = 20 keV.

3. Program MULTSCT - Multiple Scattering Monte Carlo Code for KeV Electron Transport

3.1 Objective

To solve the transport problem for a beam of electrons incident on a metal slab.

3.2 Quantities Calculated

- 1) $T(t, E)$ - transmission fraction as a function of slab thickness t , and energy, E .
- 2) $B(t, E)$ - backscatter fraction as a function of slab thickness, t , and energy, E .

For the above two items, the maximum slab thickness t is taken to be approximately 1 electron range unit. The transmission and backscatter fractions are calculated for 20 user selected t values. The energy dependence of these functions is given in histogram form. There are 10 energy bins of equal width ($0.1 \times E_0$, E_0 = source energy).

- 3) $T(t)$ - transmission fraction as a function of slab thickness, t .
- 4) $B(t)$ - backscatter fraction as a function of slab thickness, t . The same t values are used here as in items 1 and 2.
- 5) $W(z)$ - energy deposition profile (KeV) histogram for the slab of maximum thickness (~ 1 range unit). The slab is divided into 20 zones defined by the thickness values, t (user supplied). The energy (KeV), normalized to unit particle incidence deposited in each zone is given. The energy flow (KeV) in both the forward and back directions across the zone boundaries is also given.
- 6) $T_\ell(t, E)$ - Legendre coefficients of the transmission angular distribution as a function of slab thickness, t , and energy E . The same values of t and E apply as for $T(t, E)$. The T_ℓ are coefficients of the Legendre expansion

$$T(t, E, \mu) = \sum_{\ell=0}^5 \left(\ell + \frac{1}{2}\right) T_\ell(t, E) P_\ell(2\mu - 1),$$

where μ is the cosine of the emergent polar angle. For transmission $\mu \geq 0$.

- 7) $B_l(t, E)$ - Legendre coefficients of the backscattered angular distribution as a function of slab thickness, t , and energy, E . The same values of t and E apply as for $B(t, E)$. The B_l are coefficients of the Legendre expansion

$$B(t, E, |\mu|) = \sum_{l=0}^5 (l + \frac{1}{2}) B_l(t, E) P_l(2|\mu| - 1) .$$

- 8) $N_{T,t}(E/E_0)$ - Emergent energy distribution, Transmission. This function is defined for the 20 slab thicknesses t used in item 1 and 20 histogram intervals E/E_0 of width 0.05. This information is contained in the $T(t, E)$ array but the energy resolution there is twice as coarse as that given here.
- 9) $N_B(E/E_0)$ - Emergent energy distribution, Backscatter. This function is defined for the maximum slab thickness (essentially infinite), and the same 20 histogram intervals E/E_0 as defined for item 8.
- 10) $F_{t,n,m}^T(\mu, E)$ - Angle-energy moments matrix for emergent electrons transmitted through a slab of thickness t .

$$F_{t,n,m}^T = \langle \mu^n E^m \rangle_t .$$

There are 20 such matrices corresponding to the 20 values of t selected for item 1.

- 11) $F_{n,m}^B(\mu, E)$ - Angle-energy moments matrix for emergent electrons backscattered from the maximum slab thickness (essentially infinite).

$$F_{n,m}^B = \langle |\mu|^n E^m \rangle .$$

- 12) $Q(z)$ - Charge deposition profile histogram for the slab of maximum thickness. The slab is divided into 20 zones defined by the thickness values, t (user supplied). The charge, normalized to unit charge incidence, deposited in each zone is given.

Every Monte Carlo output quantity listed above is accompanied by a one- or two-digit integer from 0 to 99 (estimates even greater than 99 are shown as 99) which is the best estimate of the statistical standard error expressed as a percent of the final value.

3.3 Principles of Operation

The ARCON multiple scattering Monte Carlo algorithm for electron transport is based on the method of Curgenven and Duncumb⁽¹⁵⁾ which was further developed by Love, et al.⁽¹⁶⁾ and Myklebust et al.⁽¹⁷⁾. The Bethe range corresponding to the energy, E_0 , of the incident electron beam is divided into 100 equal trajectory steps. The electron energy at the midpoint of each step is computed by a fourth-order Runge-Kutta integration of the stopping power formula (Eqn. 40).

A beam of electrons is assumed incident on the face of a semi-infinite scattering medium. Every Monte Carlo case history is allowed a maximum of 100 collisions. The actual number may be less if the electron is back-scattered out of the medium. The scattering angle, ω , after each collision is computed as⁽¹⁶⁾

$$\cos(\omega/2) = \cos(\omega_0/2) \left(\frac{E}{E_0} \right) \xi^{\frac{1}{2}}, \quad (57)$$

where ω_0 is the minimum scattering angle for the incident electron with energy E_0 , E is the electron energy, and ξ is a random number uniformly distributed on the interval (0,1). The authors⁽¹⁶⁾ supply an expression for $\tan(\omega_0/2)$ in terms of the bulk backscatter fraction, η . This expression which is independent of energy in the 5 to ~40 KeV range, a least-squared polynomial fit resulting from several Monte Carlo runs for a wide range of materials, is given as

$$\tan(\omega_0/2) = .02209 + .10716\eta + .03009\eta^2 + .37555\eta^3 \quad (58)$$

After every collision, the electron energy is decremented to the value obtained by integration of the stopping power formula corresponding to the total electron trajectory length. The electron penetration depth, z , polar angle direction cosine with respect to the z direction, $\cos\theta$, and the collision number are stored in an array sufficiently large to contain this information for the entire electron case history. The particle is then assumed to travel in a straight line for another path increment ($0.01 \times$ range) along the direction indicated by the angles θ and ϕ , where ϕ is the azimuthal angle. The above procedure is repeated unless the electron either escapes from the medium (backscatter) or undergoes 100 collisions.

The energy and charge deposition profiles for these calculations are computed for a pre-specified set of spatial zones by the simple device of counting the number of particles and total energy current flowing into and out of each zone.

3.3.1 Incorporation of Electric Field Equations

Energy loss in electron transport calculations is accounted for by the Bethe model. The quantitative measure of the energy loss mechanism, interaction with atomic electrons, is provided by the stopping power calculation. To within a good approximation, the energy has over a small trajectory segment, Δs , for kilovolt electrons can be given by

$$E_{n+1} = E_n - \left| \frac{dE}{ds} \right|_{E_n} \Delta s, \quad (59)$$

where E_n and E_{n+1} are, respectively, the pre- and post-collision electron energies for the n -th collision, $\left| \frac{dE}{ds} \right|_{E_n}$ is magnitude of the stopping power at energy E_n , and Δs is the pathlength increment between collisions (for this algorithm, $\Delta s = 0.01 \times$ total electron range). Now if an electric field, say \mathcal{E}_z , is applied along the z -direction, the resulting force, F_z , exerted on the electron will be

$$F_z = e\mathcal{E}_z \quad (60)$$

The resulting electrostatic energy contribution, E_e , to the electron kinetic energy will be

$$E_e = F_z \Delta s' , \quad (61)$$

where $\Delta s'$ is the distance traversed between collisions. Note that the quantity $\Delta s'$ is used here rather than Δs , since strictly speaking the intercollision distance is altered by the presence of the electric field. However, to first order, we may take

$$\Delta s' \approx \Delta s . \quad (62)$$

Then with the inclusion of the electrostatic energy term (Eqn. 61), the energy equation (Eqn. 59) becomes

$$E_{m+1} \approx E_m - \left| \frac{dE}{ds} \right|_{E_m} \Delta s + F_z \Delta s . \quad (63)$$

In addition to the above, we may also account for the small change in energy due to an incremental amount of deceleration or slowing down resulting from the increase in the intercollision trajectory step size. If the electric field is applied along the z-direction (Fig. 22), then the incremental change in pathlength is approximately given by

$$\Delta s' - \Delta s \approx \Delta z \cos \theta , \quad (64)$$

where Δz is electron displacement due to the presence of E_z . It can be shown from elementary considerations that

$$\Delta z = \frac{1}{4} F_z \left(\frac{\Delta s}{E} \right)^2 , \quad (65)$$

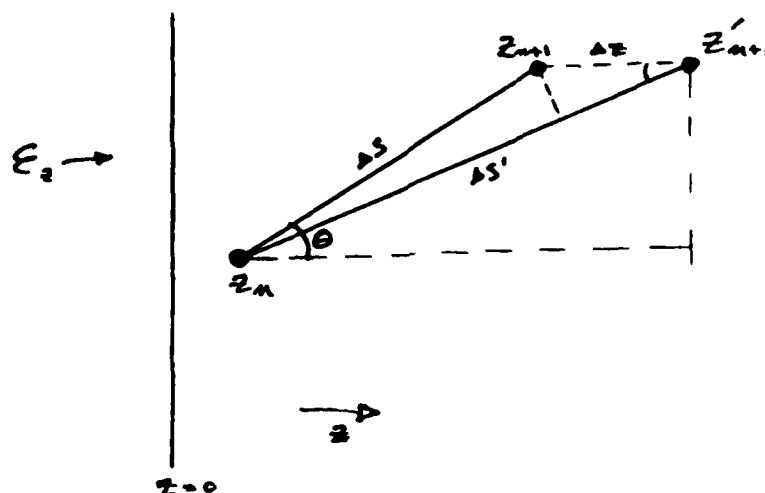


Figure 22. Diagram of electron trajectory correction due to presence of an electric field.

where E is the electron kinetic energy. If Eqns. (64) and (65) are combined to yield an approximate expression for $\Delta s'$, and then if $\Delta s'$ is substituted for Δs in Eqn. (63), the result is

$$E_{n+1} = E_n - \left| \frac{dE}{ds} \right|_{z_n} \left\{ \Delta s + \frac{1}{4} \frac{F_z}{E_n} (\Delta s)^2 \cos \theta \right\} + F_z \left\{ \Delta s + \frac{1}{4} \frac{F_z}{E_n} (\Delta s)^2 \cos \theta \right\} \quad (66)$$

The above expression is included in the MULTSCAT program. As can be seen, in the absence of the applied electric field F_z , the energy loss algorithm reverts to that of Eqn. (59).

3.4 Description of Routines

The MULTSCAT routines will be described only if they differ substantially from their counterparts, in MCEL (Section 2). Reference will be made to the corresponding subsections of Section 2 for those subroutines that are essentially the same as the MCEL subroutines. A program listing of MULTSCT is given in Vol. II.

3.4.1 MULTSCT (= Main Program)

(See Section 2.4.1)

3.4.2 SETRUN

This subroutine initializes the various parameters necessary for the Monte Carlo calculation. It consists of DATA statements specifying: 1) default values of the coordinates and angular orientation of the incident electron beam; 2) density values for Al, Cu, Au*; 3) bulk backscatter fractions for Al, Cu, Au*. Input data cards follow these DATA statements the number of such cards is variable depending on whether some of the default values given in the data statement are to be overwritten. Basically, the information to be read in consists of a specification of the number of histories to be run (NMAX); the target material (MAT ; 1/2/3 = Al/Cu/Au; a debug printout parameter (NPRNT : 0/1 = off/on); input code (INCODE (I) : 0/1 = off/on—I = 1, read bulk backscatter fraction; I = 2, read target thicknesses; I = 3, read random number generator seed); time limit for the run in seconds (TLIM); incident beam polar angle cosine (CTHO); incident beam energy in KeV (EO); low energy cut-off value (ECUT) in KeV; electric field force in eV/cm (FORCE).

This subroutine also calls subroutine ESET, which calculates the path-length vs. energy table for 100 multiple collisions and returns a value for the Bethe range corresponding to the incident electron energy.

All of the input information is then printed out. This subroutine is called only once.

* Density and backscatter fraction data for mylar and/or lucite can be substituted for any of these materials.

3.4.3 ESET

This subroutine calculates a table of electron energies vs. pathlength for 100 equal trajectory steps. This calculation is performed by Runge-Kutta integration of Eqn. (40). The tangent of the minimum scattering angle (TBO) is also completed according to Eqn. (58). The Bethe range (RTOTAL) for the incident electron energy is taken from a table of values⁽¹¹⁾ (RBETHE) which is entered in the form of a DATA statement for 20 energy values, ranging from 10 to 150 KeV, for three materials, Al, Cu, Au. In the case of mylar and lucite, these values are entered directly into the code via replacement statements.

3.4.4 SETHIS

(See Section 2.4.4)

3.4.5 PENET

The primary function of this subroutine is that of translating the electron from its present position to the point of next collision and calculation of the new electron position coordinates. For this Monte Carlo algorithm, the intercollision distance ($DRB = RTOTAL/100$) in the absence of an applied electric field, is fixed in subroutine ESET. If the applied electric field has non zero value, a correction term is added in accordance with Eqn. (65). In addition, PENET also performs the function of checking to determine if the electron case history should be terminated. This condition can occur in either of two ways: 1) the electron can exit from the scattering medium (transmission or backscatter); or 2) the maximum allowed number of collisions ($MAXCOLL = 100$) has been reached. In either case, the history termination parameter (IFLAG) is set equal to 1.

3.4.6 ENERGY

When a collision has taken place, the post-collision electron energy is selected from a table of energy vs. collision number supplied by subroutine ESET. An energy correction term is added for the applied electric field (Eqn. 66), if one is present.

3.4.7 ANGLES

After the coordinates of a collision site have been computed by PENET, the change in direction of motion of the electron is determined. The cosine and sine of the scattering angle are computed by making use of Eqn. (57). Specifically, $\tan^2(\omega/2)$ is calculated, and then $\cos \omega$, $\sin \omega$ (COM, SOM) from

$$\cos \omega = \frac{1 - \tan^2(\omega/2)}{1 + \tan^2(\omega/2)} ; \sin \omega = (1 - \cos^2 \omega)^{\frac{1}{2}} \quad (67)$$

the algorithm for determining the post-collision polar and azimuthal trajectory cosines (θ , ϕ) is exactly as described in Section 2.4.6, Eqns. 51-53.

3.4.8 SCORE, PROC, STATS

(See Sections 2.4.8, 2.4.9, 2.4.10)

3.5 Comparison of MULTSCT Results with other Calculations and Experimental Data

The validity of the semi-empirical nature of the MULTSCT algorithm, namely the dependence of the multiple collision scattering angle on the bulk backscatter fraction for a semi-infinite medium, was tested for two different situations. In the first case a 200 keV electron beam was assumed normally incident on an Aluminum slab, while in the second instance a 20 keV electron beam was assumed normally incident on a Gold slab target.

Figure 23 shows a comparison of the energy deposition profiles for the 200 keV beam case as calculated by MULTSCT and TIGER. While the MULTSCT program does not contain nearly as much physics as does TIGER, it should be noted that the agreement is nonetheless very good. It should also be noted that the TIGER calculation requires about 9 times the computational effort of MULTSCT, and one MULTSCT run yields transmission and backscatter data, such as energy and angular distributions as well as total emergent current fractions, for up to 20 slab thicknesses.

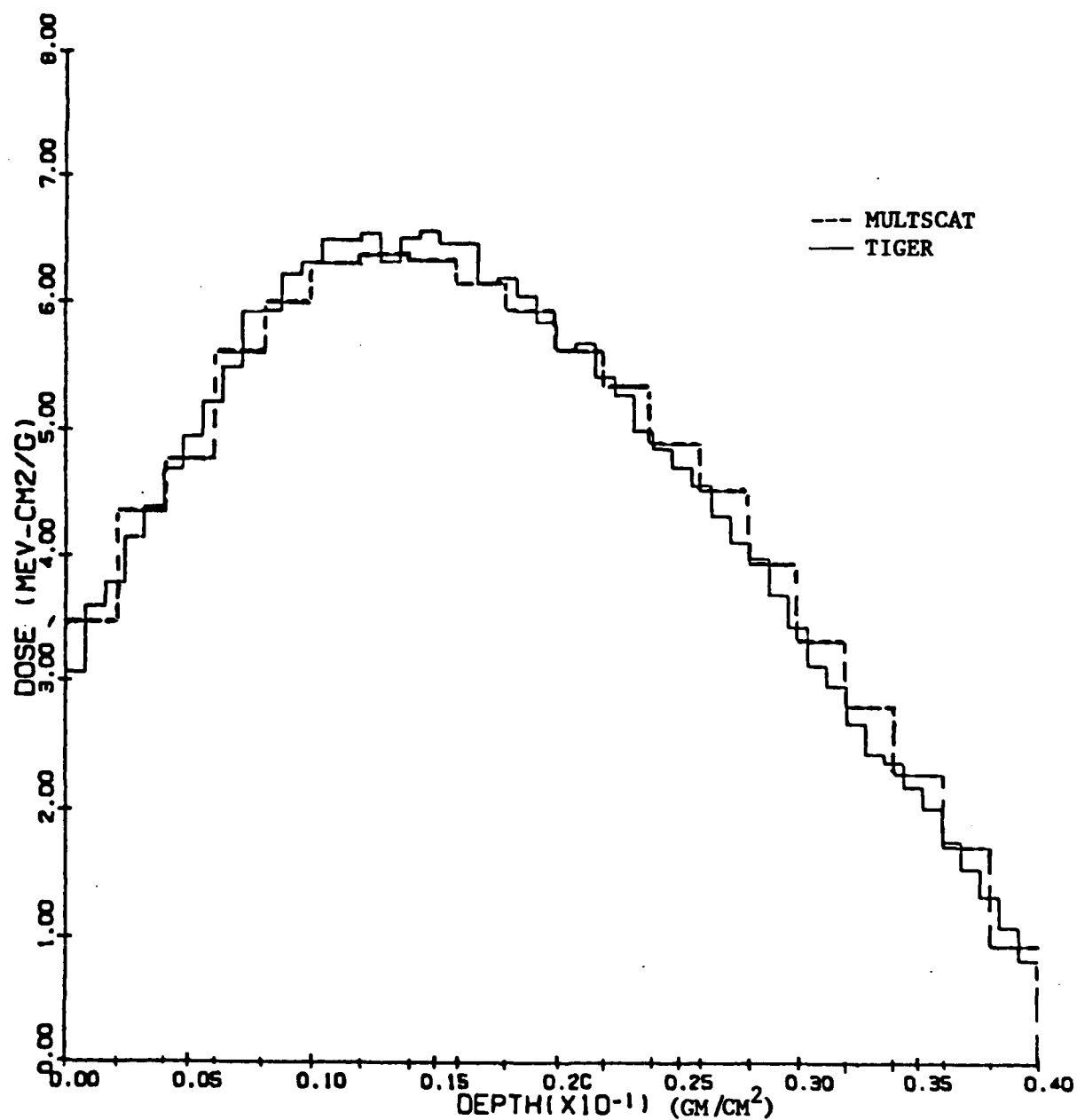


Figure 23. Comparison of Energy Deposition Profiles as Calculated by MULTSCAT and TIGER for 200 keV Electron Beam Normally Incident on Aluminum.

The MULTSCT total transmission and backscatter fractions (+) for the 20 keV beam incident on Gold are shown in Figures 24 and 25, respectively. These plots, taken from Ref. 14, also contain the Monte Carlo data of Reimer and Krefling(o)⁽¹⁴⁾ and the experimental data of Spyra and Kulenkampff(x)⁽¹⁴⁾. The agreement is fairly good, better for the transmission case than for the backscatter.

3.6 MULTSCT Simulation of Polymer Irradiation by Electrons

The MULTSCT program was used to simulate the polymer irradiation due to the incidence of a monoenergetic electron beam at the surface of a mylar slab⁽¹⁵⁾. Ten program runs were made with incident energies ranging from 20 keV to 2 keV in 2 keV increments. Energy deposition and current density profiles were obtained for these cases. Examples of these curves are shown in Figures 26 and 27. The calculations of Ref. 18 provide a good example of the utility of a program such as MULTSCT from which a large number of data could be obtained at a relatively reasonable cost. MULTSCT was also used to estimate the effect of the space charge induced electric fields in the mylar dielectric relative to the stopping power of the material. No noticeable effect due to space charge electric fields was found in our results.

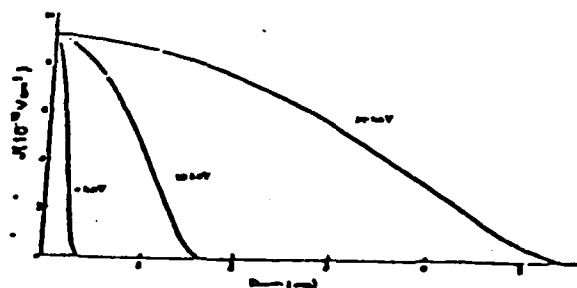


Figure 26. (18) Current density of 10^{-9} A/cm² incident electrons inside the mylar.

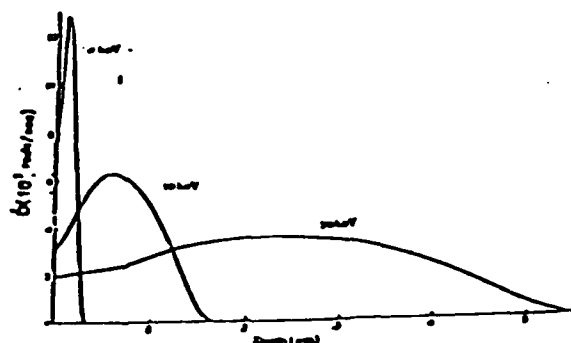


Figure 27. (18) Dose rate due to 10^{-9} A/cm² incident electrons.

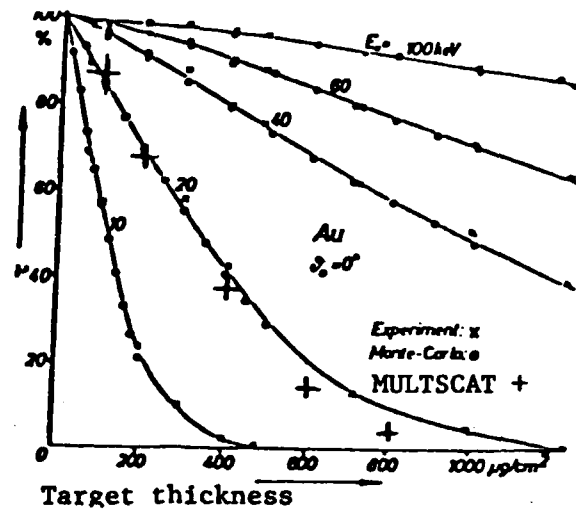


Figure 24. Comparison of transmission, T , as a function of film thickness for 20 keV electron beam incident on Au (reproduced from Ref. 14).

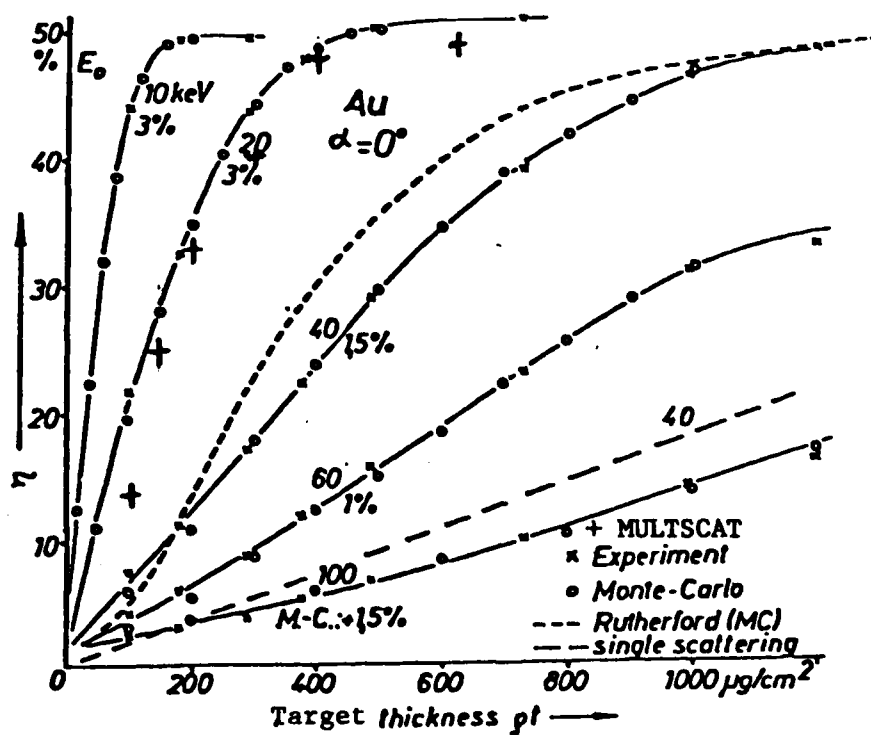


Figure 25. Comparison of the backscattering coefficient η as a function of film thickness for 20 keV electron beam incident on Au (reproduced from Ref. 14).

4. Program MCINTF, a set of Three Monte Carlo Programs to Treat the Interface Dose Problem for Electrons in the 1 MeV Energy Range.

4.1 Objective

To decrease the computation time and increase statistical accuracy of the Monte Carlo Method in calculating electron flux, current and energy deposition profiles near a material interface located deep within the scattering medium. Since these codes are in the developmental stage, i.e. they have not been tested for a realistic situation, only the principles of operation and a list of the quantities calculated will be given here. Code listings are provided in Vol. II.

4.2 Principles of Operation

The basic idea is that of using the transmitted electron current through a very thick slab (e.g., 1 c_m Au) as a source function for a Monte Carlo calculation in a very narrow region surrounding a material interface (e.g., Au - Al), perhaps 10 mean free paths thick on either side. When an electron is found to escape from this narrow region its reflection probability, backscatter energy and angle distributions from a nearly "infinite" (e.g., several electron ranges) Au or Al slab are sampled. The electron is then forced back into the Monte Carlo region. This process of forcing is repeated until the statistical weight (product of successive total albedo values) of the electron falls below a predetermined cut off value. This procedure may yield accurate interface flux, current and dose values with a significant saving in computational effort. This is due to the fact that the Monte Carlo calculation is confined to a narrow region about the interface thus making it possible to obtain "good" statistical accuracy. Naturally, the success of this scheme depends heavily on the accuracy of the infinite medium albedo functions and the quality of the cross-section data. For testing purposes, the scheme has been exercised with physically unrealistic cross-section data to expedite the programming and testing processes. The results of the tests are promising, and indicate that the introduction of realistic electron cross-section data would be justified.

Basically, there are three separate Monte Carlo codes. The first, BIGSLAB, is used to generate transmission and albedo distributions of electrons scattered out of very thick homogenous media (Au or Al). This code serves the dual purpose of providing both the source functions (from the transmission data) for input into the Monte Carlo calculation for the

interface region (the second code) and the albedo data, also to be used in the second code, for forcing the electrons back into the interface region.

The second Monte Carlo program, INTFC, accepts the transmission distribution data from BIGSLAB as a source function and performs a standard single scattering Monte Carlo calculation of the electron transport in the neighborhood of the material interface. When an electron is scattered out of this region of approximately 10 mean free paths on either side of the interface, INTFC then makes use of the albedo distribution data from BIGSLAB to reflect the electron back into the Monte Carlo region.

The third Monte Carlo program, MCSPLIT, is the benchmark program with which the accuracy of the above described procedure is evaluated. This program makes use of a well known statistical biasing technique called history splitting⁽³⁾. This technique is commonly used in deep penetration problems. MCSPLIT is a straightforward single scattering Monte Carlo calculation of electron transport in a very thick medium (Au - Al) with the material interface deeply imbedded. The electron beam is assumed normally incident on a surface of the medium. Normally this is the Monte Carlo situation which the procedure involving BIGSLAB and INTFC is designed to circumvent because of the cost and difficulty of obtaining meaningful results at the interface. The accuracy of such a calculation can be improved considerably by the technique of history splitting if detailed knowledge of particle transmission and backscatter in a tightly confined region is desired. When an electron reaches the neighborhood of interest (i.e., crosses a defined boundary known as a splitting plane) it splits into n identical particles each with weight W/n , where W is the incoming weight. The Monte Carlo procedure is then carried out on each of these fractional particles independently. The advantage is that n times as many particles are processed in the region of interest while the total statistical weight is preserved.

Description of the quantities calculated by the three programs BIGSLAB, INTFC, and MCSPLIT are given below.

4.3 Program BIGSLAB , Quantities Calculated

- 1) $T(t,E)$ - transmission fraction (or current normalized to unit particle incidence) as a function of slab thickness, t , and energy, E .
- 2) $T(t)$ - transmission fraction as a function of slab thickness, t .
- 3) $B(t,E)$ - backscatter fraction (or current normalized to unit particle incidence) as a function of slab thickness, t , and energy, E .

- 4) $B(t)$ - backscatter fraction as a function of slab thickness, t .
- 5) $F_T(t, E)$ - transmitted flux (normalized to unit particle incidence).
- 6) $T_T(t)$ - transmitted flux as a function of slab thickness, t .
- 7) $F_B(t, E)$ - backscattered flux (normalized to unit particle incidence) as a function of slab thickness, t , and energy, E .
- 8) $F_B(t)$ - backscattered flux as a function of slab thickness, t .

The above 8 items are calculated for 10 values of t ranging from 0 to approximately 100 mean free paths or more evaluated at the source energy. There is a provision for user selection of the t values. The energy dependence of these functions is given in histogram form. There are 20 energy bins of equal width ($0.05 \times E_0$, E_0 = source energy).

- 9) $\mu_T(E)$ - average value of the cosine of the emergent polar angle of the transmitted electrons as a function of emergent energy, E . (Two tables are given for this quantity. The first has 20 energy bins of width $0.05 E_0$, and the second has 10 energy bins of width $0.1 E_0$).
- 10) $(\sin\theta\cos\phi)_T$ - average value of the x direction cosine of the transmitted electrons as a function of emergent energy, E . (As in item 9 above, two tables are given).
- 11) $T_l(E)$ - Legendre coefficients of the transmission polar angle distribution as a function of energy, E . There are 10 energy bins of width $0.1 E_0$. Only transmission through the slab of maximum thickness is considered. The T_l are coefficients of the Legendre expansion

$$T(E, \mu_T) = \sum_{l=0}^9 (l + \frac{1}{2}) T_l(E) P_l(\mu_T),$$

where μ_T is the cosine of the emergent polar angle. For transmission, $\mu_T \geq 0$. An improvement in this formulation is planned for the future, that of expansion in terms of $P_l(2\mu_T - 1)$. Fewer terms should be required to achieve the same accuracy.

- 12) $T_{lm}^+(E)$, $T_{lm}^-(E)$ - Spherical harmonic coefficients of the transmission angular distribution. These coefficients are listed for the same 10 energy bins as given in item 11. Again, only transmission through the maximum slab thickness is considered. The T_{lm} are the coefficients of the expansion (19)

$$T(\theta_T, \varphi_T, E) = \sum_{l=0}^{\infty} \left\{ T_{l0}(E) Y_{l0}(\theta_T, \varphi_T) + \left[\sum_{m=1}^l T_{lm}^+(E) Y_{lm}^+(\theta_T, \varphi_T) + T_{lm}^-(E) Y_{lm}^-(\theta_T, \varphi_T) \right] \right\}$$

where

$$T_{l0}(E) = \sqrt{\frac{2l+1}{4\pi}} T_l(E),$$

and $Y_{lm}^{\pm}(\theta, \varphi) = \sqrt{\frac{2l+1}{2\pi} \frac{(l-m)!}{(l+m)!}} P_l^m(\cos \theta) \begin{cases} \cos m\varphi \\ \sin m\varphi \end{cases},$

$$P_l^m(\cos \theta) (= P_l^m(\mu))$$

are the associated Legendre functions.

These coefficients, T_{lm}^+ , in principle, provide all of the necessary information for an adequate description of the emergent angular distribution of the transmitted electrons. Clearly, if the incident electron beam is normal to the surface of the scattering material, there will be no ϕ dependence in the transmission angular distribution. However, this information would be useful for slant incident beams. For the purposes of providing a source function for program INTFC, knowledge of the T_{l0} coefficients is sufficient at the present time.

- 13) $A_l(|\mu_B|, \phi_B)$ - Infinite Medium albedo for 10 energy bins of width $0.1 E_0$, as a function of μ_B and ϕ_B , where $\mu_B = \cos \theta_B$, θ_B and ϕ_B being the backscatter polar and azimuthal angles respectively. There are 10 μ_B bins of width 0.1 and 12 ϕ_B bins, of width 30 degrees.
- 14) $A_l(|\mu_B|)$ - Infinite medium albedo for 10 energy bins of width $0.1 E_0$. The same μ_B bin width applies here as in item 13.
- 15) $A_l(E)$ - Legendre coefficients of the albedo polar angle distribution as a function of energy, E . There are 10 energy bins of width $0.1 E_0$. Only backscatter from an infinite medium is considered. The A_l are the coefficients of the Legendre expansion

$$A(E, \mu_B) = \sum_{l=0}^9 (l + \frac{1}{2}) A_l(E) P_l(|\mu_B|),$$

where μ_B is the cosine of the emergent polar angle of backscattered particles. For backscatter, $\mu_B < 0$. An improvement in this formulation is planned for the future that of expansion in terms of $P_l(2|\mu_B|-1)$. Fewer terms should be required to achieve the same accuracy.

- 16) $A_{lm}^+(E)$, $A_{lm}^-(E)$ - Spherical harmonic coefficients of the infinite medium albedo angular distribution. These coefficients are listed for the same 10 energy bins as given in item 15. The A_{lm} are the coefficients of the expansion

$$A(\theta_B, \phi_B, E) = \sum_{l=0}^9 \left\{ A_{l0}(E) Y_{l0}(\theta_B, \phi_B) + \left[\sum_{m=1}^l A_{lm}^+(E) Y_{lm}^+(\theta_B, \phi_B) + A_{lm}^-(E) Y_{lm}^-(\theta_B, \phi_B) \right] \right\}.$$

where
$$A_{\ell 0}(E) \equiv \sqrt{\frac{2\ell+1}{4\pi}} A_{\ell}(E) ,$$

and the $Y_{\ell m}^{\pm}$ are as defined in item 12.

These coefficients, $A_{\ell m}^{\pm}$, in principle, provide all of the necessary information for adequate description of the albedo angular distribution for infinite medium backscatter. The ϕ dependence is necessary here because albedo information for off-normal incident beams must be collected. If enough cases of various incident obliquities are run, this should provide adequate albedo angular information to be used in program INTFC for forcing electrons back into the Monte Carlo region with approximately correct backscatter directions.

Every Monte Carlo output quantity listed above is accompanied by a one or two-digit integer from 0 to 99 (estimates even greater than 99 are shown as 99) which is the best estimate of the statistical standard error expressed as a percent of the final value.

4.4 Program INTFC , Quantities Calculated

- 1) $J^+(E, \mu)$ - positive direction electron current (normalized to unit particle incidence) across the material interface plane as a function of energy, E , and polar angle (w.r.t. plane normal) cosine, μ .
- 2) $J^+(\mu)$ - total of $J^+(E, \mu)$ over all energy bins.
- 3) $J^-(E, \mu)$ - negative direction electron current (normalized to unit particle incidence) across the material interface plane as a function of energy, E , and polar angle (w.r.t. plane normal) cosine, μ .
- 4) $J^-(\mu)$ - total of $J^-(E, \mu)$ over all energy bins.
- 5) $F^+(E, \mu)$ - positive direction electron flux (normalized to unit particle incidence) across the material interface plane as a function of energy, E , and polar angle (w.r.t. plane normal) cosine, μ .

- 6) $F^+(\mu)$ - total of $F^+(E, \mu)$ over all energy bins.
- 7) $J_l^+(E)$ - Legendre coefficients of the polar angle distribution of $J^+(E, \mu)$ as a function of energy, E . The J_l^+ are coefficients of the Legendre expansion

$$J_l^+(E, \mu) = \sum_{l=0}^9 (l + \frac{1}{2}) J_l^+(E) P_l(\mu).$$

- 8) $J_{lm}^{++}(E), J_{lm}^{+-}(E)$ - spherical harmonic coefficients of the positive direction, electron current angular distribution. The $J_{lm}^{+(\pm)}$ are the coefficients of the expansion

$$J^+(\theta, \varphi, E) = \sum_{l=0}^9 \left\{ J_{l0}^+(E) Y_{l0}(\theta, \varphi) + \left[\sum_{m=1}^l J_{lm}^{++}(E) Y_{lm}^+(\theta, \varphi) + J_{lm}^{+-}(E) Y_{lm}^-(\theta, \varphi) \right] \right\},$$

$$\text{where } J_{l0}^+(E) = \sqrt{\frac{2l+1}{4\pi}} J_l^+(E),$$

and the Y_{lm} are as defined for the BIGSLAB program.

- 9) $J_l^-(E)$ - Legendre coefficients of the polar angle distribution of $J^-(E, \mu)$ as a function of energy, E . The J_l^- are coefficients of the Legendre expansion

$$J^-(E, \mu) = \sum_{l=0}^9 (l + \frac{1}{2}) J_l^-(E) P_l(\mu).$$

- 10) $J_{lm}^{-+}(E), J_{lm}^{--}(E)$ - (same as item 8, but for negative direction electron current).

All of the above energy dependent quantities are defined for 10 energy bins of equal width $0.1E_0$. The μ -dependent quantities are defined for 10 μ -bins of equal width 0.1.

4.5 Program MCSPLIT , Quantities Calculated

- 1) $J^+(E, \mu, z)$ - positive direction electron current (normalized to unit particle incidence) across detector planes located at 3 values of z , as a function of energy, E , and polar angle (w.r.t. plane normal) cosine, μ .
- 2) $J^+(\mu, z)$ - total of $J^+(E, \mu, z)$ over all energy bins.
- 3) $J^-(E, \mu, z)$ - negative direction electron current (normalized to unit particle incidence) across detector planes located at 3 values of z , as a function of energy, E , and polar angle (w.r.t. plane normal) cosine, μ .
- 4) $J^-(\mu, z)$ - total of $J^-(E, \mu, z)$ over all energy bins.
- 5) $F^+(E, \mu, z)$ - positive direction electron flux (normalized to unit particle incidence) across detector planes located at 3 values of z , as a function of energy, E , and polar angle (w.r.t. plane normal) cosine, μ .
- 6) $F^+(\mu, z)$ - total of $F^+(E, \mu, z)$ over all energy bins.
- 7) $J_l^+(E, z)$ - Legendre coefficients of the polar angle distribution of $J^+(E, \mu, z)$ as a function of energy, E . The J_l^+ are coefficients of the Legendre expansion

$$J^+(E, \mu, z) = \sum_{l=0}^q (l + \frac{1}{2}) J_l^+(E, z) P_l(\mu).$$

- 8) $J_{lm}^{++}(E, z), J_{lm}^{+-}(E, z)$ - spherical harmonic coefficients of the positive direction, electron current angular distribution. The $J_{lm}^{+(\pm)}$ are the coefficients of the expansion

$$J^+(\theta, \varphi, E, z) = \sum_{l=0}^q \left\{ J_{l0}^+(E, z) Y_{l0}(\theta, \varphi) + \left[\sum_{m=1}^l J_{lm}^{++}(E, z) Y_{lm}^+(\theta, \varphi) + J_{lm}^{+-}(E, z) Y_{lm}^-(\theta, \varphi) \right] \right\},$$

$$\text{where } J_{l0}^+(E', z) = \sqrt{\frac{2l+1}{4\pi}} J_l^+(E, z),$$

and the Y_{lm} are as defined for the BIGSLAB program.

- 9) $J_l^-(E, z)$ - Legendre coefficients of the polar angle distribution of $J^-(E, \mu, z)$ - as a function of energy, E . The J_l^- are coefficients of the Legendre expansion

$$J^-(E, \mu, z) = \sum_{l=0}^9 (l + \frac{1}{2}) J_l^-(E, z) P_l(\mu)$$

- 10) $J_{lm}^{+-}(E, z)$, $J_{lm}^{--}(E, z)$ - (same as item 8, but for negative direction electron current).

All the above energy dependent quantities are defined for 10 energy bins of equal width $0.1E_0$. The μ -dependent quantities are defined for 10 μ -bins of equal width 0.1.

The three z values at which the above 10 quantities are evaluated correspond to the material interface plane and two additional detector planes, one on either side of and close to the material interface.

5. Application of the TIGER⁽¹⁰⁾ Monte Carlo Code to the Determination of Charge Deposition in Electron Irradiated Polymers

Electron irradiation experiments⁽¹⁸⁾ performed at RADC yielded measurements of electron beam current profiles in the polymer C_6H_9O . Six such experiments were made corresponding to normally incident electron beam energies of 0.4, 0.6, 0.8, 1.0, 1.2 and 1.4 MeV. Simulations of three of these experiments the 0.4, 1.0 and 1.4 MeV cases, were performed using the TIGER code from which energy and charge deposition profiles were calculated. The charge deposition histograms for the three cases are shown in Figures 28a,b,c. The smooth curves are least-squares spline fits to the histogram data. The smoothing algorithm⁽²⁰⁾ used performed piecewise cubic polynomial curve fits to the data points while taking into account their estimated errors (supplied in the TIGER runs). The smoothed Monte Carlo results were then numerically integrated using adaptive Simpson's rule⁽²¹⁾ to obtain the charge fraction values corresponding to the experimental penetration depth bins. The agreement between theory and experiment was found to be excellent. Table 3⁽¹⁸⁾ shows the comparison for the 1.0 MeV case. It was also found that the energy deposition profiles obtained with TIGER agreed well with those calculated using the Tabata⁽²²⁾ curve fit algorithm. The comparison of the energy deposition profiles for the 1.0 MeV case is given in Table 4. More complete tables are given in Ref. 18. The complete program listing (program CHDP) for these calculations is given in Vol. II.

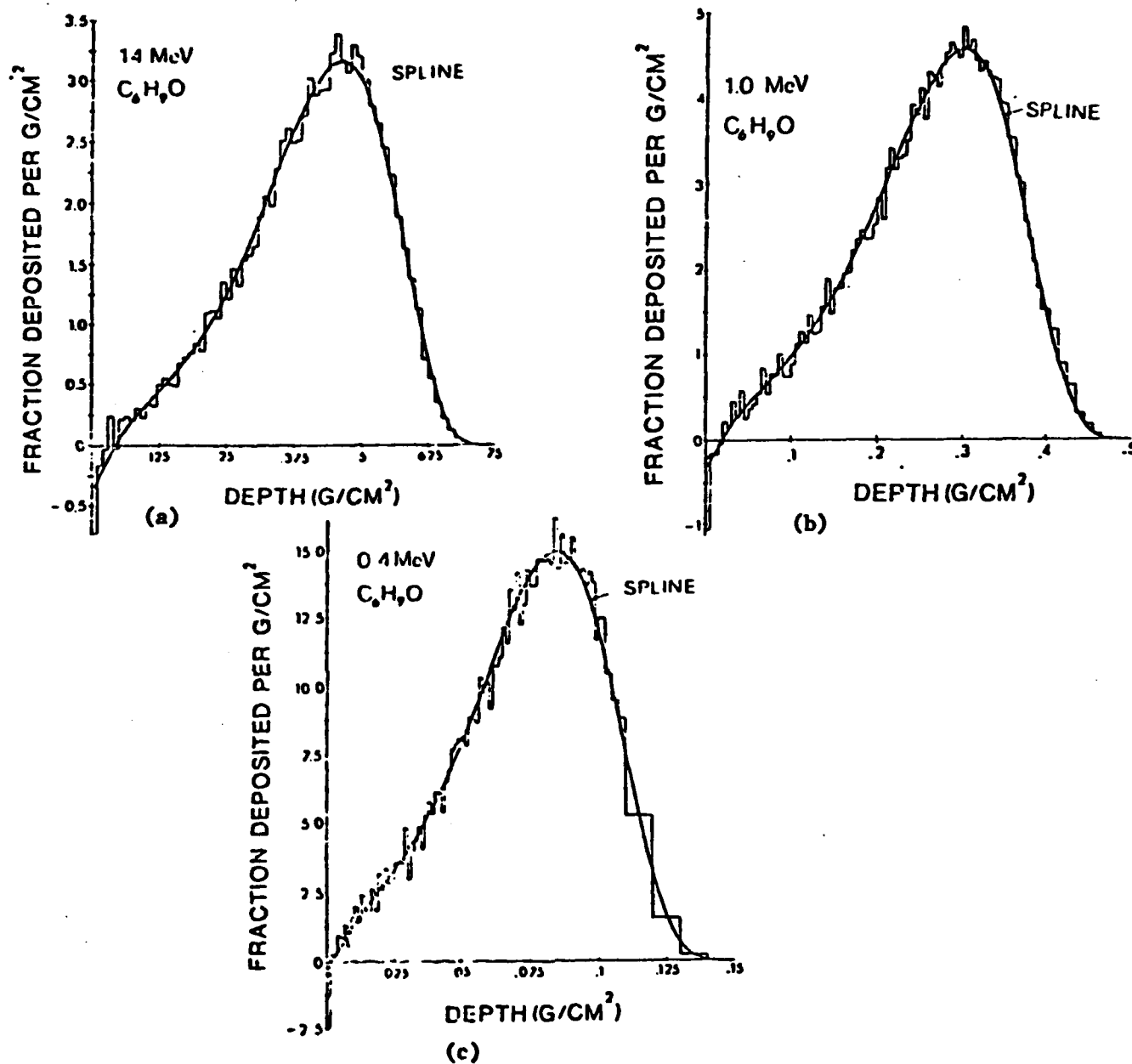


Figure 28. (Ref. 18) Monte Carlo histogram results fitted to smoothed spline for (a) 1.4 MeV, (b) 1.0 MeV, (c) 0.4 MeV, electron beams normally incident on C_6H_9O .

Table 3⁽¹⁸⁾

Comparison of Charge Deposition
Fraction in C₆H₉O Sheets of Width
for 1.0 MeV Electron 10.7 mg/cm²
Beam Source

DEPTH BIN LIMITS (mg/cm ²)	MONTE CARLO	EXP.
0-10.7	-.003 ^a	-.0072
10.7-21.4	-.001	.0003
21.4-32.1	.001	.0026
32.1-42.8	.003	.0039
42.8-53.5	.004	.0054
53.5-64.2	.006	.0067
64.2-74.9	.007	.0081
74.9-85.6	.008	.0096
84.9-95.6	.009	.0137 ^a
+ 0.5% ^a	+ .002	+ .0003
95.6-106.3	.011	.0118
106.3-117.0	.012	.0139
117.0-127.7	.014	.0152
127.7-138.4	.016	.0193
138.4-149.1	.017	.0183
149.1-159.8	.020	.0232
159.8-170.5	.022	.0241 ^a
+ 2% ^a	+ .002	+ .0007
164.3-175.0	.023	.0248 ^a
175.0-185.7	.025	.0256
185.7-196.4	.028	.0277
196.4-207.1	.030	.0300
207.1-217.8	.033	.0323
217.8-228.5	.036	.0345
228.5-239.2	.039	.0366
239.2-249.9	.041	.0388 ^a
+ 3% ^a	+ .002	+ .0004
249.2-259.9	.043	.0430 ^a
259.9-270.6	.045	.0427
270.6-281.3	.047	.0433
281.3-292.0	.049	.0443
292.0-302.7	.050	.0452
302.7-313.4	.050	.0468
313.4-324.1	.049	.0474
324.1-334.0	.047	.0443 ^a
+ 4% ^a	+ .002	+ .0004
324.8-335.5	.047	.0453 ^a
335.5-346.2	.044	.0420
346.2-356.9	.040	.0392
356.9-367.6	.036	.0358
367.6-378.3	.031	.0317
378.3-389.0	.025	.0273
389.0-399.7	.019	.0224
399.7-410.4	.014	.0177 ^a
+ 4% ^a	+ .002	+ 1.5%
409.7-420.4	.010	.0140 ^a
420.4-431.1	.006	.0095
431.1-441.8	.004	.0063
441.8-452.5	.002	.0039
452.5-463.2	.001	.0021
463.2-473.9	.000	.0009
473.9-484.6		.0004
484.6-495.3		.0001
+ 5% ^a	+ .001	+ 3%

Table 4⁽¹⁸⁾

Comparison of Energy Deposition Data
for Monte Carlo and Published Algorithm⁽²¹⁾
Techniques for 1.0 MeV Electron Beam
Source

10mg/cm ² bin midpoint [mg/cm ²]	Tiger smoothed Monte Carlo [MeV/(g/cm ²)]	Reference ²¹ [MeV/(g/cm ²)]
5.	1.83	2.02
15.	1.88	2.06
25.	1.98	2.12
35.	2.07	2.19
45.	2.15	2.28
55.	2.26	2.38
65.	2.38	2.48
75.	2.48	2.58
85.	2.61	2.69
95.	2.74	2.79
105.	2.87	2.89
115.	2.99	2.98
125.	3.10	3.07
135.	3.21	3.14
145.	3.30	3.21
155.	3.37	3.25
165.	3.42	3.29
175.	3.45	3.31
185.	3.47	3.31
195.	3.46	3.29
205.	3.45	3.25
215.	3.42	3.20
225.	3.36	3.13
235.	3.29	3.04
245.	3.21	2.94
255.	3.11	2.82
265.	2.96	2.69
275.	2.80	2.55
285.	2.64	2.40
295.	2.47	2.25
305.	2.27	2.09
315.	2.05	1.92
325.	1.82	1.76
335.	1.61	1.60
345.	1.39	1.44
355.	1.14	1.28
365.	.916	1.14
375.	.692	1.00
385.	.516	.833
395.	.361	.647
405.	.261	.500
415.	.162	.384
425.	.099	.294
435.	.050	.223
445.	.026	.169
455.	.010	.127
465.	.003	.094
475.	.002	.070

6. REFERENCES

1. T. R. Hill, "ONETRAN: A Discrete Ordinates Finite Element Code for the Solution of the One-Dimensional Multigroup Transport Equation," LA-5990-MS, Los Alamos National Laboratory (1975).
2. B. G. Carlson and K. D. Lathrop, "Transport Theory—The Method of Discrete Ordinates," Computing Methods in Reactor Physics, H. Greenspan, C. N. Kelber, and D. Okrent, Eds., Gordon and Breach, Science Publishers, Inc., New York (1968).
3. J. J. Duderstadt and W. R. Martin, Transport Theory, pp. 469-470, John Wiley and Sons, New York (1979).
4. Y. Ishiguro, "Multiregion Problems in Plane Geometry and Numerical Techniques in One-Group Transport Theory," Inst. Energia Atomica, Sao Paulo, Publication IEA491 (1977).
5. K. M. Case, Ann. Phys., 9:1, 23 (1960).
6. H. C. Van deHulst, Multiple Light Scattering, Tables, Formulas and Applications, Vol. 2., Academic Press, New York (1980).
7. J. E. Morel, Nucl. Sci. Eng., 71, 64 (1979).
8. L. V. Spencer, Phys. Rev., 98, 1597 (1955).
9. J. H. Renken and K. G. Adams, "DTF-69: One-Dimensional Multigroup Photon Transport Discrete Ordinates Code," ORNL-RSIC Code Package CCC-130, Radiation Shielding Information Center (1971).
10. J. A. Halbleib, Sr. and W. H. Vandevender, "TIGER: A One-Dimensional, Multilayer Electron/Photon Monte Carlo Transport Code," Sandia Laboratories Report SLA-73-1026 (1974).
11. M. J. Berger and S. M. Seltzer, "Stopping Powers and Ranges of Electrons and Positrons," U. S. Dept. of Commerce, National Bureau of Standards, Publication No. NBSIR 82-2550, 6, (1982).
12. L. V. Spencer, "Energy Deposition by Fast Electrons," National Bureau of Standards, NBS Monograph 1 (1959).
13. D. Liljequist, J. Phys. D: Appl. Phys., 11, 839 (1978).

REFERENCES (Continued)

14. L. Reimer and E. F. Krefting, "The Effect of Scattering Models on the Results of Monte Carlo Calculations," National Bureau of Standards Special Publication 460. Proceedings of a Workshop on the Use of Monte Carlo Calculations in Electron Probe Microanalysis and Scanning Electron Microscopy held at NBS, Gaithersburg, Maryland, October 1-3, 1975, pp 45H (1976).
15. L. Curgenven and P. Duncumb, "Tube Investments Laboratory Res. Rep. No. 303 (1971).
16. G. Love, M.G.C. Cox and V. D. Scott, J. Phys. D: Appl. Phys., 10, 7 (1977).
17. R. L. Myklebust, D. E. Newbury and H. Yakowitz, "NBS Monte Carlo Electron Trajectory Calculation Program," National Bureau of Standards Special Publication 460, 105 (1975).
18. A. R. Frederickson and S. Woolf, "Electric Fields in keV Electron Irradiated Polymers," IEEE Trans. Nuc. Sci., NS-29, No. 6, 2004, (1982).
19. E. Butkov, Mathematical Physics, Addison Wesley, pp. 380-381 (1968).
20. "ICSSCU-Cubic Spline Data Smoother," IMSL Library, 2, Edition 8, Chapter I, International Mathematical & Statistical Libraries, Inc. (1980).
21. L. F. Shampine and R. C. Allen, Jr., Numerical Computing: An Introduction, W. B. Saunders Co., pp. 238-242 (1973).
22. T. Tabata and R. Ito, Nucl. Sci. Eng., 53, 226 (1974).

END

FILMED

5-84

DTIC